

The Physical Basis of the Explosion Source and Generation of Regional Seismic Phases

**Jeffry L. Stevens
G. Eli Baker
Heming Xu**

**Science Applications International Corporation
10260 Campus Point Drive
San Diego, CA 92121**

Final Report

31 August 2007

APPROVED FOR PUBLIC RELEASE; DISTRIBUTION UNLIMITED.



**AIR FORCE RESEARCH LABORATORY
Space Vehicles Directorate
29 Randolph Road
AIR FORCE MATERIEL COMMAND
Hanscom AFB, MA 01731-3010**

NOTICE AND SIGNATURE PAGE

Using Government drawings, specifications, or other data included in this document for any purpose other than Government procurement does not in any way obligate the U.S. Government. The fact that the Government formulated or supplied the drawings, specifications, or other data does not license the holder or any other person or corporation; or convey any rights or permission to manufacture, use, or sell any patented invention that may relate to them.

This report was cleared for public release and is available to the general public, including foreign nationals. Qualified requestors may obtain additional copies from the Defense Technical Information Center (DTIC) (<http://www.dtic.mil>). All others should apply to the National Technical Information Service.

AFRL-VS-HA-TR-2007-1139 HAS BEEN REVIEWED AND IS APPROVED FOR PUBLICATION IN ACCORDANCE WITH ASSIGNED DISTRIBUTION STATEMENT.

//Signature//

ROBERT J. RAISTRICK
Contract Manager

//Signature//

PAUL TRACY, Acting Chief
Battlespace Surveillance Innovation Center

This report is published in the interest of scientific and technical information exchange, and its publication does not constitute the Government's approval or disapproval of its ideas or findings.

REPORT DOCUMENTATION PAGE				Form Approved OMB No. 0704-0188	
Public reporting burden for this collection of information is estimated to average 1 hour per response, including the time for reviewing instructions, searching existing data sources, gathering and maintaining the data needed, and completing and reviewing this collection of information. Send comments regarding this burden estimate or any other aspect of this collection of information, including suggestions for reducing this burden to Department of Defense, Washington Headquarters Services, Directorate for Information Operations and Reports (0704-0188), 1215 Jefferson Davis Highway, Suite 1204, Arlington, VA 22202-4302. Respondents should be aware that notwithstanding any other provision of law, no person shall be subject to any penalty for failing to comply with a collection of information if it does not display a currently valid OMB control number. PLEASE DO NOT RETURN YOUR FORM TO THE ABOVE ADDRESS.					
1. REPORT DATE (DD-MM-YYYY) 31-08-2007		2. REPORT TYPE Final Report		3. DATES COVERED (From - To) 18-08-2004 to 18-08-2007	
4. TITLE AND SUBTITLE The Physical Basis of the Explosion Source and Generation of Regional Seismic Phases				5a. CONTRACT NUMBER FA8718-04-C-0025	
				5b. GRANT NUMBER N/A	
				5c. PROGRAM ELEMENT NUMBER 62601F	
6. AUTHOR(S) Jeffrey L. Stevens, G. Eli Baker and Heming Xu				5d. PROJECT NUMBER 1010	
				5e. TASK NUMBER SM	
				5f. WORK UNIT NUMBER A1	
7. PERFORMING ORGANIZATION NAME(S) AND ADDRESS(ES) Science Applications International Corporation 10260 Campus Point Drive San Diego, CA 92121				8. PERFORMING ORGANIZATION REPORT NUMBER	
9. SPONSORING / MONITORING AGENCY NAME(S) AND ADDRESS(ES) Air Force Research Laboratory 29 Randolph Road Hanscom AFB, MA 01731-3010				10. SPONSOR/MONITOR'S ACRONYM(S) AFRL/RVBYE	
				11. SPONSOR/MONITOR'S REPORT NUMBER(S) AFRL-RV-HA-TR-2007-1139	
12. DISTRIBUTION / AVAILABILITY STATEMENT Approved for Public Release; Distribution Unlimited.					
13. SUPPLEMENTARY NOTES					
14. ABSTRACT The goal of this project is to understand explosion generation of shear waves. We quantify the contribution of surface reflected pS, S*, scattered Rg, and S directly generated by non-spherical source elements to local and regional S-wave phases in high and low velocity source media through simulations and data analysis. Data include a large set of historical local records of Semipalatinsk nuclear explosions digitized for this project by <i>Institute for the Dynamics of the Geospheres (IDG)</i> in Moscow, Russia, Soviet Deep Seismic Sounding experiments, regional records of NTS explosions, and local and regional Kazakh depth of burial experiment records. Simulations include non-linear, Lagrangian finite-difference calculations to model source generation, 2 and 3D finite-difference calculations to model near source scattering effects, a new modal scattering calculation to estimate the upper bound on Rg-to-Lg scattering, and wavenumber synthetics for multiple source and propagation effects. We find that source generated S waves dominate the regional S phases for a high velocity source region, and trapped pS dominates Lg for low velocity sources, although direct generation is necessary for Sn. Rg scattering may contribute in both cases, but at lower frequencies (< 1 Hz).					
15. SUBJECT TERMS Nuclear explosion, Shear waves, Lg					
16. SECURITY CLASSIFICATION OF:			17. LIMITATION OF ABSTRACT SAR	18. NUMBER OF PAGES 152	19a. NAME OF RESPONSIBLE PERSON Robert J. Raistrick
a. REPORT UNCLASSIFIED	b. ABSTRACT UNCLASSIFIED	c. THIS PAGE UNCLASSIFIED			19b. TELEPHONE NUMBER (include area code) 781-377-3726

Contents

Executive Summary	1
1. Introduction	6
2. Explosion Shear Wave Generation: High Velocity Source Media	6
2.1. Introduction	6
2.2. Previous Work: Observations of Lg and Implications for the Generation Mechanism	7
2.2.1. Historical	7
2.2.2. Lg Spectral Slopes	8
2.2.3. Spectral Nulls in Lg and Rg	8
2.2.4. Peaks in Coda Spectrograms	8
2.2.5. Coda Spectral Peaks	8
2.2.6. Source Amplitude and Corner Frequency Scaling of P and S Waves	9
2.2.7. Near Source Tangential Component Shear Waves	9
2.2.8. Lg Group Velocities	9
2.2.9. Source Array Estimates of Slowness to Identify Phases	10
2.2.10. The Correlation of Lg Amplitude with Yield	10
2.3. Previous Work: Numerical Simulations of Lg Generation Mechanisms	12
2.3.1. Generation and Scattering of pS and S*	12
2.3.2. Rg Upper Bound and Rg Scattering Calculations	12
2.3.3. Research Bearing on the Assumptions of Rg Upper Bound Calculations	12
2.3.4. Numerical Studies of Rg Scattering into Downgoing Body Waves	13
2.3.5. Direct Generation of S by the Explosion Source	14
2.3.6. Summary	15
2.4. Simulations	15
2.4.1. Introduction	15
2.4.2. Finite Difference Scattering Calculations: Trapping pS in High Velocity Media	15
2.4.3. Models	16
2.4.4. Scattering of the Surface P-to-S Converted Phase	16
2.4.5. Rg scattering Due to Topography	18
2.4.6. 3D Finite-Difference Calculations	20

2.4.7.	Upper Bound on Rg-to-Lg Amplitude from Modal Scattering Calculations	22
2.4.8.	Nonlinear Source Simulations Predict Depth, Yield, and Scaled Depth Dependence of S	23
2.4.9.	Depth and Frequency Dependence of S*	26
2.5.	Local Records of STS Explosions	28
2.5.1.	Local Sg	29
2.5.2.	Implications of Sg Travel Times for Source Generation	30
2.5.3.	Comparison of Local and Regional Records	32
2.5.4.	Regional Phase Amplitudes of Degelen Explosions.....	33
2.5.5.	Accuracy of Yield Prediction by Each Phase	35
2.5.6.	Regional Amplitudes of Degelen Compared with Balapan Explosions	36
2.6.	P and S Corner Frequencies of Local Degelen Recordings: Observations.....	38
2.7.	P and S Corner Frequencies of Local Degelen Recordings: Simulations.....	46
2.7.1.	Spectral Nulls are Azimuthally Dependent and Different for Rg and Sg.....	55
2.8.	Conclusions.....	56
3.	Explosion Shear Wave Generation in Low Velocity Source Media.....	59
3.1.	Introduction.....	59
3.1.1.	Previous Work on Co-located Overburied and Normally Buried Explosions.....	60
3.1.2.	Previous Work on Source Scaling and S and P Corner Frequencies	60
3.1.3.	Normally Buried vs. Overburied Explosions' Spectra at NTS: Low Frequency Null	60
3.1.4.	Normally Buried vs. Overburied Explosions' Spectra at NTS: Corner Frequencies	66
3.2.	Simulations	70
3.2.1.	Is a Vertical/Radial Lg Null Consistent With Other Mechanisms?.....	71
3.2.2.	Relative Contribution of Each Mechanism to Lg	72
3.2.3.	The Effect of a Temporally and Spatially Distributed Source.....	77
3.3.	Possible Sources of Spectral Nulls in Rg and Lg	80
4.	Kazakh Depth of burial explosions.....	87
4.1.	Introduction.....	87
4.2.	Kazakh Depth of Burial Explosions	87
4.3.	S Waves on Local Records	89
4.4.	Rg Decay Rate	91
4.5.	Regional Recordings.....	97

4.5.1. P and S Spectra at KUR	97
4.5.2. P and S Spectra at MAK	100
5. An Upper Bound on Rg to Lg Scattering Using Modal Energy Conservation.....	103
5.1. Summary	103
5.2. Introduction.....	103
5.3. Upper Bound Calculation	104
5.4. Surface Wave Excitation.....	105
5.5. Conversion to Lg.....	107
5.6. Rapid Scattering	108
5.7. Examples.....	109
5.8. Conclusions.....	114
6. The Effect of proximity to a previous explosion on near field peak velocities	114
References	117
Appendix A: Description of Local Semipalatinsk Seismograms	123
Appendix B: Nearfield Parametric Data from Semipalatinsk Explosions.....	125

Figures

1. Local data provided by IDG covers a range of yields and source depths. Data from the 1987/12/20 Degelen Explosion recorded from 20-80 km and filtered 1-5 Hz shows that S (marked at 3.3 km/s) is generated close to the source.1
2. Because of the free surface and variation of overburden pressure with depth, a real explosion is quite different from the idealized spherical source. The figures above show regions of nonlinear deformation for explosions in Degelen granite at three different scaled depths.2
3. Lg spectra for a point explosion and a CLVD with $\frac{1}{2}$ the explosion moment at depths of 600 meters in Degelen (left) and NTS (right) structures. Also shown is the upper bound on the spectra for scattered Rg to Lg. In a high velocity structure the direct CLVD dominates, while in a low velocity structure pS from the explosion is comparable to or larger than direct S from the CLVD. Rg scattering may be significant at low frequencies depending on what fraction of Rg is actually scattered to S waves trapped in the crust – the upper bound assumes that 100% of the energy in Rg scatters to Lg.....3
4. Radial record section from the DSS explosion Quartz 3 shows that S waves (blue) exist at all distance ranges and that Rg (red) can persist to large distances.....4
5. Near field peak particle velocities are higher for the first explosions (11, 12 and 15), and reduced later explosions (13 and 14) close to the earlier explosions (left). However, the difference in near field velocity is not apparent in m_b (right).....5
6. Yield and Nuttli's (1986a) m_b (Lg) estimates (left) and closer look (right) at the center of the plot.10
7. Models used in the scattering calculations. The far left plot shows the 1D homogenous base model. The second plot shows a 200 x 200 km shaded relief image centered on Degelen Mountain. The next 3 plots show 5 km-deep-by-10-km-wide slices of the heterogeneous models described in the text. The source is always 325 m deep, and its position for the models with topography is in the center (horizontally) of the snapshots shown.....16
8. Radial (left) and vertical (right) component Lg (3.6 to 3.0 km/s) at 225 km for each of the models. All five traces are plotted at the same scale. Percentages to the left of each radial and right of each vertical trace are rms amplitudes as a percent of the radial and vertical records' RMS amplitudes respectively for the homogeneous base model with topography added.17
9. Snapshots of the curl of the velocity just after the explosion, for the homogeneous base model (top row) and model with topography (bottom row) illustrate the effect of topography on pS. The black line in the lower row shows the free surface.17

10. Point explosion synthetic seismograms 20 km east of the source, for the models without (black) and with (red) topography. Traces in the same filter band are plotted on the same scale.	18
11. Cross-sections of vertical velocity (left) centered on Rg at 1, 2, and 3 seconds for the homogeneous base model with a flat free surface (left column) and the same model plus topography (right column). Each pair (same time, different models) is plotted with the same color axis.....	19
12. Q vs. frequency (left) and group velocity vs. frequency (right) for the homogeneous flat (black) and topographic (red) models. The decay of Q with frequency is due to the implementation of the Q model in the numerical calculations.	20
13. Three-component snapshots of the absolute value of velocity at 2 (2 left columns) and 4 (2 right columns) seconds, from 3D finite difference calculations for a topographic model (columns 1 and 3) and flat free surface model (columns 2 and 4). Velocities at each time are plotted on the same scale.....	21
14. Surface velocities from 0.25 to 1.5 seconds for the topographic model, with corresponding plots for the flat model at 1.5 and 5 seconds (right column of both upper and lower set of plots). The area shown increases with time for each plot. The topography of each area is shown in the bottom row.	21
15. Synthetic Lg seismograms (left) for a Degelen structure and sources with moments of $1e22$. The upper two traces are for CLVD Rg scattered to higher modes, for source depths of 300 m (top) and 50 m (middle). The bottom trace is for the Lg directly generated by a 300 m depth CLVD. Corresponding spectra are shown to the right.....	23
16. Near source permanent deformation due to cracking (upper) and yielding (lower) for explosions in a granite halfspace, at 51% (left), 78% (middle), and 210% (right) of scaled depth. In the cracking images, yellow squares indicate hoop cracks, red and blue lines indicate radial and in-plane tangential cracking respectively. Grid lines in both plots were initially straight. Positions shown above represent the permanent displacement after the explosions	24
17. Vertical component seismograms at 300 km, filtered from 1 – 3 Hz, from nonlinear source calculations in granite (Degelen structure) for a range of yields, depths, and scaled depths. Seismograms are scaled by yield. Bottom two traces are explosion and CLVD synthetics.	25
18. Log Lg amplitude from Figure 17 seismograms vs. log yield (left) and Log Lg amplitude divided by yield vs. scaled depth (right).....	25
19. Lg at 675 km from a spherical explosion source in the Degeeln velocity model at 0.5-1 Hz (left) and 3-4 Hz (right). Sources are from 50 to 600 m depth.	26
20. Predicted depth dependence of rms Lg amplitudes at 675 km from spherical explosion sources in the Degelen velocity model at different frequencies. Sources are from 50 to 600 m depth.....	27

21.	Lg/P ratios observed at BRVK (blue), predicted by nonlinear source calculations (red, labeled CRAM), and predicted for a spherical explosion source (green) for Degelen and Balapan explosions vs. yield (top left), depth (top right), and scale depth (bottom left). Degelen explosions are shallow and lower scaled depth than Balapan explosions. A vertical line separates the areas in the depth and scaled depth plots.	28
22.	Record section of vertical and Hilbert transformed radial seismograms from the 1.1 Kt 10-16-87 Degelen nuclear explosion, filtered from 0.5 to 3 Hz. Velocity is reduced by 5.5 km/s. The distinct Sg and Rg arrive at approximately 3.3 and 2.6 km/s respectively.	30
23.	Same data as Figure 16, but filtered from 1.5 to 3 Hz to reduce the dominance of Rg and allow Sg to stand out more clearly.	30
24.	Data from the 12/20/87 3.2 Kt Degelen explosion (left) and wavenumber synthetics right, from 7.5 to 2.9 km/s group velocity (to cut off the dominant Rg) and filtered from 1-5 Hz.	31
25.	Fits to the observed (squares) and synthetic (asterisks) P, S, and S-P times from the 12/20/87 3.2 Kt Degelen explosion and wavenumber synthetics.	31
26.	Overlain vertical and Hilbert transformed radial records of Balapan explosions (the closest record to 80 km distance for each event is plotted). To highlight S the large Rg is not plotted (left). Vertical records of the same events at BRVK, at 680 to 690 km, are plotted on the right. Both local and regional records are normalized by their P wave amplitudes. Yields and depths are noted to the left of the traces.....	32
27.	Same as Figure 25, but for Degelen explosions. Sn and Lg are prominent and large, except for the largest events, which appear more similar to the Balapan explosion records. The difference in S/P ratios may be accounted for by P and S source scaling.....	33
28.	1.2 Hz amplitude vs yield for 5 phases, from 41 vertical BRVK records of 14 Degelen explosions (top left). Amplitude residuals at 1.2 Hz vs. source depth for 13 Degelen explosions (top right). Slopes of log amplitude vs. log yield curves for each phase over a range of frequencies (bottom). Confidence bounds represent 25th and 75th percentiles.	35
29.	Individual phase amplitudes normalized by the Mueller-Murphy source for each event's depth and yield vs. scaled depth. Degelen events are to the left, below a scaled depth of .815, and Balapan events are to the right.	37
30.	Lg to P amplitude ratios at 0.7 (left) and 1.2 Hz (right), normalized similarly (blue squares) and by P and S-wave specific Mueller-Murphy sources (red circles) as described in the text vs. scaled depth. Degelen events are to the left, below a scaled depth of .815, and Balapan events are to the right.	37
31.	P (left) and S (right) spectra, normalized to unit rms amplitude below 1 Hz, for the station closest to 50 km for each event (ranging from 49 to 57 km). Lower row shows how the different corner frequencies lead to offsets in the curves.	39

32.	Average Pg and Sg spectral estimates from radial and vertical records at 22, 30, and 37 km (top), and at 59, 71, and 83 km (bottom) for the 3.2 Kt, 103 m depth Degelen explosion.....	40
33.	Individual spectra of radial and vertical component records, and for S, one tangential, from stations at 11.1, 16.2, and 23.9 km. The P spectral slopes increase above 10 Hz, and the S at approximately 6 Hz.....	41
34.	Stacks of radial and vertical records, and for the S spectra one tangential component record, from stations at 11.1, 16.2, and 23.9 km. Individual spectra are normalized to ensure equal weighting, so relative P to S amplitude is lost. The peak at 1-2 Hz is thought to be due to the instrument response. The P spectral slope increases sharply at approximately 10 Hz, and the S at approximately 6 Hz.	42
35.	Overlain radial and Hilbert transformed vertical P- and S-wave traces from stations at 11, 16, and 24 km (from top down) from the 12/15/1971, 1.4 Kt explosion. Records are from 0.5 seconds before P to just before the Rg arrival, and are filtered into three separate passbands. The in synch traces at the end of each set of records identify Sg, which is of similar amplitude to P, in the two lower passbands. There is no apparent S above 8 Hz, although P is still clear, evidence of a lower S than P corner frequency.....	43
36.	Pg and Sg corner frequencies vs. yield (top left), depth (bottom left), scaled depth (bottom right), and their ratio vs. yield (top left). The upper left also shows best fit curves to both Pg and Sg corner frequencies vs yield.	44
37.	Rg (dashed) and Sg (solid) spectra each of the Degelen explosions, at the closest station to each to have clearly separated good signal-to-noise S. Vertical line indicates 1 Hz.....	45
38.	Overlain vertical and Hilbert transformed radial seismograms from 29.7 and 30.6 km respectively from the 3.2 (left) and 78 (right) Kt Degelen explosions, in a range of passbands. The vertical line indicates 3 km/s group velocity.....	46
39.	Simple Degelen velocity model (solid) and a modified model that includes a gradual increase in velocity from 3.6 to 5.0 km/s in the uppermost 160 meters, and a more gradational increase from 5.2 to 6.2 km/s (dashed).	47
40.	P and S* spectra from spherical explosions source wavenumber synthetic seismograms at the depth of each Degelen explosion source, for the two Degelen velocity models of Figure 39.	47
41.	Predicted source spectra normalized by yield for largest (78 Kt, 267 m depth) and smallest (1.1 Kt, 82 m depth) Degelen explosions based on the Mueller-Murphy granite source spectra and RVP.	48
42.	Source spectra from the RVP for each Degelen explosion, normalized by yield.....	48
43.	Spherical explosion source synthetic P (upper) and S* (lower) spectra for simple model (left) and gradient model (right), convolved with spectra predicted based on the RVP for each Degelen explosion and normalized by yield.	49

44.	Spherical explosion source S*-to-P spectral ratios for the simple (left) and gradient (right) models.....	50
45.	P and S spectra from CLVD wavenumber synthetic seismograms at the depth of each Degelen explosion source, for the two Degelen velocity models of Figure 39.....	51
46.	P and S spectra from CLVD wavenumber synthetic seismograms at the depth of each Degelen explosion source, convolved with spectra predicted based on the RVP for each Degelen explosion and normalized by yield, for the two Degelen velocity models of Figure 39.	52
47.	CLVD S-to-P ratios for simple (left) and gradational (right) models.....	52
48.	Observed S-to-P ratios for records from each Degelen explosion recorded closest to 50 km distance.	53
49.	P, S, and Rg spectra (upper left, upper right, and lower left respectively) for a 325 m depth point explosion in a homogeneous Degelen velocity structure (solid) and the same model plus the actual Degelen topography in 3D (dashed).	54
50.	Seismograms at 25 km for a 325 m depth point explosion in a homogeneous Degelen velocity structure (upper) and the same model plus the actual Degelen topography in 3D (lower) in 3 passband.....	55
51.	Individual Rg spectra from local (67 – 89 km) vertical records at different azimuths have nulls at different frequencies (left). Stacked local Rg spectra (right, top trace) and BRVK Lg spectra don't have corresponding nulls.	56
52.	Network average normally buried event spectra for Pg, Lg, and Lg coda for all 3 components, normalized by the corresponding spectra of Techado. Also, the ratio of a straight line with a 1/f slope relative to Techado's spectra (black).	63
53.	Individual station spectra for Baseball Pg, Lg, and Lg coda windows from MNV (red), KNB (blue), LAC (green), and ELK (purple), plus the network average spectra (black).	64
54.	Individual station spectra for Techado Pg, Lg, and Lg coda windows from MNV (red), KNB (blue), LAC (green), and ELK (purple), plus the network average spectra (black).	64
55.	Network average Pg, Lg, and Lg coda spectra for all 3 components for Baseball (red), Caprock (purple), Glencoe (blue), Techado (aquamarine), and Borrego (green).	65
56.	P (red) and S (blue) spectral curves from MNV. Radial and vertical spectra are averaged for P, and all three components are averaged for S. Predicted P and S spectra for two events are shown at bottom left.	67
57.	P-to-S spectral ratios of five nuclear explosions recorded at 237 km distance, at MNV. P spectra are the radial and vertical average, and Lg spectra are based on all three components. Red lines show the predicted Mueller-Murphy source for each event (fit to minimize the DC offset between curves). All predicted spectral ratio curves are shown on the bottom left. Dashed maroon curves show the predicted spectral ratio for Caprock compared with the Techado observations	

	(upper left), and vice-versa, that is, the predicted spectral ratio for Techado overlain on the Caprock observations.....	68
58.	Same as Figure 57, but for station LAC, at 300 km distance.	69
59.	Average P-to-S ratios are MNV for the two largest (blue) and two smallest (red) events.	70
60.	Same as Figure 58, but for station LAC.	70
61.	Lg seismograms (upper) and spectra (lower) at 300 km from each of four mechanisms: pS (red) from a spherical explosion at 600 m depth, the upper bound on the scattered spherical explosion Rg (maroon), direct S (blue) from a CLVD with half the spherical explosion's moment, at 300 m depth, and the upper bound on the scattered CLVD Rg (cyan).....	72
62.	Same as Figure 61 (lower plot), but using a multi-taper spectral estimator.	74
63.	Lg spectra at 300 km from each of four mechanisms: pS (red) from a spherical explosion at 200 m depth, the upper bound on the scattered spherical explosion Rg (maroon), direct S (blue) from a CLVD with half the spherical explosion's moment, at 100 m depth, and the upper bound on the scattered CLVD Rg (cyan).....	74
64.	Lg and Lg coda seismograms (upper) at 300 km, separated by a vertical line at 100 seconds, and corresponding spectra of the Lg coda from each of four mechanisms: pS (red) from a spherical explosion at 600 m depth, the upper bound on the scattered spherical explosion Rg (maroon), direct S (blue) from a CLVD with half the spherical explosion's moment, at 300 m depth, and the upper bound on the scattered CLVD Rg (cyan).....	76
65.	Same as Figure 64, except the spherical explosion is at 200 m depth, and the CLVD of half the moment is at 100 m.	77
66.	Permanent deformation (left column) produced by 2D Lagrangian finite-difference simulations of the sources of Baseball (top) and Techado (bottom). Cracks predicted by the Baseball simulation are shown in the upper right. The Techado simulation produces no cracks.	78
67.	Lg spectra for the Baseball (top left), Techado (top right), point CLVD (bottom left), and spherical point explosion (bottom right). The vertical line is at 0.55 Hz in each plot.	79
68.	Lg spectra for the Baseball (black), a spherical point explosion (red), and a point CLVD (blue).	80
69.	Stations within 200 km of Quartz 3.	81
70.	Radial component record section east of Quartz 3, with Rg (red) and Sg (blue) color coded.....	82
71.	Three component record from 409 km east of Quartz 3. Phases are color coded, with P maroon, Lg blue, Lg coda green, and Rg (red).....	82
72.	Vertical component Rg spectra from recordings east of Quartz 3.....	83

73.	Stacks of vertical and radial component Rg spectra, and radial and tangential Sg spectra from recordings east of Quartz 3.	83
74.	Lg (blue) and Rg (red) spectra from the three component records at 409 km east of Quartz 3 shown in Figure 71.	84
75.	Vertical component record section west of Quartz 3, with Rg (red) color coded. Sg is only prominent on the horizontal component records.	85
76.	Vertical component Rg spectra from recordings west of Quartz 3.....	85
77.	Stacked vertical component Rg spectra from recordings east (red) and west (black) of Quartz 3.	86
78.	Seismograms (left) and spectra for a flat-lying model (upper seismogram and solid spectra) and the same model plus the topography at Degelen Mt. (lower seismogram and dashed spectra).....	87
79.	Hilbert transformed tangential and radial records in 3 passbands, at 12.7 km from the 300 m depth explosion show Rg (off axis on the tangential) where it aligns with vertical. Preceding the Rg, at ~3.8 seconds, is an S arrival (at 3.34 km/s) with comparable amplitude to P at less than 5 Hz, consistent with regional S spectra.	90
80.	Record sections at 2-5 Hz. Red and blue lines are 3 and 2 km/s respectively.....	90
81.	Vertical component seismograms from 0.8 to 4 Hz for 34 m depth Balapan explosion.	91
82.	Map of station and 34 m depth event locations.	92
83.	Fits to Rg group and phase velocity curves.	92
84.	S wave velocity model derived from data.....	93
85.	S wave Q model derived from data.....	93
86.	Amplitude data fit for 1.5 degrees of freedom.....	94
87.	Q vs. frequency from 0.5 to 4 Hz for the 34 m depth Balapan explosion.	94
88.	Q vs. frequency from .5 to 4 Hz for the 300 m depth Balapan explosion.	96
89.	3-component seismograms for the 50 (upper set), 300 (middle set), and 550 (lower set) meter depth of burial explosions recorded at 85 km distance, at station KUR, filtered from 0.5 to 1 Hz on the left, and 1 to 2 Hz on the right. The upper trace of each set is the tangential component. Below those are overlain the vertical and the Hilbert transformed radial seismograms. All records for each 3-component set are plotted on the same scale.	97
90.	P (left) and S (right) spectra of the three depth of burial events recorded at KUR.	98
91.	P (blue) and S (red) spectra of the three depth of burial events recorded at KUR, and the P-to-S spectral ratio (lower right).....	99
92.	Three component records of the depth of burial explosions recorded at KUR, filtered from 0.7 to 5 Hz. Each set of records is normalized by its vertical P wave amplitude.....	99

93.	P (left) and S (right) spectra of the three depth of burial events recorded at MAK.....	100
94.	P (blue) and S (red) spectra of the three depth of burial events recorded at MAK, and the P-to-S spectral ratio (lower right).....	101
95.	Three-component recordings at MAK for the three depth of burial explosions, at 0.7-1.2 Hz. normalized by the vertical P-wave amplitude. All records are plotted on the same scale.	102
96.	Three-component recordings at MAK for the three depth of burial explosions, at 1.5-3.0 Hz, normalized by the vertical P-wave amplitude. All records are plotted on the same scale.	102
97.	Calculated region of nonlinear deformation for a 31 kiloton explosion at 300 meters depth in a Degelen granite structure (from Stevens et al., 2005).	103
98.	Rg propagates from the origin to radius R where it is scattered to Lg.	104
99.	P velocity of upper 10 km used for the Degelen and Nevada test sites. Upper mantle shear velocity is 4.5 km/s.	110
100.	Model energy transfer function for Degelen and NTS structures.	110
101.	Lg velocity spectra calculated at a distance of 500 km in the Degelen earth structure at source depths of 100, 200, 400 and 800 meters. The four figures are for the direct explosion (upper left), direct CLVD (upper right), upper bound scattered explosion (lower left), and upper bound scattered CVLD (lower right) sources.	111
102.	Lg velocity spectra calculated at a distance of 500 km in the NTS earth structure at source depths of 100, 200, 400 and 800 meters. The four figures are for the direct explosion (upper left), direct CLVD (upper right), upper bound scattered explosion (lower left), and upper bound scattered CLVD (lower right) sources.	112
103.	Relative sizes of Lg velocity spectra from a point explosion, a point CLVD with half the explosion moment, and the upper bound scattered Rg to Lg for the same sources in Degelen (top) and NTS (bottom) structures at explosion depths of 300 meters (left) and 600 meters (right), with the CLVD at 2/3 of the explosion depth.	113
104.	Location of five Degelen explosions (left) and peak particle velocity vs. scaled range (right). Lines on the map show tunnels from the tunnel entrance to the shot location. Number is by the entrance point. Red lines are fault locations. Peak velocities are lower than is typical for some events located near previous events.	116
105.	m_b vs. yield for the events in Table 10. Red triangles mark the four events marked in Table 10 as close to another event and having reduced near field peak velocities. The solid line is the nominal m_b /yield curve for this region from Murphy (1995). The effect of previous events on local peak velocities (Figure 104) is not observed in m_b	116

Tables

1. Candidate Shear Wave Generation Mechanisms	2
2. Relative importance of S generation mechanisms.	5
3. Local/near regional data that contain P through Rg arrivals. SD stands for scaled depth, column 6 lists the number of distinct seismograms for each component (there are multiple recordings at many distances – we count these only once). The last column lists location within Semipalatinsk, D for Degelen or B for Balapan.	29
4. Parametric information for Degelen nuclear explosions for which we evaluate, along with events of Table 2, regional phase amplitudes at BRVK	33
5. Median Log ₁₀ yield errors +/- 2 SMAD.....	36
6. Local/near regional Degelen explosion parameters. SD stands for scaled depth, Pg and Sg columns present the respective corner frequencies in Hz.	43
7. Predictions based on numerical simulations.	57
8. Observations and implications for source mechanisms.	58
9. Metadata and availability of 3-component data from NTS events used in Patton and Taylor (1995) to investigate the effects of spall.....	61
10. Model from 34 m depth event Rg inversion.	95
11. Near Field Tabular Data collected by IDG.	115
12. Local/near regional data that contain P through Rg arrivals. SD stands for scaled depth, column 6 lists the number of distinct seismograms for each component (there are multiple recordings at many distances – we count these only once). The last column lists location within Semipalatinsk, D for Degelen or B for Balapan.	123
13. Local tabular data collected by IDG	125

Executive Summary

This report addresses two fundamental issues in nuclear monitoring: the explosion source and the generation and evolution of regional phases. This is a joint project between *SAIC* and the *Institute for the Dynamics of the Geospheres (IDG)* in Moscow, Russia. IDG provided extensive local records (10-100 km) and parametric data including explosion yields and depths for Degelen and Balapan nuclear explosions (Figure 1).

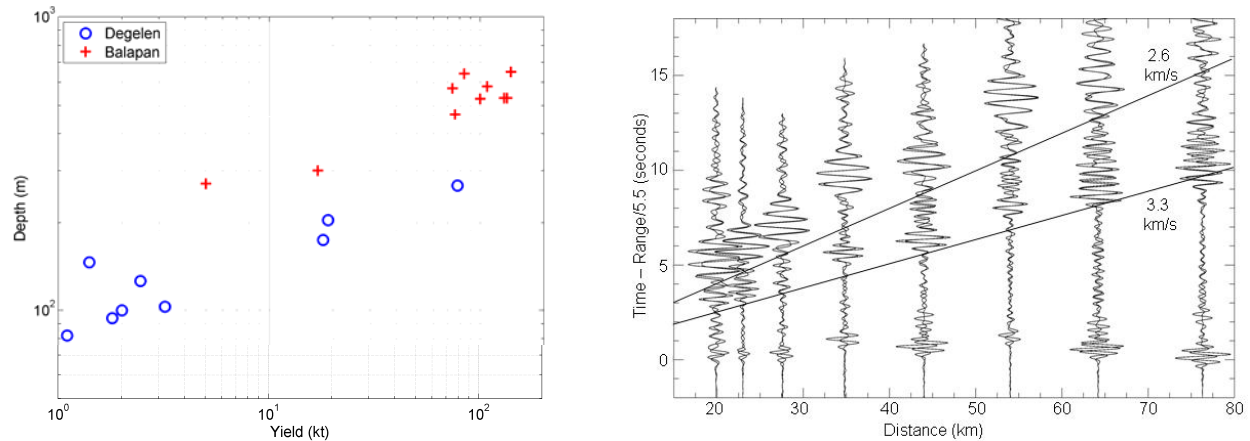


Figure 1. Local data provided by IDG covers a range of yields and source depths. Data from the 1987/12/20 Degelen Explosion recorded from 20-80 km and filtered 1-5 Hz shows that S (marked at 3.3 km/s) is generated close to the source.

Previous research has examined a number of possible explosion shear wave source mechanisms, most commonly demonstrating feasibility of one particular mechanism or another. We have attempted the next step, trying to distinguish between competing mechanisms. We do so by analyzing explosion seismograms, 3-components wherever possible, for a wide range of source conditions, from local to regional distances. Observations, ours and others, are modeled with numerical simulations. The focus is on identifying predicted differences in shear wave characteristics between different mechanisms that can be accurately estimated from existing data.

Table 1. Candidate Shear Wave Generation Mechanisms

Mechanism	Description
pS	The conversion of P to S at the free surface is a strong source of shear waves in a low velocity structure. In a high velocity structure, however, most S waves leak to the mantle.
Direct S generation	A realistic explosion source is not spherical due to the presence of the free surface and variation in overburden with depth. The source asymmetry generates S waves.
S*	S* is the nongeometric phase generated by the interaction of the curved P wavefront with the free surface. Unlike pS, S* is trapped in the crust in high velocity structures.
Rg scattering	A large fundamental mode Rg is generated by explosions. In some structures it disappears rapidly, while in others it persists to large distances. Some of this Rg scatters to regional S phases.

To understand explosion shear wave generation in high velocity media, we analyze newly obtained local data as well as historical regional records of Semipalatinsk (STS) explosions. We use synthetic calculations to quantify the contributions of four candidate shear wave generation mechanisms (Table 1). Modal scattering calculations provide an upper bound on the contribution of scattered Rg from CLVD and spherical explosion components of an explosion source. Nonlinear, Lagrangian, finite-difference source calculations (Figure 2) coupled to aavenumber integration code for propagation to regional distance predicts the S generated directly by nonspherical source elements.

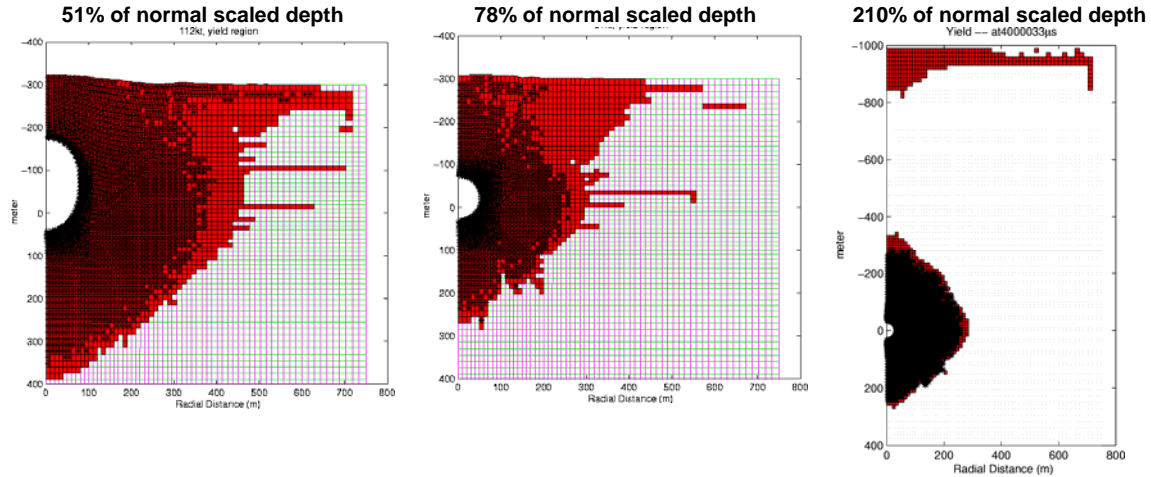


Figure 2. Because of the free surface and variation of overburden pressure with depth, a real explosion is quite different from the idealized spherical source. The figures above show regions of nonlinear deformation for explosions in Degelen granite at three different scaled depths.

These calculations also show that the amplitude of Lg produced by nonspherical source elements, for a range of scaled depths that more than spans those of the actual events, is less than the observed variation. The calculations are supplemented with wavenumber integration calculations for point spherical explosion and CLVD sources. Those calculations also predict the contribution of P-to-S scattering, both pS and S*. The calculations predict that shear waves generated by the nonspherical source elements provide the dominant contribution to Lg. The upper bound on the contribution of Rg is generally smaller except at low frequencies (Figure 3).

The upper bound on Rg to Lg scattering is derived assuming that all of the energy in Rg is forward scattered very readily into the higher modes than make up Lg.

Local events have impulsive Sg arrivals, distinct from the Rg (See Figure 1). The local Sg arrival times indicate that it comes from the source location at the origin time. Spectra of local events' Sg and Pg are similar, but Sg has a lower corner frequency, consistent with its generation within the same source volume as Pg. The local to near regional Sg spectral shapes are very different from those of the local Rg, which peak at much lower frequency.

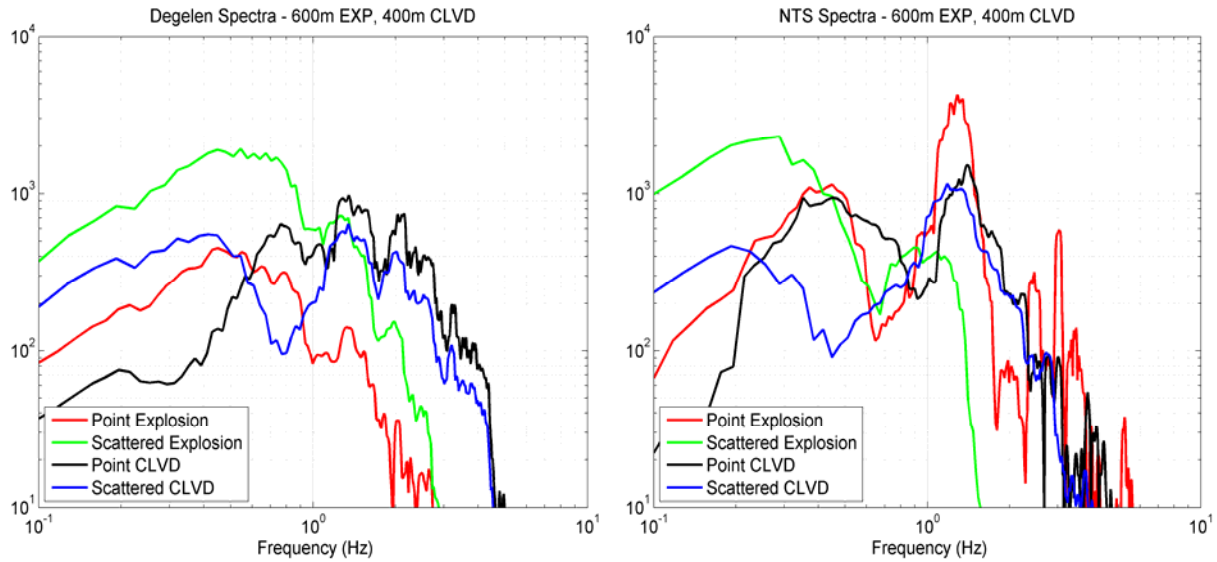


Figure 3. Lg spectra for a point explosion and a CLVD with $\frac{1}{2}$ the explosion moment at depths of 600 meters in Degelen (left) and NTS (right) structures. Also shown is the upper bound on the spectra for scattered Rg to Lg. In a high velocity structure the direct CLVD dominates, while in a low velocity structure pS from the explosion is comparable to or larger than direct S from the CLVD. Rg scattering may be significant at low frequencies depending on what fraction of Rg is actually scattered to S waves trapped in the crust – the upper bound assumes that 100% of the energy in Rg scatters to Lg.

Similar numerical studies of shear wave generation in low velocity source media predict that pS and direct S from nonspherical source elements both may contribute significantly to Lg. The upper bound on the contribution of scattered CLVD and spherical explosion Rg is again smaller. The data analysis focuses on additional investigation of previously studied, adjacent, overburied and normally buried Nevada Test Site (NTS) explosions, supplemented with analysis of Soviet Deep Seismic Sounding (DSS) records (Figure 4). A spectral null in the ratio of vertical component Lg spectra of normally buried to overburied events was interpreted previously as evidence that scattered Rg was the dominant source of explosion Lg. That work however simply assumed that pS and direct S from nonspherical source elements were negligible. As noted above, our calculations show the opposite. Further calculations indicate that pS and direct S from nonspherical source elements share the same spectral null, which is dependent on source structure, as that controls the modal structure. Other work besides that on the NTS explosions has linked common spectral nulls between Rg and Lg and concluded that Rg is the dominant source of Lg. The DSS records show that Rg spectral nulls, while persistent along one azimuth from the source, vary with azimuth. That is inconsistent with the source of the null being an

isotropic feature that depends solely on source depth, as assumed in previous work. The DSS records also show Sg, distinct from Rg, moving out at a different rate from the persistent Rg from very near the source and continuing to regional distances. The Sg and Lg have persistent spectral nulls that are distinct from the Rg spectral nulls. These observations are inconsistent with Rg scattering being the source of Sg and Lg.

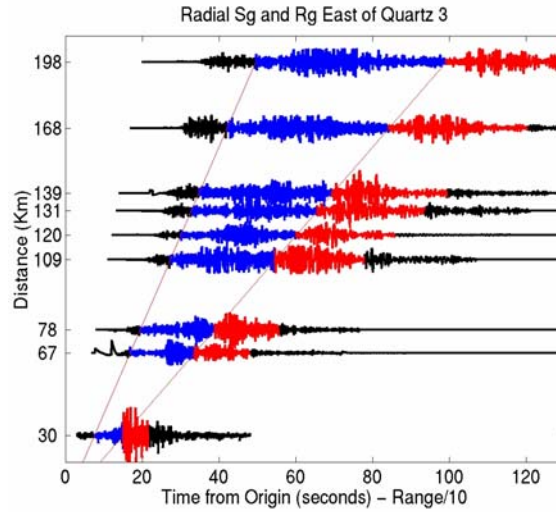


Figure 4. Radial record section from the DSS explosion Quartz 3 shows that S waves (blue) exist at all distance ranges and that Rg (red) can persist to large distances.

We have also re-examined records of the previously studied Kazakh depth of burial explosions. Comparison of local Rg and regional Lg and Sn spectra were previously interpreted as indicating that Rg scattering is the dominant source of regional shear waves. We suggest that variations in source conditions of the explosions makes interpretation ambiguous. Specifically, the effect on seismic generation of different source media for the shallowest explosion, and different amounts of cratering caused by each of the untamped explosions, has not been quantified. Also, variations in near source Sg amplitude, which moves out at a different velocity than Rg from the source of the three explosions, are consistent with variations in regional S amplitude. That does not rule out Rg contributing to regional S, but it is consistent with an alternate mechanism for generation of Lg and Sn, that is, source generation of S. Also, the conclusion of previous work rests on comparison of vertical component, regional, P-to-S spectral ratios, which showed an increase with increasing source depth. We estimate the near-regional and regional S spectra using horizontal components, which have higher signal-to-noise ratio, and find that the P-to-S spectral ratios do not necessarily increase with source depth.

Table 2 summarizes our conclusions about the relative importance of the different S generation mechanisms. All of the conclusions have qualifiers. As discussed in the report, all of the mechanisms depend to differing degrees on depth and scaled depth. pS is expected to be the dominant phase in low velocity structures and to contribute little to S in high velocity structures, however topography and crustal heterogeneity could redirect the S wave increasing high velocity S and reducing low velocity S. Table 2 summarizes our conclusions for most explosions over a fairly wide range of structural types, depths and scaled depths.

Table 2. Relative importance of S generation mechanisms.

Low Velocity Structure	High Velocity Structure
pS	Direct S generation
Direct S generation	S* (for shallow sources)
S* (for shallow sources)	Rg Scattering (larger < 1 Hz, larger for fundamental Love)
Rg Scattering (larger < 1 Hz, larger for fundamental Love)	pS (larger if redirected)

Addressing a different issue also important to nuclear monitoring, we have used near field STS measurements to investigate the effect of proximity of previous explosions on subsequent explosion sources. These show that peak particle velocities are reduced for events detonated near a prior event, but that m_b is not affected.

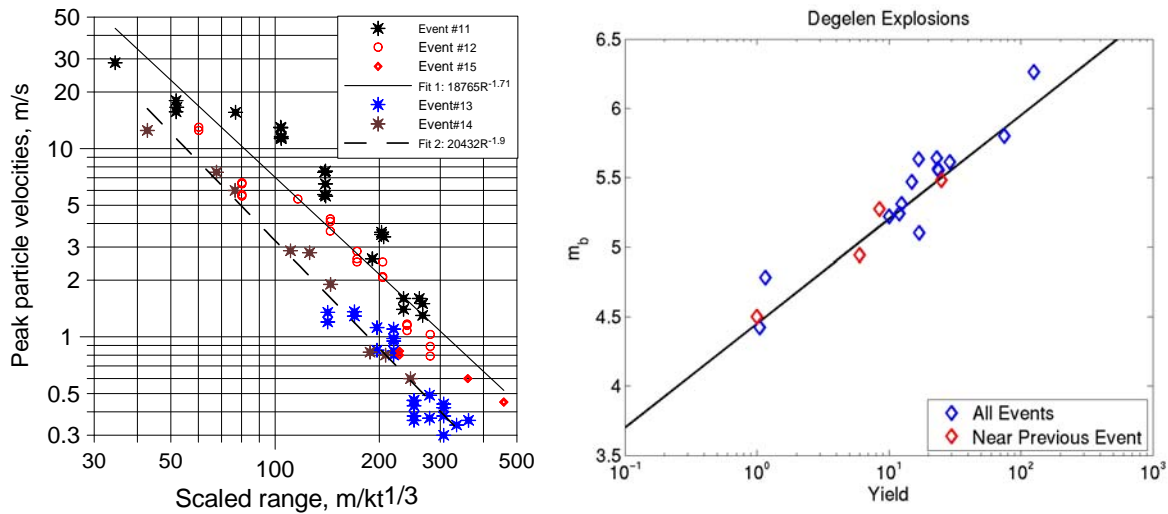


Figure 5. Near field peak particle velocities are higher for the first explosions (11, 12 and 15), and reduced later explosions (13 and 14) close to the earlier explosions (left). However, the difference in near field velocity is not apparent in m_b (right).

Our partners at IDG provided 309 local records, including 3-component seismograms of some events, recorded from 7 to 98 km from 19 Degelen and Balapan explosions. They also provided near-field parametric data, including peak velocities, from 19 more, mostly earlier STS explosions. They provided previously unknown yields and depths of these events. We include these data, the seismic records in SAC format and in simple ascii flat files, and the parametric data in ascii tables. Two appendices describe the data deliverable.

1. INTRODUCTION

The objective of this project is to determine the source physics and corresponding generation and evolution of local and regional seismic waves from nuclear explosions. This is a joint project between SAIC and Institute for the Dynamics of the Geospheres (IDG) in Moscow, Russia. The motivation for this work is that for regional discriminants to be transportable, the contributions of the physical sources of Lg and other regional phases must be quantitatively understood. Lg is of particular concern, because Lg calculated from a point explosion source in a plane-layered medium is smaller and more dependent on earth structure than observed.

Previous research has examined a number of possible explosion shear wave source mechanisms, most commonly demonstrating feasibility of particular mechanisms. Our goal is to distinguish between competing mechanisms. We do so by identifying, through a wide range of types of numerical simulations, predicted differences in shear wave characteristics between different mechanisms that can be accurately estimated from existing data.

We are preparing four manuscripts for publication. These provide chapters 2 through 5 of this final report. Chapter 2 focuses on high velocity media. We use synthetic calculations to introduce and quantify the candidate shear wave generation mechanisms in high velocity media. We then analyze newly obtained local data as well as historical regional records of Semipalatinsk (STS) explosions. This first chapter includes some material from a previous contract, specifically on 3D finite-difference calculations, for completeness in the discussion of numerical calculations. Chapter 3 examines shear wave generation in low velocity source media, focusing on additional analyses of previously studied co-located overburied vs. normally buried Nevada Test Site (NTS) explosions, supplemented with analysis of Soviet Deep Seismic Sounding (DSS) records. Chapter 4 extends the analysis of previously studied depth of burial explosion records. The 5th chapter introduces a new modal scattering method of predicting the upper bound on Rg-to-Lg scattering. An additional chapter, Chapter 6, uses near field STS measurements to investigate the effect of proximity of previous explosions on subsequent explosion sources. An appendix provides information on the data deliverable.

2. EXPLOSION SHEAR WAVE GENERATION: HIGH VELOCITY SOURCE MEDIA

2.1. Introduction

Lg is important to explosion yield estimation and earthquake/explosion discrimination, but the source of explosion generated Lg is still an area of active investigation. A spherical explosion in a whole space generates no shear waves. Thus, in the earth, shear waves from explosions must be generated by non-spherical components of the source or by conversion of P and/or Rg waves to S. The free surface is generally the most important factor for both source asymmetry and conversion of P and/or Rg to S, including S* the strongly depth dependent nongeometric phase generated by conversion of the curved P wavefront. In addition to the effect of proximity to the free surface, non-sphericity may be due to some asymmetry of the source or source conditions, including heterogeneity of the media and pre-existing stress, the latter leading to tectonic release.

Both source generation and scattering mechanisms have been investigated extensively, but conclusions regarding the source of Lg, of different studies, often with different source conditions, have not converged. Most studies have focused on demonstrating feasibility of a mechanism, as the data cannot guarantee uniqueness. This work is intended as the basis for the first of a two part series of papers which have the goal of better quantifying the relative contributions of each mechanism, identifying observations that can discriminate between possible mechanisms, and ultimately identifying which mechanism(s) dominate under different conditions. This chapter addresses explosion sources in high velocity source media, utilizing local and regional records from Semipalatinsk (STS) nuclear explosions. The 2nd paper in the series (Chapter 3) addresses explosion sources in low velocity media, focusing on reanalysis of an important data set, nearly co-located overburied and normally buried explosions at Nevada Test Site (NTS). It also uses data from the so-called Peaceful Nuclear Explosions (PNEs) of the former Soviet Union to address the origin of Rg and Lg spectral nulls. These papers will be complemented by a third article, which Chapter 4 forms the basis of, focusing on reanalysis of another important previously studied data set, from the depth of burial experiments at the Balapan area of STS.

The data analyses are complemented by a variety of numerical simulations, done to model specific observations and more generally, to bound the theoretical contributions of different mechanisms. We use nonlinear source calculations coupled to wavenumber synthetics, compared with point explosion and compensated linear vector dipole (CLVD) synthetics, to investigate the effect of depth and scaled depth on S-wave generation and regional S-wave phases. The CLVD is the lowest order nonspherical correction to the spherical source and is commonly used to approximate the nonspherical source elements of an underground explosion source, which are due to proximity of the free surface. 2D and 3D finite-difference calculations are used to investigate effects of topography and lateral heterogeneity on P-to-S and Rg-to-S scattering and trapping of the scattered S. Chapter 5 forms the basis of a fourth article, describing a new type of modal scattering calculation that lets us place an upper bound on the contribution of Rg to Lg. The final chapter uses new near field parametric data from historical STS explosions, delivered by IDG for this project, to investigate the effect of proximity to a previous explosion on particle velocity.

2.2. Previous Work: Observations of Lg and Implications for the Generation Mechanism

2.2.1. Historical

Although the goal of this work is to understand how shear waves are generated by explosion sources, we have so far only discussed Lg. This is because, for regional seismograms, Lg is often the largest and most consistent phase and so provides the best opportunity for observing the shear waves. It was identified very early in the history of modern seismology (Press and Ewing, 1952) because of its amplitude, despite being a diffuse, scattered phase, not generally associated with any apparent ray path. Its very definition as whatever energy arrives within a particular group velocity window (typically 3.6 to 3.0 km/s), distinguishes it from other regional phases, which typically are impulsive and can be picked.

2.2.2. Lg Spectral Slopes

That explosion Lg spectral slopes are steeper (drop off faster with increasing frequency) than Lg from earthquakes has been widely cited. This has been interpreted as evidence of Rg scattering (e.g. Gupta and Wagner, 1998) because Rg also falls off rapidly with frequency. Goldstein (1995) however provides an alternate explanation. Since Lg is generated by a shallow source, it excites different modes, and preferentially excites surface wave modes that are trapped in shallow, low Q layers and therefore attenuate more rapidly. This argument is supported by the result of Priestley and Patton (1997), who found that NTS explosion Lg attenuates more rapidly than that of earthquakes near NTS, which they attribute to higher Q in the shallowest layers. Distinctly different modal excitation was confirmed by Baker et al (2004), who observe different Lg group velocities from explosions and earthquakes. Because any shallow S-wave source, including conversion from P and/or Rg presumably will preferentially excite shallow modes, the steep explosion Lg spectral slope does not by itself rule out any mechanism.

2.2.3. Spectral Nulls in Lg and Rg

Spectral nulls in vertical component Lg have been interpreted as evidence of Rg scattering (e.g. Patton and Taylor, 1995; Gupta et al, 1997). Patton and Taylor (1995) show that the vertical component Lg spectra of normally buried explosions at NTS, divided by that of nearby overburied explosions, have a distinct spectral null. They argue that this is due to Rg generated by a CLVD source between the explosion depth and the surface, and then scattered into Lg. More recently, Patton and Phillips (2006), present an argument for the null resulting from interference between the Rg from the spherical part of the explosion source and the Rg from the non-spherical part, modeled as a CLVD, which again is scattered into Lg. Chapter 3 examine these data further. Gupta et al (1997) reviewed Lg spectra generated by explosions and concluded that the spectra are consistent with Rg scattering from a CLVD source, and that the period of the observed spectral dip scaled with source depth.

2.2.4. Peaks in Coda Spectrograms

Gupta et al (2005) showed that the amplitude of explosion spectrograms decreases more gradually from explosion Lg through the subsequent coda than do earthquake spectrograms, and that peaks within the coda decrease in both amplitude and frequency with time. They interpret these peaks as evidence of discrete scattering from Rg to S in the vicinity of the source. Saikia et al. (2005) make similar observations of peaks within the coda of shallow events, but not of normal-depth earthquakes. They also attribute the peaks to Rg-to-S conversion.

2.2.5. Coda Spectral Peaks

Mayeda, et al. (2000) suggest that decreasing frequency of coda spectral peaks from 0.25 to 0.9 Hz with amplitude at NTS is an effect of Rg-to-S scattering. Peak frequencies correlate with depth of burial but not scaled depth. Phillips et al. (2002) also observe decreasing frequency of coda spectral peaks, from 0.8 to 3 Hz, with spectral amplitude for Degelen explosions. Myers et al (1999) also present an explanation of differences in amplitude and spectral shape of regional S from the Kazakh depth of burial explosions as an effect of Rg-to-S scattering. Those data are examined further in Chapter 4.

2.2.6. Source Amplitude and Corner Frequency Scaling of P and S Waves

Recent work on source scaling of explosion S and P waves, some of it conflicting, also bears on the mechanisms generating the S and P waves. Fisk et al (2006) find for Degelen and Balapan at Semipalatinsk (STS), Lop Nor (LN), and Novaya Zemlya (NZ) that P and S corner frequencies scale similarly with yield, with the S-wave spectra shifted to lower frequency by the ratio of the source S-wave to P-wave velocity ratio. They conclude that S-waves are generated by mechanisms operating on the same length scale as the P-wave mechanism, which is consistent with S-waves being generated within the same source volume as the P-waves, and is inconsistent with P-to-S conversion, which should produce similar corner frequencies in both phases' spectra. Fisk et al (2007) make a similar finding for the Nevada Test Site (NTS). The Rg-to-S scattering mechanism does not predict a consistent relationship between P and S corner frequencies, as the Rg corner frequency varies with source depth. Murphy et al (2006) perform similar analyses of STS and LN data, and also find that the source scaling of P and S are similar, with S-wave corner frequencies reduced by the source S/P ratio. Stevens et al (2006) present results for Degelen and Balapan consistent with Fisk et al (2007) and Murphy et al (2006). Patton and Phillips (2006) also investigate source scaling of P and Lg coda for multiple test sites, and conclude that there is a difference in the source scaling. The data sets used in these studies overlap, so the discrepancy between observations must be, as noted by Patton and Phillips (2006), due to differences in the methods used by each group. This is an important observation, and resolving the contradictory results presented should be pursued in further investigations.

2.2.7. Near Source Tangential Component Shear Waves

The existence of tangential component shear waves has long been recognized, and the transfer of energy from the vertical and radial to the tangential component has been a longstanding area of inquiry, with explanations proposed based on anisotropy (Maupin, 1990) and along path scattering (e.g. Kennett and Mykkeltveit, 1984, McLaughlin et al., 1997). Gupta and Blandford (1983) investigated generation of transverse shear waves from explosions. On 3-component records 100s of meters from the sources at shot depth, they observed much smaller transverse than radial displacements for Salmon, a tamped nuclear explosion in salt, and from Gasbuggy, a deep explosion in sedimentary rocks. Starting at tens of km distance, they present evidence of the tangential-to-radial amplitude ratio increasing with distance, which they attribute to scattering. Stevens et al. (2004) observe however, for over- and underburied events in high and low velocity media, and even decoupled explosions, that tangential shear waves are ubiquitous near the source, and often arrive sooner and are larger than on the radial or vertical components, suggesting their generation at or very near the source is more common than gradual conversion over a significant distance.

2.2.8. Lg Group Velocities

Baker et al (2004) attribute slow Lg group velocity for very shallow events, observed in two different tectonic environments, to the greater excitation of shallow modes. Preferential trapping of higher frequency energy, due to their narrower eigenfunctions, near the surface in slow, low Q media not only explains the slow group velocities but also is consistent with attenuation causing the relative steepness of Lg spectral slopes.

2.2.9. Source Array Estimates of Slowness to Identify Phases

Hong and Xie (2005) use 67 Balapan explosions recorded at the regional station BRVK to estimate phase velocities of the regional phases. They found the 0.5 to 2 Hz Lg phase velocity of 4.2 km/s to be consistent with crustal S multiples, and inconsistent with lower phase velocity expected from scattered Rg. They conclude that although scattered Rg could contribute to Lg, it cannot be the dominant source of Lg energy.

2.2.10. The Correlation of Lg Amplitude with Yield

Lg amplitude was first shown to be an accurate measure of NTS nuclear explosion magnitudes by Baker (1970a,b). A strong correlation between Lg amplitude and explosion yield was demonstrated by Nuttli (1986a), and confirmed and extended to other areas by Nuttli (1986b, 1987, 1988), Patton (1988), Hansen et al. (1990), Ringdal et al. (1992), and Israelsson (1994). These works demonstrated that $m_b(Lg)$ is stable for a given source area and station, and is apparently independent of depth or scaled depth. Further, for a given test site, the same medium, and a consistent set of stations, Lg amplitudes correlate between stations.

The extent to which this correlation can constrain source generation mechanisms depends on the scatter in plots of Lg amplitude with yield. The amplitudes reported by Nuttli (1986a) for NTS explosions and shown in Figure 12 of that paper are replotted in Figure 6. We have updated the yields (Springer, et al, 2002) and removed data from explosions above the water table, as the data were originally assumed to be in hard rock and in tuff below the water table. While there is good correlation with yield from 12 to 1300 Kt, indicating why Lg is useful for yield estimation, for constraining shear wave generation mechanisms we are interested in the scatter, shown on the right. For yields of 110 and 115 Kt, the $m_b(Lg)$ s are 5.86 and 6.09, a 70% difference in Lg amplitude. Similarly, four explosions with $m_b(Lg)$ from 6.04 to 6.09 have yields from 220 to 115 Kt. Nuttli (1986b) shows similar scatter for $m_b(Lg)$ vs. $m_b(P)$ of Novaya Zemlaya (NZ) explosions. For a single value of $m_b(P)$ or $m_b(Lg)$, values spanning 0.3 magnitude units, or a factor of two in amplitude are typical.

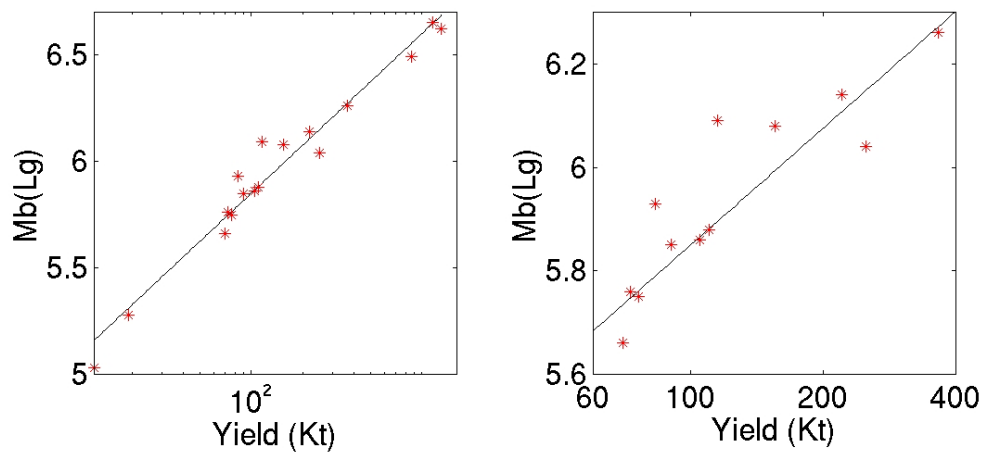


Figure 6. Yield and Nuttli's (1986a) $m_b(Lg)$ estimates (left) and closer look (right) at the center of the plot.

Later work shows similar, and even greater, variance. In Patton (1988), the plots presented of $m_b(\text{Lg})$ vs $\log(\text{yield})$ show a full magnitude unit, a factor of 10 in amplitude, of fairly uniform variation in $m_b(\text{Lg})$ for events around 100 Kt recorded at KNB, and at least 0.6 magnitude units of uniform variation for a 4 station network averaged $m_b(\text{Lg})$. That variation is observed after removal of outliers. That is the range of variation that we might compare with predictions of variation with depth and scaled depth for different mechanisms. This reported variation however must be considered a lower bound, for the reason that follows.

Many Lg amplitude measurements may be biased by, or may even consist entirely of P-coda rather than Lg. For this work, the term Lg refers to energy arriving within the Lg window (typically 3.6 to 3.0 km/s group velocity) only when the amplitude in that window is significantly greater than that preceding the Lg window. That is the only situation where we can reliably infer that the energy within the Lg window is predominantly composed of shear waves generated at or near the source that have traveled as shear waves trapped in the crust (or equivalently, as higher mode surface waves). When the amplitudes in the Lg and pre-Lg windows are comparable, there is no discernable Lg as it is defined above. This distinction must be made explicitly because the use of the term Lg to refer to whatever is measured within the Lg window has historically been the norm. It does not matter for empirical estimation of yield whether the energy in the Lg window represents coda or shear waves generated at or near the source, but the distinction is crucially important for constraining models of Lg generation. Since coda correlates more strongly with magnitude than direct Lg (e.g. Mayeda, 1993; Mayeda and Walter, 1996), without a comparison of Lg and pre-Lg amplitudes, very strong correlations of coda with yield could mistakenly be interpreted to imply strong correlation of source or near source generated shear wave amplitudes with yield.

Nuttli's papers (1986a, 1986b, 1987, 1988) on the $m_b(\text{Lg})$ -yield relationship, where $m_b(\text{Lg})$ is calculated from the Lg amplitude in the 3.6 to 3.2 group velocity window, do not explicitly state the S/N criteria for identifying Lg, but note that for small events the microseismic noise prevented measurement, so it appears Nuttli compared the amplitude in the Lg vs. pre-event windows. Thus it's not clear how often the Lg used was larger than the pre-Lg amplitude. Nuttli (1986a) shows seismograms from two NTS explosions recorded at BRK. It is difficult to follow the trace, or to be certain where the peaks are, in either of the WWSSN paper records. In one, it appears most likely that the arrivals in the Lg window are no larger than those preceding Lg. In the second, it looks like peaks in the Lg window could be larger than those in the pre-Lg window. No seismograms are shown in the other papers, which perform similar analyses for the Shagan River, Degelen, and Novaya Zemlya test sites. The least scatter in any of Nuttli's papers is in the $m_b(\text{Lg})$ vs. $m_b(\text{P})$ comparison for 30 Novaya Zemlya (NZ) explosions (Nuttli, 1988). Propagation from NZ to all the stations used is across the Barents Sea. Although the crust there is continental, it thins and is overlain by very thick sediments which strip out Lg, particularly from shallow events. The "Lg" Nuttli measured for the NZ study is thus likely predominantly coda, which, as mentioned above, predicts yield better than Lg does, but does not bear on S-wave generation.

2.3. Previous Work: Numerical Simulations of Lg Generation Mechanisms

2.3.1. Generation and Scattering of pS and S*

It has long been recognized that shallow explosions produce large nongeometric shear waves, called S*, when the source is close enough to the free surface or other subsurface interface that the wavefront is strongly curved (Gutowski et al., 1984; Vogfjörð, 1997). Although often assumed to be an unlikely source of Lg due to its strong depth dependence, Vogfjörð (1997) showed that at 1 Hz, it could contribute significantly and in some cases dominantly to Lg. The amplitude of 1 Hz S* can be very large to surprising depths, and Vogfjörð showed that the strength of its contribution depends largely on whether the energy, which peaks in a narrow range of take-off angles that depend on source P and S-wave velocities, is trapped in the crust. Under appropriate conditions, Vogfjörð finds that it can be the dominant source of Lg.

Xie et al (2005) used a combination of finite-difference calculations and an analysis of slowness to determine which phases scattered near the source, by heterogeneity within the crust, will contribute to Lg. Specifically, they simulated the contribution of trapped pS and S* to Lg, finding greater high frequency contribution from pS and greater low frequency contribution from S*. Myers et al. (2006), using the 3D structure at NTS, also find that S is enhanced relative to P at 1 Hz due to near source topographic scattering from P.

2.3.2. Rg Upper Bound and Rg Scattering Calculations

There is a large body of numerical modeling work that bears on Rg scattering, much of it focused on the contribution of scattered Rg to Lg. Most have focused on demonstrating the feasibility of the mechanism. Attempts have also been made to quantify the contribution to Lg from scattered Rg (Stevens et al., 2007). Stevens et al. (2007) provide an explicit upper bound on the amplitude of Lg attainable from Rg. We use those results below to compare the maximum attainable Lg amplitude due to Rg scattering with Lg due to S*, pS, and direct S from nonspherical source elements.

Xie et al (2006) extend the method of Xie et al. (2005) to 3D and to topographic scattering, and apply it to Rg. One interesting result is that the increase in Lg due to topographic scattering is similar to, but somewhat greater than the loss of Rg, although their spectra are similar. The authors' speculate that additional S*-like scattering from P augments the low frequency Lg. Adding realistic attenuation to the surface layer further diminishes high frequency Lg relative to low. Jih (1995), reports that energy scattered from Rg into body waves by topography or heterogeneity commonly propagates into the mantle, and so does not contribute to Lg. Intrinsic attenuation however, disrupts the modal structure, leading to conversion of Rg to higher modes, which are trapped in the crust.

2.3.3. Research Bearing on the Assumptions of Rg Upper Bound Calculations

The work on observations of Rg scattering to teleseismic P, and teleseismic P scattering to Rg, bears on the assumption in the upper bound estimate of all Rg scattering to higher modes. Studies of teleseismic P to Rg scattering provide evidence that steeply incident P-waves scatter into Rg, and that the extent of such scattering correlates strongly with topographic roughness.

Reciprocity suggests that Rg should scatter into P waves that will propagate into the mantle. Indeed, this is suggested as the main source of coherent teleseismic P coda, that is, the coda that is generated near a shallow source and then travels as teleseismic P-waves (Dainty, 1990).

There are also specific instances in which large Rg phases are observed to be scattered from teleseismic P-waves by topographic features. Key (1967) found that apparent sources of Rg, peaked just above 1 Hz, correlate closely with topographic features near the Eskdalemuir array. The topographic relief of the strongest scatterer at Eskdalemuir is approximately 600 feet (183 m). The group velocity was estimated to be 2.5 km/sec, so at 1 Hz, the relief is about 7% of the wavelength. This is much less than the prediction of Frankel and Clayton (1986) that relief should be approximately half the wavelength to scatter Rg, but the scatterer is also associated with a deep river valley, and resonance in the valley or strong impedance between sediments and bedrock could play a role. Similarly, Bannister et al (1990) found that 1-3 Hz Rg is scattered from teleseismic P-waves at two distinct locations with “prominent topography” near the NORESS array. Hedlin et al (1991) find that one of the locations is associated with a very sharp topographic feature at the edge of a deep lake. They conclude that steepness as well as total relief of the topography is important, as is the existence of a low velocity basin. The location Hedlin et al (1991) find for the second prominent scatterer is not associated with any surface feature, indicating that subsurface anomalies may also scatter Rg effectively. Revenaugh (1995) showed that Rg scatters from teleseismic P-waves due to much more subtle topographic relief. Applying migration to envelope functions of teleseismic coda recorded at the stations of the southern California seismic network (SCSN), he finds a clear correlation between topographic roughness and the extent of scattering.

Another set of studies address the near source scattering of Rg to teleseismic P coda. Gupta and Wagner (1992), using Degelen and Shagan River explosions recorded at the NORESS and EKA arrays, find that the ratio of P-to-P coda amplitudes follow a depth dependence predicted by near source Rg to P scattering. The correlation with depth is observed for 0.5-2 Hz data, but not for 3-5 Hz where Rg is not expected except for the shallowest events. They conclude that most explosion teleseismic P coda is due to near source Rg scattering. Also, for two explosions at the same location, the ratio of shallower to deeper explosions teleseismic P coda increases with time, which they interpret as evidence of more Rg for the shallower event leading to a progressive increase in scattered energy relative to that seen for the deeper event.

In yet another type of study, Wuenschel (1976) used a seismograph array and a downhole instrument to identify energy scattered from incident P-waves beneath a sedimentary layer as Rg, and to identify downgoing energy beneath the sediments as P, scattered from the Rg. These studies indicate that much of the energy in Rg is not available to scatter to S-waves that will be trapped in the crust.

2.3.4. Numerical Studies of Rg Scattering into Downgoing Body Waves

Levander (1990) reviewed the literature on this subject up to that date, and the following material is taken directly from that paper. Hudson (1967) derived the expressions for scattering of body waves off of a 3 dimensional topographic irregularity and calculated that scattered Rg amplitude would be up to half of the incident P-wave wave amplitude for the shallow river valley observed by Key (1967), consistent with observations. Results of subsequent studies of several

types are similar (Bouchon, 1973; Bard, 1982; Boore et al, 1981; Gangi and Wesson, 1978), as they find that the amplitude of topographically scattered Rg is a significant fraction of incident P and SV wave amplitudes.

P to Rg scattering by sediment filled valleys has been another area of extensive investigation. Bard and Bouchon (1980) used discrete wavenumber simulations to show that significant teleseismic P and SV to Rg scattering will occur in both flat bottomed and cosine profile valleys. Levander and Hill (1985) used finite difference simulations to show that the amplitude of the scattered wavefield from teleseismic P-waves is composed of the fundamental and first two Rayleigh modes and is a large fraction of the incident signal.

Ruud et al (1993) simulated Rg propagation with 2D finite-difference calculations and combinations of Von Karman distributed perturbations of layer thicknesses, lateral velocity variations, and topography. They found that Rg was much more sensitive to topography than to irregularity at other interfaces or to random lateral heterogeneities in velocity and infer that the hilly topography around NORESS and NORSAR are responsible for scattering Rg to P and S that are lost to the mantle. This is in contrast to Rg propagation 300 km ESE of ARCESS and up to 600 km in Sweden.

The numerical and observational studies verify that there is significant scattering of near source Rg into P, which propagates into the mantle. A very useful goal of future work would be to accurately estimate how much Rg energy is lost to P and S scattered into the mantle, and under what conditions. Such an estimate would allow us to much more accurately bound the contribution of Rg to Lg.

2.3.5. Direct Generation of S by the Explosion Source

Attempts to model the explosion source, including S-wave generation have been ongoing for decades. Because realistic 3D explosion source models are computationally intensive, early efforts focused on the shear wave generating capability of symmetric physical models of the explosion source. Massé (1981) reviewed models current at that time and found all of them lacking. Citing unexplained phenomena, including generation of SH, he stated, “it is obvious that the seismic source for an underground nuclear explosion remains poorly defined after 2 decades of study”. Since that time much progress has been made, although as noted in this paper, much is still unresolved. Massé suggested that the source could be composed of multiple mechanisms, a spherical source, spall, interaction of the P-wave with the free surface, and block motion along thrust faults in a conical zone. The latter was the precursor to the compensated linear vector dipole (CLVD), the first higher term in a spherical expansion. The CLVD is the most commonly used representation of the non-spherical shear-wave generating part of the explosion source. Day and McLaughlin (1991) presented a method of modeling spall as a tension crack. Stevens et al (2006) report on 2D, non-linear, Lagrangian, finite-difference calculations of the explosion source which allow plastic deformation and cracking. The stresses and displacements on a monitoring surface outside of the nonlinear region are coupled to wavenumber integration simulations to propagate waveforms to regional distances. We build on that work here.

2.3.6. Summary

Much of the previous research has focused on the feasibility of mechanisms. Rg-to-S scattering is commonly presented as an explanation for spectral peaks, nulls, and slopes, but uniqueness of the explanation is not addressed. Quantitative analysis of the relative contributions of different mechanisms is also lacking. Some more recent work has considered whether observations are inconsistent with and so can rule out any possible mechanisms. Specifically, the observations of consistent S-to-P velocity ratio scaling of S and P wave corner frequencies with yield (Fisk et al, 2006, 2007; Murphy et al. 2006; Stevens et al., 2006), are inconsistent with Rg-to-S and P-to-S scattering. Patton and Phillips (2006) however make similar observations and come to the opposite conclusion. The phase velocities estimated for Balapan sources are inconsistent with Rg scattering (Hong and Xie, 2005). An important goal of this paper is to identify other observations that can be used to rule out possible mechanisms under some source conditions. For example, is the correlation of amplitude with yield strong enough to distinguish between mechanisms that predict depth or scaled depth dependences? Can near source travel times distinguish between scattering and source generation of S? Near source tangential component S-waves also require more consideration to determine whether they can be used to infer a source mechanism.

2.4. Simulations

2.4.1. Introduction

We perform several types of simulations that provide insight into the generation of shear waves by explosions. 2 and 3D finite-difference calculations illuminate the effects of near source scattering on both pS and Rg. Modal scattering calculations provide an upper bound on the contribution of Rg to Lg. Wavenumber synthetics for spherical explosion and CLVD sources provide a means of comparing scattered Rg vs. direct S, trapped pS, and S* amplitudes, and provide further insight into the implications of spectral nulls and peaks. Nonlinear Lagrangian finite-difference calculations, coupled with wavenumber synthetic calculations, provide estimates of the size and nature of the contribution of nonspherical source elements to Lg, and their dependence on scaled depth.

2.4.2. Finite Difference Scattering Calculations: Trapping pS in High Velocity Media

In a homogeneous flat lying velocity structure, surface P-to-S (pS) converted energy from explosions in source media with shear wave velocity less than upper mantle shear wave velocity is trapped in the crust. Conversely, pS from explosions in media with shear wave velocity greater than that of the mantle will not be trapped, at least, not as long as the velocity structure is composed of homogeneous flat-lying layers. To assess whether topography and/or lateral heterogeneity could scatter pS in a high velocity source medium to the extent that a significant amount is trapped in the crust and so propagates as Lg, we perform 2D finite-difference calculations.

2.4.3. Models

We perform calculations for a point explosion source at 325 m depth using five models. The first is a homogeneous, horizontally layered velocity model appropriate for Degelen Mountain (Figure 7, left side). The second is that base model plus the topography at Degelen Mountain. (Figure 7, 2nd from left). It uses a topographic profile along an east-west line through Degelen, while maintaining the average upper layer thickness. The third model is the base model plus zeroth order Von Karman distributed P- and S-wave velocity variations with a 5% standard deviation, an aspect ratio of 1, and a correlation length of 1 km in the upper 1.5 km, (Figure 7, center). The correlation length corresponds to the R_g wavelength in the passbands of interest in an attempt to most effectively scatter R_g , which we consider next. The fourth model combines the topography and upper layer heterogeneity, (Figure 7, second from right). The fifth model adds heterogeneity throughout the crust to the 4th model. The heterogeneities below the surface layer also have 5% standard deviation, but are asymmetric with a 5:1 horizontal-to-vertical aspect ratio.

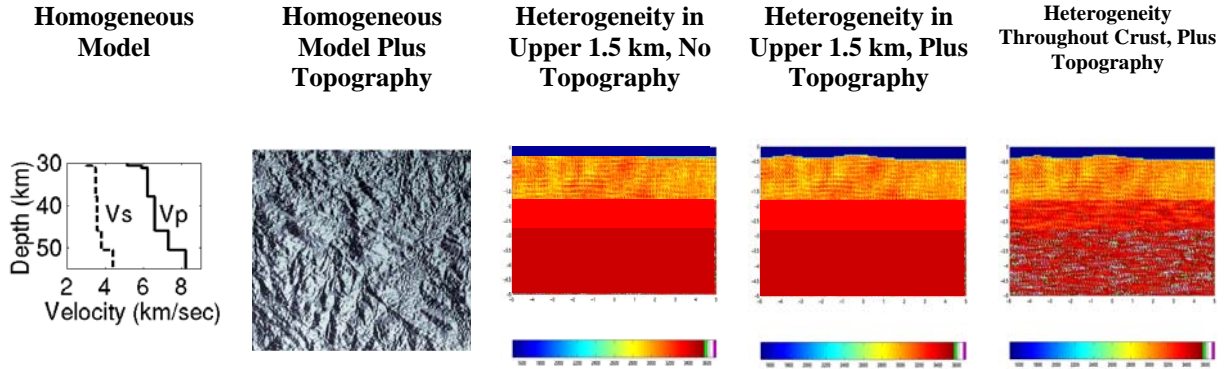


Figure 7. Models used in the scattering calculations. The far left plot shows the 1D homogenous base model. The second plot shows a 200 x 200 km shaded relief image centered on Degelen Mountain. The next 3 plots show 5 km-deep-by-10-km-wide slices of the heterogeneous models described in the text. The source is always 325 m deep, and its position for the models with topography is in the center (horizontally) of the snapshots shown.

2.4.4. Scattering of the Surface P-to-S Converted Phase

Figure 8 shows L_g windows (3.6 to 3.0 km/s) filtered from 3 to 5 Hz, at 225 km for a point explosion source at 325 m depth and each model of Figure 7. Percentages are relative to the rms L_g amplitude of the seismograms for the base model plus topography. For the base model alone, there is some L_g , due to S^* . The addition of topography has the greatest effect. For the base model plus topography, L_g is more prominent, indicating that the incidence of pS is sufficiently randomized by the irregular free surface that a significant amount is now trapped in the crust (Figure 9). Adding heterogeneity to just the surface layer makes little difference relative to the base model. The addition of heterogeneity throughout the crust (model 5) causes an increase in coda after both P and L_g , but does not amplify L_g .

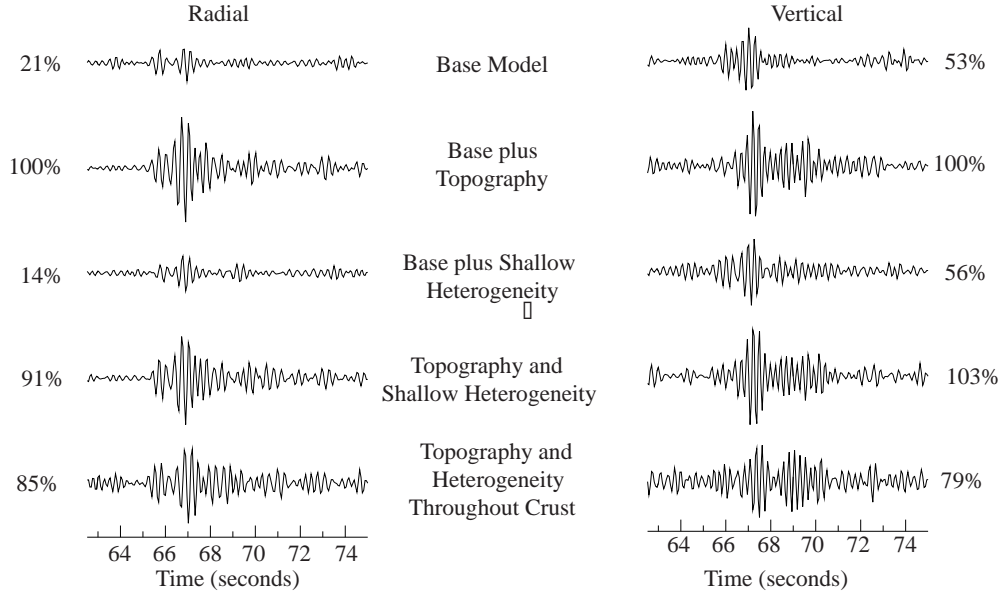


Figure 8. Radial (left) and vertical (right) component Lg (3.6 to 3.0 km/s) at 225 km for each of the models. All five traces are plotted at the same scale. Percentages to the left of each radial and right of each vertical trace are rms amplitudes as a percent of the radial and vertical records' RMS amplitudes respectively for the homogeneous base model with topography added.

Figure 9 illustrates how broken up the pS wavefront is in the model with topography (lower row), compared with the flat-layered base model (upper row). It shows snapshots of the curl of the velocity, which isolates the shear waves (specifically the pS phase) shortly after the explosion. The source is at 325 meters below the free surface, in the horizontal center of the snapshots. The scattering results shown in Figure 8 and Figure 9 indicate that even in a high-velocity source medium where pS should not contribute to Lg, topographic scattering can trap more Lg than is produced by S*, at least at high frequency.

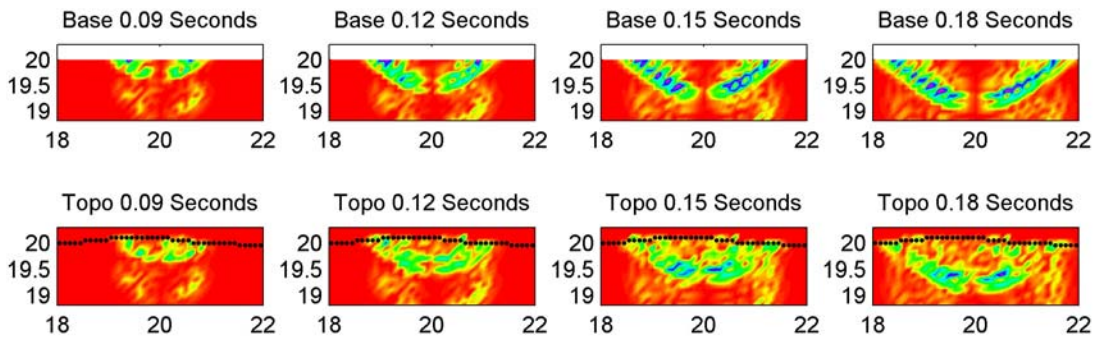


Figure 9. Snapshots of the curl of the velocity just after the explosion, for the homogeneous base model (top row) and model with topography (bottom row) illustrate the effect of topography on pS. The black line in the lower row shows the free surface.

2.4.5. Rg scattering Due to Topography

As with the P-to-S converted phase, the effect of topographic scattering is dominant compared to the effect of scattering due to heterogeneity. Therefore, in this section we focus only on comparisons between the homogeneous base model of Figure 7 (left), and the same model plus topography.

Attenuation is greater for the model with topography, but the most dramatic effect is on dispersion. Figure 11 shows point explosion seismograms at 20 km east of Degelen. At 0.5–1 Hz, the waveforms appear unaffected by topography. In the 1-2 Hz and 2-4 Hz records, on the other hand, Rg is quite delayed for the model with topography. By 4-6 Hz, the Rg is too attenuated to identify. There is also more P coda for the model with topography.

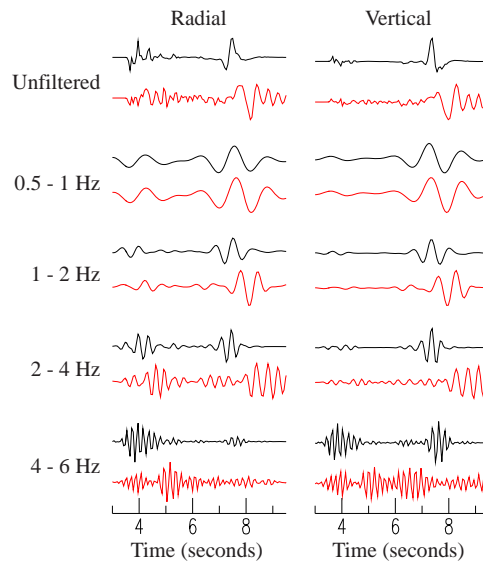


Figure 10. Point explosion synthetic seismograms 20 km east of the source, for the models without (black) and with (red) topography. Traces in the same filter band are plotted on the same scale.

To examine further what Rg scatters to, we look at cross-sections of the vertical velocity, centered on the Rg phase near the source (Figure 11). This provides insight into the potential contribution of topographically scattered Rg to Lg. The cross-sections (Figure 11, left column) show a compact Rg phase in the model without topography, while in the model with topography the Rg energy has been spread out all along the surface (right column). The downgoing phase in the cross-sections at 1 second is P-to-S scattered energy. At least during the first three seconds shown here, the main effect of topography on Rg is to cause strong dispersion of the phase rather than scattering into downgoing S.

Our results regarding scattering from Rg to downgoing body waves appear to be inconsistent with some previous work and observations. Jih (1995) also used finite-difference calculations and found that Rg does scatter to downgoing body waves. There appear to be two important differences between the models used. The local topography in our models is the real topography at Degelen. The topography of Jih's model is not explicitly listed, and while the average slope

appears to be moderate, it looks as if it is locally much steeper than anything in our model. Second, Jih used a very low Q near the surface (Jih, pers. comm., 2004), which disrupts the modal structure. Such low Q may be appropriate at NTS, but not at Degelen. Further, near-receiver observations of teleseismic P-to-near-receiver-Rg scattering (e.g. Key, 1967; Bannister, et al., 1990; Revenaugh, 1995), through reciprocity, imply near-source Rg-to-downgoing-P scattering, and observations of secondary arrivals at teleseismic arrays have been interpreted as near-source Rg-to-P scattering (McLaughlin and Jih, 1988). We don't observe such scattering in these simulations.

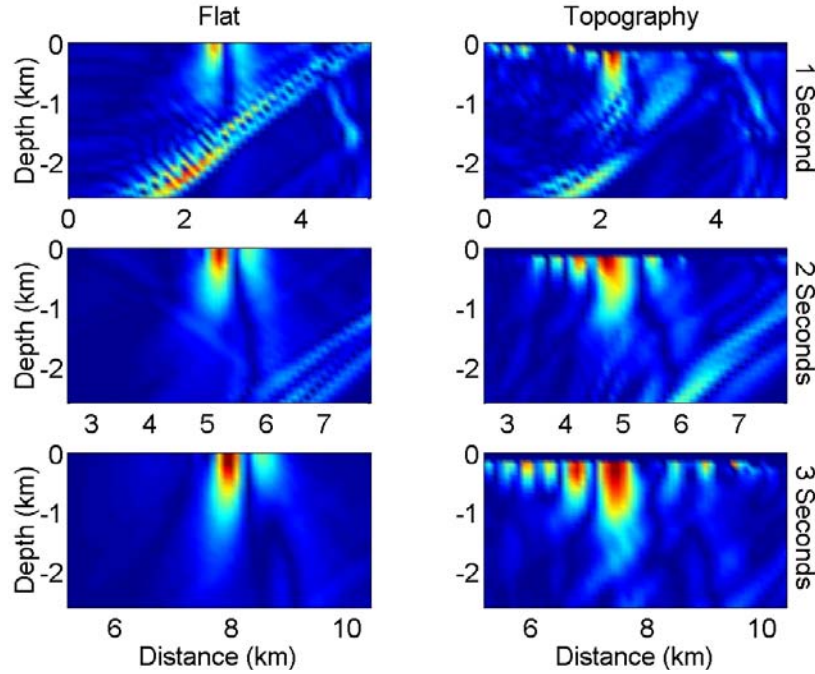


Figure 11. Cross-sections of vertical velocity (left) centered on Rg at 1, 2, and 3 seconds for the homogeneous base model with a flat free surface (left column) and the same model plus topography (right column). Each pair (same time, different models) is plotted with the same color axis.

To better quantify the effect of topography on Rg, we estimate Q as a function of frequency for the homogeneous model with a flat free surface, and for the similar model with topography. The decrease in Q in the second model can be attributed to topographic scattering. The left side of Figure 12 shows frequency vs. the estimated intrinsic Q values. The Q values determined for the base model are consistent with those of the original model structure (the frequency dependence is caused by the particular implementation of attenuation in the finite difference calculation). Attenuation is greater for the model with topography (Figure 12, left side). The effect of dispersion is less than the measurement error for the model without topography, but is dramatic for the model with topography. There the Rg is slowed at all frequencies, considerably at higher frequencies. Such dispersion could explain the observations interpreted as scattered Rg in explosion but not earthquake Lg coda (Gupta et al, 2005; Saikia et al., 2005).

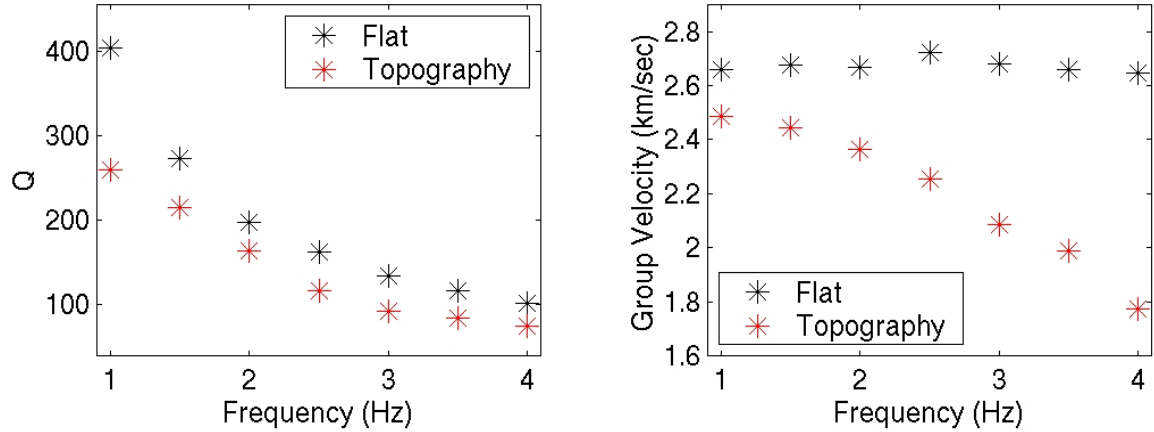


Figure 12. Q vs. frequency (left) and group velocity vs. frequency (right) for the homogeneous flat (black) and topographic (red) models. The decay of Q with frequency is due to the implementation of the Q model in the numerical calculations.

2.4.6. 3D Finite-Difference Calculations

We performed similar calculations to those described above for a 3D model to address two issues, the validity of the 2D scattering calculations and scattering to the tangential component. Computational constraints limit us to a small model size, 30 km long by 14 km wide and 7 km deep, so we focus on scattering near the source. The source is 5 km from the left (west) edge of the model.

Results for the vertical and radial components are, to first order, similar to those of the 2D calculations. Figure 13 shows snapshots of all three components of velocity in the radial-vertical plane. There is significant dispersion, with Rg energy in the topographic model distributed along the surface later than that in the flat model. The downgoing surface pS reflected phase is disrupted, but not scattered significantly to the tangential. There is, however, topographic scattering to the tangential. Shear wave energy propagates downward from the Rg position at the surface on the tangential component. Timing is similar to that of the S^* phase on the vertical component, but S^* is slightly earlier and is also visible in the flat model plots.

Scattering from Rg to downgoing tangential, but not radial or vertical shear waves, is the most interesting result of the 3D calculations and is physically reasonable. Consider decomposing the Rg disturbance of the free surface with topography into vertical, radial, and tangential components. Radial and vertical stress or displacement of the free surface should just lead to continuing propagation of Rg waves. Love wave modes however require a velocity discontinuity or gradient to exist. The surface velocity is high in the Degelen model and the gradient with depth is low, so most of the energy scattered to the tangential propagates away from the surface. This modeling result and explanation are consistent with the observation that tangential shear waves near the source are often earlier and larger than their radial counterparts (e.g. Stevens, et al, 2004).

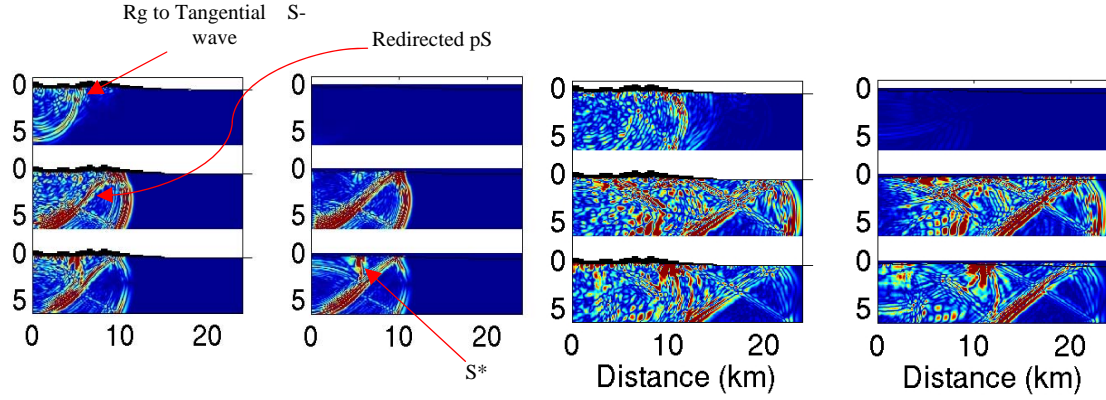


Figure 13. Three-component snapshots of the absolute value of velocity at 2 (2 left columns) and 4 (2 right columns) seconds, from 3D finite difference calculations for a topographic model (columns 1 and 3) and flat free surface model (columns 2 and 4). Velocities at each time are plotted on the same scale.

Figure 14 shows three components of velocity at the surface, with the corresponding topography shown in the bottom row. At 1 second and later, the images encompass Rg, but not the P or pS phases. Scattering to the tangential at 0.25 seconds (left column) appears to follow the ridge topography above the source. The wavefronts are very disrupted, and the distribution of energy on the tangential is irregular.

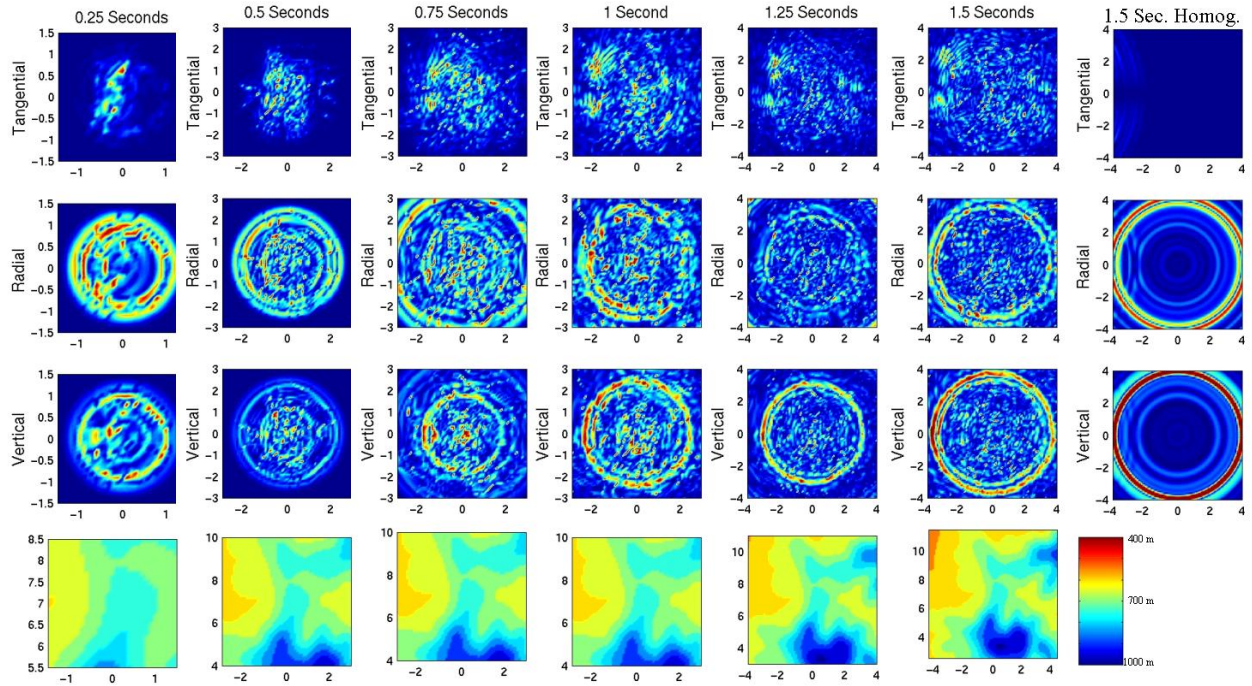


Figure 14. Surface velocities from 0.25 to 1.5 seconds for the topographic model, with corresponding plots for the flat model at 1.5 and 5 seconds (right column of both upper and lower set of plots). The area shown increases with time for each plot. The topography of each area is shown in the bottom row.

The finite-difference modeling indicates that for the actual topography at Degelen Mt,

- 1) topography is much more effective than heterogeneity at scattering P and Rg,
- 2) topography can alter the incidence of pS, leading to a significant increase in Lg amplitude,
- 3) the topography at Degelen Mt. can scatter Rg into tangential shear waves, but not radial or vertical.
- 4) topography significantly increases the dispersion of Rg.

Like much previous research, these finite-difference calculations have demonstrated the feasibility of different mechanisms, particularly trapping of pS even in a high velocity source media and scattering of Rg into tangential S-waves, and they offer an explanation for the observed slow decay of Lg coda due to dispersion of Rg. They also provide an estimate of the effect of topographic scattering on the contribution of trapped pS to Lg. Modal scattering calculations (Stevens, et al, 2007) complement these results with a much more concrete estimate of the upper bound of the possible contribution of scattered Rg to Lg.

2.4.7. Upper Bound on Rg-to-Lg Amplitude from Modal Scattering Calculations

Stevens et al (2007) present a method for estimating the contribution to Lg from scattered Rg, and estimate that contribution for different source conditions. The method assumes complete and rapid scattering of Rg into higher modes. The distribution of modes is determined by the distribution for a vertical point force. This distribution is reasonable since the strongest Rg scattering occurs at the earth's surface. The method however provides an extreme upper bound for several reasons.

The method ignores scattering of Rg into downgoing body waves that propagate down into the mantle. Such scattering is generally strong, as shown by numerous studies of near receiver teleseismic P to Rg scattering by distinct topographic features (e.g. Key, 1967; Bannister et al, 1990; Hedlin et al, 1991) and by correlation of topography with P-to-Rg scattering strength (Revenaugh, 1995; Revenaugh and Mendoza, 1996). Assuming reciprocity, Rg should scatter into P waves that will propagate into the mantle. This is thought to be the main source of coherent teleseismic P coda from shallow sources (Dainty, 1990; Gupta and Wagner, 1992).

By assuming scattering of Rg entirely into higher modes, we also ignore Rg-to-Rg scattering. The finite-difference calculations described above however showed that Rg scatters off topography most strongly to Rg, leading to strong dispersion.

By assuming instantaneous scattering of all Rg at the source, we ignore the effect of a slower, more spatially distributed scattering of Rg. Although Rg disappears rapidly in some areas, we note that 0.5 to 1 Hz explosion Rg is not only clearly observable, but can have comparable amplitude to vertical and radial Lg on station BRVK recordings at 650 km from Degelen

(Stevens, et al, 2005). We also ignore intrinsic attenuation of Rg, even though intrinsic Q is generally fairly low in the near surface.

With all these qualifications, we might expect the Lg resulting from scattered Rg to be extremely large. Figure 15 however shows that around 1 Hz, the contributions to Lg of the direct S from a CLVD source and the upper bound on contributions from scattered Rg are approximately equal if the CLVD is at 50 m depth. The scattered Rg upper bound, but not the direct CLVD contribution, diminishes significantly with depth. Above 1 Hz, the scattered Rg upper bound is insignificant compared to that of the direct CLVD's contribution. Addition of the contribution of spherical explosion Rg does not change the results. Results of more simulations are provided in Chapter 5.

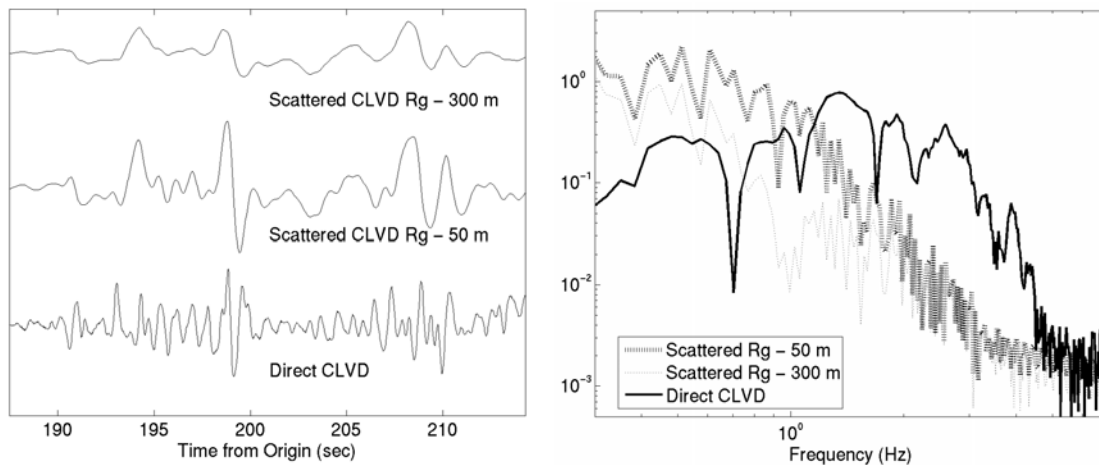


Figure 15. Synthetic Lg seismograms (left) for a Degelen structure and sources with moments of $1e22$. The upper two traces are for CLVD Rg scattered to higher modes, for source depths of 300 m (top) and 50 m (middle). The bottom trace is for the Lg directly generated by a 300 m depth CLVD. Corresponding spectra are shown to the right.

2.4.8. Nonlinear Source Simulations Predict Depth, Yield, and Scaled Depth Dependence of S

Two of the major contributors to the generation of shear waves by explosions are the effects of the free surface and gravity. These cause substantial vertical asymmetry in the source. To better characterize the nonspherical components of the explosion source, we perform nonlinear, Lagrangian finite-difference source calculations. With these, we can first address the validity of the assumption that the CLVD is an appropriate representation of the nonspherical elements of an explosion source. We can then assess the dependence of the shear wave generation on scaled depth, and compare that prediction with observations.

Figure 16 shows regions of nonlinear deformation and cracking from three nonlinear source calculations. The calculations were performed in a granite half space with material properties appropriate to Degelen. To obtain waveforms, the stresses and displacements at a monitoring surface outside of the nonlinear region are coupled to wavenumber integration code and propagated to regional distances in a Degelen velocity structure. The first two images represent

explosions at the same depth (300 meters) but different yields (31 kt and 112 kt) and therefore different scaled depths. Normal containment depth is approximately $122 W^{1/3}$ meters where W is yield in kilotons, so the explosions are both underburied at 51% and 78% of normal containment depth, respectively. Note the strong distortion of the cavity by the largest event (left). The images on the right represent a 10 Kt explosion at 557 m depth, so at 2.1 times the containment depth.

Figure 17 shows waveforms for these and additional simulations of explosions in granite at different depths and scaled depths and. Scaled depths range from 0.51 to 6.8, and yields from 0.3 to 112 Kt. The waveforms at 300 km and scaled by yield are very similar up to a scaled depth of 3. The Lg phase, at 83 to 100 seconds, is diminished at the highest scaled depths. Explosion and CLVD synthetics are included as the bottom 2 traces. Figure 18 shows that $\log(\text{amplitude})$ vs. yield (left) varies less than observed in previous work, as discussed above over a much greater range of scaled depths than are actually observed. The plot on the right of Figure 18 shows that amplitudes of Lg generated by nonspherical source elements have little variation with scaled depth below a scaled depth of 3.

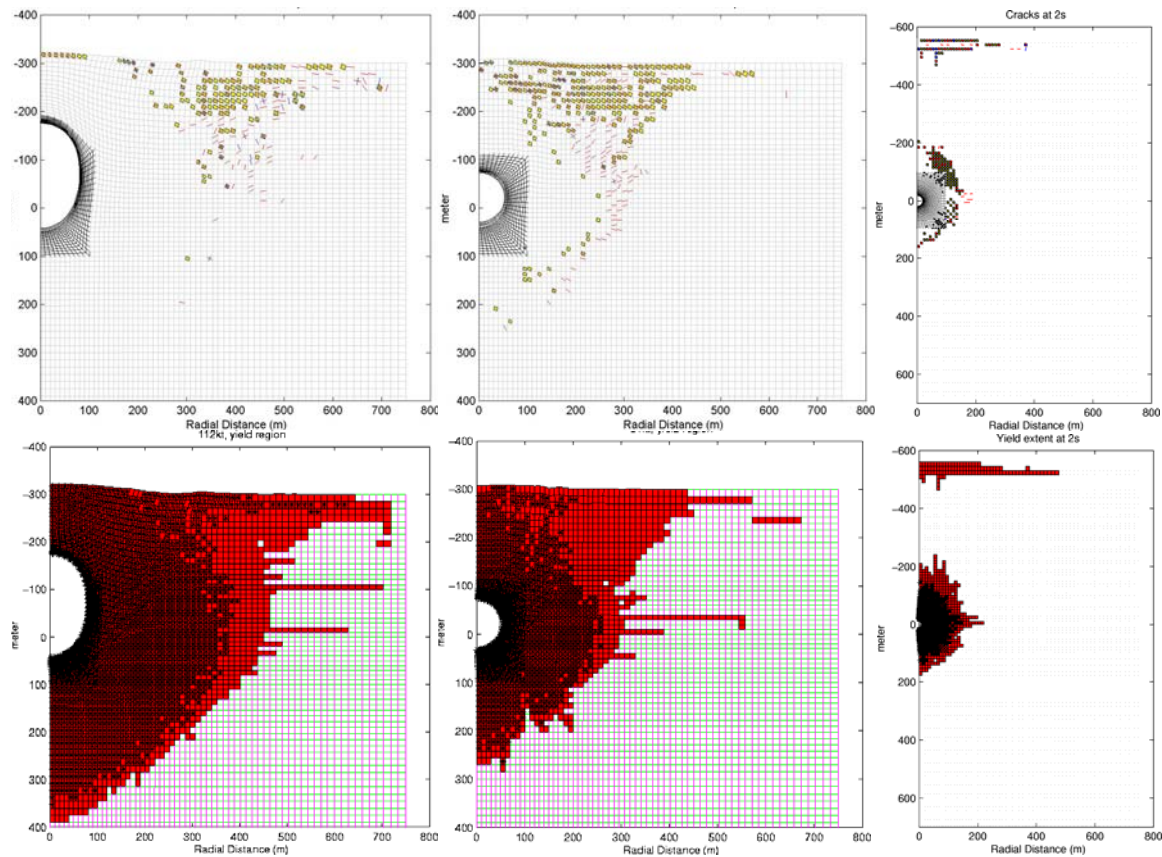


Figure 16. Near source permanent deformation due to cracking (upper) and yielding (lower) for explosions in a granite halfspace, at 51% (left), 78% (middle), and 210% (right) of scaled depth. In the cracking images, yellow squares indicate hoop cracks, red and blue lines indicate radial and in-plane tangential cracking respectively. Grid lines in both plots were initially straight. Positions shown above represent the permanent displacement after the explosions

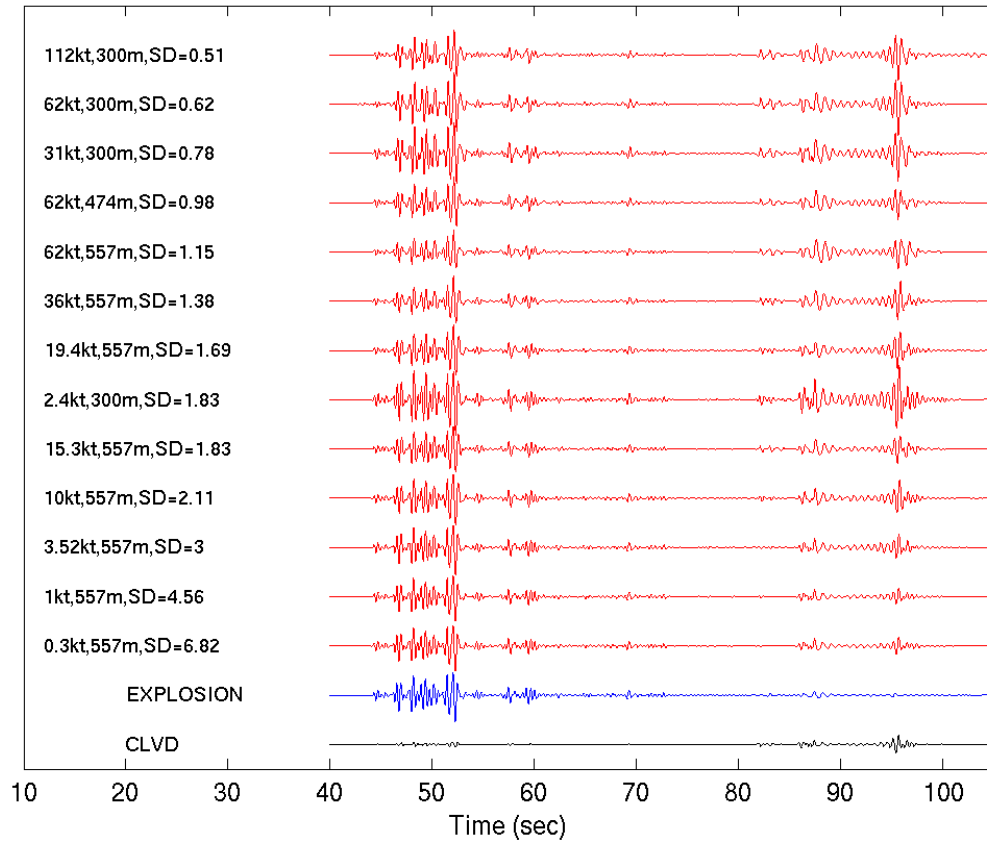


Figure 17. Vertical component seismograms at 300 km, filtered from 1 – 3 Hz, from nonlinear source calculations in granite (Degelen structure) for a range of yields, depths, and scaled depths. Seismograms are scaled by yield. Bottom two traces are explosion and CLVD synthetics.

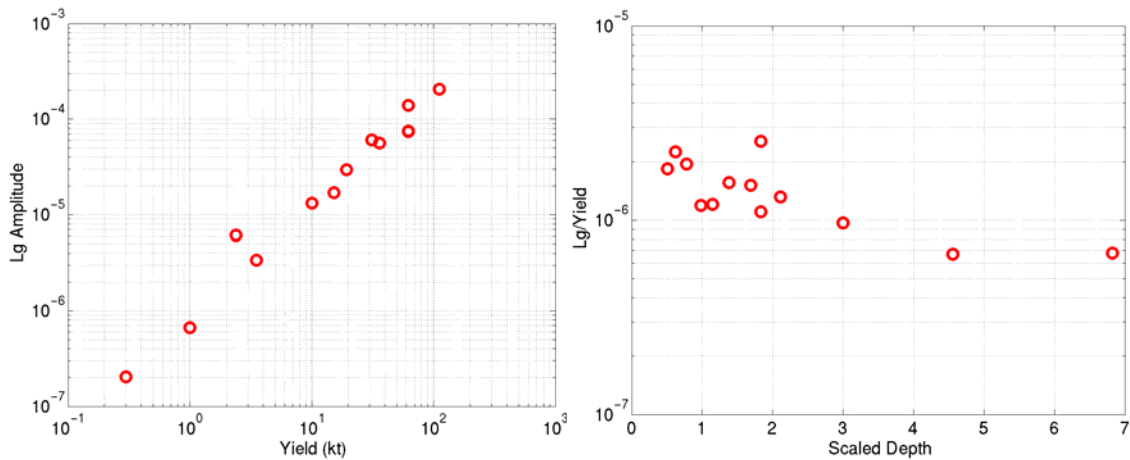


Figure 18. Log Lg amplitude from Figure 17 seismograms vs. log yield (left) and Log Lg amplitude divided by yield vs. scaled depth (right).

2.4.9. Depth and Frequency Dependence of S*

As noted earlier, because the source P-wave velocity at Degelen is greater than the mantle S-wave velocity, the pS energy in the base model (Figure 7) should propagate into the mantle. The source of the Lg in that model's records (Figure 8) is S*, the non-geometric P-to-S scattered phase (e.g. Vogsfjord, 1997). The S* mechanism predicts conversion of P to S waves from sources within a small fraction of the wavelength from the surface due to curvature of the P wavefront. Actual Degelen sources were largely between 100 and 300 m depth. Balapan explosions are commonly twice as deep.

S* is often dismissed as a possible source of Lg due to its strong depth dependence. We quantify the predicted depth dependence so we can assess whether it is greater than that observed in previous work or in data analyzed below. Figure 19 shows the Lg seismograms at 675 km for spherical explosion sources in the Degelen velocity structure at 50 m increments of source depth from 50 to 600 m. At 0.5 to 1 Hz, the source depth effect is small, but it is dramatic at 3 to 4 Hz.

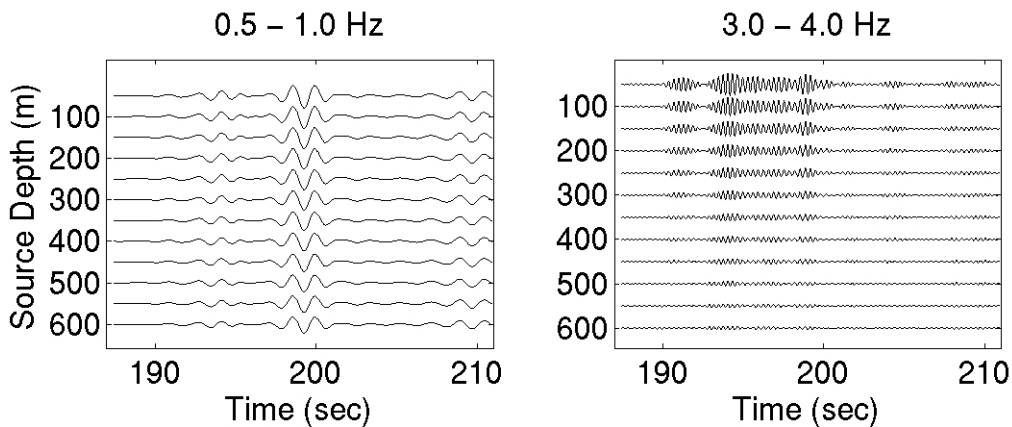


Figure 19. Lg at 675 km from a spherical explosion source in the Degeeln velocity model at 0.5-1 Hz (left) and 3-4 Hz (right). Sources are from 50 to 600 m depth.

Figure 20 shows the depth dependence of \log_{10} Lg amplitude vs. yield at different frequencies. Previous amplitude vs. yield studies that found no depth dependence used measurements of Lg amplitude at 1 Hz. The predicted difference in 1 Hz Lg amplitudes for 50 and 600 m depth sources is a factor of 2.0, or 0.3 magnitude units, which is within the scatter of previous studies that generally spanned much smaller depth ranges. At higher frequencies, the depth dependence of S* is greater. At 3.8 Hz, the difference in Lg amplitude between 50 and 600 m depth sources is a factor of 5.5, or 0.74 magnitude units. To further evaluate the possible contribution of S*, we should examine higher frequency measurements, and examine the amplitude of S* relative to that of other mechanisms.

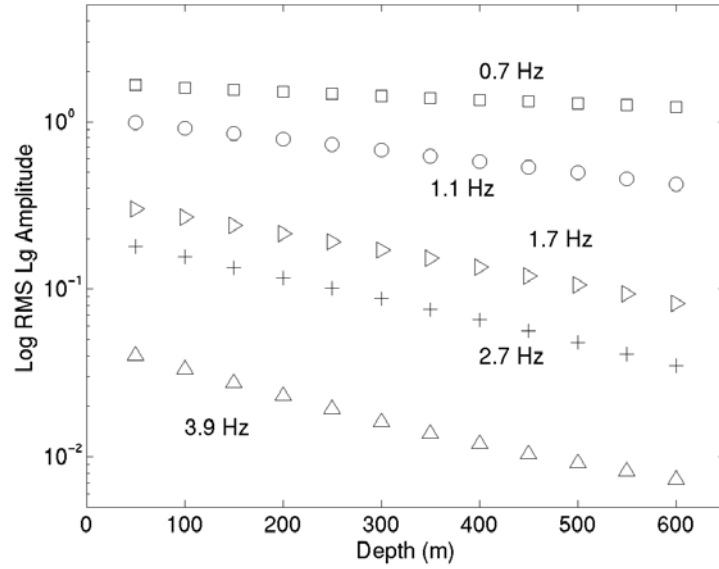


Figure 20. Predicted depth dependence of rms Lg amplitudes at 675 km from spherical explosion sources in the Degelen velocity model at different frequencies. Sources are from 50 to 600 m depth.

Figure 21 shows the amplitude ratio of Lg/P observed at BRVK for each STS explosion, and the prediction based on the finite-difference source calculations, vs. predictions for S*, determined by spherical explosion synthetics. The nonlinear source calculations predict the observed Lg/P ratios over the range of depths and scaled depths observed. S* predicts an Lg/P ratio within the range observed at Degelen, albeit at the low end of the range. It predicts smaller ratios than are observed for the deeper Balapan explosions. The separation between the predicted Lg/P ratios for the two mechanisms is small, and indicates that while direct generation of S provides the greater contribution to S phases, S* could contribute to Lg, especially at lower frequencies for shallow explosions.

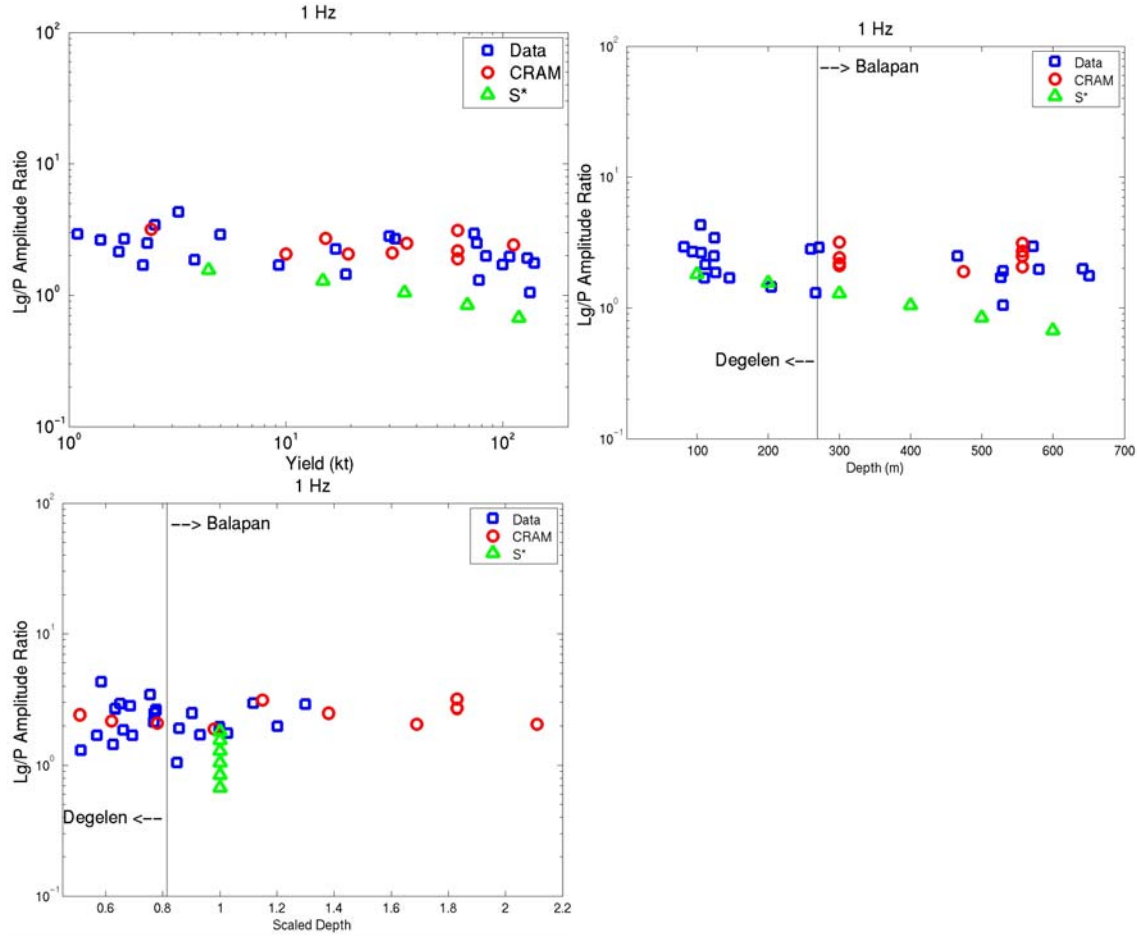


Figure 21: Lg/P ratios observed at BRVK (blue), predicted by nonlinear source calculations (red, labeled CRAM), and predicted for a spherical explosion source (green) for Degelen and Balapan explosions vs. yield (top left), depth (top right), and scale depth (bottom left). Degelen explosions are shallow and lower scaled depth than Balapan explosions. A vertical line separates the areas in the depth and scaled depth plots.

2.5. Local Records of STS Explosions

Table 3 lists the source parameters, the range, and the number of recordings of each component of STS explosions used in this study. Previous researchers have drawn inferences regarding source generation from the dependence of regional phase amplitudes and spectral slopes, nulls, and peaks on yield, source depths, and scaled depths. These 3-component local recordings, from 7 to 98 km, allow us to more completely assess the proposed mechanisms. Specifically, we compare peak and corner frequencies of local P, Sg, and Rg spectra. We also examine the local travel time curves of Sg to determine its most probable origin. We then compare the correlation of yield with regional Pn, the entire P wavetrain, Sn, Lg, and Lg coda recorded at BRVK, 650 km from Degelen and 690 km from Balapan. Instrument responses for historical BRVK explosion records (Richards et al, 1992) make possible the comparison of individual phase amplitudes with yield, rather than just amplitude ratios.

Table 3. Local/near regional data that contain P through Rg arrivals. SD stands for scaled depth, column 6 lists the number of distinct seismograms for each component (there are multiple recordings at many distances – we count these only once). The last column lists location within Semipalatinsk, D for Degelen or B for Balapan.

Date	Time	Yield	Depth	SD	Data t/r/z	Range (km)	m _b	Lat	Lon	Loc
71/12/15 ¹	07:52:59	1.3-1.5	146	1.07	3/9/9	7-77	^A 4.68	50.031	77.972	D
85/06/30	02:39:05	100	527	0.93	0/6/5	49-88	^A 5.92	49.857	78.659	B
85/07/20	00:53:16	76	466	0.90	0/8/7	56-86	^A 5.89	49.943	78.783	B
87/05/06	04:02:08	18	174	0.54	0/9/9	13-83	^I 5.6	49.777	77.984	D
87/07/17	01:17:09	78	267	0.51	1/7/6	15-84	^I 5.8	49.769	78.035	D
87/10/16	06:06:07	1.1	82	0.65	0/8/8	19-76	^I 4.6	49.802	78.14	D
87/12/13	03:21:07	130	530	0.86	0/5/5	57-60	^A 6.06	49.957	78.792	B
87/12/20	02:55:09	3.2	103	0.57	0/8/9	13-83	^S 3.8	49.774	77.975	D
88/04/22	09:30:09	2	---	---	0/3/3	57-81	^I 4.9	49.824	78.102	D
88/05/04	00:57:06	134	530	0.85	0/6/4	53-84	^A 6.09	49.931	78.741	B
88/06/14	02:27:09	5	271	1.30	0/7/6	67-89	^A 4.8	50.034	78.964	B
88/09/14	04:00:00	140	651	1.03	3/7/7	60-94	^A 6.03	49.879	78.823	B
88/10/18	03:40:09	2.45	126	0.77	0/8/9	13-83	---	49.802	78.002	D
88/11/12	03:30:06	17	---	---	5/6/7	68-88	^A 5.24	50.048	78.96	B
88/11/23	03:57:09	19	204	0.63	6/9/9	14-83	^I 5.4	49.765	78.029	D
88/12/17	04:18:09	84	642	1.20	6/6/6	67-98	^A 5.83	49.879	78.924	B
89/01/22	03:57:09	108	580	1.00	6/9/9	58-88	^A 6.10	49.934	78.815	B
89/02/12	04:15:09	74	572	1.12	4/7/9	51-85	^A 5.86	49.911	78.704	B
89/10/04	11:29:57	1.8	94	0.63	5/8/7	16-85	^I 4.6	49.751	78.005	D

¹ No instrument response information available at BRVK for this event

^A and ^I indicate m_b from AWE and ISC respectively, ^S indicates Ms from Geoscience Australia's database (http://www.ga.gov.au/oracle/nukexp_form.jsp), which is also the source of event locations

2.5.1. Local Sg

First we examine the character of the local records. Figure 22 shows a record section from 20 to 77 km for the 1.1 Kt Degelen explosion of 10-16-1987. Shown are the Hilbert transformed radial components overlain on the vertical. Where the records align, the particle motion is retrograde. We see that not only Rg, but Sg are identifiable through their retrograde particle motion, suggesting that Sg can be modeled as one or more higher modes of Rg. The fundamental mode Rg dominates the records, which are filtered from 0.5 to 3 Hz, but a distinct Sg is apparent at 3.3 km/s. Sg is much more easily visible in Figure 23, which is filtered from 1.5 to 3 Hz.

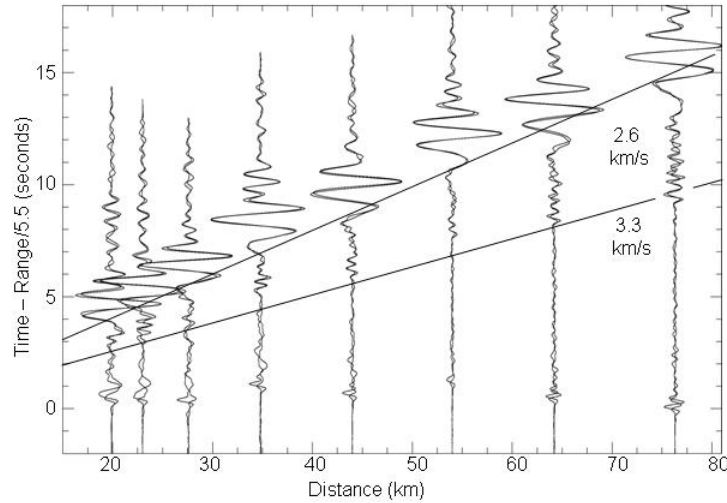


Figure 22. Record section of vertical and Hilbert transformed radial seismograms from the 1.1 Kt 10-16-87 Degelen nuclear explosion, filtered from 0.5 to 3 Hz. Velocity is reduced by 5.5 km/s. The distinct Sg and Rg arrive at approximately 3.3 and 2.6 km/s respectively.

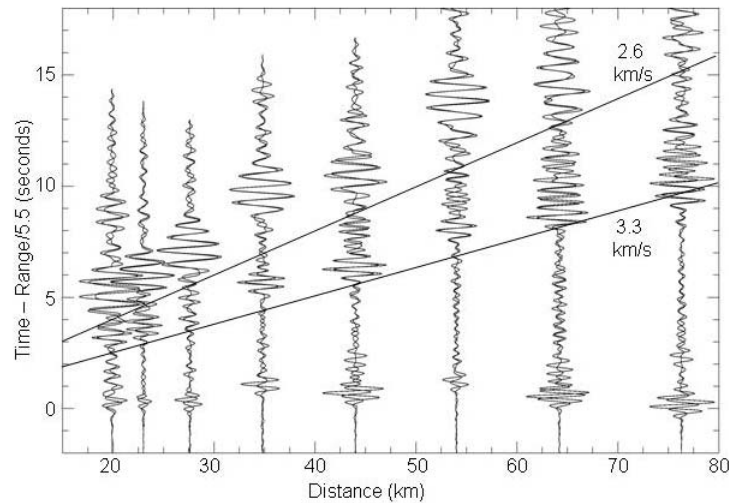


Figure 23. Same data as Figure 16, but filtered from 1.5 to 3 Hz to reduce the dominance of Rg and allow Sg to stand out more clearly.

2.5.2. Implications of Sg Travel Times for Source Generation

The local travel time curves bear on source generation. Specifically, if the local Sg phase were generated at the source, the S arrival times should follow a smooth curve consistent with predicted times. If the Sg were generated by scattering from Rg, we would expect some increased delay, and more erratic travel times if the first significant scatterer encountered were not in line with the stations. Further, if Sg were generated by Rg scattering, we would expect to see multiple instances of Sg, assuming that Rg scatters off of more than one point. If scatterers are so densely spaced that Rg-to-Sg phases overlap, we should expect a drawn out coda to the Sg. The stations are aligned with the propagation direction from Degelen, but vary with azimuth from Balapan.

Figure 24 shows record sections of observations (left) and synthetics (right) for the 12/20/87 3.2 Kt Degelen explosion, from 7.5 to 2.9 km/s group velocity, which excludes the very large Rg phase. Velocity is reduced by 6.0 km/s. Sg is clear in the data and matched by the synthetics. Figure 19 shows the travel time curves for both the data and synthetics. There is no increased delay of the observed travel times relative to the synthetics and the observed travel times are not erratic. Rather, they are closely aligned and match the synthetics very well. The observed Sg is distinct and rather than being drawn out, it is actually even more impulsive than in the synthetics. The source time and location of Sg is indistinguishable from that of Pg. As Sg travels at the Lg velocity and is observed at up to 90 km in the local records, the simplest explanation for Lg at regional distance is that it is the continuation of this locally observed source-generated Sg phase. Results are the same for the other Degelen explosions. Thus, while other mechanisms could augment Lg, they do not appear to be required to explain Lg from Degelen explosions.

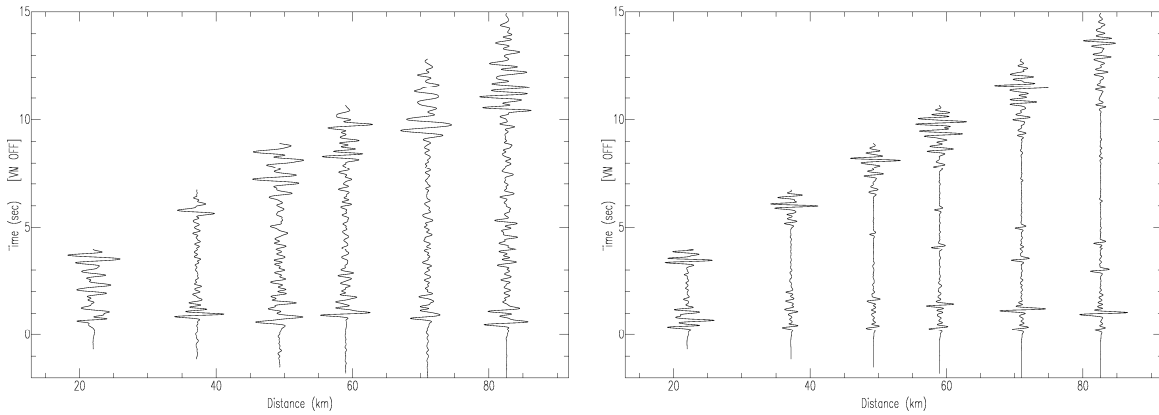


Figure 24. Data from the 12/20/87 3.2 Kt Degelen explosion (left) and wavenumber synthetics right, from 7.5 to 2.9 km/s group velocity (to cut off the dominant Rg) and filtered from 1-5 Hz.

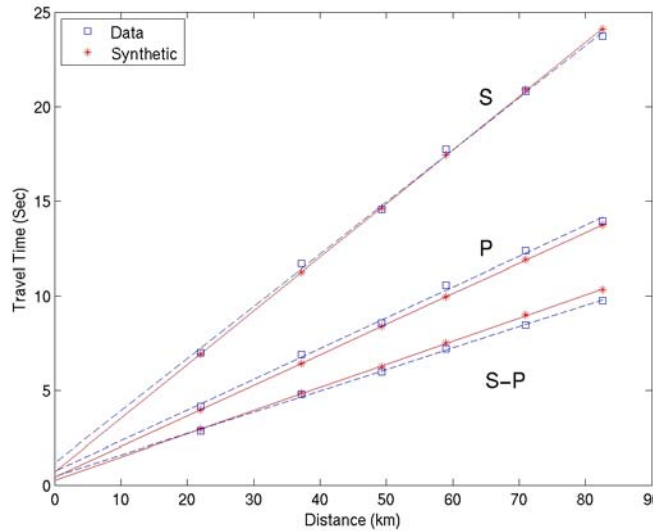


Figure 25. Fits to the observed (squares) and synthetic (asterisks) P, S, and S-P times from the 12/20/87 3.2 Kt Degelen explosion and wavenumber synthetics.

2.5.3. Comparison of Local and Regional Records

Figure 26 shows local records of each of the Balapan explosions recorded at approximately 80 km (left) vs. the corresponding records from BRVK, at approximately 685 km. Figure 21 shows the same for the Degelen explosions. Both the local and regional records are normalized by the P-wave amplitudes. The Degelen records have much larger Sn and Lg amplitudes relative to P, which may be explained by the relative source spectra of S and P. That is, the Balapan explosions are mostly at yields and depths where the corner frequencies of the predicted P and S source spectra fall to the left of the 0.5 to 2 Hz frequency band. Sn is not prominent and Lg is relatively smaller on the records of the largest Balapan events compared with the smallest. The S spectral corners of the smaller Degelen explosions are more likely to be to the right of the frequency band we are examining, and all of the Degelen explosions except the largest have clear Sn and large Lg relative to P.

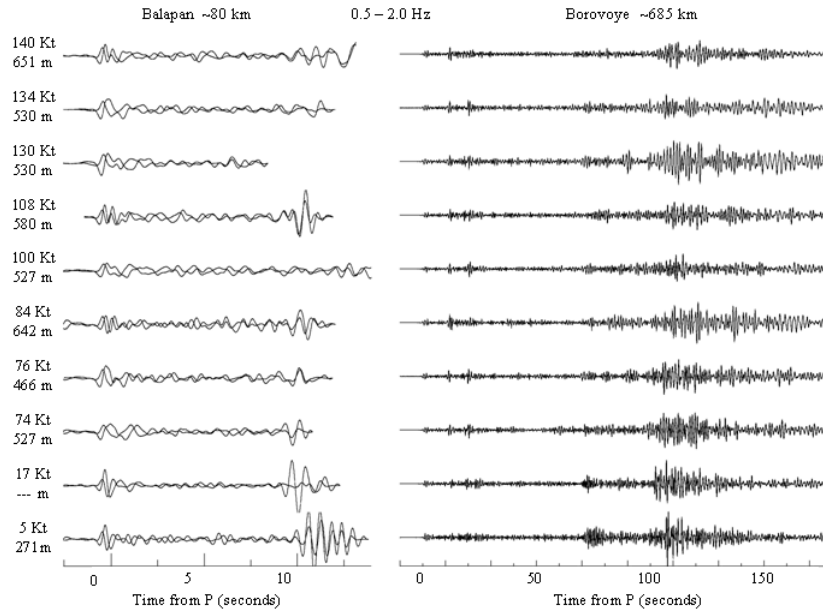


Figure 26. Overlain vertical and Hilbert transformed radial records of Balapan explosions (the closest record to 80 km distance for each event is plotted). To highlight S the large Rg is not plotted (left). Vertical records of the same events at BRVK, at 680 to 690 km, are plotted on the right. Both local and regional records are normalized by their P wave amplitudes. Yields and depths are noted to the left of the traces.

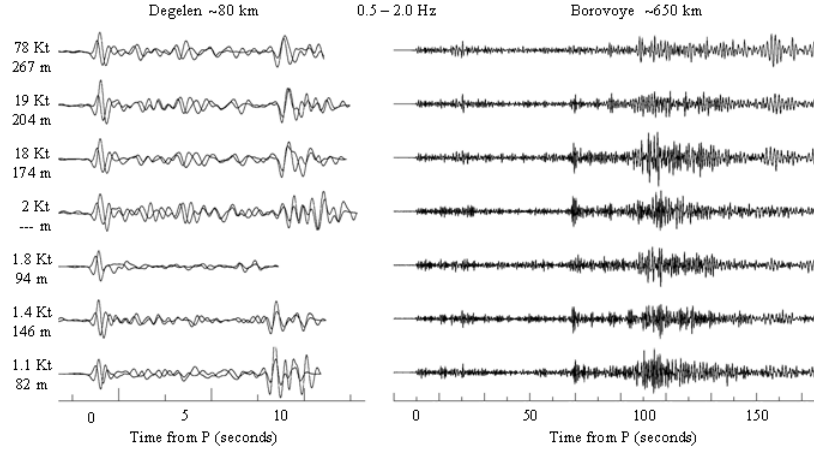


Figure 27. Same as Figure 26, but for Degelen explosions. Sn and Lg are prominent and large, except for the largest events, which appear more similar to the Balapan explosion records. The difference in S/P ratios may be accounted for by P and S source scaling.

2.5.4. Regional Phase Amplitudes of Degelen Explosions

We quantify the observations made above by comparing regional phase amplitudes at BRVK with yield, depth, and scaled depth for the events of Table 3. We also examine records for six Degelen explosion for which we have no local records of sufficient length to include Sg and Rg, but for which we have information on depths and yields (Table 4).

Table 4. Parametric information for Degelen nuclear explosions for which we evaluate, along with events of Table 3, regional phase amplitudes at BRVK

Date	Time	Yield	Depth	SD	Lat	Lon
12/16/74	06:23:00	3.8	126	0.66	49.949	79.011
3/26/78	03:57:00	30	260	0.69	49.766	78.008
9/25/80	06:21:13	2.2	110	0.69	49.826	78.071
7/17/81	02:37:18	9.3	146	0.56	49.777	78.126
12/25/82	04:23:08	1.7	112	0.77	49.799	78.037
10/18/84	04:57:08	1.4	106	0.78	49.775	78.133

Figure 22 shows regional phase amplitude measurements for 14 Degelen explosions made at 650 km distance, at BRVK. We first compare phase amplitudes with yield, depth, and scaled depth from just Degelen explosions, as the lower source media velocities and much flatter topography at Balapan may also affect amplitudes. We used 41 seismograms, recorded on eight different instruments and inverted the results for instrument corrections.

There are small but consistent offsets between the amplitudes recorded on different instruments, reflecting systematic error in reported gain of some, or all, instruments. The slope of the \log_{10} amplitude vs. \log_{10} yield curves for each instrument type are similar for each phase and frequency, so using the average slope for each frequency, we estimate the offset between the KS instrument, which has the most recordings, and the other instruments. As a check on the validity, we estimate the offset separately for each phase and find that the results are consistent. These offsets were used to correct \log_{10} amplitude measurements from all other instruments to that of

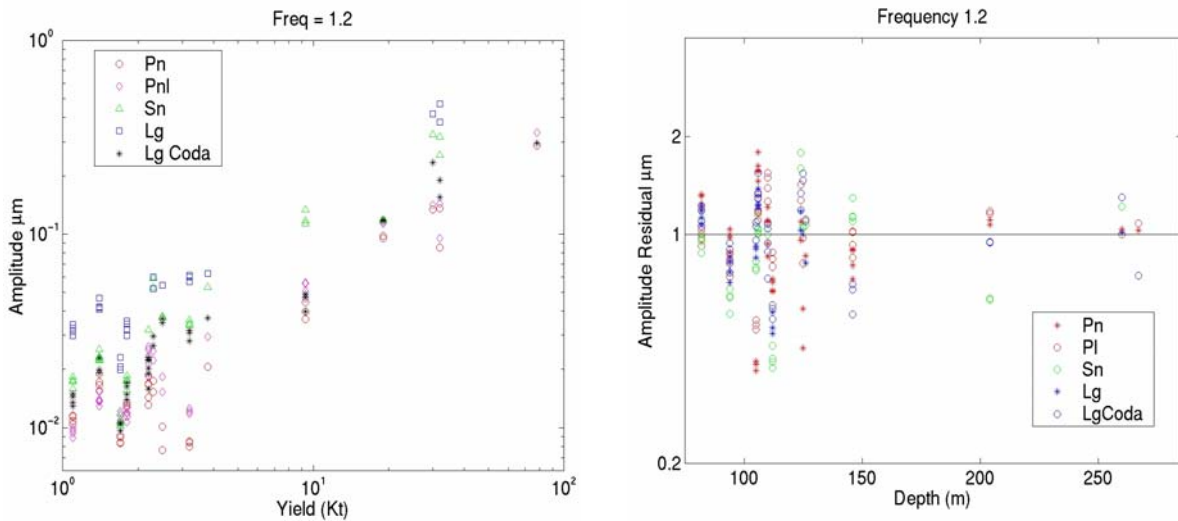
the KS instrument. The corrections are small, approximately 3% to 5% of the individual \log_{10} phase amplitudes, but may aid in resolving any trends in amplitude with yield, source depth, or scaled depth. They also provide confidence that the reported instrument responses at BRVK are extremely accurate.

Pn (the first 5 seconds), the entire P wavetrain (Pn through 5.4 km/s), Sn (first 10 seconds after the picked arrival time), Lg (3.6 to 3.0 km/s), and Lg coda (3.0 to 2.5 km/s) vary similarly with yield. Their yield dependence is well fit by the relation $\text{slope} = 0.855 - 0.034 \cdot f$, where f is frequency. Amplitudes of Lg coda and the entire P wavetrain generally correlate with yield more accurately than do Lg or Sn.

No statistically significant dependence is apparent between any of the amplitudes and depth or scaled depth. That is consistent with the nonlinear source calculations, which predict no dependence of phase amplitudes on depth or scaled depth, despite significant differences in the simulations of the permanent deformation around cavities of 20% and 50% underburied explosions.

This still fails to resolve whether S^* is a significant contributor to Lg. At 2.3 Hz, Lg is only observed at S/N greater than 1.5 for five of the larger Degelen explosions, and none of the Balapan explosions. At 1.3 Hz and below it is observed for all events, but there, the predicted depth dependence is small. The lack of Lg at the higher frequencies is consistent with S^* as the source of Lg, but is not conclusive. For that, we look to the predicted absolute amplitudes relative to other phases and to the local Sg amplitude dependence.

No strong dependence is apparent between ratios of the different phases and the parameters, although Lg/Lg Coda ratios at 1.1 Hz, and Sn/Pn ratios at 2.4 and 3.7 Hz appear to decrease slightly with depth and yield. Lg signal to pre-Lg noise amplitude ratios dropped below 1.5 above 2.4 Hz.



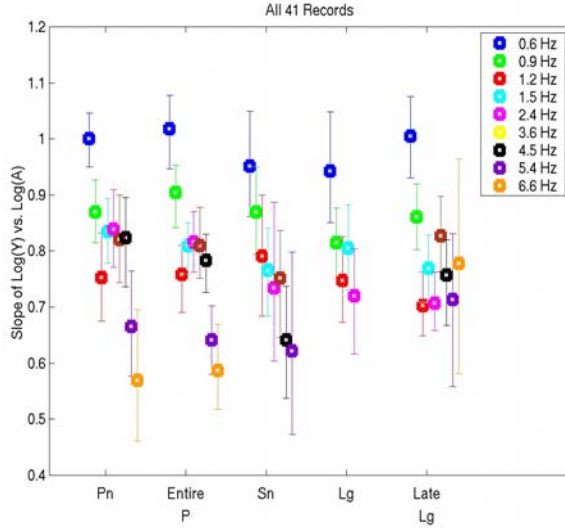


Figure 28. 1.2 Hz amplitude vs yield for 5 phases, from 41 vertical BRVK records of 14 Degelen explosions (top left). Amplitude residuals at 1.2 Hz vs. source depth for 13 Degelen explosions (top right). Slopes of log amplitude vs. log yield curves for each phase over a range of frequencies (bottom). Confidence bounds represent 25th and 75th percentiles.

2.5.5. Accuracy of Yield Prediction by Each Phase

Table 5 shows the median of the yield residuals for each phase with 2 smad error bounds on the median, for a range of frequencies, based on a common set of recordings for each phase. We use only those records with signal-to-noise ratio greater than 1.5 for all phases (Lg drops below the pre-Lg noise level in all records at higher frequencies). Pre-event noise is used to assess S/N for Pn, Pnl, and Lg Coda. Pre-Sn and pre-Lg windows are used to assess S/N for those two phases.

Errors in predicted yield are smallest for the entire P wavetrain, except for the 3 highest passbands, where the coda based estimate is more accurate. Below 1 Hz, Lg and Sn yield estimates have at least twice the error of the P wavetrain. They are closer in accuracy at 1.2 and 1.5 Hz, and the Lg error is comparable at 2.4 Hz.

Composition of some phases appears to vary with frequency. The entire P wavetrain is made up of Pn and Pg. Their relative contributions vary from low frequency, where both appear significant, to high frequency where Pn appears to dominate. This suggests that the stability of the Pnl amplitude with yield is due more to Pg than Pn. At low frequency, Lg coda stands out in the seismogram and is likely composed of similar waves to Lg that could be modeled as higher mode surface waves. At higher frequencies, its amplitude decreases monotonically with time and is more like typical coda, commonly considered to be composed of multiply scattered shear waves.

Table 5. Median Log₁₀ yield errors +/- 2 SMAD.

Hz	npts	Pn	Pnl	Sn	Lg	Lg Coda
¹ 0.6	32	0.10±0.05	0.07±0.03	0.18±0.10	0.18±0.08	0.12±0.05
0.9	18	0.11±0.10	0.05±0.04	0.13±0.05	0.10±0.07	0.07±0.04
1.2	27	0.19±0.09	0.08±0.05	0.13±0.07	0.11±0.06	0.12±0.05
1.5	24	0.11±0.08	0.07±0.04	0.12±0.07	0.11±0.06	0.12±0.05
2.4	22	0.15±0.09	0.09±0.06	0.22±0.14	0.09±0.05	0.11±0.07
3.6	34	0.08±0.05	0.06±0.03	0.12±0.05	*	0.10±0.05
4.5	34	0.10±0.05	0.09±0.04	0.16±0.08	*	0.08±0.04
5.4	29	0.13±0.08	0.12±0.07	0.14±0.08	*	0.06±0.03
¹ 6.6	23	0.12±0.08	0.12±0.08	0.07±0.06	*	0.09±0.07

¹ 0.6 Hz is at or below the low frequency corner of most of the instruments, and 6.6 Hz is at the upper end of most of the known response curves, so the calibrations applied to these measurements may be less accurate than those at the intermediate frequencies.

* insufficient signal at common instruments over a large yield range

2.5.6. Regional Amplitudes of Degelen Compared with Balapan Explosions

The effect of depth and scaled depth is difficult to probe with the Degelen explosions alone, as all of them are shallow, 82 to 267 m depth, and are significantly underburied, with scaled depths from 0.51 to 0.78 for events with calibrated BRVK records. The explosions at Balapan, approximately 50 km from Degelen, extend the range of yields, depths, and scaled depths that the BRVK data cover. The Balapan explosions range from 271 to 642 m depth, with scaled depths from 0.86 to 1.30. The complete data set does not however allow us to simply extend the comparison of amplitudes with yields, depths, and scaled depths, because the velocity structures and topography at Degelen and Balapan differ significantly. Degelen is quite mountainous, while Balapan is flat. Source velocities at Degelen are high all the way to the surface, with the 5.175 km/s P-wave velocity and 3.025 km/s S-wave velocity used for the entire upper 1.5 km in our modeling being typical. Patton et al. (2005) reports 4.201 and 2.520 km/s P- and S-wave velocities at the surface, and 4.818 and 2.890 km/s at 500 m depth at Balapan. Even so, with much of the path to BRVK similar, we may glean additional insight from a comparison of amplitudes within Balapan, and between Balapan and Degelen.

As Figures 20 and 21 show, the smaller events have much more distinct Sn and greater Lg amplitude relative to P than do the larger events. We measured the same phase amplitudes for the Balapan explosions at BRVK as we did earlier for the Degelen explosions. Figure 29 shows the individual phase amplitudes vs. scaled depth for each event, at 1.2 Hz. The amplitudes have been normalized by the predicted Mueller-Murphy source spectra for their yields and depths. In Figure 30, the Lg/P ratio is plotted vs. scaled depth at 0.7 and 1.2 Hz. At higher frequency, the Lg drops to pre-Lg noise levels. The Lg and P ratios are normalized in two ways, by the Mueller-Murphy source (Mueller and Murphy, 19715) for each event's depth and yield (blue squares) and by the Mueller-Murphy source with the source P-wave velocity replaced by the S-wave wave velocity (red circles). That shifts the corner frequency by the ratio of the S-to-P velocity. Murphy et al (2006) found that source scaling of S waves is predicted by the Mueller-Murphy source if the source P-wave velocity is replaced by the S-wave wave velocity. The scatter of the data exceeds the differences observed in any Lg/P with either scaling, so these data do not have the resolution

to confirm or deny the hypothesis that S and P are scaled similarly. Results are similar for Sn/P and Lg coda to P ratios.

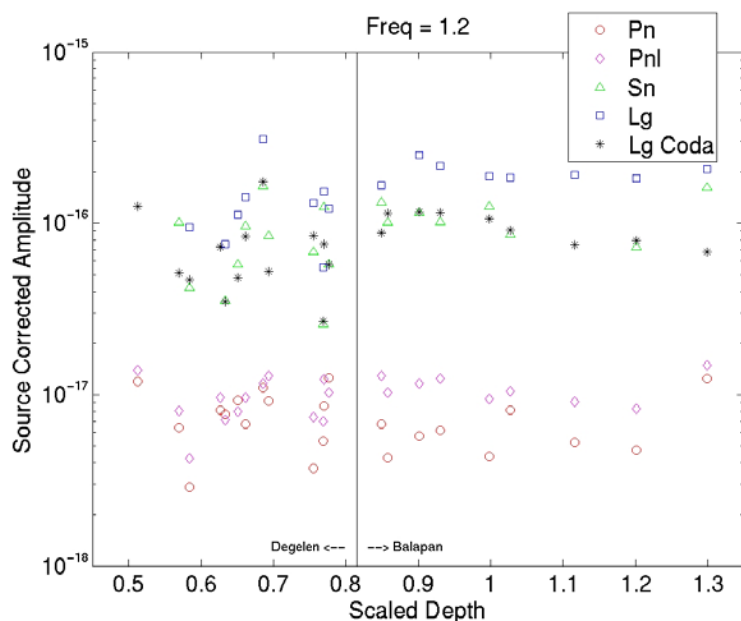


Figure 29. Individual phase amplitudes normalized by the Mueller-Murphy source for each event's depth and yield vs. scaled depth. Degelen events are to the left, below a scaled depth of .815, and Balapan events are to the right.

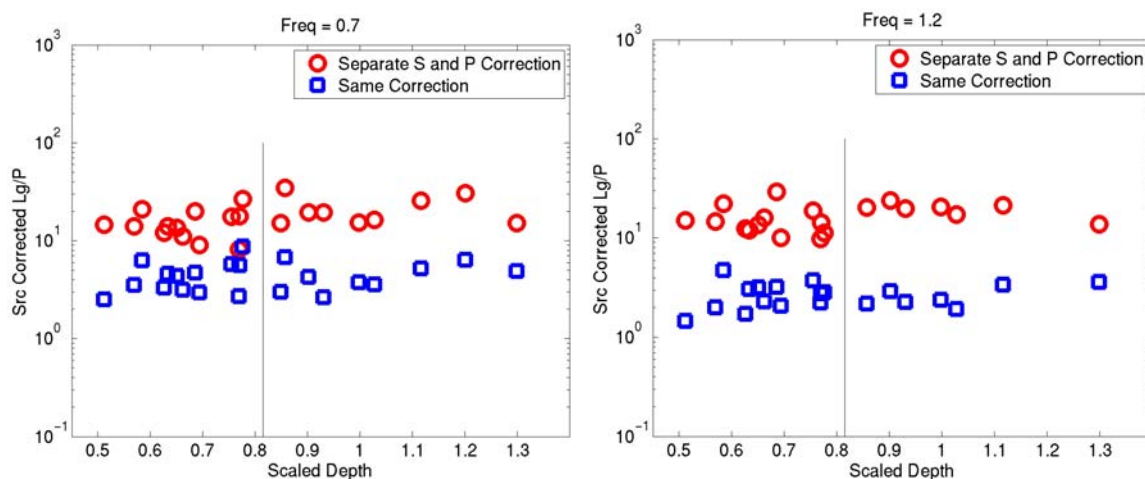


Figure 30. Lg to P amplitude ratios at 0.7 (left) and 1.2 Hz (right), normalized similarly (blue squares) and by P and S-wave specific Mueller-Murphy sources (red circles) as described in the text vs. scaled depth. Degelen events are to the left, below a scaled depth of .815, and Balapan events are to the right.

2.6. P and S Corner Frequencies of Local Degelen Recordings: Observations

The primary observation used to distinguish direct S from P-to-S and Rg-to-S scattering has been the relative source scaling of the P and S phases (Fisk et al, 2006, 2007; Murphy et al., 2006; Stevens et al., 2006; Patton and Phillips, 2006). Most previous work on P and S corner frequencies has found that they differ by the ratio of P to S-wave velocities. This has been interpreted as indicating that the S is generated in the same source volume as the P. We extend that work in two ways. First, previous studies are based on regional records and so require corrections for attenuation that, at least, increase confidence bounds on estimates. The local STS records provide a unique opportunity to 1) compare P and S spectra relatively unaffected by attenuation, and 2) compare S and Rg spectra on the same records. Second, we examine the assumption that S-wave spectra will be similar to the P-wave spectra, but shifted by the velocity ratios, if they are generated in the same volume. This assumption ignores the sensitivity of S-wave excitation to proximity to the free surface due to the shape of P-SV eigenfunctions near the surface. The goal of the numerical calculations and analysis of local records' spectra is to identify differences in spectra due to the S-wave generating mechanisms that can be estimated from the local records, and so distinguish between direct source generation, P-to-S scattering, S^* , and Rg-to-S scattering as the dominant source of the S waves.

Each of those four mechanisms predict different relationships between the P, S, and Rg spectra. If the S waves are source generated, they should have two distinct features. The first is S-wave corner frequencies less than the P-wave corner frequencies by the ratio of the P-to-S wave velocities. Second, the Mueller-Murphy source predicts the spectral shape of explosion P waves to be flat below the corner frequency, except for a small peak at frequencies just below the corner. That peak is assumed to be due to rebound of the nonlinearly deformed region generating a signal that destructively interferes with the lower frequency parts of the initial signal. If S is generated at the source, its spectra should also be marked by the source volume rebound, with a peak similar to, but lower frequency than that of the P spectra. If the S is from scattered P waves, it should have the same corner frequency and peak as the P spectra. If it's largely due to S^* , it should have the P wave spectra, modified by the effect of S^* 's dropoff with the ratio of wavelength-to-depth. The effect is to steepen the spectral slope above the corner frequency. Of course, if S is due to scattered Rg, it should have similar spectra to the Rg.

This analysis focuses on the Degelen rather than Balapan records. Spectral estimates of the Balapan explosions were poorly resolved, as most of them were large explosions with predicted corner frequencies below the apparent instrument response low frequency corner. Figure 31 shows individual P (left column) and S (right column) spectral curves for each Degelen explosion, at the station closest to 50 km for each event. It is difficult to pick an accurate corner frequency from these individual spectra, but by normalizing the records to have similar amplitude below 1 Hz, we can compare the high frequency offsets (the lower sets of traces zoom in on those). It is very clear that the predicted variation in corner frequency with yield can be observed in these records. To resolve whether P and S corner frequencies differ, we must examine multiple records for each event. It is also clear, and an important observation, that most of the Sg spectra have a peak just before the corner.

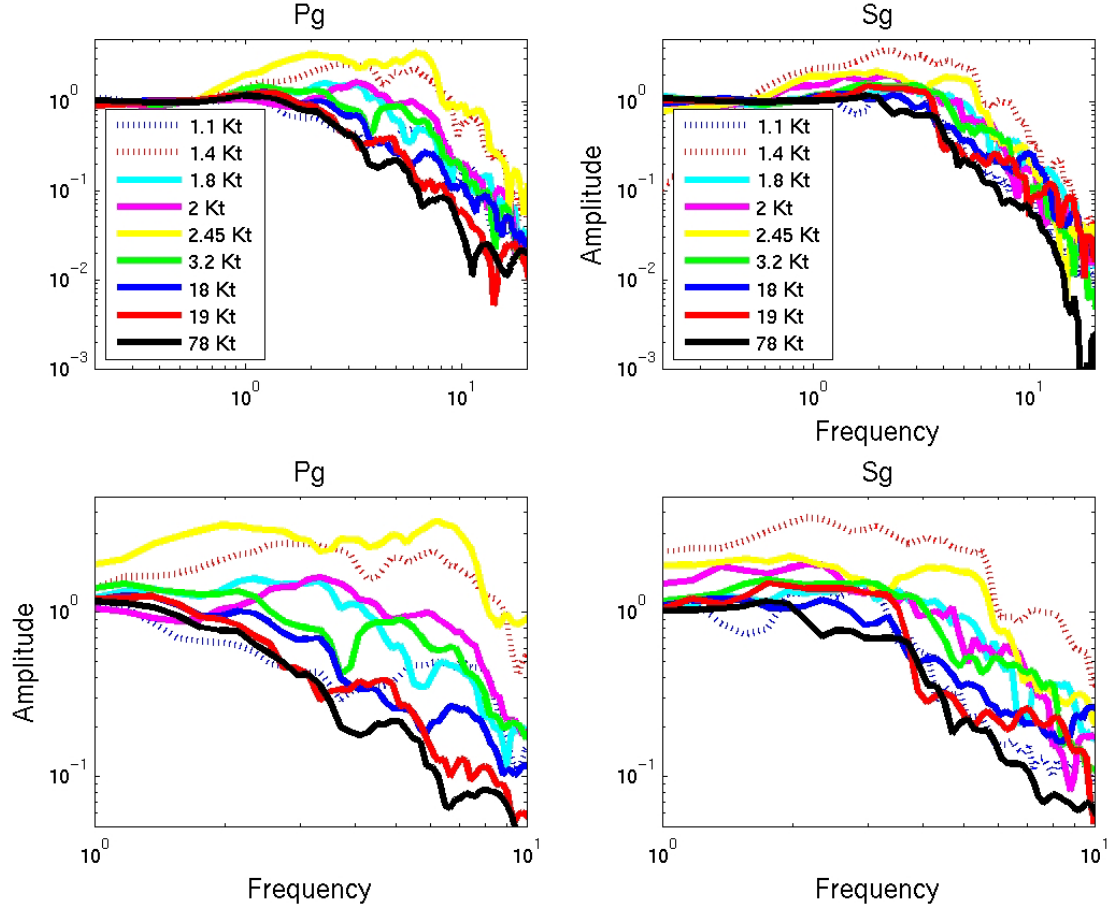


Figure 31. P (left) and S (right) spectra, normalized to unit rms amplitude below 1 Hz, for the station closest to 50 km for each event (ranging from 49 to 57 km). Lower row shows how the different corner frequencies lead to offsets in the curves.

Local Degelen records range from approximately 10 to 80 km distance. We stack spectra, since individual spectra often have poorly resolved corner frequencies. This carries some risk of downward bias of the corners due to attenuation at more distant stations, especially at the highest frequencies, and loss of resolution. We examine these effects using the 12/20/87, 3.2 Kt event, which had good signal to noise ratio records and distinct S waves. Stacked spectra from the three closest and the three most distant stations (Figure 32) are very similar. The apparent S wave corner frequencies at the closest and furthest individual stations where Sg can be identified, 22 km and 83 km respectively (not shown), are 5.0 and 4.5 Hz, indicating a possible bias due to attenuation over 63 km of propagation, although there is quite a bit of random variation between spectra from individual stations that is not correlated with distance. The P-wave corner frequency is just over 6 Hz at both, with perhaps 2 or 3 tenths of a Hz reduction due to attenuation. That gives us confidence that at such frequencies the effect of attenuation is less than the difference between P and S spectra. Whether even higher frequency corners are more biased is still a question.

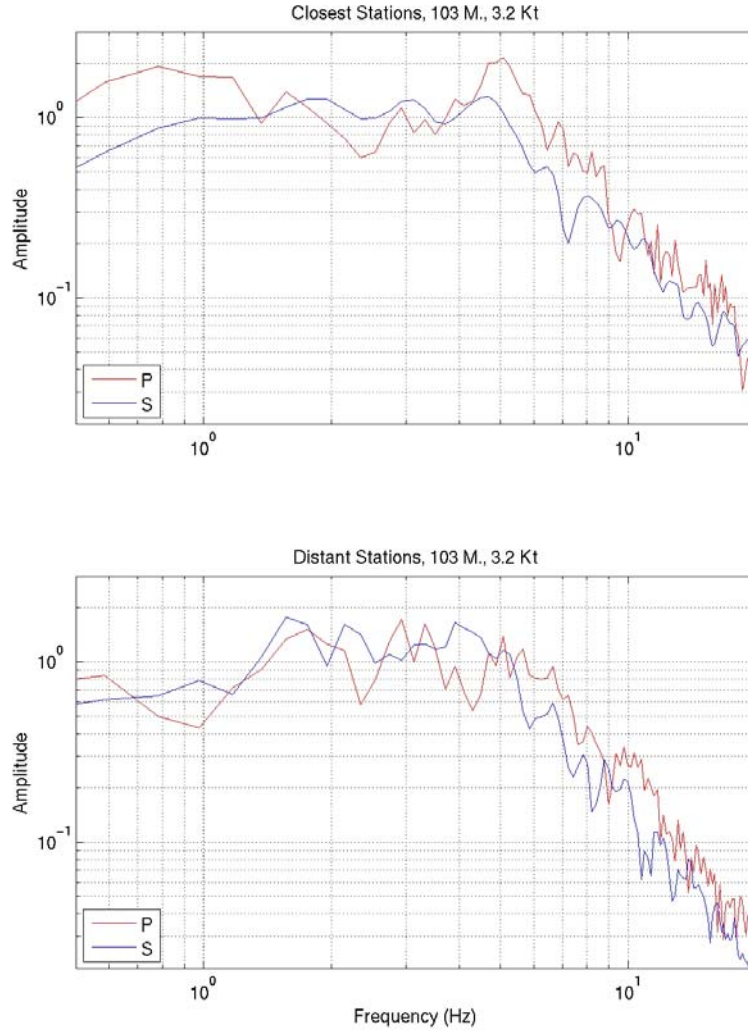


Figure 32. Average Pg and Sg spectral estimates from radial and vertical records at 22, 30, and 37 km (top), and at 59, 71, and 83 km (bottom) for the 3.2 Kt, 103 m depth Degelen explosion.

For the 12/15/1971, 1.4 Kt explosion the P and S corner frequencies are more poorly resolved in individual records (Figure 33). These records illustrate the steps taken to overcome difficulties estimating corner frequencies using these data. One immediately apparent complication is that while the exact instrument response is not known, it appears that the explosion's P and S corner frequencies are above the instrument's corner frequency, diminishing resolution. This likely contributes to the situation that the corner frequencies one might pick from individual spectral curves vary from record to record. Nonetheless, it is clear that the P and S spectra follow different trends. The P corners are generally somewhat above 10 Hz, and the S corners are around 6 to 7 Hz. The stacked spectra (Figure 34) also show this. The peak at 1 to 2 Hz and sharp dropoff thereafter is likely due to the instrument response. Although not known for these data, narrowband responses with 1-4 Hz peaks are typical for Soviet short period systems of that era (Kim et al., 2001). As a further check on this interpretation of the corner frequencies, and to ensure that the spectra represent the intended phases, we examine the waveforms in different passbands. By overlaying the Hilbert transformed radial on the vertical component, we can identify the S wave by its retrograde particle motion, which is expected for higher mode

surface waves. Figure 35 shows such plots of the P through S wave windows, with Rg cut off, of the records from the three closest stations. Very clear S-waves are apparent, of comparable amplitude to the P-waves at 4-8 Hz, but above 8 Hz, no S waves stand out from the P coda, consistent with the S wave corner frequency of 6 to 7 Hz and the P above 10 Hz. Recall that, to distinguish between mechanisms, it is only necessary to answer whether the S wave corners are the same, or are consistently less than the P-wave corners, or whether they more closely resemble the Rg spectra. For the two records examined thus far, the S-wave corner frequencies are clearly less than those of the P waves.

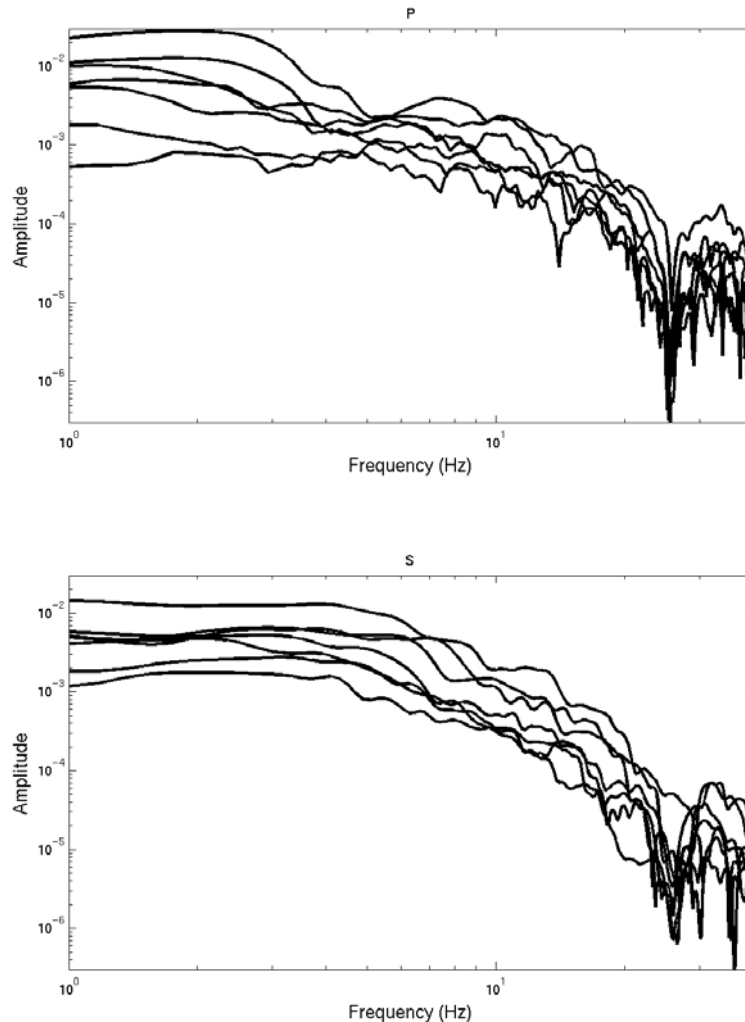


Figure 33. Individual spectra of radial and vertical component records, and for S, one tangential, from stations at 11.1, 16.2, and 23.9 km. The P spectral slopes increase above 10 Hz, and the S at approximately 6 Hz.

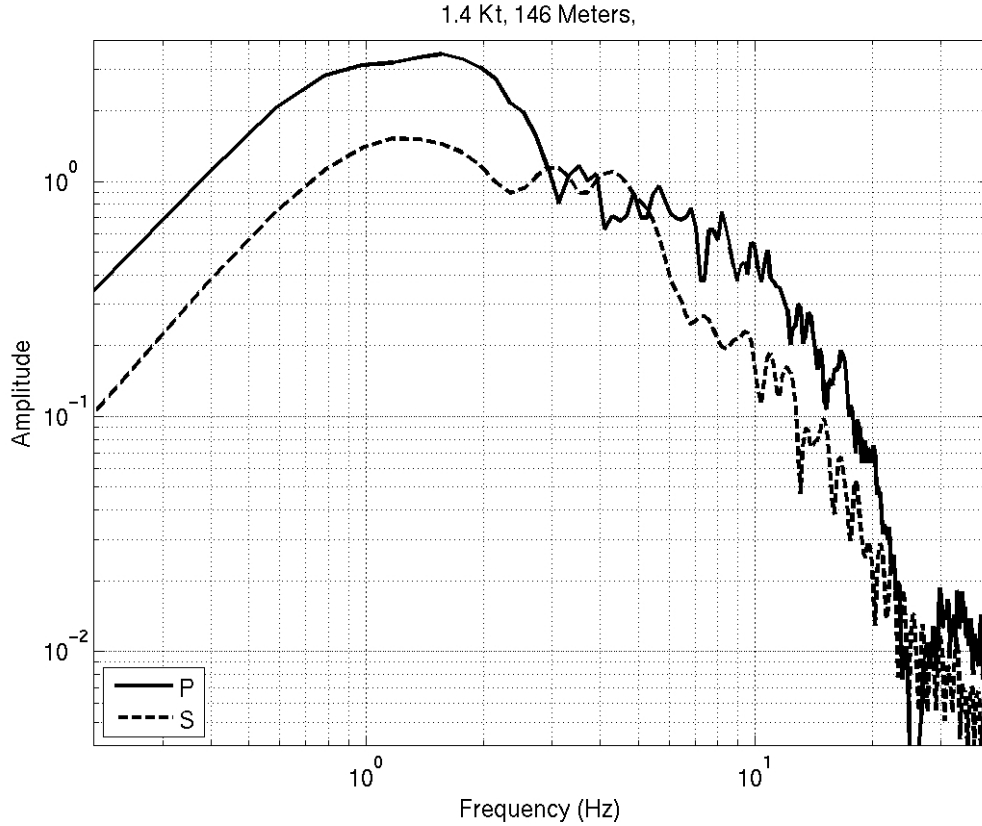


Figure 34. Stacks of radial and vertical records, and for the S spectra one tangential component record, from stations at 11.1, 16.2, and 23.9 km. Individual spectra are normalized to ensure equal weighting, so relative P to S amplitude is lost. The peak at 1-2 Hz is thought to be due to the instrument response. The P spectral slope increases sharply at approximately 10 Hz, and the S at approximately 6 Hz.

We carefully window out the Sg, identifying it by its retrograde motion, and confirm our corner frequency estimates from the spectra by examination of filtered time series for all of the STS records. Degelen records are better resolved, as they provide closer in records and a greater overall range, and have more small events. The S-wave corner is too low to permit good resolution for the larger events most common at Balapan. Even for the largest Degelen event, at 78 Kt, the S-wave corner predicted by the Mueller-Murphy source is less than 1 Hz, and the S-wave windows, even at more distant stations can be just a couple of seconds long.

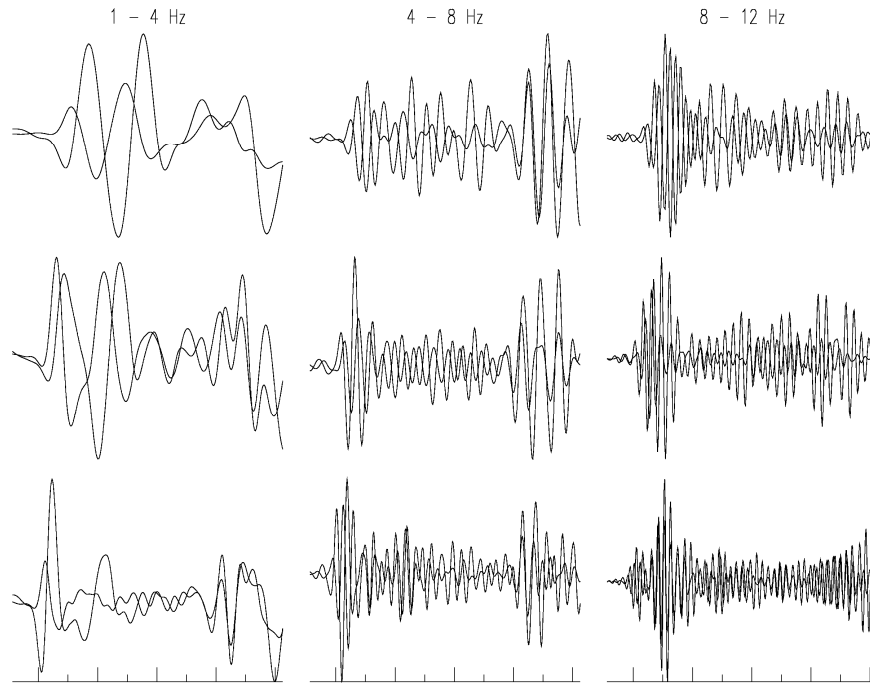


Figure 35. Overlain radial and Hilbert transformed vertical P- and S-wave traces from stations at 11, 16, and 24 km (from top down) from the 12/15/1971, 1.4 Kt explosion. Records are from 0.5 seconds before P to just before the Rg arrival, and are filtered into three separate passbands. The in synch traces at the end of each set of records identify Sg, which is of similar amplitude to P, in the two lower passbands. There is no apparent S above 8 Hz, although P is still clear, evidence of a lower S than P corner frequency.

Table 6 provides the S and P corner frequencies estimated for each explosion from local records, using the methods described above of stacking spectra from various distances, and examining the seismograms to identify the S phase and confirm the interpretation of the spectra.

Table 6. Local/near regional Degelen explosion parameters. SD stands for scaled depth, Pg and Sg columns present the respective corner frequencies in Hz.

Date	Time	Yield	Depth	SD	Pg	Sg	Loc
71/12/15	07:52:59	1.3-1.5	146	1.07	11.0	6.0	D
87/05/06	04:02:08	18	174	0.54	5.2	3.3	D
87/07/17	01:17:09	78	267	0.51	? ¹	? ¹	D
87/10/16	06:06:07	1.1	82	0.65	5.4 ^P	3.7 ^P	D
87/12/20	02:55:09	3.2	103	0.57	6.2	5.0	D
88/04/22	09:30:09	2	---	---	3.8	2.5	D
88/10/18	03:40:09	2.45	126	0.77	6.3 ^P	4.7 ^P	D
88/11/23	03:57:09	19	204	0.63	5.2	3.2	D
89/10/04	11:29:57	1.8	94	0.63	5.7	4.8	D

¹ P and S are apparent in the seismograms, but corners are unresolvable.

^P Poorly resolved

Figure 30 shows the P- and S-wave corner frequencies at Degelen vs. yield. Both corner frequencies decrease with yield, as expected, and the median P- to S-wave corner frequency is

1.5, with a scaled median absolute deviation of just 0.2. Most of the deviation from the decline with yield and from the median ratio of the corner frequencies may be due to limited resolution. The important result is that S-wave corner frequencies are consistently similar to, but approximately 1.5 times lower than the P-wave corner frequencies. This is consistent with direct source generation of shear waves being the dominant source of shear waves for the STS explosions, and inconsistent with S*, P-to-S scattering, or Rg-to-S scattering being the dominant source of S. Other observations include that the corner frequencies don't appear to vary significantly over the small range of depths sampled (Figure 30, bottom left), and as expected, the corner frequencies appear to increase with scaled depth, although that observation is dependent on the only explosion at Degelen that was not underburied (Figure 30, bottom right).

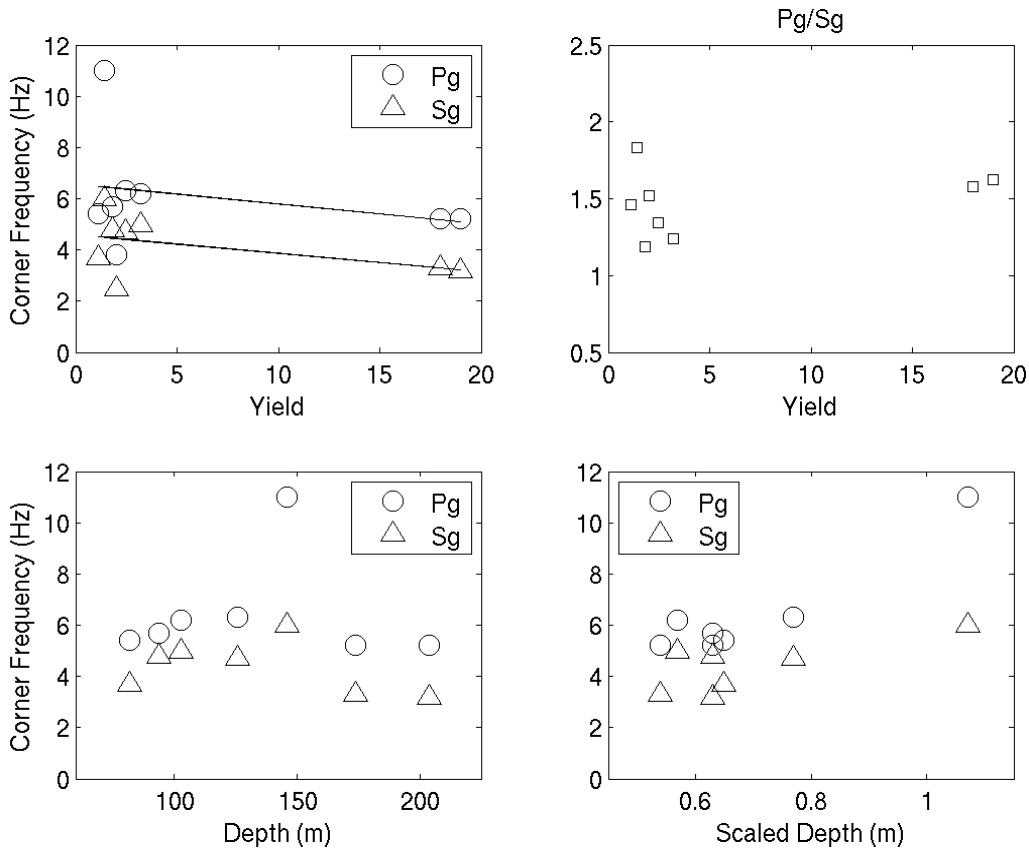


Figure 36. Pg and Sg corner frequencies vs. yield (top left), depth (bottom left), scaled depth (bottom right), and their ratio vs. yield (top right). The upper left also shows best fit curves to both Pg and Sg corner frequencies vs yield.

To compare Rg and Sg spectra, we plot each from the station closest to each explosion that has a distinct Sg phase separate from the Rg (figure 31). Rg peaks are between 0.7 and just under 2 Hz, varying with depth. Rg spectra are distinctly different from corresponding Sg spectra. The 78 Kt explosion spectra is included to show the lower Rg spectral peak there, even though we were unable to accurately identify the S-wave corner, as the corresponding S-wave spectra for this event are not consistent between stations.

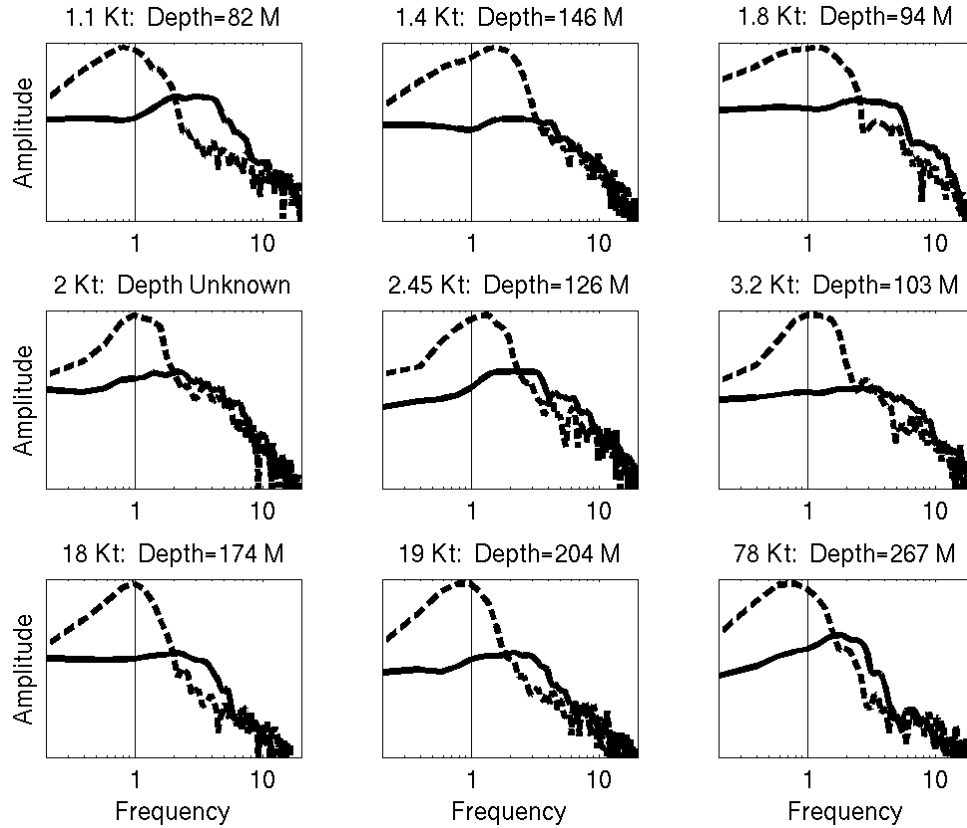


Figure 37. Rg (dashed) and Sg (solid) spectra each of the Degelen explosions, at the closest station to each to have clearly separated good signal-to-noise S. Vertical line indicates 1 Hz.

Figure 38 provides further comparison of the difference between Rg and Sg, showing bandpass filtered seismograms of the largest and one of the small Degelen explosions, both recorded at approximately 30 km. In each passband, the vertical and Hilbert transformed radial are overlain, and both phases are identified by synchronicity of the traces, which distinguishes the retrograde motion expected for the fundamental mode Rg and the higher modes that make up Sg. For both, at the lowest frequencies the much larger Rg extends into the time of the Sg arrival making it impossible to see whether Sg exists at the frequency. At 0.5 to 1.5 Hz (second row) and 1.5-3 Hz (third row), Sg emerges, much smaller than Rg but clearly visible. For the 3.2 Kt explosion, at just 103 m depth, Rg is clear even in the 8-12 Hz passband. Such high frequency Rg is reasonable for the source depth. It arrives at approximately 11 seconds, or 2.7 km/s, so the explosion source depth is 0.4 of a wavelength at 10 Hz. Rg not only peaks at a much different frequency than Sg and is present at lower frequencies, but it persists to higher frequency than the Sg, which has comparable amplitude to Rg in the 3-5 and 5-8 Hz passbands. This observation is inconsistent with Sg being scattered from Rg. A similar observation is made for the 78 Kt explosion. There is no clear Sg in this record above the 1.5-3 Hz window, while Rg persists to the 5-8 Hz window. Sg can be seen in at slightly higher frequency in some records of the 78 Kt explosion at greater distance, although not as clearly or at as high of frequency as Rg.

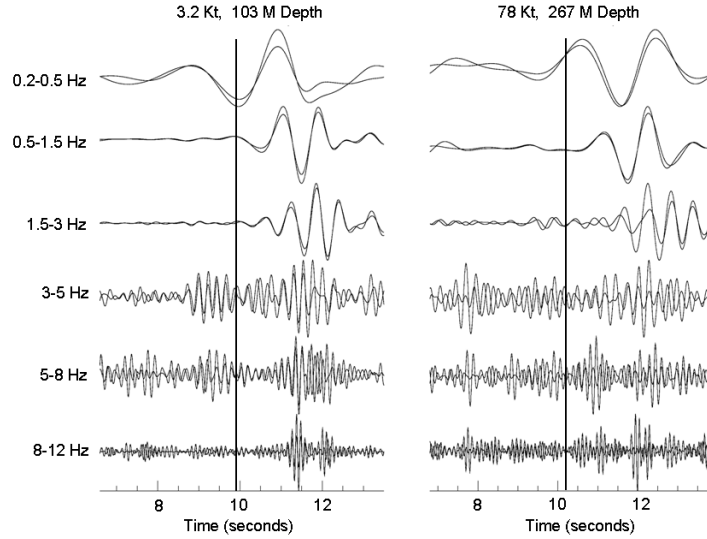


Figure 38. Overlain vertical and Hilbert transformed radial seismograms from 29.7 and 30.6 km respectively from the 3.2 (left) and 78 (right) Kt Degelen explosions, in a range of passbands. The vertical line indicates 3 km/s group velocity.

2.7. P and S Corner Frequencies of Local Degelen Recordings: Simulations

Other spectral features besides the relative S-to-P corner frequencies may bear on the source generating mechanism. The absolute value of the corner frequencies and the relative spectral slopes may distinguish between S^* and pS. The spectra from point spherical explosion and CLVD sources can be predicted using wavenumber synthetics, but they only tell part of the story. The Mueller-Murphy source (Mueller and Murphy, 1971) is commonly used to account for the effects of yield, depth, and material properties on the source spectra. Degelen granite is stronger than the granite at the source of the Piledriver explosion, which was used to estimate the granite Mueller-Murphy source. Thus the RVP calculated for Degelen granite material properties is likely more appropriate for the data we are modeling. Shallow velocity structure also affects the spectra. In this section we present simulations of P and S spectra from spherical explosion and CLVD sources at the depths of the Degelen explosions, examine their sensitivity to small changes in shallow structure and the effect of Mueller-Murphy and RVP source spectra, and assess whether the observations can be used to further distinguish source mechanisms.

CLVD synthetics are particularly sensitive to small variations in the shallowest velocity structure, and so we produce synthetics for two versions of the Degelen velocity model, to ensure that artifacts due to model sensitivity are identified as such and not interpreted. Figure 39 shows upper layers of the basic Degelen model (solid lines), and one in which the upper 160 meters gradually increases in velocity from 3.6 to 5 km/s, and in which the upper crustal velocity (from 1.5 to 6.5 km depth) increases more gradually from 5.2 to 6.2 km/sec (dashed lines). Knowledge of variations between specific source locations in the uppermost layers, where sensitivity is greatest, does not exist.

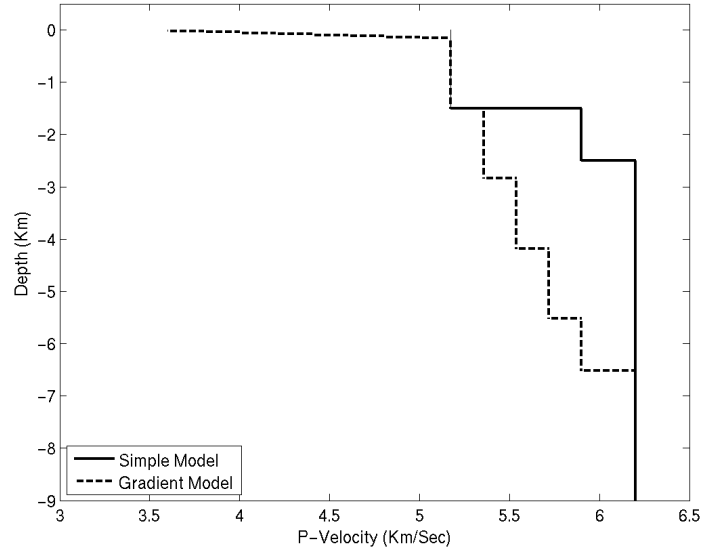


Figure 39. Simple Degelen velocity model (solid) and a modified model that includes a gradual increase in velocity from 3.6 to 5.0 km/s in the uppermost 160 meters, and a more gradual increase from 5.2 to 6.2 km/s (dashed).

Figure 40 shows the spectra of spherical explosion P and S* at the depth of each Degelen source for the two models. For an explosion source, the spectra are similar for the two models. The S* spectra are all similar, except that the deeper sources have slightly steeper slopes.

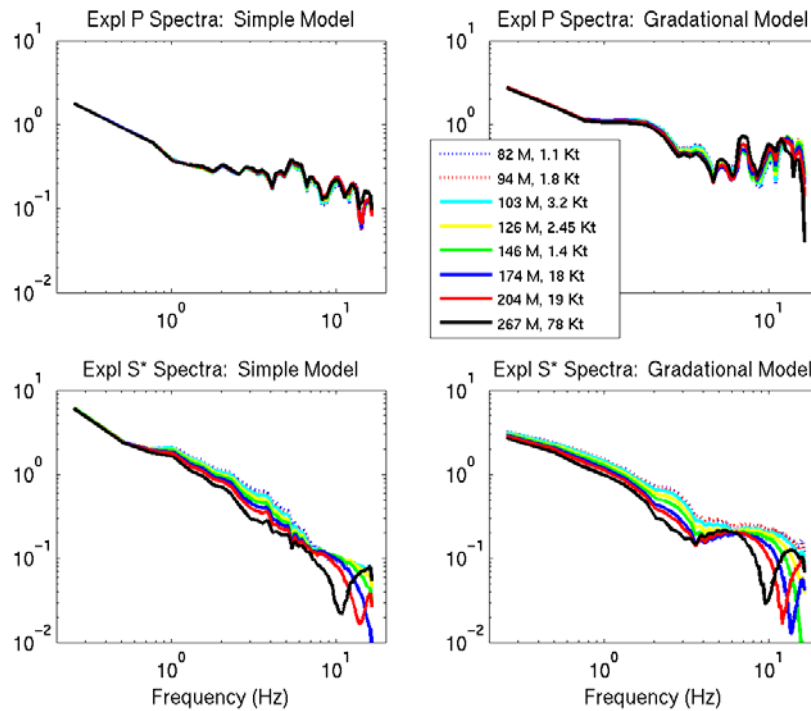


Figure 40. P and S* spectra from spherical explosions source wavenumber synthetic seismograms at the depth of each Degelen explosion source, for the two Degelen velocity models of Figure 39.

Figure 41 shows the predicted source spectra, normalized by their yields, for the largest and smallest Degelen explosions, based on their depths and yields and the Mueller-Murphy granite source vs. the RVP for Degelen granite. Figure 42 shows the RVP source spectra for each of the Degelen explosions, based on their depths, yields, and the material properties of Degelen granite. Each source spectra is normalized by that event's yield. As Degelen granite is stronger than that used to develop the Mueller-Murphy model, the RVP source spectral corner frequencies are higher.

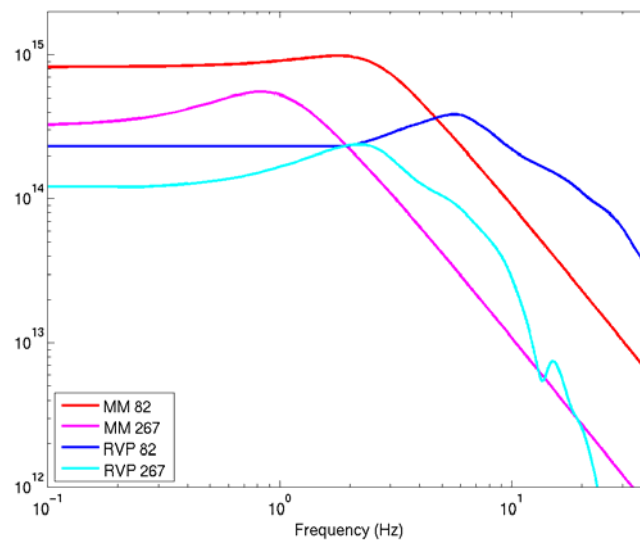


Figure 41. Predicted source spectra normalized by yield for largest (78 Kt, 267 m depth) and smallest (1.1 Kt, 82 m depth) Degelen explosions based on the Mueller-Murphy granite source spectra and RVP.

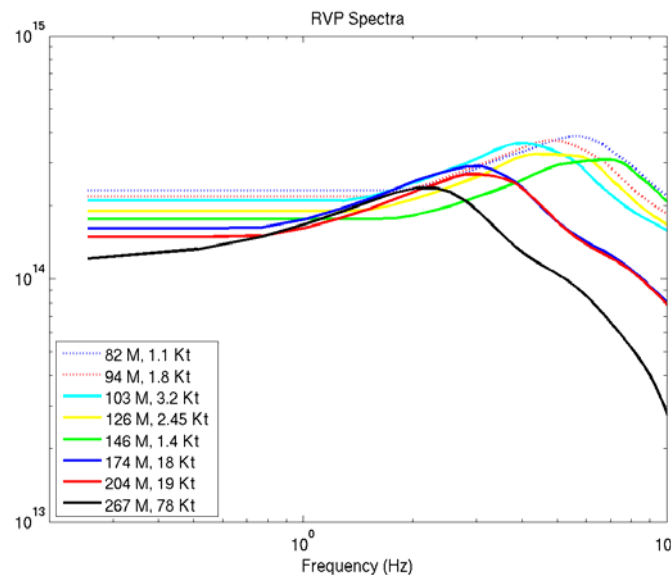


Figure 42. Source spectra from the RVP for each Degelen explosion, normalized by yield.

Figure 43 shows the spherical explosion synthetic spectra, normalized by yield, and convolved with the appropriate RVP source. For both the P and S, for both models, it is clear that the corners decrease with yield, although, as with the observations, picking exact corner frequencies is difficult. Figure 44 shows the ratio of the S* to P spectra for the explosion sources. This comparison has the advantage of not requiring an assumption of a particular source spectra. For the simple model, the ratio is much higher above a few Hz. Also, all the spectral ratios are identical below 1 Hz, with a clearly steeper S* slope than P slope above 1 Hz. This would provide a good prediction for comparison with observations to test the hypothesis that S* is the dominant source of the explosion Sg. Unfortunately, sensitivity to variations in the model structure lead to very different spectral ratios for the gradational model. Since we do not have precise information about variations in the shallowest structure between explosion locations, we must look for broader differences between S* and CLVD S-wave spectra.

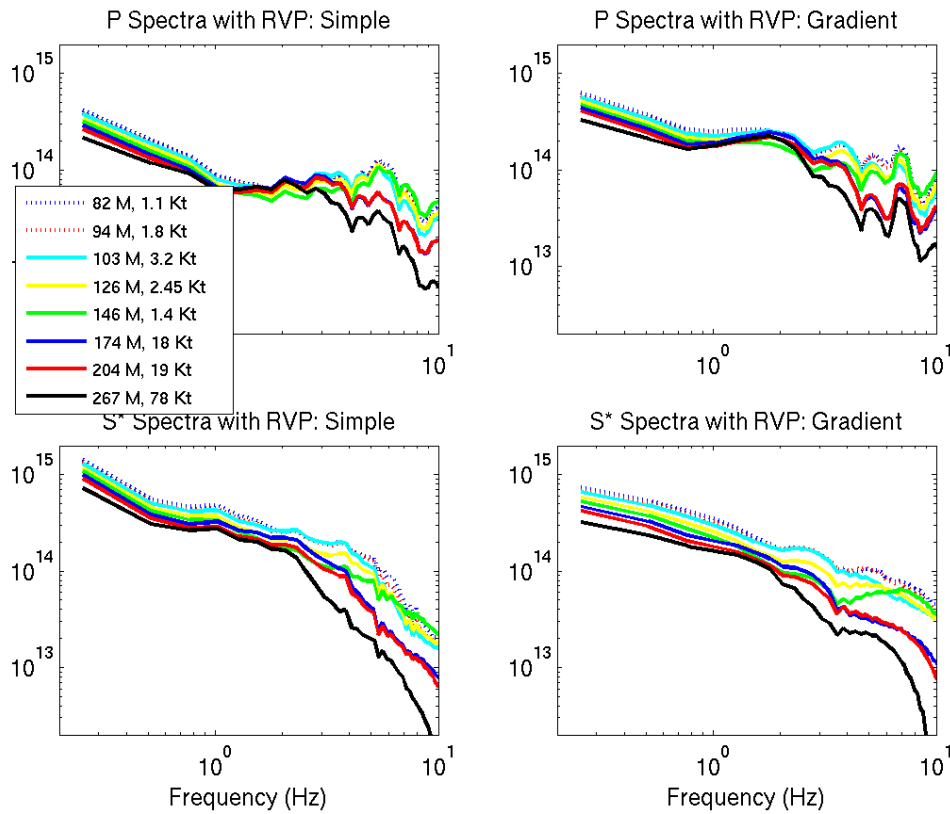


Figure 43. Spherical explosion source synthetic P (upper) and S* (lower) spectra for simple model (left) and gradient model (right), convolved with spectra predicted based on the RVP for each Degelen explosion and normalized by yield.

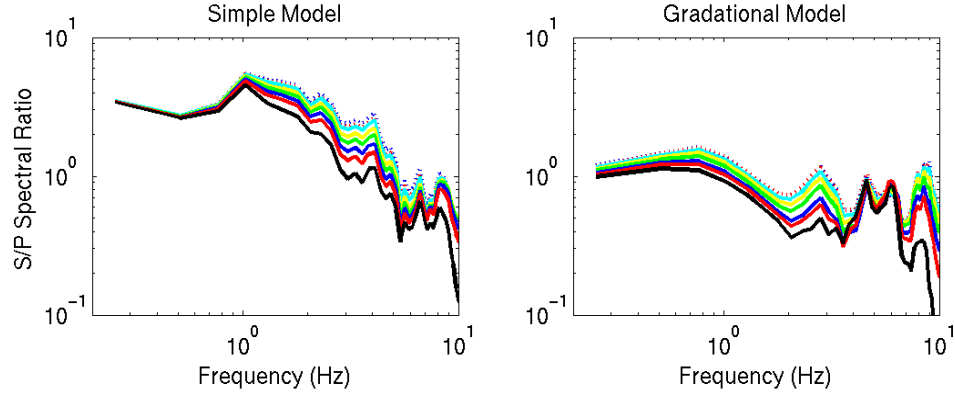


Figure 44. Spherical explosion source S*-to-P spectral ratios for the simple (left) and gradient (right) models.

The CLVD S spectra is much more complex than the spherical explosion S* spectra, and is more sensitive to the velocity model (Figure 45). The complexity is great enough that it obscures much of the spectral shape of the RVP. For the spherical explosion, we used the same RVP source spectra for P and S*, since S* is scattered from P. For the CLVD, we use the RVP source for the P-wave, but scale the corner frequency by the S-to-P wave velocities, as suggested by previous studies (Murphy et al., 2006; Fisk 2006, 2007). Again, one can see that the P and S corners diminish with yield, but the complexity due to shallow structure makes it difficult to pick the corners precisely and could lead to errors in identifying the corner frequencies (Figure 46). The S-to-P spectra ratios are also quite complex, with nulls and multiple peaks, which vary depending on source depth and model (Figure 47). These simulations demonstrate that details of the individual spectra vary depending on shallow near source structure, which is likely to vary between source locations and is poorly known. Although this result is frustrating, it is very important to recognize, so we understand what features in the observations can be interpreted. This suggests that general trends, observed in multiple events' spectra, and for individual event spectra averaged over multiple records, are much more reliable than differences between individual spectra. Figure 48 shows the observed spectral ratios from the station closest to 50 km distance from each Degelen explosion. While the variability between spectra and the multiplicity of peaks and troughs is much more similar to the predicted CLVD spectral ratios than to those of the spherical explosion source, interpreting this by itself as evidence of a particular mechanism would be reaching. It is however consistent with all the other spectral evidence point to direct source generation.

The solid conclusions that can be made from the local Degelen spectra are that

- 1) the S-wave corner frequencies are consistently lower than the P-wave corner frequencies by approximately the ratio of the S-to-P wave velocities, as predicted for source generated S-waves,
- 2) the S and Rg wave spectra are distinctly dissimilar, which is inconsistent with Rg-to-S scattering,
- 3) the absolute value of the corner frequencies vary with yield much more than the predicted S* corner frequencies, indicating that S* does not dominate the spectra, and
- 4) the S-wave spectra are peaked just before the corner frequency, again indicating direct generation at the source.

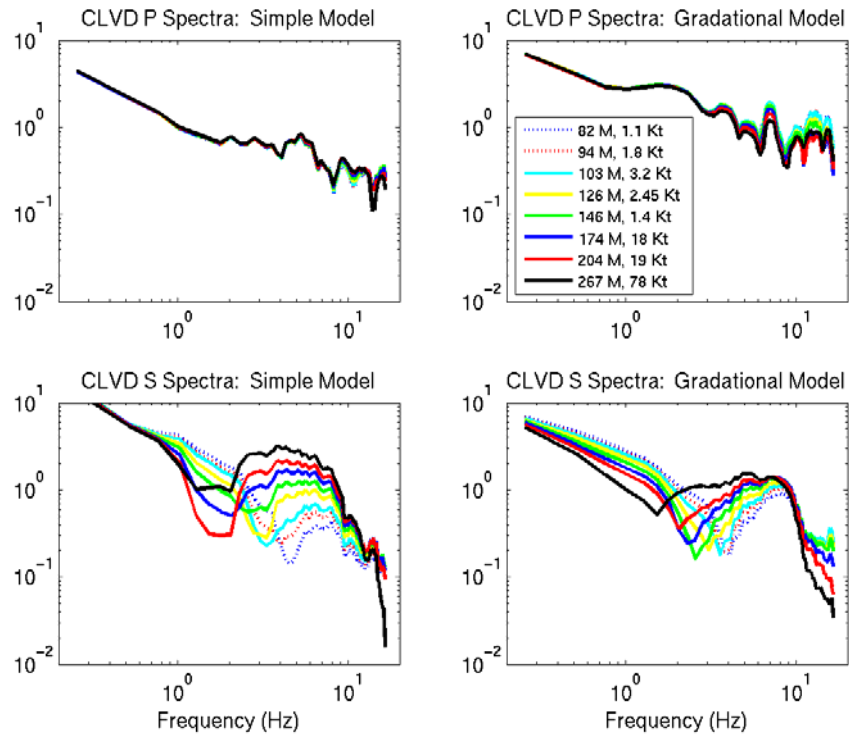


Figure 45. P and S spectra from CLVD wavenumber synthetic seismograms at the depth of each Degelen explosion source, for the two Degelen velocity models of Figure 39.

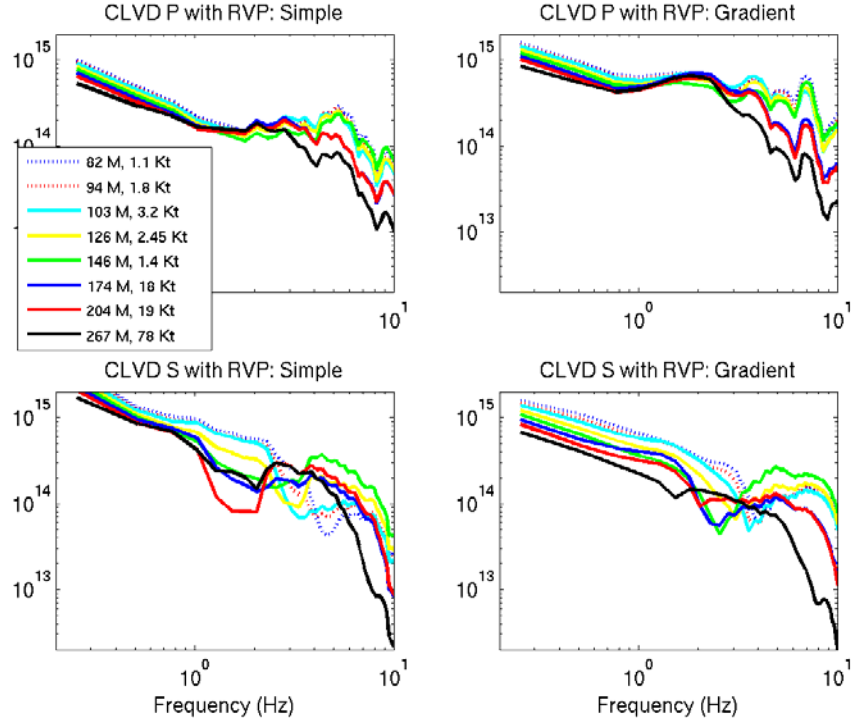


Figure 46. P and S spectra from CLVD wavenumber synthetic seismograms at the depth of each Degelen explosion source, convolved with spectra predicted based on the RVP for each Degelen explosion and normalized by yield, for the two Degelen velocity models of Figure 39.

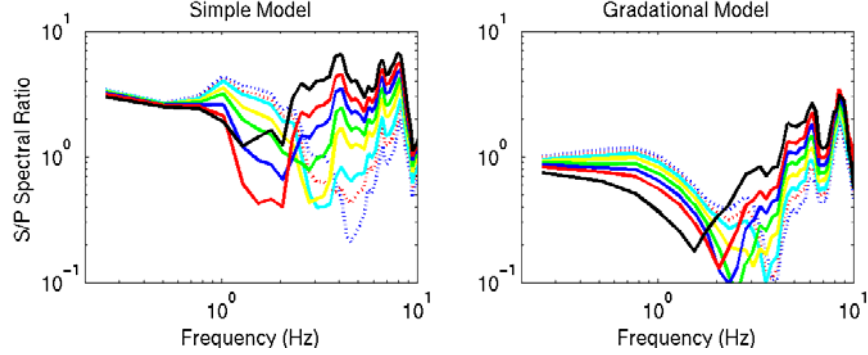


Figure 47. CLVD S-to-P ratios for simple (left) and gradational (right) models.

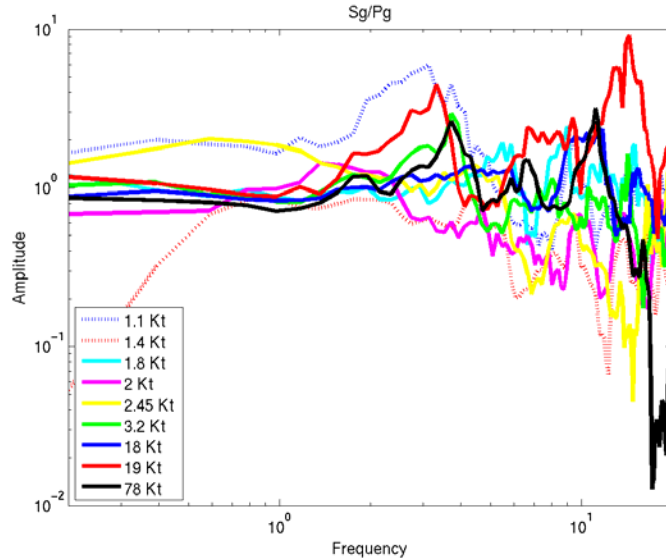


Figure 48. Observed S-to-P ratios for records from each Degelen explosion recorded closest to 50 km distance.

We have not addressed the effect of scattering, particularly its frequency dependence, on spectral shapes. This is in general beyond the scope of this project. We present here, however, one result from the 3D scattering calculations using the actual topography at Degelen Mt. Figure 49 shows the P, S, and Rg spectra at 25 km for a 325 m depth point explosion in two models from Figure 7, the homogeneous model for the Degelen velocity structure, and the same model plus the 3D topography at Degelen Mt. The differences between synthetics are due to topographic scattering. S in the model with topography has more energy from DC out to approximately 5 Hz, which is the upper frequency limit of the calculation's validity, but that additional S may not all come from the same source. The homogeneous model's S-wave is due to S*. Around 1-2 Hz, the P spectra is smaller in the topographic model. That is consistent with Myers et al. (2006) calculations which showed enhanced S relative to P at 1 Hz due to topographic scattering of the P-wave, using the 3D structure at NTS. Rg is larger at 1-2 Hz in the topographic model, suggesting enhanced generation due to topography. Around 3 to 5 Hz, the P and Rg spectra are both smaller in the topographic model. In fact, from the waveforms, we see that Rg is almost completely absent above 3 Hz, while it is still dominant in the homogeneous model (Figure 50). If the Rg scattered to Sg, that would suggest that Rg contributes to S at higher frequencies than is usually thought, rather than at around 1 Hz. We have no measures however of how much Rg is scattered into downgoing waves (lost to the mantle) and coda vs. into Sg. P scattering into S is consistent with Xie et al.'s (2005) findings that random shallow heterogeneities scatter pS into Lg at higher frequencies and S* into Lg at lower frequencies.

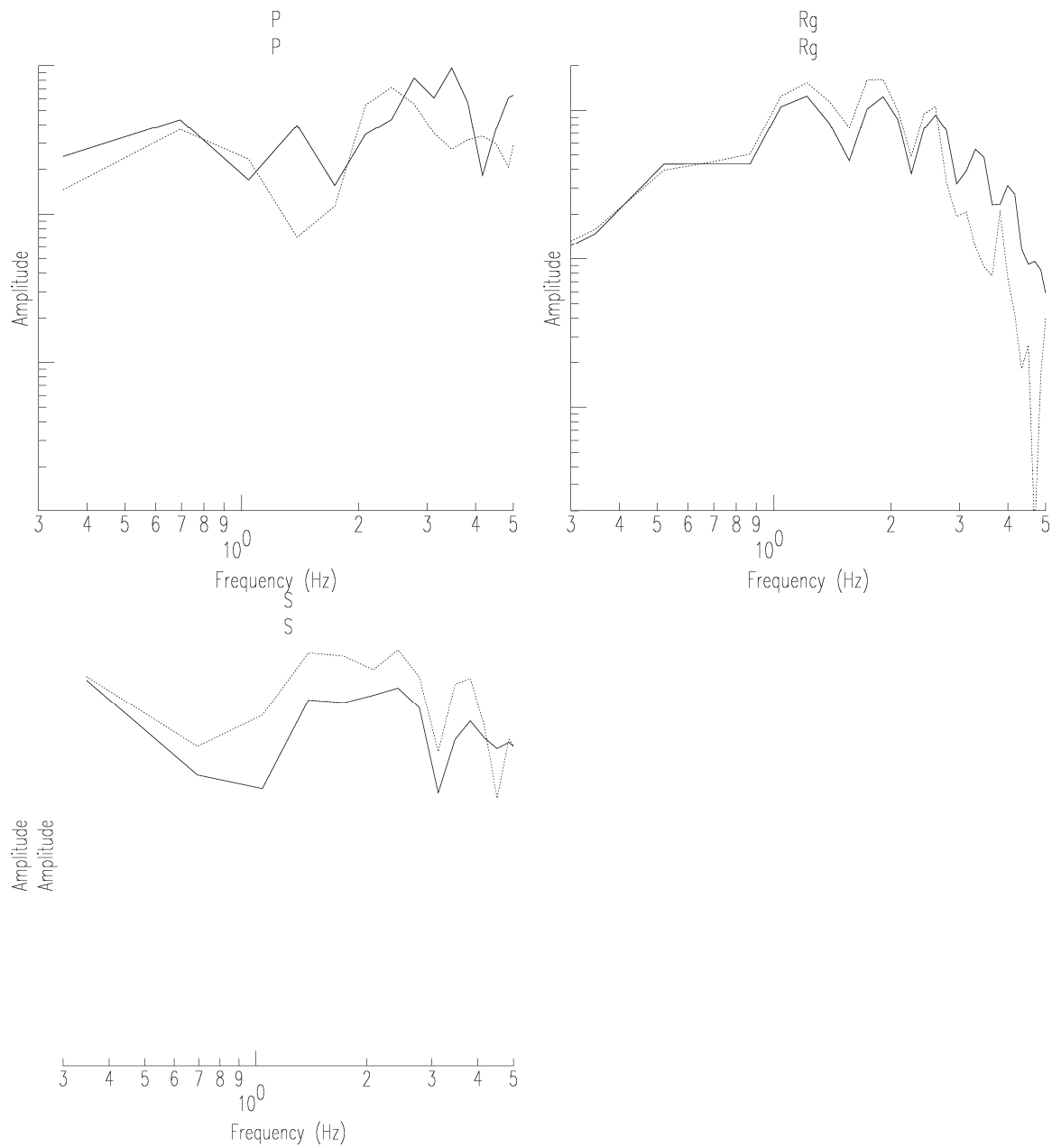


Figure 49. P, S, and Rg spectra (upper left, upper right, and lower left respectively) for a 325 m depth point explosion in a homogeneous Degelen velocity structure (solid) and the same model plus the actual Degelen topography in 3D (dashed).

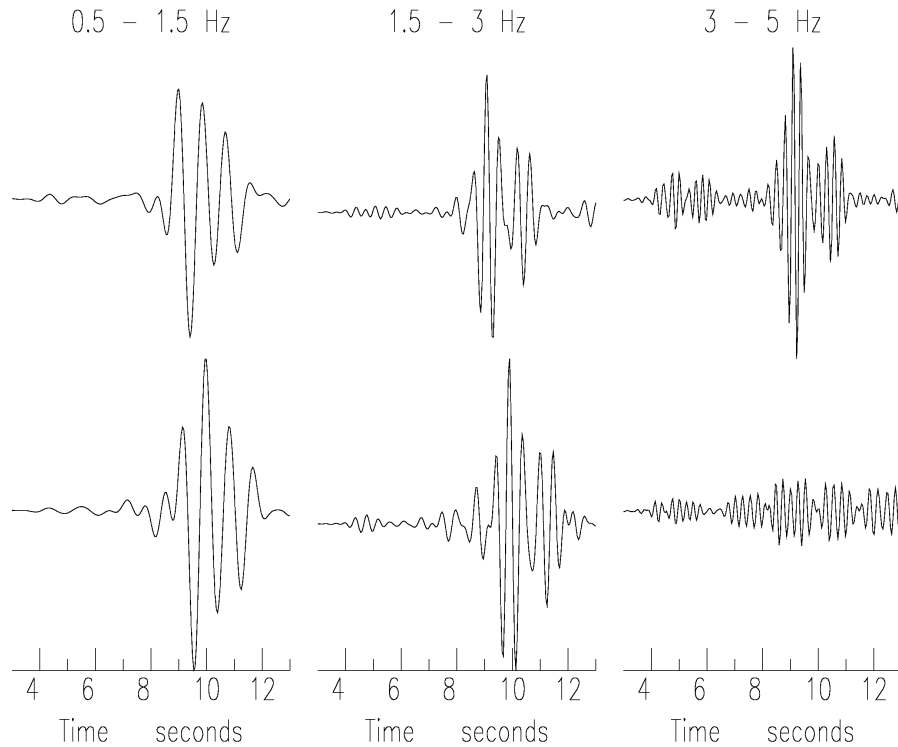


Figure 50. Seismograms at 25 km for a 325 m depth point explosion in a homogeneous Degelen velocity structure (upper) and the same model plus the actual Degelen topography in 3D (lower) in 3 passband

2.7.1. Spectral Nulls are Azimuthally Dependent and Different for Rg and Sg

As previously discussed, common spectral nulls in Rg and Lg have been cited as supporting scattered Rg as the dominant contribution to Lg. The proposed mechanisms for the Rg spectral nulls predicts they will be independent of azimuth, while the inference that shear wave phases are a result of scattered Rg depends on both having the same null. We test the prediction of azimuthal independence using Balapan records at a range of azimuths. Chapter 3 complements that effort with Deep Seismic Sounding (DSS) recordings in two directions extending from near source to regional distance.

Figure 51 (left) shows the Rg spectra from recordings of a Balapan explosion that span approximately 45° in azimuth. There are some distinct nulls in the individual Rg spectra, but they are not consistent, and the stacked spectrum has no distinct null corresponding to even the small nulls in the regional Lg spectra from the same event (Figure 51, right). In synthetics, simple addition of a second Rg, smaller and lagged in time to an initial Rg phase, produces a phase with nulls whose position depends on the lag time. Spectral nulls could simply result from near source Rg-to-Rg scattering, for which we have seen much evidence.

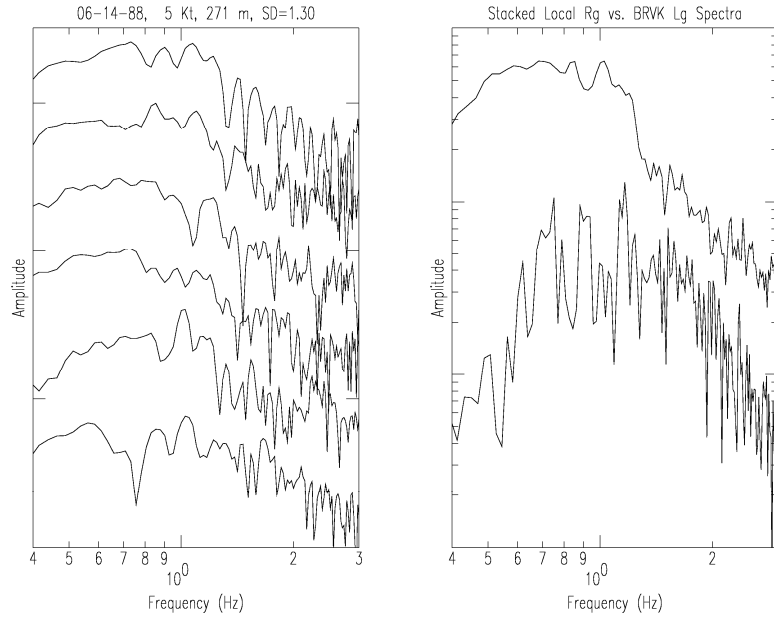


Figure 51. Individual Rg spectra from local (67 – 89 km) vertical records at different azimuths have nulls at different frequencies (left). Stacked local Rg spectra (right, top trace) and BRVK Lg spectra don't have corresponding nulls.

2.8. Conclusions

We have compared the contributions of different explosion shear wave source mechanisms to determine which dominate in high velocity source material. Rather than simply determining whether data are consistent with a particular mechanism, the objective wherever possible has been to find means of eliminating mechanisms. We have used numerical simulations to make predictions that can be tested with the data available, most notably local STS records. We have also used numerical simulations to predict and directly compare the contribution of different mechanisms. The results consistently point to direct generation by nonspherical source elements as the dominant source of explosion shear waves in high velocity source media.

Nonlinear source calculations indicate that direct generation of shear waves by nonspherical source elements produces Lg amplitudes with less variance than is observed in data, for a greater range of scaled depths than spanned by the data. A spherical explosion source plus a CLVD source of half the magnitude and at half the depth of spherical source provides a good approximation to the nonlinear source. Comparison of Lg spectral amplitudes of wavenumber synthetics for such composite sources with spectra from modal scattering calculations indicate that Rg at most, for the shallowest sources, could provide comparable amplitude Lg at 1 Hz to the directly generated S from the CLVD. Deeper explosions will provide even less. In the real Earth around STS, intrinsic Q, scattering to P and S waves that propagate into the mantle, and gradual scattering of Rg in this high velocity region will reduce the contribution from Rg. S* from the explosion source can also provide comparable amplitude at 1 Hz to the direct S.

Analysis of local records of Degelen and Balapan explosions complement these calculations. The local Sg travel times are consistent with direct generation. Instantaneous scattering very near

the source could also produce the observed travel times, although if scattering to S from either P or Rg were the dominant source of Sg, we would expect such scattering to occur away from the source as well. This is less likely given the compact, impulsive character of Sg.

Sg spectral corner frequencies decrease with yield, and are less than those of the corresponding P wave corner frequencies by approximately a factor of 1.5. They have an “elastic rebound” peak similar to those of the P wave spectra. The spectra of Rg, which has a depth dependent peak frequency, has no correlation with the Sg spectra. All of these observations are inconsistent with Rg scattering being the dominant source of Sg. The consistently lower yield and depth dependent corner frequency of the S relative to the P-wave is consistent with direct generation of S by the source dominating over P scattering to S, either as pS or S*.

Finally, observations of common spectral nulls in Rg and Lg have been interpreted as demonstrating that scattered Rg is the dominant source of Lg (Patton and Taylor, 1995; Gupta et al, 1997; Patton and Phillips, 2006). Rg recorded over a span of azimuths 50 km from Balapan explosions have different spectral nulls at different azimuths. This violates the assumption that the Rg spectral null depends dominantly on source depth. In this case, regional Lg does not share a spectral null with local Rg. For Balapan therefore, one of the main arguments purported to demonstrate a link between local Rg and regional Lg does not hold.

Table 7. Predictions based on numerical simulations.

Method	Result
Finite-difference scattering calculations for the Degelen velocity model with the actual Degelen Mt. topography and random lateral heterogeneities.	Topography dominates scattering over random heterogeneity within the media.
	The actual topography at Degelen can sufficiently alter the incidence of pS so that a significant amount is trapped in the crust and contributes to Lg. Spectra of 3D calculations shows loss of P energy and increase in Rg and Sg at 1-2 Hz. Sg increases at 2-5 Hz as well, where Rg loses significant energy.
	The effect of the topography at Degelen on Rg is to significantly decrease its velocity, and increase dispersion and scattering attenuation.
	The actual topography at Degelen scatters Rg into tangential, but not radial or vertical shear waves.
	<i>Each of the above only shows feasibility of a mechanism, but does not demonstrate that its contribution will be dominant.</i>
Modal Scattering calculations (compared with wavenumber synthetics for spherical explosion and CLVD sources).	At 1 Hz, for the Degelen velocity structure, an extreme upper bound estimate of the contribution of scattered Rg to Lg is barely comparable to the contribution of directly generated S from non-spherical source elements at 50 m depth. The relative contribution of scattered Rg is much less above 1 Hz or for deeper sources. <i>This shows that direct S generation contributes more to Lg than Rg scattering.</i>
Nonlinear source simulations	For a range of scaled depths exceeding that observed, the Lg amplitude due to direct S from nonspherical source elements varies less than is observed in previous studies of Lg yield scaling and in the current study. There is no apparent depth or scaled depth dependence. <i>This shows that predicted depth and scaled depth dependence and yield scaling do not exclude any mechanisms.</i>

Method	Result
Wavenumber synthetics	
- spherical explosion source (combined with Mueller-Murphy or RVP source spectra)	<p>The predicted variation in S* amplitude at 1 Hz over the range of source depths at STS is too small to distinguish in regional observations.</p> <p>S* corner frequencies for the range of depths and yields at Degelen should all be similar to the P-wave corner frequencies. The S*-to-P spectral ratios should be similar for all events, with the greatest difference being a slightly steeper slope above 1 Hz.</p>
- CLVD source (combined with Mueller-Murphy or RVP source spectra)	S corner frequencies should be less than P corner frequencies by the S-to-P velocity ratio, but sensitivity to near source velocity structure, reflected in multiple spectral peaks and nulls, will make the corner frequencies difficult to pick. Resolution can be improved by stacking multiple spectra.

Table 8. Observations and implications for source mechanisms.

Observation	Implication
Regional (BRVK) amplitudes for STS Pn, the entire P wavetrain, Sn, Lg, and Lg coda, and all possible combinations of S/P ratios have the same source scaling, and show no depth or scaled depth dependence.	This is consistent with the findings of most, but not all, previous research on source scaling of different phases. The resolution however is not sufficient to distinguish the differences predicted by different mechanisms. For that, we examine local records.
Local Degelen Sg is impulsive and temporally compact, with little variance in the travel times from those predicted.	This is consistent with direction generation of shear waves at the source, or a single, almost instantaneous near source scattering into Sg. It is inconsistent with a scattering source for Sg from P or Rg anywhere but very near the source.
Spectra of local Degelen records shows that:	
Sg corner frequencies are consistently smaller than P corner frequencies by the ratio of the S-to-P wave velocities	This is consistent with direct generation of S at the source, and inconsistent with trapped pS, S*, or Rg scattering being the dominant source of Sg.
Sg spectra are peaked just before the corner frequency.	This is similar to the shape of the P spectra, where the peak is attributed to elastic rebound. Hence, this indicates that the Sg is generated at the source.
Rg and Sg spectra have distinctly different peaks, corner frequencies, and patterns of variation with depth and yield. For some events, Rg is apparent at higher frequencies than Sg.	This is inconsistent with Rg scattering providing the dominant source of Sg.
Individual records' Sg/P spectral ratios are complex, with peaks and nulls much more similar to those predicted for CLVD sources than for S*.	This is consistent with source generation of Sg.
Rg spectral nulls are different at different azimuths for Balapan events.	This demonstrates that for Balapan, the assumption in previous work that Rg spectral nulls are source depth dependent is not valid. That assumption was the basis for concluding that Rg was the dominant source of Lg in several previous works.

3. EXPLOSION SHEAR WAVE GENERATION IN LOW VELOCITY SOURCE MEDIA

3.1. Introduction

This paper addresses explosion shear wave generation in low velocity source media. Understanding the generation of shear waves by explosions is important to nuclear monitoring, because of the role that the ratio of shear wave to P wave amplitude plays in discrimination, and the role of Lg in particular in regional magnitude estimation. Despite decades of research, however, there is no consensus regarding which shear wave generating mechanisms might dominate under any particular source conditions. We list the candidate mechanisms here. Detailed discussion of previous work and simulation methods used to model each mechanism are provided in Chapter 2, which addressed the problem in high velocity source media.

The explosion shear wave source mechanisms under consideration include scattering from P, both pS and S*, scattering from Rg, and direct generation by non-spherical components of the source. pS will be trapped in the crust if the source P-wave velocity is less than the mantle S-wave velocity, which is the case we consider in this chapter. S*, the nongeometric phase generated by conversion of the curved P wavefront can be significant for shallow events. Rg is a candidate source because it generally is the largest amplitude phase near shallow sources, particularly at low frequencies where Lg is also enriched, and it scatters rapidly. Nonlinear source calculations have shown that nonspherical source elements can also reproduce the local and regional phases observed in the data.

In this chapter we focus on two datasets. The first is a set of nearly co-located nuclear explosions at the Nevada Test Site (NTS), three normally buried and two overburied. These data were analysed by Patton and Taylor (1995), and more recently by Patton and Phillips (2006). Those studies concluded, based on a null at 0.55 Hz in the ratio of the normally buried to overburied vertical component Lg spectra, that scattered Rg was the source of Lg. We find that the spectral null is also consistent with other mechanisms, and investigate means, both data analysis and numerical simulations, of testing which mechanisms dominate. At higher frequency in the same data, we compare P and S spectra to test the hypothesis that the source generation mechanisms differ. Because the existence of common spectral nulls in Rg and Lg has been interpreted as proof that Rg scattering is the source of Lg (Patton and Taylor, 1995; Gupta et al, 1997), we also examine spectral nulls in Rg, and Sg and Lg from the Deep Seismic Sounding (DSS) experiment Quartz-3, an 8.5 Kt, 726 m depth nuclear explosion in low velocity source media. Recordings range from 10s to 100s of km from the source in two directions, providing an opportunity to compare characteristics of Rg, Sg, and Lg spectral nulls with predictions.

The data analyses are complemented by simulations to assess the relative importance of each mechanism's contribution. We use nonlinear source calculations to estimate the contribution of the nonspherical source elements, Rg modal scattering calculations to bound the contribution of scattered Rg, and spherical explosion source wavenumber synthetics to estimate pS and S* amplitudes.

3.1.1. Previous Work on Co-located Overburied and Normally Buried Explosions

Patton and Taylor (1995) addressed the problem of shear wave generation by explosions in low velocity source media with a unique data set of adjacent overburied and normally buried explosions. They interpret a 0.55 Hz null in the ratio of Lg spectra from normally buried to overburied explosions as the result of imprinting of the CLVD generated Rg spectra onto Lg, where the null is a result of depth of the CLVD. Recently, Patton and Phillips (2006) revised that conclusion. They still assume that Rg-to-S scattered energy is the dominant source of S and ignore S-waves generated by P-to-S scattering and by the CLVD component of the source. They also assume that the Rg spectral null is not filled in by interference by multiply scattered Rg phases. The newer work addresses the source of the null in Rg. Specifically Patton and Phillips (2006) argue that interference between the isotropic explosion Rg and the CLVD Rg phases leads to a null in the sum of the phases.

3.1.2. Previous Work on Source Scaling and S and P Corner Frequencies

Recent work on source scaling of S relative to P, some of it conflicting, also bears on the mechanisms generating the S and P waves.

Fisk et al (2007) find for NTS that P and S corner frequencies scale similarly with yield, with the Lg spectra shifted to lower frequency by the ratio of the source S-wave to P-wave velocity ratio. They conclude that S-waves are generated by mechanisms operating on the same length scale as the P-wave mechanism, which is consistent with S-waves being generated within the same source volume as the P-waves, and is inconsistent with P-to-S conversion, which should produce similar corner frequencies in both phases' spectra. We note that the Rg-to-S scattering mechanism also does not predict a consistent relationship between P and S corner frequencies. Similar results were found for other test sites. Fisk (2006) and Murphy et al (2006) find that the source scaling of P and S are similar, with S-wave corner frequencies reduced by the source S/P ratio for the Semipalatinsk and Lop Nor test sites. Fisk (2006) also found similar results at the Novaya Zemlya test site. These results were found using regional phases. Baker et al (2007a) obtained the same results using local Pg and Sg recordings at Semipalatinsk. In contrast to other previous work, Patton and Phillips (2006) report different P and S phase scaling at NTS and STS.

3.1.3. Normally Buried vs. Overburied Explosions' Spectra at NTS: Low Frequency Null

Patton and Taylor (1995) normalized the vertical component Pg and Lg spectra of three normally buried explosions by those of two nearby overburied explosions. They attribute a consistent spectral null at 0.55 Hz in the Lg spectral ratios to Rg from the source, which scatters into Lg. We have expanded on their analysis using 3-component records and examining non-normalized records of Pg, Lg, and late Lg coda (3.0 to 2.0 km/s). We also analyze late Lg, because the modal modeling results, as described above, indicate that even if all Rg is instantaneously scattered to higher modes, it will contribute more to the Lg coda than it does to Lg. We do not use spectral ratios, because a spectral peak at 0.55 Hz in the overburied events' spectra causes a corresponding null in spectral ratios, which makes interpretation ambiguous.

Our results confirm the existence of a null in the vertical component Lg window, and there is a hint of it in the radial Lg window, but there is no corresponding tangential Lg null. We also find no corresponding Pg or late Lg spectral null.

Table 9 lists the distances from the normally buried events to each of the overburied events, $m_b(Lg)$ from Patton and Taylor (1995), depths, scaled depths, and which components were available at each of the 4 LLNL stations used for the 5 events used in Patton and Taylor (1995).

Table 9. Metadata and availability of 3-component data from NTS events used in Patton and Taylor (1995) to investigate the effects of spill.

	Dist ¹ (km)	Dist ² (km)	($m_b(Lg)$)	Dep.	SD	ELK 412 km	MNV 238 km	LAC 301 km	KNB 287 km
Caprock	0.34	1.36	6.16	600	0.77	-	T,R,Z	T,R,Z	N,Z
Baseball	2.14	0.45	5.89	564	0.94	T,R,Z	T,R,Z	T,R,Z	T,R,Z
Glencoe	2.97	2.06	5.84	610	1.62	N,Z	T,R,Z	T,R,Z	E,Z ³
Techado	-	1.70	4.66	533	3.07	T,R,Z	T,R,Z	T,R,Z	Z
Borrogo	1.70	-	4.26	564	4.85	T,R,Z	T,R,Z	T,R,Z	T,R,Z

¹ Distance from Techado

² Distance from Borrogo

³ East component exists but is extremely poor quality

For consistent comparison, we perform spectral estimates similar to those made by Patton and Taylor (1995). They estimated spectra of Pg and Lg, using group velocity windows from 6.0 to 5.0 km/s and 4.0 to 3.0 km/s respectively, by differentiating to obtain acceleration, applying 10% cosine tapers, and then dividing the spectra by f^2 to obtain displacement spectra. The one way in which our estimates differ is that we use longer records to obtain the Pg spectra. The spectral null, which is the most important observation of Patton and Taylor (1995) is at 0.55 Hz. At MNV, the Pg time window spans only 4 cycles at that frequency, even before tapering, so we use a window extending to 4.0 km/s, which is dominated by the Pg coda, giving us 11 cycles at MNV. This is the same length as the Lg window. The existence of the 0.55 Hz null depends on an accurate amplitude estimate at 0.4 Hz. Thus we need to obtain an accurate spectral estimate from a time series that spans just 8 cycles, and the untapered portion of the time series spans only 6 cycles at the frequency of interest. To ensure meaningful results we first assess the accuracy of the spectral estimate.

We generated 256 realizations of time series of comparable length to the Lg window at MNV, with flat spectra except for a null at 0.55 Hz. We then estimated the spectra using the Fourier transform amplitude, Welch's method, and the multitaper method (Thompson, 1982; Park et al, 1987). All the methods identified the spectral null in most realizations of short time series, but failed in some (not necessarily the same ones). The Fourier transform generally resolves the true null, but has somewhat more spurious spectral nulls. The multitaper method produces smoother spectral curves, with the true spectral null generally less sharply defined, but with fewer spurious spectral features. Welch's method was somewhat less accurate in the position of null than the other methods. We proceed using the Fourier amplitude, for consistency with previous work.

Patton and Taylor (1995) showed individual vertical component Pg and Lg spectra of Baseball and Techado at ELK, the ratios of Baseball to Techado vertical component Lg spectra

at each station, and network average vertical component Lg and Pg ratios for each event relative to Techado. They highlight the prominent spectral null in the ratios of the normally buried event spectra relative to those of the overburied event Techado. There is no similar null in the ratios of the spectra of the two overburied events, or in any of the Pg spectral ratios. Patton and Taylor (1995) attribute the null to scattering from Rg produced by the CLVD component of the normally buried events, which is absent in the overburied events, with a refined mechanism proposed in Patton and Phillips (2006).

We further test this hypothesis in a few ways. First, we examine spectra of tangential and radial Pg, Lg, and late Lg (3.0 to 2.0 km/s group velocity) along with the vertical component spectra. The hypothesis that the dominant source of Lg is scattered Rg predicts that the tangential Lg must be scattered directly from Rg or from the vertical and radial Lg, so all three components should share the characteristic null. Figure 52 shows the network average ratios of Pg, Lg, and Lg coda spectra of the normally buried events to the corresponding Techado spectra, for all three components. In addition, we plot the ratio of a straight line with a $1/f$ slope relative to the spectra of each phase from Techado. These plots show two important results. First, while the vertical component Lg spectral ratios have a prominent null at 0.55 Hz, there is no consistent corresponding feature in the radial or tangential Lg spectral ratios, as the scattering hypothesis would predict. Second, the ratio of the straight reference curve to the vertical component Lg spectra of Techado has the same prominent null at 0.55 Hz as the vertical component Lg spectral ratios of the normally buried explosions. This is due to a spectral peak in the Techado spectra around 0.55 Hz. Borrego's vertical component Lg spectra has a similar spectral peak. This indicates that the null in the ratios is due at least in part to a spectral peak in the vertical Lg spectra of Techado. To avoid the ambiguity this causes regarding the source of the spectral null, we must examine the raw spectra, not spectral ratios. The prominent null in all three components of the coda spectral ratios, including the reference line, is also due to a peak in Techado's spectra.

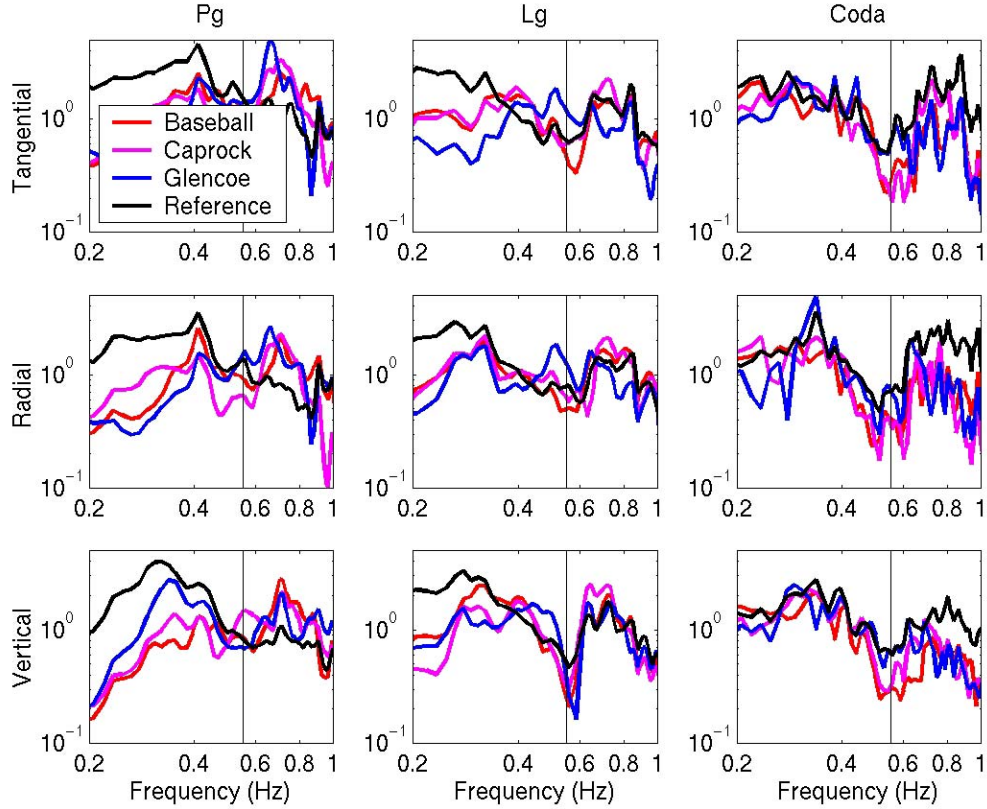


Figure 52: Network average normally buried event spectra for Pg, Lg, and Lg coda for all 3 components, normalized by the corresponding spectra of Techado. Also, the ratio of a straight line with a $1/f$ slope relative to Techado's spectra (black).

Figure 53 shows all 3 components of spectra for Pg, Lg, and coda windows of Baseball. Individual station spectra are shown in lighter, colored lines. The recording stations are at different distances, so the energy recorded was subject to different amounts of attenuation. We normalize each spectral curve by the rms amplitude between 0.2 and 1 Hz before calculating the network average. No attempt was made to account for frequency dependence of attenuation. Network average spectra are represented by the thick black curves.

For Baseball, the 0.55 Hz null is clear in both the vertical component Lg, and in the radial. There is a tangential null at slightly higher frequency. There is no corresponding null in any component of the Lg coda spectra. A similar set of curves for Techado (Figure 54), shows the spectral peak in coda windows and the vertical component Lg that caused the prominent null even in the ratio of the reference line to Techado's spectra (Figure 52).

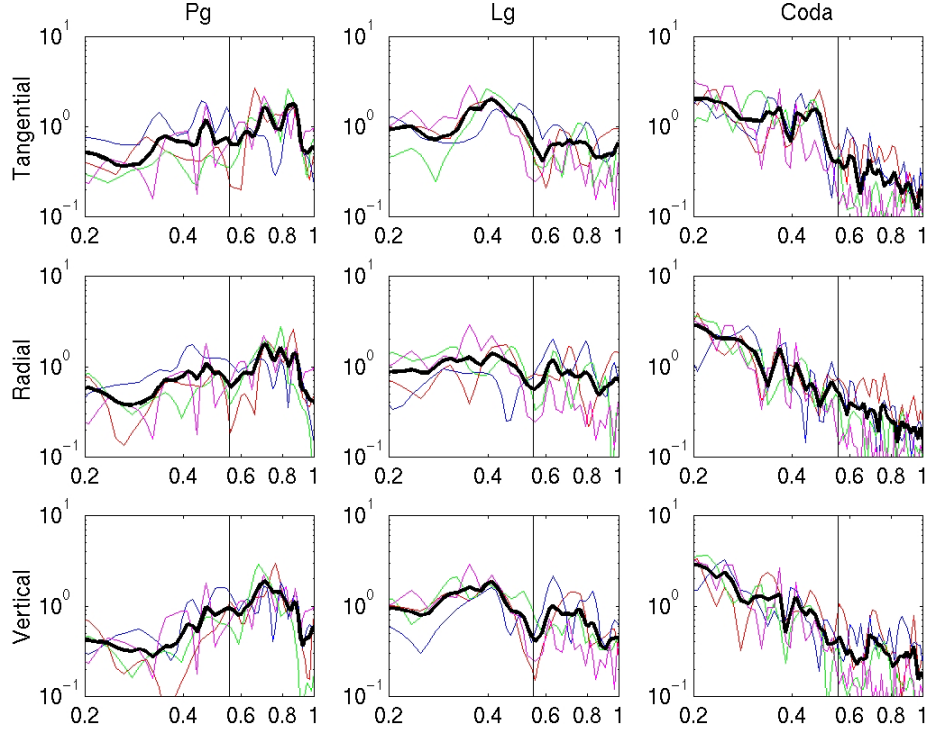


Figure 53: Individual station spectra for Baseball Pg, Lg, and Lg coda windows from MNV (red), KNB (blue), LAC (green), and ELK (purple), plus the network average spectra (black).

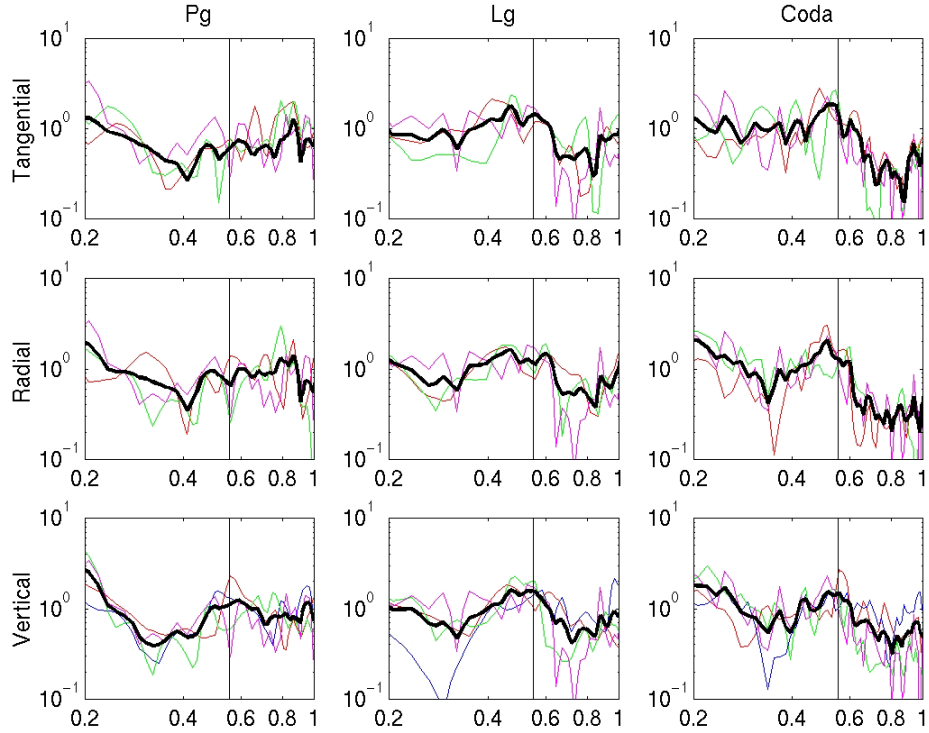


Figure 54: Individual station spectra for Techado Pg, Lg, and Lg coda windows from MNV (red), KNB (blue), LAC (green), and ELK (purple), plus the network average spectra (black).

Figure 55 presents the network average spectra for all three components of Pg, Lg, and Lg coda, for all five events. The vertical component Lg spectral null is a consistent feature of the 3 normally buried events' spectra. The null is apparent on the radial component of two of the events, but there is no corresponding null in the tangential spectra. There are also no corresponding nulls in the Lg coda spectra of any component of any event.

These figures support two important conclusions. First, the hypothesis that Rg from CLVD source is the dominant contributor to Lg predicts that the Lg coda will have the same spectral null as the Lg. This assumes that whatever null is in the original Rg will be present in any phase scattered from Rg. This assumption bears further investigation, to determine the effect of scattering on the spectra. If that assumption is correct, the lack of a null in the tangential Lg or the Lg coda that corresponds to the vertical component Lg null is inconsistent with hypothesis that it is also scattered from Rg. Second, there is a real spectral null in the Lg spectra, but only strongly in the vertical component, and not at all in the tangential. Although the observations raise questions because of differences between components, the existence of the null requires explanation. We investigate whether such a null can be observed in the spectra of shear waves generated directly by pS or a CLVD source next, along with some possible complications.

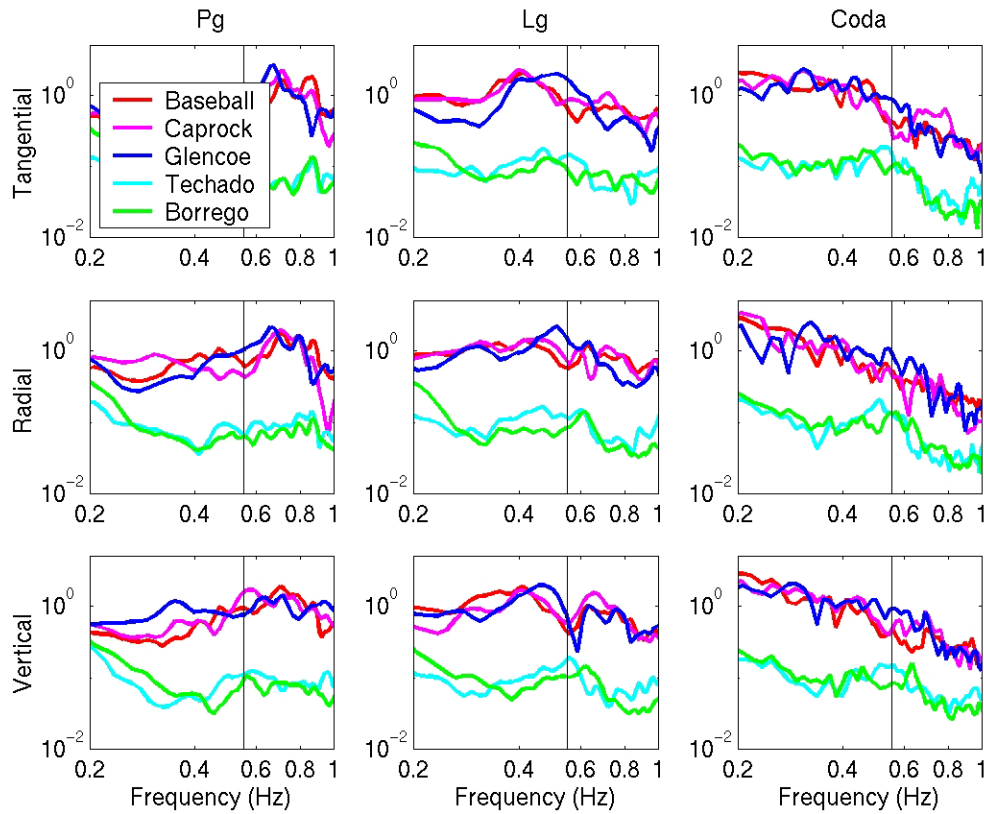


Figure 55: Network average Pg, Lg, and Lg coda spectra for all 3 components for Baseball (red), Caprock (purple), Glencoe (blue), Techado (aquamarine), and Borrego (green).

3.1.4. Normally Buried vs. Overburied Explosions' Spectra at NTS: Corner Frequencies

Fisk (2006) estimated P and S corner frequencies of NTS events, including four of the explosions analyzed above. He found Lg corner frequencies to be systematically lower than those of Pn and Pg for both the overburied and normally buried events. Spectra from single recordings are typically noisy, with multiple peaks and nulls, making it difficult to obtain accurate corner frequency estimates. To improve estimates, Fisk (2006) made corrections for geometric spreading, attenuation, site effects and instrument responses, and averaged the vertical component spectra at for stations. We do not duplicate those efforts here, but evaluate the P/S spectral ratios for evidence of consistency, or not, with Fisk's results.

For consistency with Patton and Taylor (1995), we earlier estimated the spectra from the gradient of the seismogram, using a simple fft. Given the difficulties in estimating corner frequencies, due to multiple peaks and nulls, we directly estimate the velocity spectra using multitapers, which provide fewer spurious features and have been shown to be more accurate for short time series. For both MNV and LAC, the two closest stations, and also the only two stations to record all three components of all five events, we stack the vertical and radial P spectra, and all three components of the Lg spectra.

Figure 56 shows the P and Lg spectra at MNV for all 5 events, and the predicted P and S spectra for one of the small overburied events and one of the large normally buried events. The yield dependent differences in corner frequencies stand out clearly, with distinctly lower frequency corners for the larger events. A subtle shift is also visible between the P and S spectral curves for the normally buried events (right column). That is, the P and S curves appear to have similar shapes and slopes, but with the P (red) curves shifted to the right. Borrego also appears to have this shift, although it seems to be much smaller. No shift in the P and S spectral curves is apparent for Techado. For the larger events, this is consistent with Fisk's (2006) observations, and with his conclusion that P and S are generated in the same source volume, except that the difference appears to be smaller than predicted. The similarity of the spectra at Techado, and the more subtle shift at Borrego could simply be due to very low signal-to-noise at the higher frequencies. It however is also consistent with S generation by P scattering. This would be consistent with the largely spherical source expected for the overburied events, and a more significant nonspherical component of the source for the normally buried events. That the shift is smaller than predicted even for the normally buried events could indicate that the S is not dominated by P scattering or direct generation within the source volume, but is affected by both, resulting in S spectra intermediate between the predicted P and S spectra. We next must examine the seismograms to assess whether sufficient Lg exists at the higher frequencies to accurately estimate corner frequencies there.

All the records have large P signals up through 10 Hz. Glencoe and Techado also have good vertical component Lg signal above 8 Hz. Borrego however has poor vertical component Lg signal above 4 Hz, although radial and tangential records have clear Lg at somewhat higher frequencies. This makes interpretation of P and S spectral differences for Borrego problematic. The larger events have poor vertical component Lg signal-to-noise above 6 Hz, but that doesn't affect our interpretations, as the corner frequencies are at much lower frequencies. Thus far it appears that P and S corner frequencies are shifted for the normally buried events, albeit, not as

strongly as predicted. That lack may not be due to poor resolution, since the similar magnitude, predicted, yield dependent differences in spectra are clearly observed.

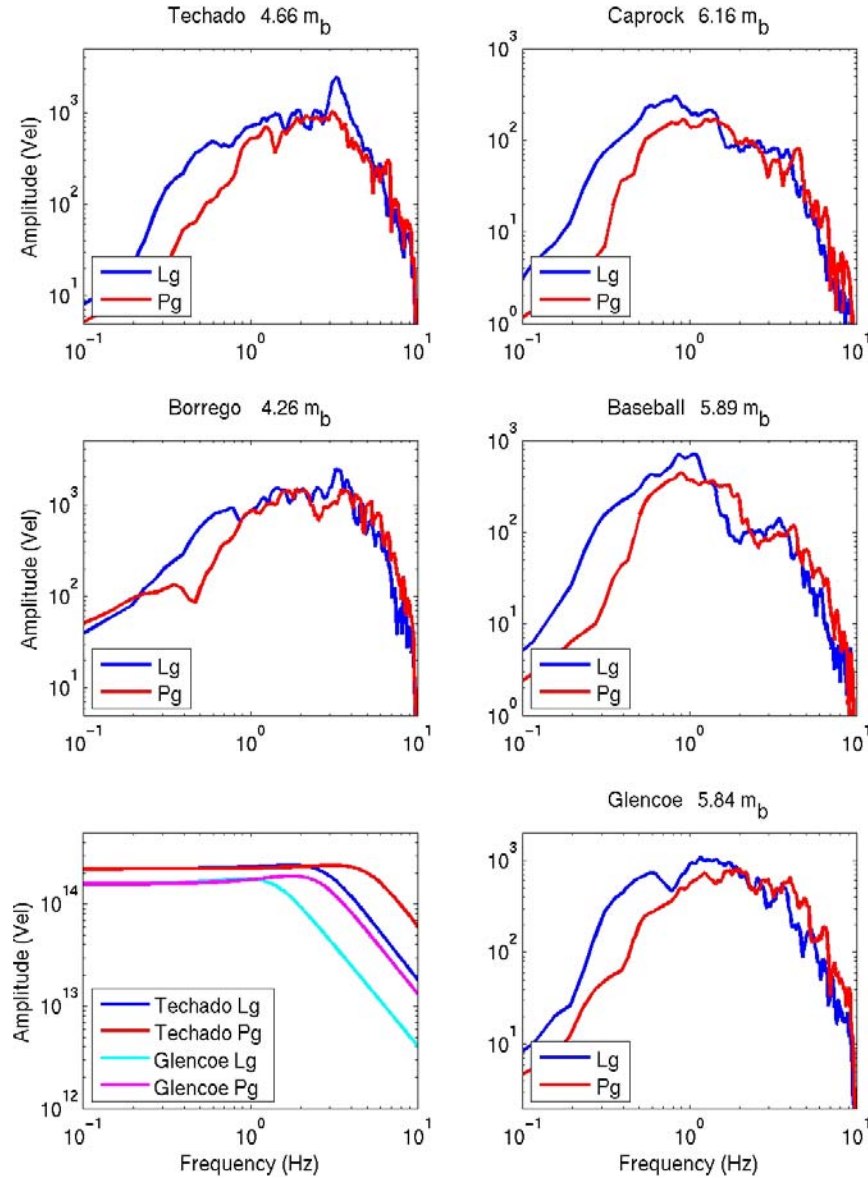


Figure 56: P (red) and S (blue) spectral curves from MNV. Radial and vertical spectra are averaged for P, and all three components are averaged for S. Predicted P and S spectra for two events are shown at bottom left.

We also examine spectral ratios. Figure 57 and Figure 58 show the P/S spectral ratios at MNV (237 km) and LAC (300 km) respectively. The spectra ratios at Techado and Caprock appear very similar, with two upward slopes (Figure 57, top). The first matches the predicted curve for Caprock, and the second matches the predicted curve for Techado. For each event, the predicted Mueller-Murphy P-to-S spectral ratio is plotted in red. In addition, Caprock's predicted spectral ratio is overlain on the observations from Techado (upper left). Similarly, Techado's

predicted spectral ratio is overlain on the observations from Caprock (upper right). A similar exercise with Borrego and Baseball would produce similarly convincing matches to the wrong predicted spectra. Figure 58 shows similar results for recordings from LAC.

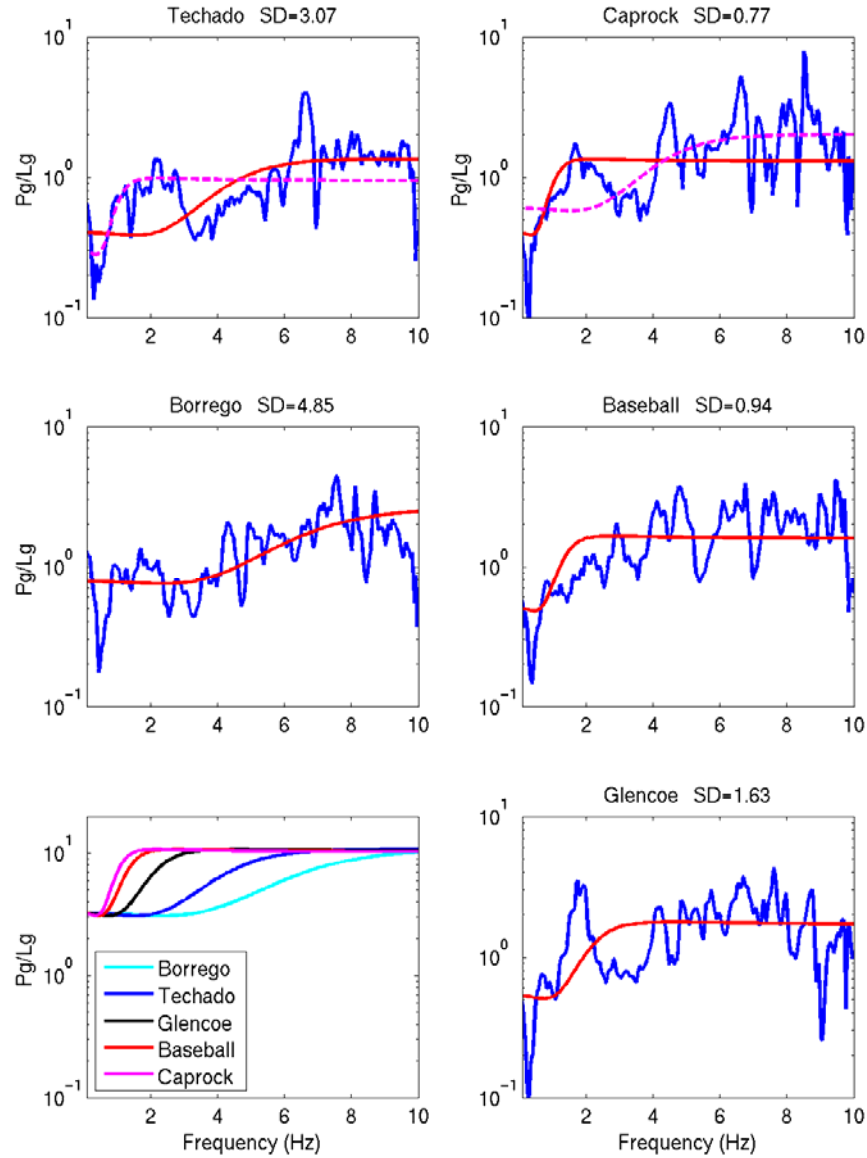


Figure 57: P-to-S spectral ratios of five nuclear explosions recorded at 237 km distance, at MNV. P spectra are the radial and vertical average, and Lg spectra are based on all three components. Red lines show the predicted Mueller-Murphy source for each event (fit to minimize the DC offset between curves). All predicted spectral ratio curves are shown on the bottom left. Dashed maroon curves show the predicted spectral ratio for Caprock compared with the Techado observations (upper left), and vice-versa, that is, the predicted spectral ratio for Techado overlain on the Caprock observations.

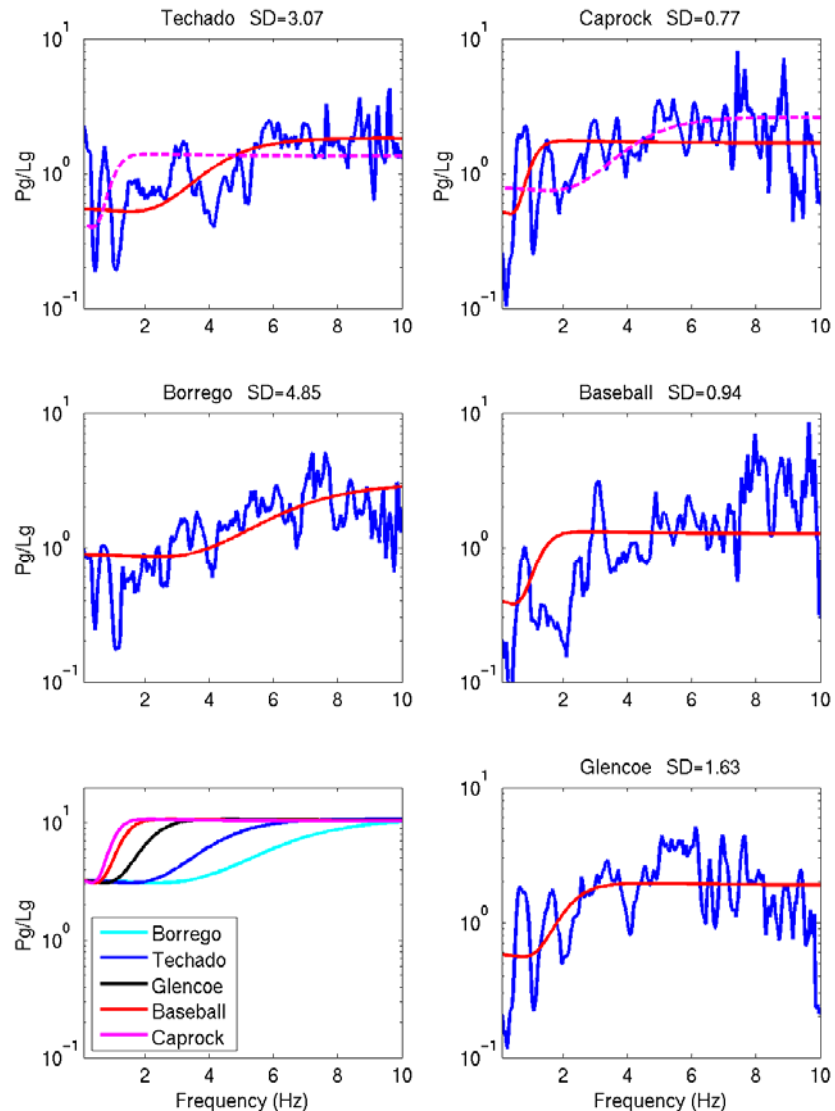


Figure 58: Same as Figure 57, but for station LAC, at 300 km distance.

Figure 59 shows the average P-to-S ratios at MNV for the two largest (blue) and two smallest (red) events. Again the radial and vertical components were averaged for P, and all three components for Lg. Below 0.3 Hz, Borrego's P is below the noise, so we ignore that part of the red curve. There is one significant difference between these curves. The large events, but not the small, have a peak at 1-2 Hz. That is the band between the predicted P and S corner frequencies, where we expect the P/S curve to increase, so the peak is consistent with the predicted spectra. The increase at high frequency in both curves, and for all the curves in Figures 6 and 7, may represent the greater effect of attenuation on Lg, which drops to near or below the noise level for many of the records at higher frequency. Figure 60 shows the same sets of averaged P-to-S ratio curves, from recordings at LAC. Again, the spectra are very similar except for the one peak between 1 and 2 Hz. This is a small feature, less conspicuous here than at MNV (Figure 8) which highlights the difficulty of accurately estimating corner frequencies, given all the other peaks and nulls in the spectra.

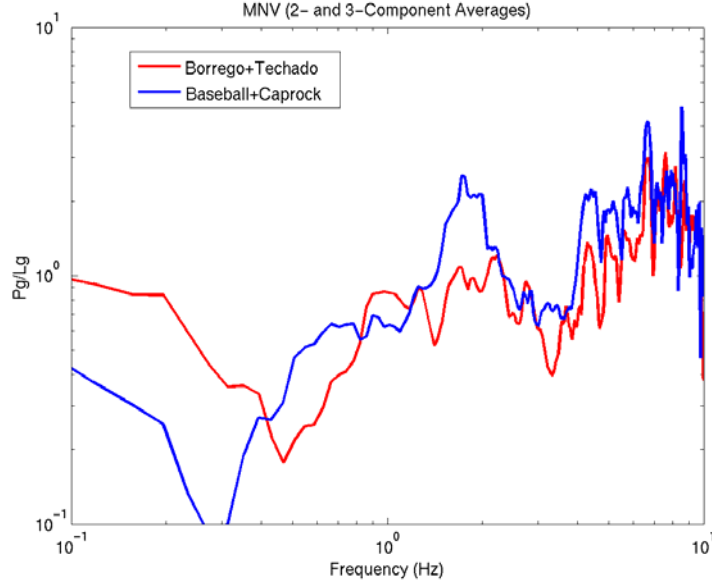


Figure 59: Average P-to-S ratios are MNV for the two largest (blue) and two smallest (red) events.

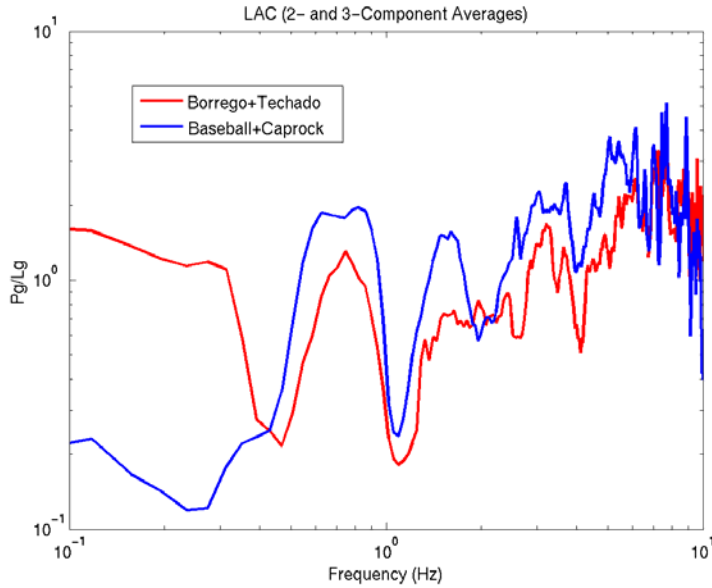


Figure 60: Same as Figure 59, but for station LAC.

3.2. Simulations

There are three separate goals of our simulations. One is to assess whether the observed low frequency spectral null in vertical and radial Lg is consistent with other mechanisms, and whether it can rule out any mechanisms. Another goal is to compare the size, or at least the bound, of the contribution of each mechanism to Lg. Finally, we more thoroughly investigate the predicted corner frequencies for the normally buried and overburied events, and determine whether the observations can be modeled with a reasonable combination of sources.

3.2.1. Is a Vertical/Radial Lg Null Consistent With Other Mechanisms?

We want to investigate whether the existence of a 0.55 Hz spectral null in normally buried events' vertical, and to a lesser extent, radial component Lg, but not in the Lg of the overburied events' Lg spectra, can eliminate any mechanisms. The observation has previously been used to infer dominance of Rg scattering, but without considering other mechanisms. Figure 61 (lower) shows the Lg spectra at 300 km for four sources: pS from a spherical explosion source, the upper bound on energy scattered from the spherical explosion Rg to S, direct S generated by a CLVD, and the upper bound on energy scattered from the CLVD Rg to S. The Lg windows of the seismograms are shown in Figure 61 (upper). All records and spectra shown in this section are velocity. The CLVD is half the moment and half the depth of the explosion source. In the case shown, the explosion is at 600 m depth, and the CLVD at 300 m. All four sources have a large null from 0.55 to 0.7 Hz. Subtle shifts in the velocity model could easily shift this to fit the observed 0.55 Hz null exactly. It appears that the position of lower frequency spectral nulls depends on the modal structure, which is dependent on the velocity structure, and on which modes are excited, which depends on source depth. Whether they are at 600 m, 300 m, or effectively at the surface in the case of pS, all the sources are very shallow and will preferentially excite the same set of modes. Thus existence of a particular null in Lg does not rule out any particular source mechanism.

To determine an upper bound on Lg from scattered Rg from both explosion and CLVD sources, we use a modal scattering calculation (Stevens et al. 2007). In this calculation, all Rg energy is instantaneously forward scattered into higher modes and energy is conserved. Excitation by a vertical point source determines the distribution of energy among modes. This is reasonable since the strongest Rg scattering occurs at the earth's surface. This is an extreme upper bound, as it ignores intrinsic Rg attenuation, realistic rates of Rg scattering, which would cause the scattered energy to arrive later, possibly after the Lg window, and Rg scattering into Pg coda and into body waves that are lost to the mantle. Supporting the significance of the latter, Gupta and Wagner (1992) and present evidence that scattered Rg is the primary source of teleseismic P coda. Numerous studies also point to the efficiency of the reciprocal problem, identifying teleseismic P to Rg scattering from single scatterers and scattering efficiency over large areas (Revenaugh, 1995). Thus the upper bound is quite liberal.

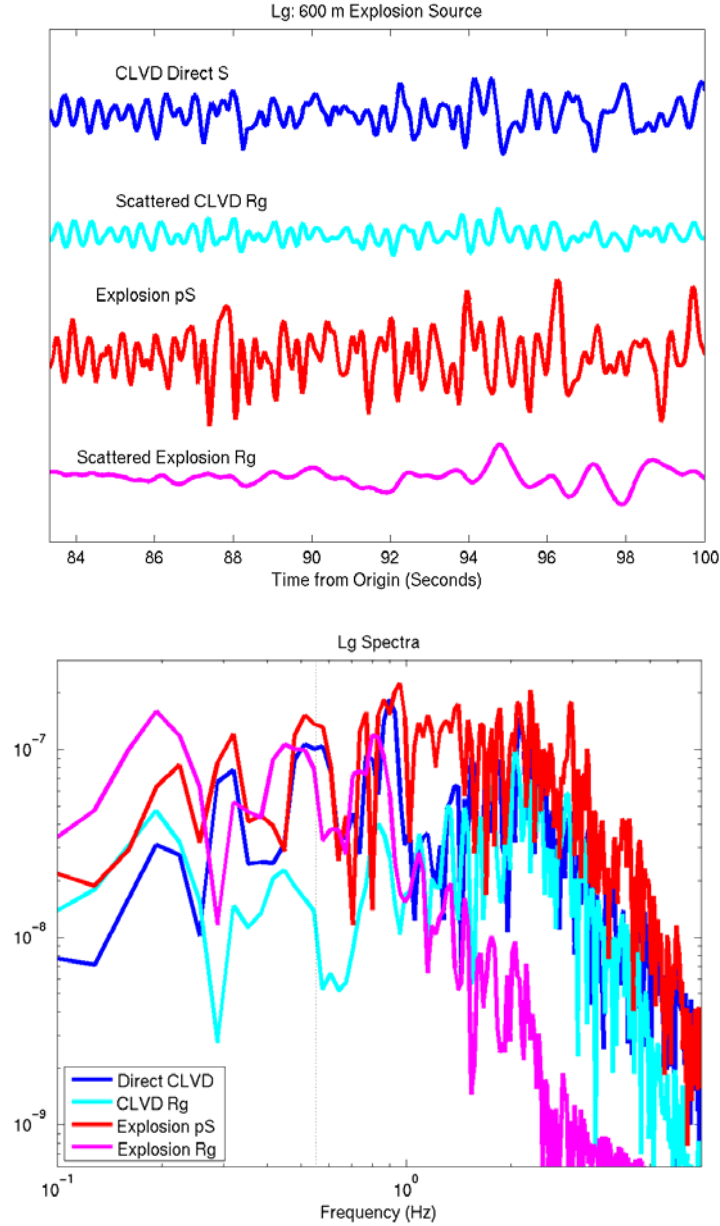


Figure 61: Lg seismograms (upper) and spectra (lower) at 300 km from each of four mechanisms: pS (red) from a spherical explosion at 600 m depth, the upper bound on the scattered spherical explosion Rg (maroon), direct S (blue) from a CLVD with half the spherical explosion's moment, at 300 m depth, and the upper bound on the scattered CLVD Rg (cyan).

3.2.2. Relative Contribution of Each Mechanism to Lg

The nonspherical part of explosion sources commonly is taken to occur at approximately half the depth, and have half the moment, of the spherical part of the source. We can see from Figure 61 that for explosions at the depth of the NTS explosions described above, trapped pS from the point explosion is the dominant contributor to Lg above approximately 0.5 Hz. Below that frequency, scattered Rg from the explosion source could become important, although we must keep in mind that this upper bound is extremely high, as it ignores scattering to P and to S-waves

lost to the mantle, intrinsic attenuation of Rg, gradual scattering of Rg (scattering in the simulations is instantaneous), and Rg-to-Rg scattering, which is typically the dominant mode of Rg scattering. Even then, the upper bound on the contribution of scattered explosion Rg to Lg at 0.1 Hz is only a factor of two greater than that of trapped pS. At 2 Hz and above, direct S from the CLVD source contributes only slightly less than pS. Although insignificant at lower frequencies, the upper bound on the contribution from scattered CLVD Rg is slightly below that of the direct CLVD S above 2 Hz. At the position of the low frequency spectral null that was interpreted as implying dominance of scattered CLVD Rg, the upper bound on the CLVD Rg's contribution is nearly an order of magnitude smaller than each of the other mechanisms' contributions.

We have used a simple FFT for spectral estimation for consistency with previous work, but note that the multi-taper method produces smoother spectra with fewer and less exaggerated peaks and nulls. Figure 62 shows the same spectra as Figure 61, but from a multi-taper spectral estimate.

Figure 63 shows the contributions of each of the mechanisms for a much shallower source, with the spherical explosion at 200 m depth, and the CLVD, again at half the spherical explosion moment, at 100 m depth. Again, pS is the largest contributor above 1 Hz, and below, the upper bound on scattered spherical explosion Rg's contribution becomes larger. Direct S from the CLVD is only slightly smaller than pS. The difference is small enough that the contribution of both may be important. The contribution from a CLVD with the same moment as the spherical explosion source is larger from 1.5 to 3 Hz and the same above 3 Hz. Another consideration is that surface scattering may be more likely to negatively affect pS, since pS normally would all be trapped, by changing the incidence and causing more loss to the mantle. Thus we can't discount the importance of direct S from the CLVD relative to pS. These figures however indicate that scattered Rg is not a significant contributor to Lg, especially for deeper events. Incidentally, the scattered CLVD Rg in this case has a null at approximately 2 Hz, rendering its contribution insignificant at the frequency.

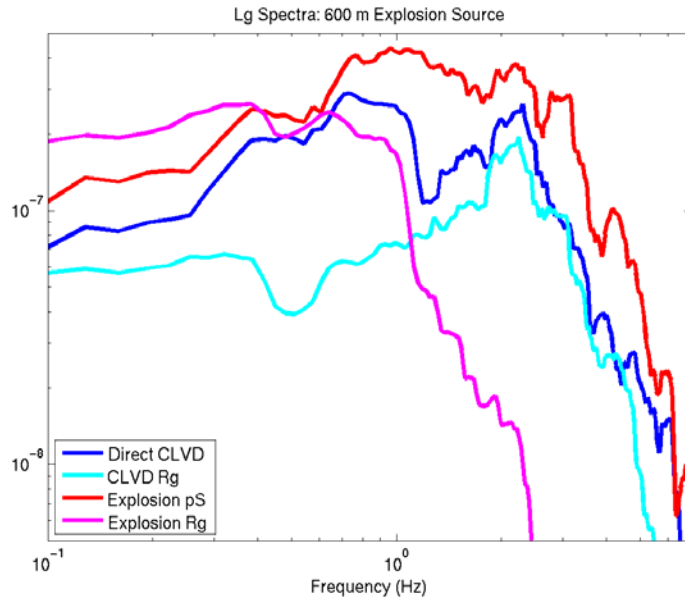


Figure 62: Same as Figure 61 (lower plot), but using a multi-taper spectral estimator.

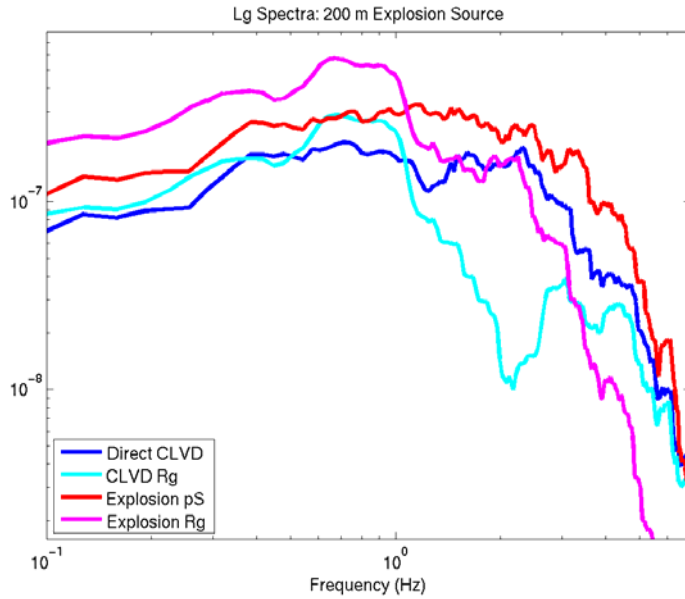


Figure 63: Lg spectra at 300 km from each of four mechanisms: pS (red) from a spherical explosion at 200 m depth, the upper bound on the scattered spherical explosion Rg (maroon), direct S (blue) from a CLVD with half the spherical explosion's moment, at 100 m depth, and the upper bound on the scattered CLVD Rg (cyan).

We next examine the Lg coda in the same way as the Lg. Figure 64 and Figure 65 show the Lg and coda (3.0 to 2.4 km/s) seismograms (upper) and coda spectra (lower) for the 600 and 200 meter spherical explosion sources with CLVD sources at half the depth and moment. Rg scattering contributes more to Lg coda than to Lg for any source depth, even when the Rg is instantaneously scattered at the source. For the deeper sources the contributions of pS to the Lg

coda are still the largest at higher frequencies. Now however the scattered CLVD Rg upper bound is almost the same as the contribution of direct S from the CLVD above 3 Hz (below that, there is a null in the CLVD Rg). Again, all four sources still share a common null. In the case of the 600 m explosion source, it is at approximately 1 Hz, further indicating that the modal structure and excitation controls the spectra, and any shallow source, surface scattered P or Rg, or direct S, will generate modes with the same spectral shape. Note that no fundamental mode Rg remains in these simulations. Gupta et al (2005) however present evidence that fundamental mode Rg, perhaps multiply scattered, is present in the Lg coda. That would leave the coda with a different spectral shape than if the entire fundamental mode is instantaneously scattered into higher modes.

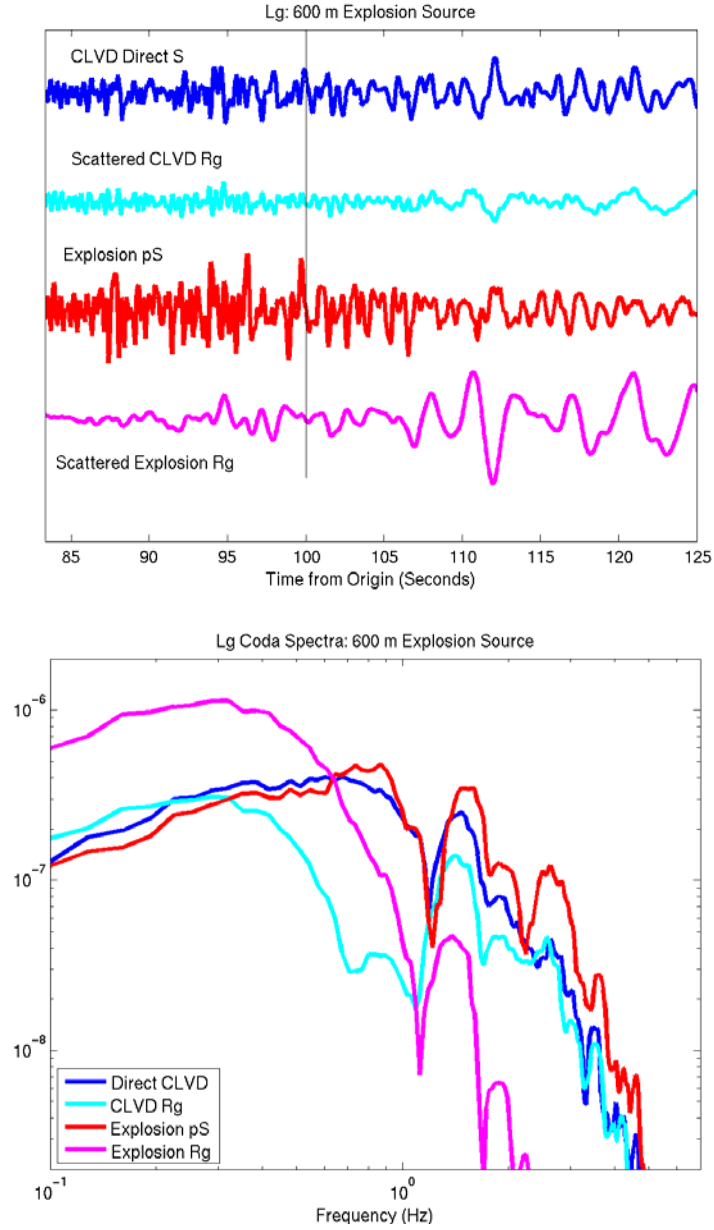


Figure 64: Lg and Lg coda seismograms (upper) at 300 km, separated by a vertical line at 100 seconds, and corresponding spectra of the Lg coda from each of four mechanisms: pS (red) from a spherical explosion at 600 m depth, the upper bound on the scattered spherical explosion Rg (maroon), direct S (blue) from a CLVD with half the spherical explosion's moment, at 300 m depth, and the upper bound on the scattered CLVD Rg (cyan).

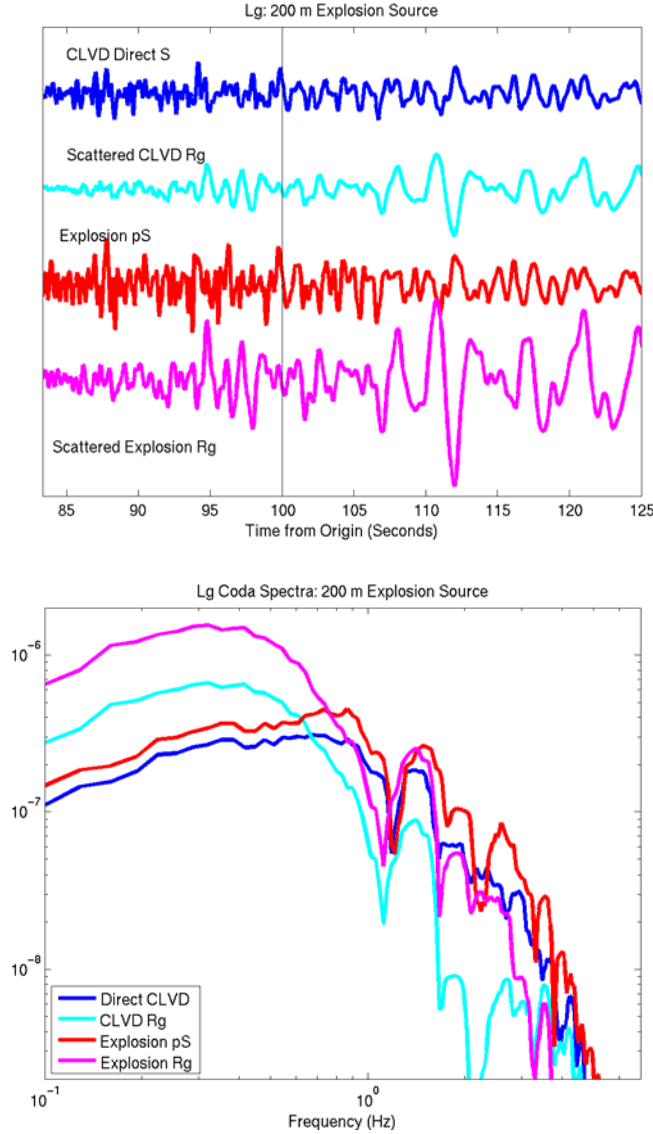


Figure 65: Same as Figure 64, except the spherical explosion is at 200 m depth, and the CLVD of half the moment is at 100 m.

3.2.3. The Effect of a Temporally and Spatially Distributed Source

We have been assuming the point explosions and point CLVD sources are good approximations to real explosion sources. Real explosions however are not point sources, and the nonspherical part of the source may differ from a point CLVD with half the explosion moment at half the depth. Further, the breadth of time and space over which deformation of an explosion cavity occurs could lead to destructive interference due to lags in phase as modes are excited, which would mask the spectral nulls. To test this, we use 2D nonlinear, Lagrangian, finite difference calculations to generate the yielding and cracking associated with a 117 Kt explosion at 564 m depth (i.e. Baseball) and a 2.8 Kt explosion at 533 m depth (i.e. Techado), both in NTS structure. The signal generated is propagated to regional distance, where we compare the spectra with that of point spherical explosion and CLVD sources. We also use these calculations to

investigate the effect event size and scaled depth of burial on the P and S corner frequencies, for comparison with predictions and observations made earlier.

Figure 66 shows the permanent deformation (upper left) and cracking (upper right) from the Baseball (top) simulation, and the permanent deformation from the Techado simulation (bottom). The Techado simulation produces no cracking, and predicts a nearly spherical cavity, while the Baseball simulation produces a significant non-spherical component of permanent deformation and extensive cracking.

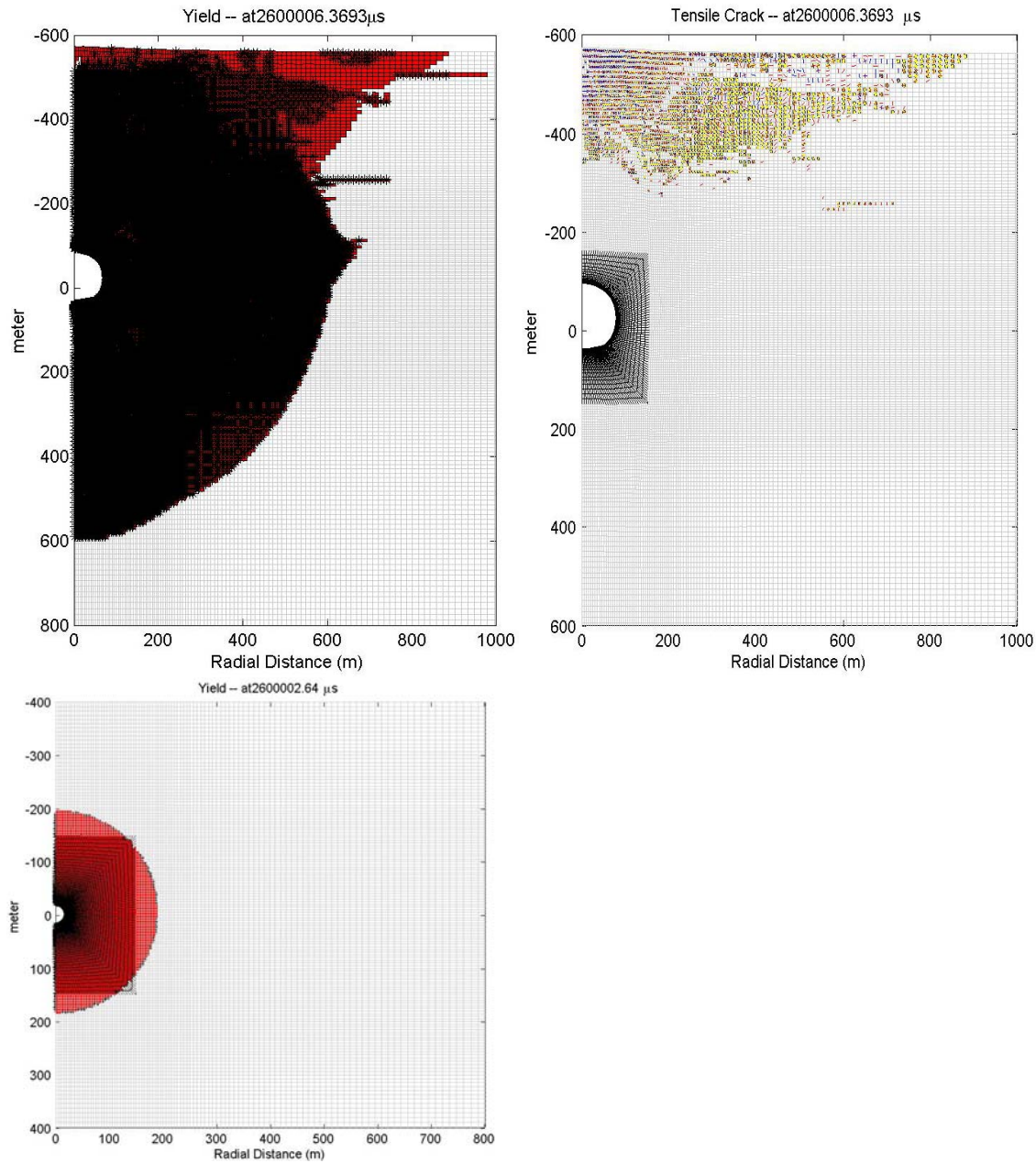


Figure 66: Permanent deformation (left column) produced by 2D Lagrangian finite-difference simulations of the sources of Baseball (top) and Techado (bottom). Cracks predicted by the Baseball simulation are shown in the upper right. The Techado simulation produces no cracks.

The velocity and stresses at a monitoring surface outside of the nonlinear region about the sources shown in Figure 66 were used as input to wavenumber integration calculations, to produce seismograms at regional distances. Figure 67 shows the Lg spectra for the two events, as well as for a CLVD and a spherical point explosion source. All spectra are corrected to the Mueller-Murphy source spectra for Baseball. For the Techado simulation, the spectrum is normalized by the ratio of the predicted Mueller-Murphy source spectra. The point explosions' spectra are normalized by the predicted spectra of Baseball. The vertical line at 0.55 Hz in each plot highlights the position of a spectral null similar to that observed in the actual data. Figure 68 shows just the simulated Baseball spectra (black) overlain on the spherical explosion (red) and CLVD (blue) sources' spectra. Despite the large nonspherical component of the area which yields, the spectra of Baseball is more similar to that of the point explosion source. The differences are minor however between the point CLVD and spherical explosion sources. The similarity of the point explosion and CLVD spectra suggest that, while the nonspherical source components of Baseball do not alter the Lg spectra compared with point spherical explosion Lg spectra, the extent of CLVD cannot be determined from the spectra. A significant CLVD component added to the explosion spectra would change little.

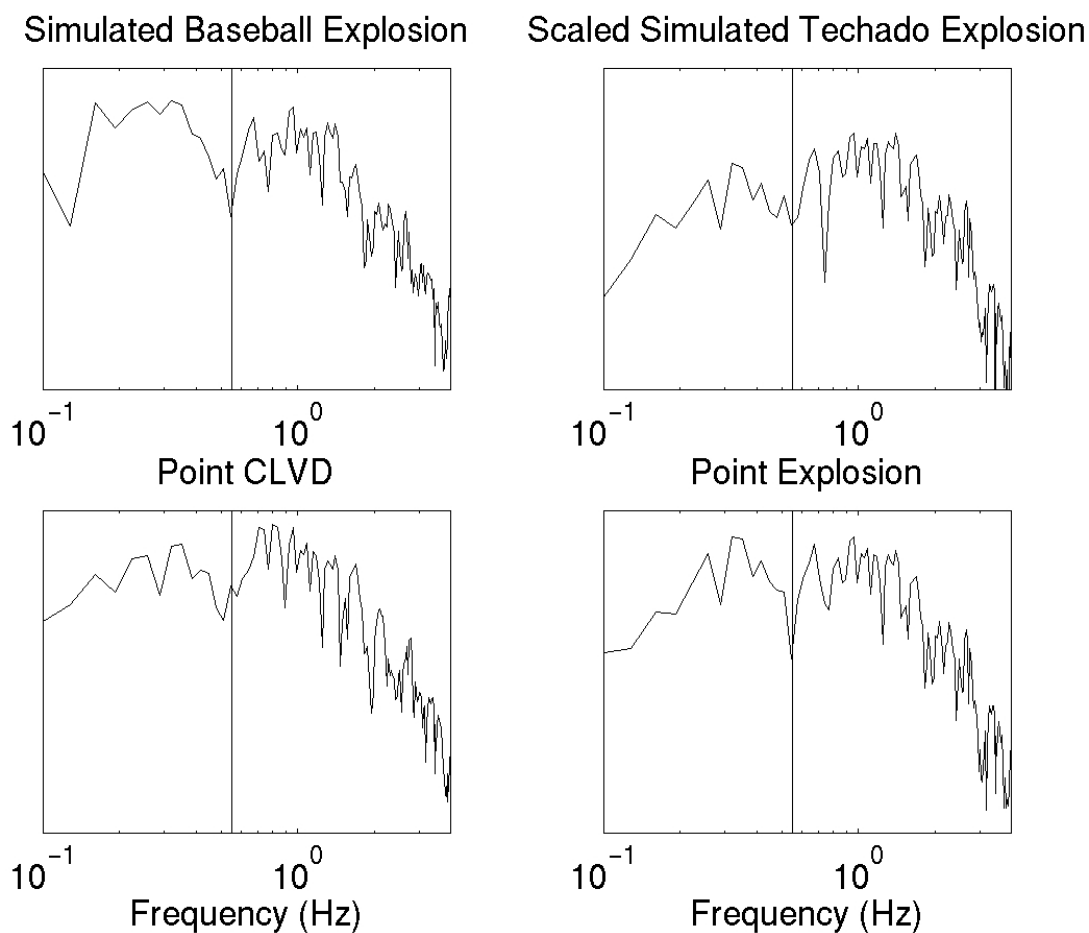


Figure 67: Lg spectra for the Baseball (top left), Techado (top right), point CLVD (bottom left), and spherical point explosion (bottom right). The vertical line is at 0.55 Hz in each plot.

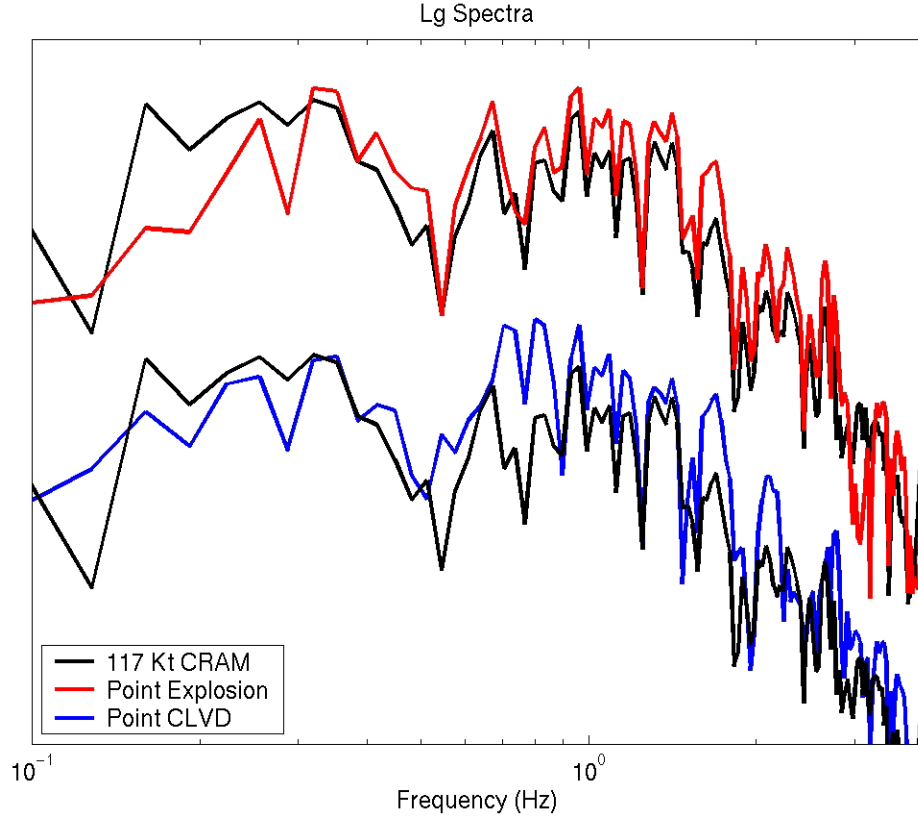


Figure 68: Lg spectra for the Baseball (black), a spherical point explosion (red), and a point CLVD (blue).

3.3. Possible Sources of Spectral Nulls in Rg and Lg

In previous work it has been assumed that there is a depth dependent spectral null in CLVD Rg, and that the Rg scatters to Lg, so Lg retains the spectra of the Rg. The simulations above have demonstrated that the same spectral null in Lg can be due to any shallow S-wave source, with scattering from Rg contributing much less amplitude to the Lg than direct S from the nonspherical source elements and trapped pS. That seems enough to reject the inference, based on spectral nulls in Lg, that scattered Rg is its dominant source. We however have an opportunity to examine other assumptions of previous work more closely using records from the DSS explosion Quartz 3. First, previous work assumed that the local Rg would have a particular spectral null based on the source depth. . Baker et al (2007a) showed that spectral nulls varied with azimuth in a high velocity source media, which is inconsistent with the null being simply source depth dependent. For Quartz 3, because the seismic recording lines extend in two directions from the source, we can observe whether the Rg spectra are azimuth dependent. Second, because Quartz 3 was recorded every 10 to 15 km for 1000s of km, we can directly compare Rg with local and regional Sg and Lg. Finally, we address the assumption that nulls in Rg will be retained in phases scattered from the direct fundamental mode Rg, by examining the spectra of coda following Rg in 3D finite-difference scattering synthetics.

Quartz 3 was an 8.5 Kt, 759 m deep nuclear explosion, overburied at 3 times normal scaled depth, with 3-component seismic lines to both the east and west of the source (Figure 69). Rg is prominent on the vertical and radial components of both lines (e.g. Figure 70), and Sg is prominent on the tangential and radial components. Large vertical component Rg and horizontal component Lg are also observed at greater distances (Figure 71). Individual Rg spectra from records east of Quartz 3 (Figure 72) have common nulls at 0.93 and 1.42 Hz (indicated by vertical lines). Stacked vertical component Rg spectra (Figure 73) show the two prominent nulls seen in the individual spectra (Figure 72), but there are no comparable Sg nulls. The Rg spectrum at 409 km is consistent with the Rg spectra observed closer to the source, while the horizontal component Lg spectra are similar to the local, horizontal component Sg spectra and different from the Rg spectra (Figure 74).

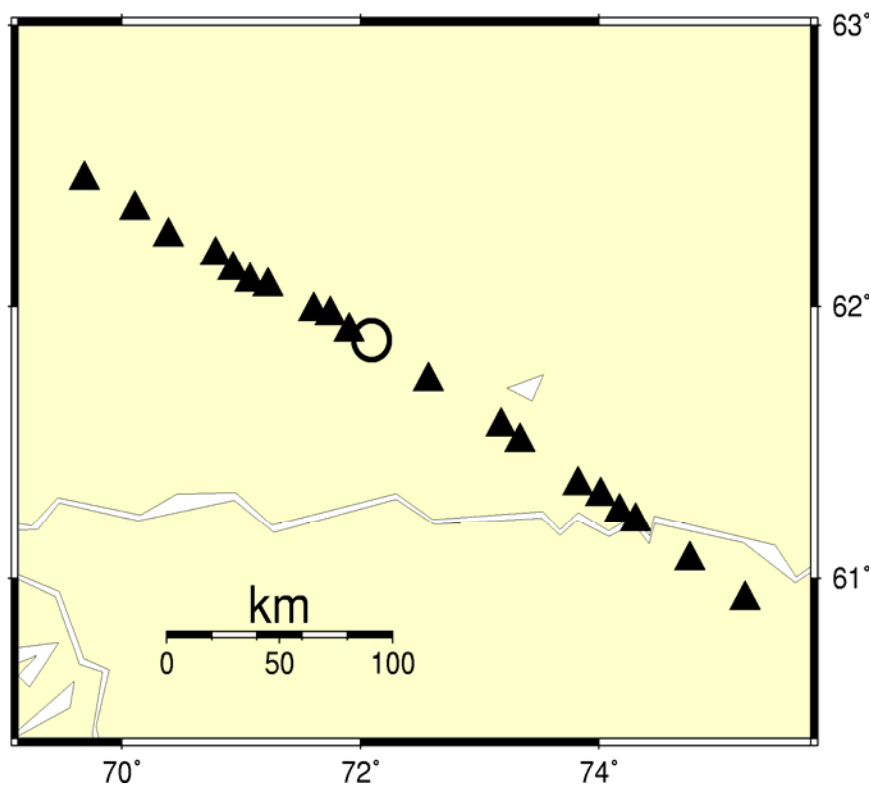


Figure 69: Stations within 200 km of Quartz 3.

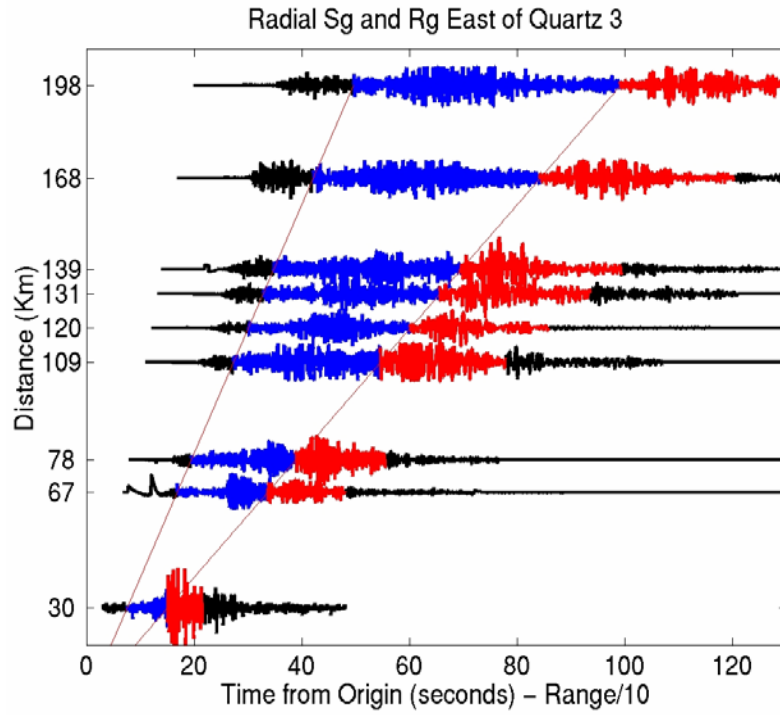


Figure 70: Radial component record section east of Quartz 3, with Rg (red) and Sg (blue) color coded.

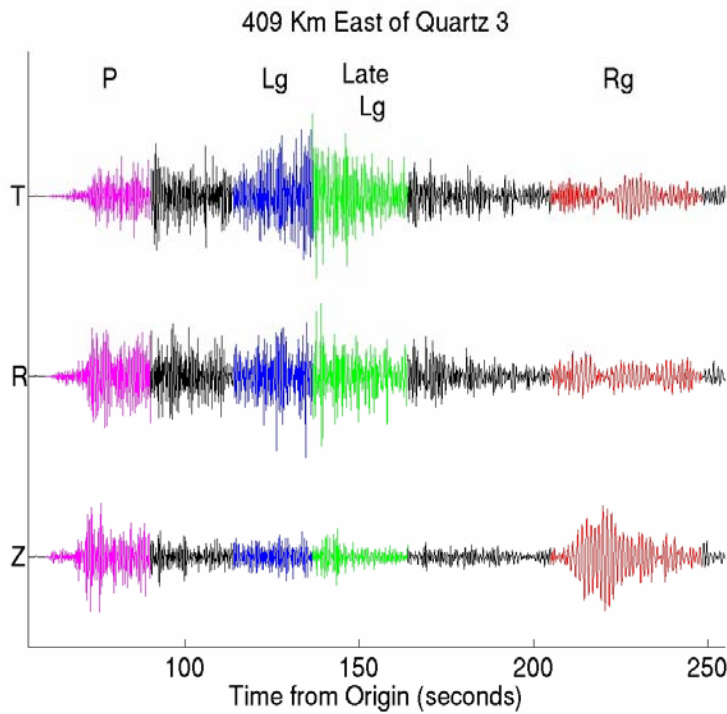


Figure 71: Three component record from 409 km east of Quartz 3. Phases are color coded, with P maroon, Lg blue, Lg coda green, and Rg (red).

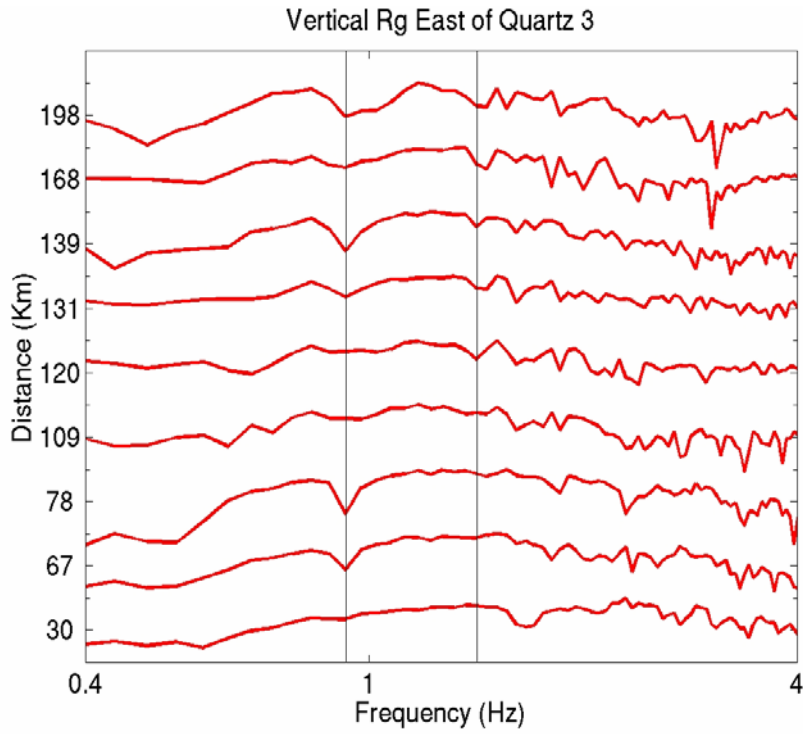


Figure 72: Vertical component Rg spectra from recordings east of Quartz 3.

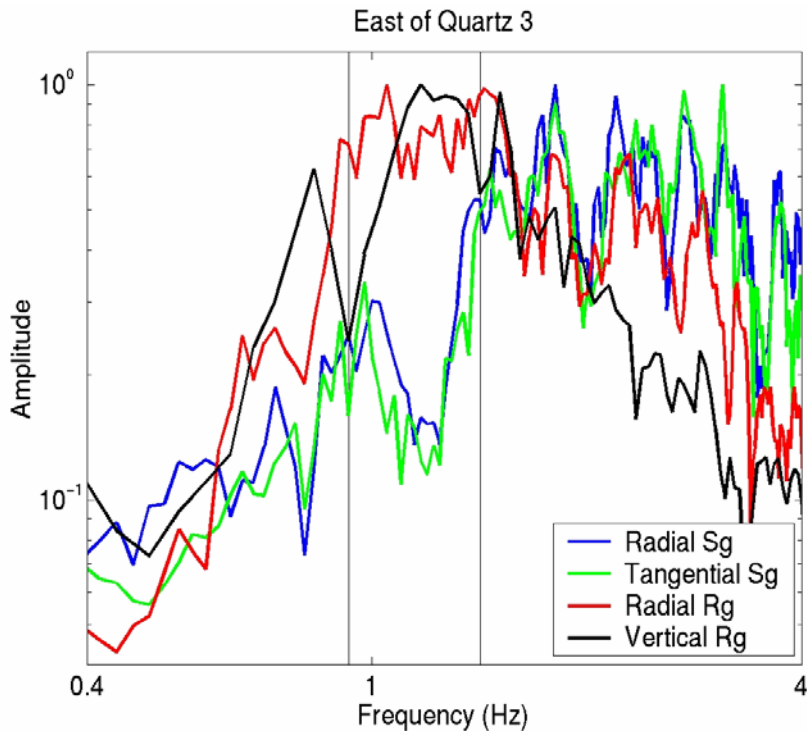


Figure 73: Stacks of vertical and radial component Rg spectra, and radial and tangential Sg spectra from recordings east of Quartz 3.

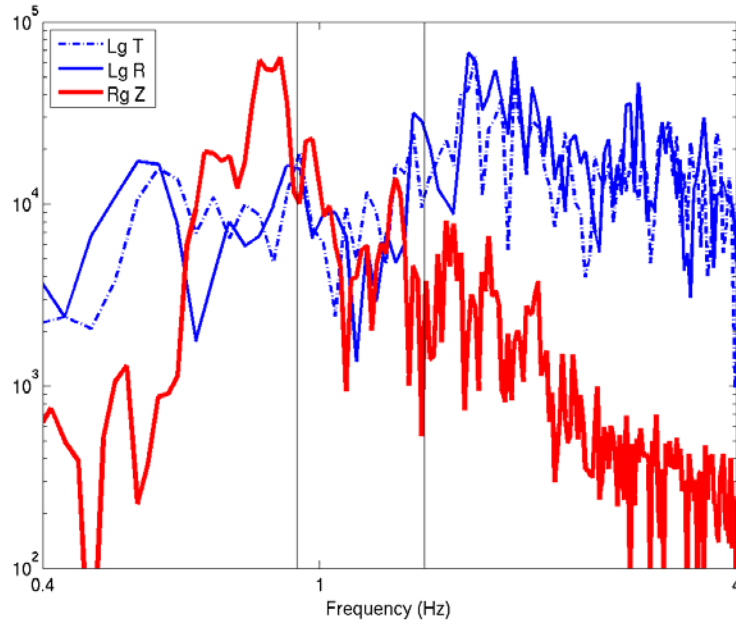


Figure 74: Lg (blue) and Rg (red) spectra from the three component records at 409 km east of Quartz 3 shown in Figure 71.

Seismograms from west of Quartz 3 appear similar to those from east of the explosion (e.g. Figure 75), but the individual Rg spectra (Figure 76) have a consistent spectral null at 1.27 Hz, not at 0.93 or 1.42 Hz as seen in the Rg spectra from east of the source (Figure 73). As observed for the recordings east of Quartz 3, Sg spectra west of Quartz 3 do not have a spectral null in common with Rg. For Quartz 3, Rg and Sg (Lg) have persistent spectral nulls, but the lack of common spectral nulls between Sg (Lg) and Rg is inconsistent with the hypothesis that spectral nulls in CLVD generated Rg are replicated in Sg and Lg. Further, while the persistence of Rg spectral nulls along a single azimuth from the explosion suggests source or very near source genesis, the azimuthal variation of the Rg spectral nulls is inconsistent with their being due to the source depth of a CLVD component of the source, as hypothesized previously.

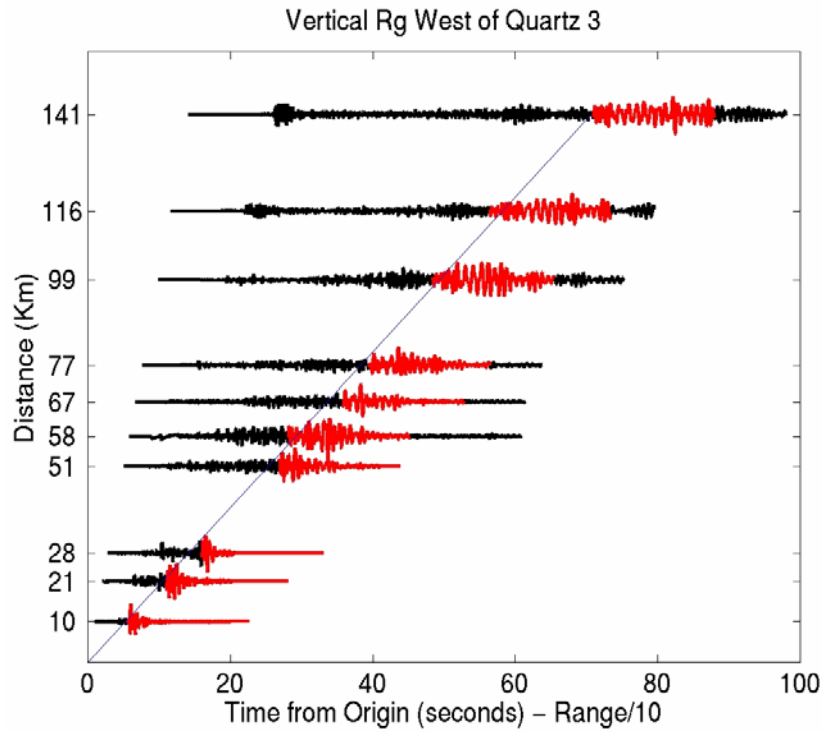


Figure 75: Vertical component record section west of Quartz 3, with Rg (red) color coded. Sg is only prominent on the horizontal component records.

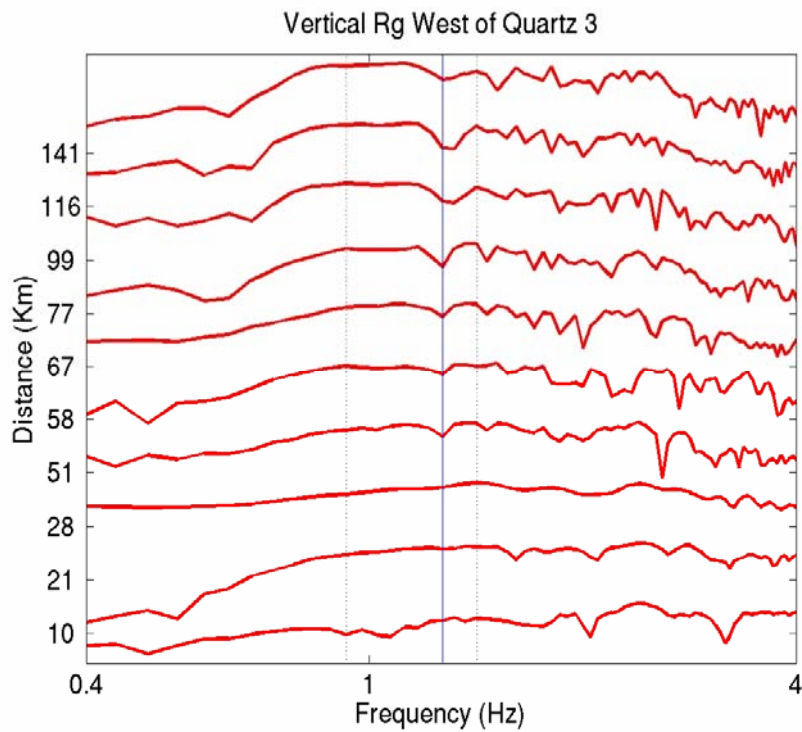


Figure 76: Vertical component Rg spectra from recordings west of Quartz 3.

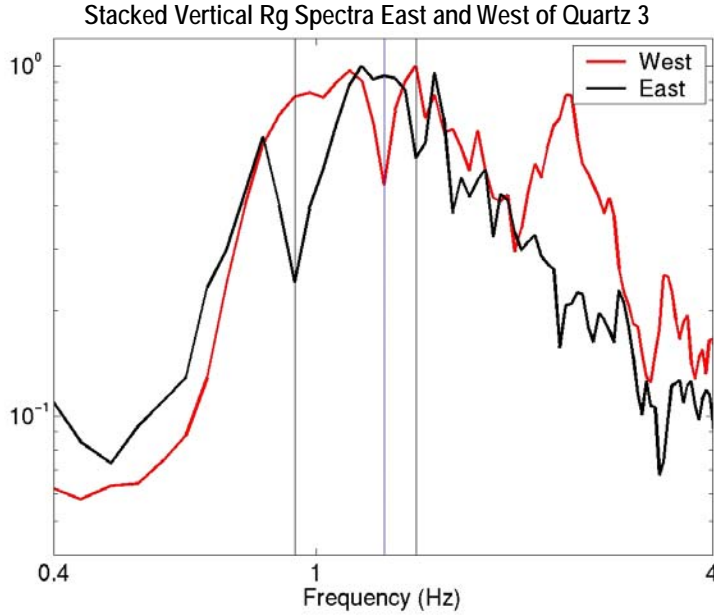


Figure 77: Stacked vertical component Rg spectra from recordings east (red) and west (black) of Quartz 3.

As we have argued regarding Lg generation, it is much easier to demonstrate feasibility of a mechanism than to disprove one. With that in mind, we suggest that many alternate explanations for the Rg spectral nulls observed at Quartz 3 likely exist, since the azimuth dependence effectively demonstrates that the Rg spectra nulls are not a simple effect of source depth. Rg-to-Rg scattering very near the source could affect the spectra through constructive or destructive interference. We show a simple modeling example that supports this. This is an extension of the analysis of 3D scattering calculations presented in Baker et al (2007a). In that we compare records at 25 km from Degelen Mt in two models, one with and one without topography. Although this is a high velocity source region, all we consider here is the effect of Rg scattering on spectra. Figure 78 shows the seismograms (left) for the flat lying model (upper) and the model with the actual topography of Degelen in 3D. Rg spectra for each are shown in the central plot. Scattering does not diminish the lowest frequency spectral null of the fundamental mode Rg, and has only a small effect on the second null just above 1 Hz (center). It is interesting however to also compare the spectra of the coda following Rg. The common argument for why scattered Rg dominates Lg is that it is by far the largest phase near the source and so is overwhelmingly the dominant source of scattered energy. If that is so, then the coda following Rg should be dominated by scattered Rg. By the argument used to support Rg-to-Lg scattering, the coda should share the same nulls as Rg. We use energy arriving after 11.6 seconds (vertical line, labeled T0, left plot) to assess the post-Rg spectra. Scattered energy following Rg has obscured the lowest frequency spectral null, and shifted the position of the null just above 1 Hz (right). Even within this short distance range, it does not share the same nulls as Rg. This casts doubt on another assumption underlying the Rg-to-Lg scattering hypothesis.

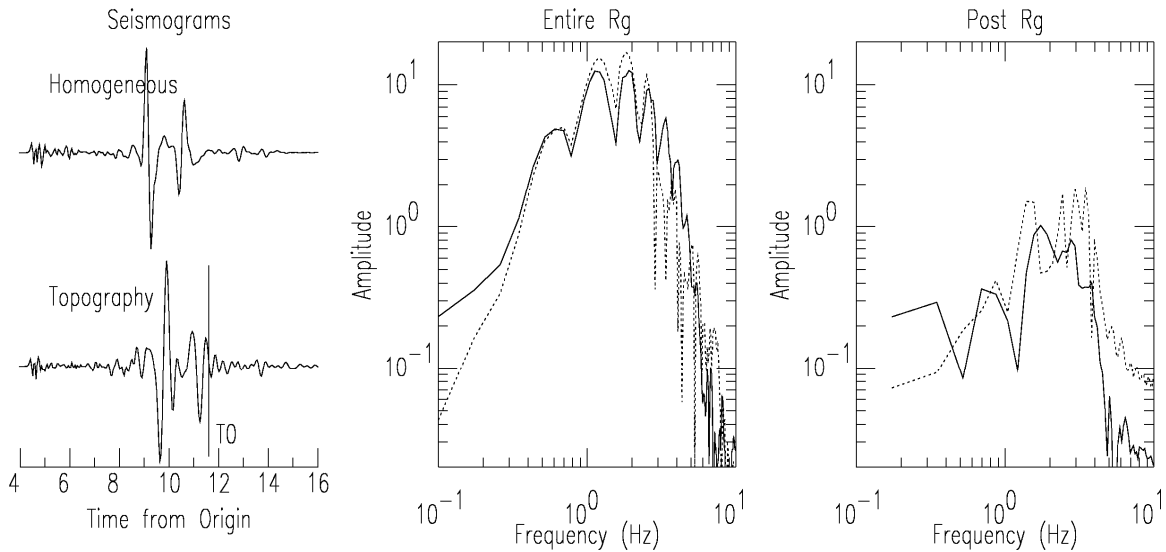


Figure 78: Seismograms (left) and spectra for a flat-lying model (upper seismogram and solid spectra) and the same model plus the topography at Degelen Mt. (lower seismogram and dashed spectra).

4. KAZAKH DEPTH OF BURIAL EXPLOSIONS

4.1. Introduction

This chapter is intended to form the basis of the third paper from this project on the source of explosion generated shear waves. The first two addressed high and low velocity source media respectively. This one focuses on a specific data set, the Kazakh depth of burial explosions used in widely cited previous work (Myers, et al, 1999; Patton et al, 2005) to infer that Rg is the dominant source of explosion Lg. The previous work demonstrated the feasibility of the Rg mechanism, but did not consider the possible contributions of other shear wave generation mechanisms. We examine the impact of assumptions made in previous analyses, re-examine observations using three components at stations previously used and an additional near regional set of records. Because previous work addressed the feasibility of a single mechanism, Rg scattering, as the source of explosion S waves, we investigate whether there are any observations that are inconsistent with any mechanisms.

This paper is organized as follows. We first describe the conditions of the explosions. We then provide background on previous work. We add to the body of observations made previously, by examining all three components of local records, as the horizontal components typically have better signal-to-noise ratio Sg. We examine the P-to-S ratio at near regional and regional distance, again using 3-components.

4.2. Kazakh Depth of Burial Explosions

Three 25 ton explosions were detonated at 3 separate depths at the Balapan area of the Semipalatinsk Test Site in Kazakhstan in the summer of 1997. Their primary purpose was to investigate the effects of depth of burial on seismic records. Additionally, 50 to 100 kg Green's

function explosions and a 5 ton explosion were detonated in the same shafts. All explosions were recorded locally. The 25 ton explosive charges were 34 m long, with the bottoms at 50, 300, and 550 meters depth. For the shallowest explosion then, the explosive extended from 16 to 50 m depth. The water table was at 30 m depth or less for all events.

None of the explosions were tamped, and all of them vented water and gasses and caused varying degrees of cratering (Demin, 1997). The shallowest explosion was detonated in a weak shale, and left a 9.5 m deep, 45 m diameter crater with 3.2 m embankment. Earth volume removed was estimated at $1,250 \text{ m}^3$. It also blew a 10.5 m section of casing 115 m from the hole. Such a loss of energy upwards decreases the amount coupled into the earth and so could affect the assumption that each source provided 25 tons of explosive force coupled into the earth. The 300 m depth explosion created a 3.1 m deep, 10 m diameter crater, removing only 20 m^3 of material and blowing out a 15 m long section of casing, which landed near the hole. The 550 m depth explosion cause surface effects intermediate between the other two explosions. It left a 10 m deep, 20 m diameter crater with 3.1 m high embankments, removed 260 m^3 of material, and blasted pieces of casing from 1.5 to 11.6 m long as far as 40 m from the hole. Propagation of the explosions' energy and gasses up the hole, venting of gasses, and cratering will have affected the seismic waves generated. The large water column above the deeper events would contribute to improved coupling, but the effects will differ from those of comparable fully tamped explosions. The effect of the cratering on seismic wave generation, and whether the size of its contribution is significant, has not been addressed.

For the shallowest explosion, the cratering, and more generally the asphericity of the yielding region, which generates shear waves directly, would be expected to generate significant shear wave energy. S^* should also be a significant source of shear waves for the shallow explosion, although the effect of the surface literally being removed makes that prediction problematic. The low P-wave velocity of the near surface should also result in crustal trapping of the pS phase, but again, removal of the free surface immediately above the source could affect the pS amplitude and character. The deeper events are sufficiently overburied that a spherical explosion source is more likely to be a good approximation of the source, at least at depth. The relative seismic contributions of the source at depth, propagation of explosive gasses up the pipe, and the surface cratering are not obvious.

Myers et al (1999) attribute spectral differences between the regional P/S amplitude ratios of the three explosions to depth dependent differences in R_g , which they assume scatters to S. They did not consider the effect of differences in the source parameters besides depth.

To our knowledge the effects of cratering were not considered in previous work, although most did note that the shallowest event created a large crater. Most previous work does not mention that the events were not tamped. Richards and Kim (2005) actually report that each of the events was fully tamped with sand and gravel. That is inconsistent with the field report on conditions of the explosions made by the National Nuclear Center of the Republic of Kazakhstan (Demin et al, 1997) from which the details described above were taken. The report includes photographs of large spouts of explosive gasses and water ejected during each of the explosions.

From the borehole log for the deepest event, the P velocity at the center of the explosive is 4.42, and is 4.16 and 4.26 km/s respectively, 10 and 20 m above the center of the explosive (Patton et al, 2005). Upper mantle S-wave velocity at Degelen is generally slightly greater than this, so the surface converted phase from this explosion should also be trapped, although even moderate scattering could cause some downgoing energy to steepen and be lost. We do not have the log for the 266 to 300 m depth explosion, but at 278 and 292 m in the shaft of the deeper explosion (2.5 km distant), P-wave velocities are 4.92 and 4.76. If the velocity structure is valid for the 266-300 m depth explosion, the high source S-wave velocities would predict that the surface P-to-S converted phase propagates into the mantle and so does not contribute to Lg. Again, scattering that even slightly changes the wavenumber of the downgoing S-waves could change that prediction, this time leading to more trapped S. The report by Demin et al (1997) refers to the source rock of the two deeper explosions as granosyenite, with average P- and S-wave velocities of 4.50 and 2.61 km/s respectively. This average also is consistent with pS being trapped, but just barely.

These considerations taken together predict more source generated S for the shallowest explosion than for either of the deeper explosions, due to significantly more non-spherical source components and S*, and possibly more completely trapped pS. Both of the other explosions should have little source generated S due to nonspherical source elements, and much smaller contributions from S*. If cratering itself is a significant source of S, the much larger crater of the shallowest explosion would again lead to relatively greater S for that event. The amount of trapped pS may be less for the 300 m depth source, although that is uncertain, as we do not know the source velocity precisely for that explosion.

Although previous work reports that indeed the shallowest event has relatively greater regional S, both in absolute terms and relative to P, we reevaluate that observation using three component records, as the S generally has the best signal-to-noise ratio on the horizontal components.

4.3. S Waves on Local Records

We find distinct Sg, separate from Rg, and extending to higher frequencies than Rg, on all 3-components of the local records of all three events. The Sg is most prominent in the records of the two shallower events. Figure 79 shows records of the 300 m depth event at 12.7 km, in 3 passbands. The tangential (top) and radial (bottom) records are both Hilbert transformed and overlain on the vertical records. The similarity of the tangential to vertical indicates significant off-axis arrivals or misorientation of the sensors. The similarity of the waveforms identifies the Rg (starting at ~5 seconds), and suggests that the Sg, at about 4 seconds, can be identified as one or more higher mode surface waves. The 5-8 Hz band records show energy only for the Sg, suggesting a difference source for the Sg and Rg.

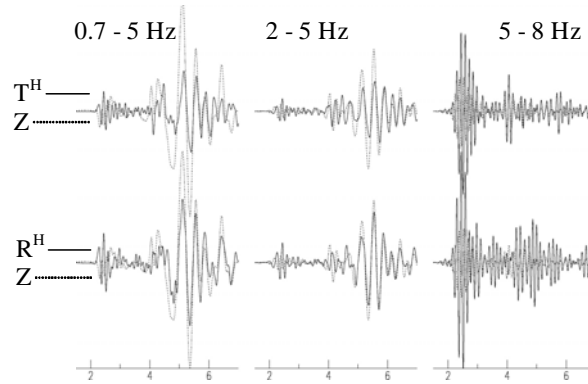


Figure 79: Hilbert transformed tangential and radial records in 3 passbands, at 12.7 km from the 300 m depth explosion show Rg (off axis on the tangential) where it aligns with vertical. Preceding the Rg, at ~3.8 seconds, is an S arrival (at 3.34 km/s) with comparable amplitude to P at less than 5 Hz, consistent with regional S spectra.

Figure 80 shows record sections of all 3 components of the local records, filtered from 2 to 5 Hz, for each of the three depth-of-burial explosions. S is apparent on all 3 components for the two shallowest explosions and on the tangential for the deepest event. These local observations are consistent with observed regional differences in shear wave amplitudes.

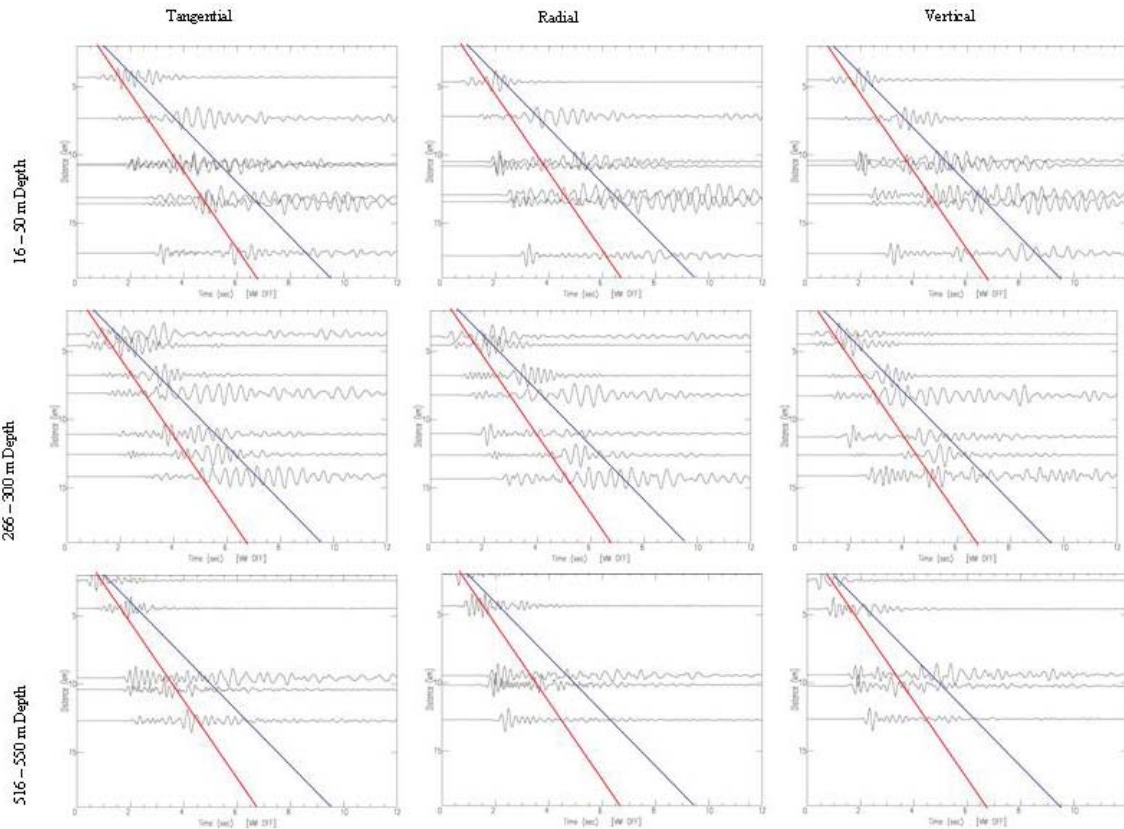


Figure 80: Record sections at 2-5 Hz. Red and blue lines are 3 and 2 km/s respectively.

4.4. Rg Decay Rate

Part of Myers et al (1999) interpretation depends on the rapid disappearance of Rg, which provides the energy that goes into regional S. Specifically they claim that Rg is rapidly attenuated at less than 20 km and find an Rg Q of approximately 10. Patton et al (2005) find a Q of $13f^{0.22}$. We invert the local Rg for velocity and attenuation structure, with a similar result. We find an Rg Q of 24. While higher than previous results, it is similar and sufficiently low that, if the scattered Rg went exclusively into Lg and if pS were lost to the mantle and the CLVD component was small, it could provide a significant boost to Lg. Some details of the inversion follow.

We separately measure group and phase velocity curves for each explosion. There are 7 records for the 50 m depth explosion. Figure 81 shows the seismograms filtered from 0.8 to 4 Hz. The records are distributed among different azimuths, so by inverting all the measurements, we obtain an average structure about the vicinity of the explosion (Figure 82). Figure 83 shows the group and phase velocity curves and the fit to the data from the model in Figure 84. Figure 85 shows the fit to the amplitude measurements. The median Rg Q is 24 (Figure 86). Table 10 shows the model. Velocities start to become quite high below the 16th layer, suggesting a limit to the resolution at lower frequencies. For simulations, we replace the upper 2.578 km of the Patton et al (2005) model, with the velocities derived from Rg inversion for the shallowest explosion. The difference is small, changing the average velocity from 5.62 to 5.33 km/s.

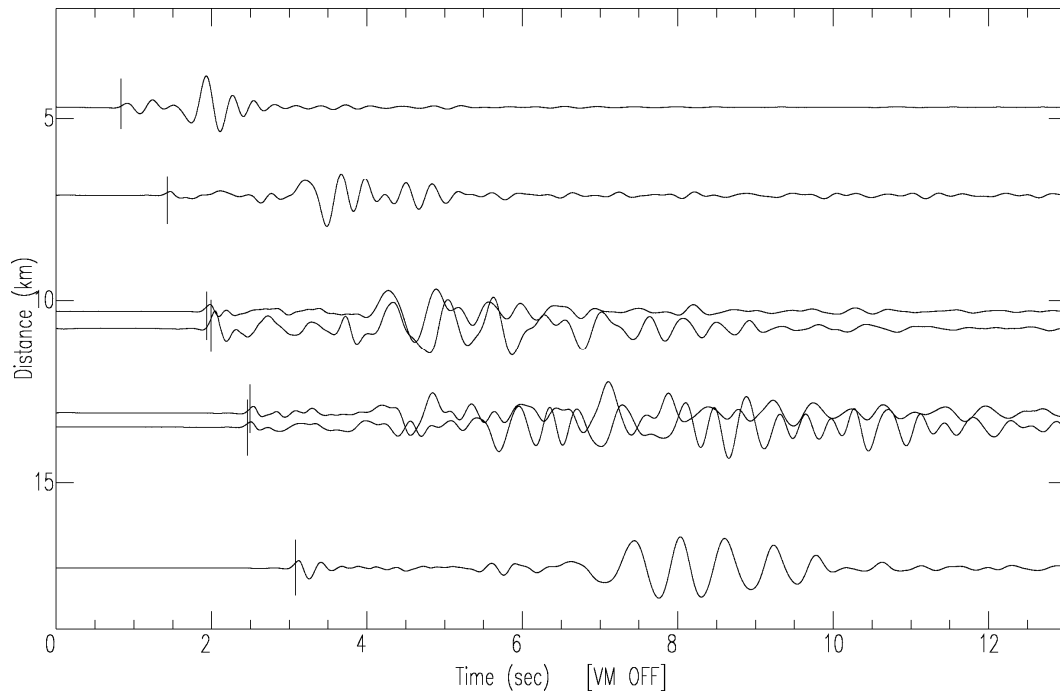


Figure 81: Vertical component seismograms from 0.8 to 4 Hz for 34 m depth Balapan explosion.

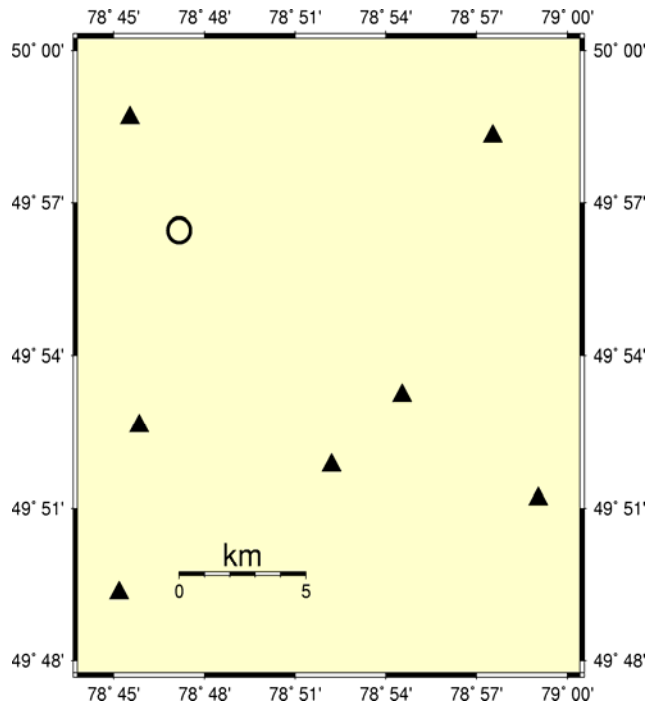


Figure 82: Map of station and 34 m depth event locations.

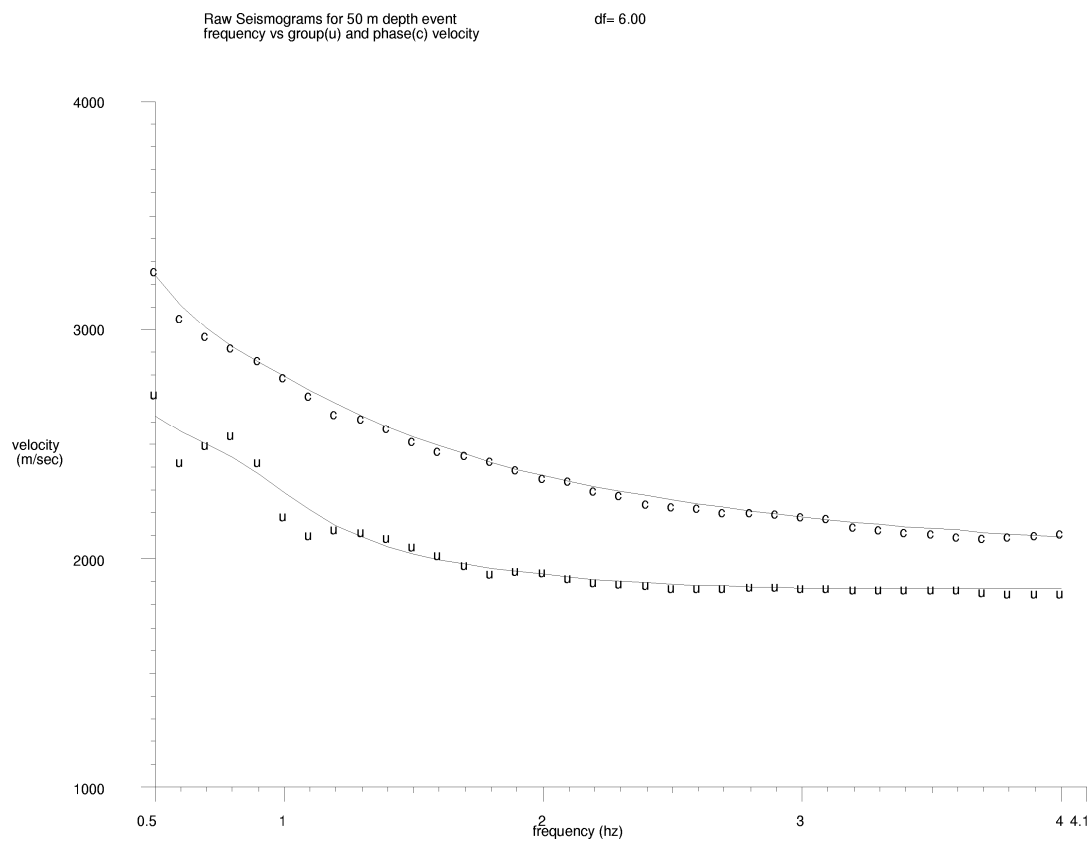


Figure 83: Fits to Rg group and phase velocity curves.

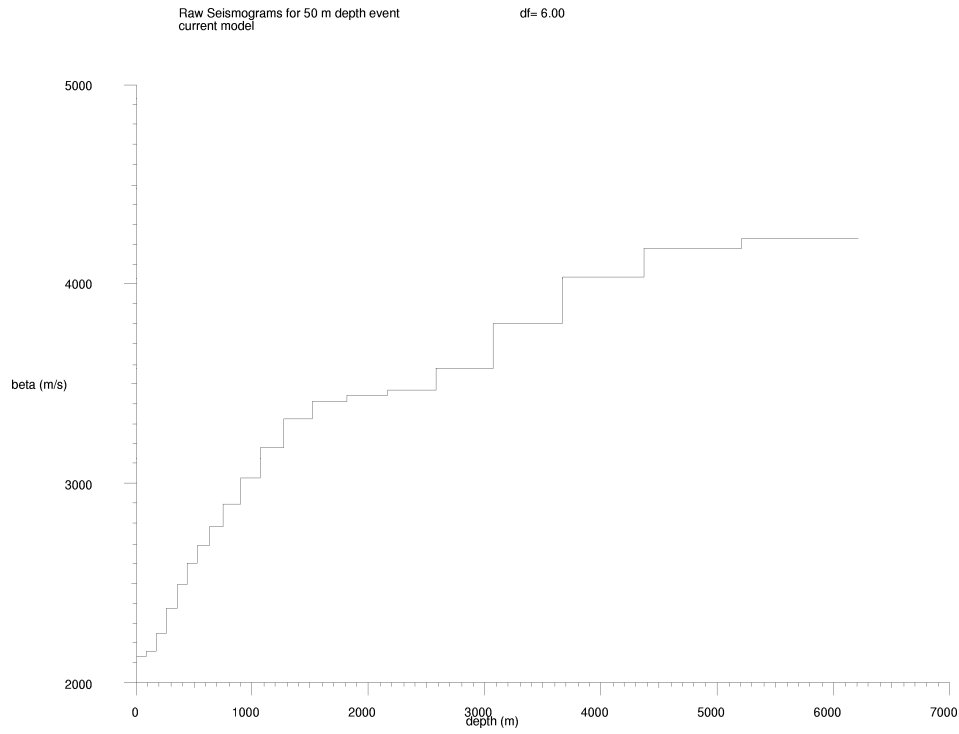


Figure 84: S wave velocity model derived from data.

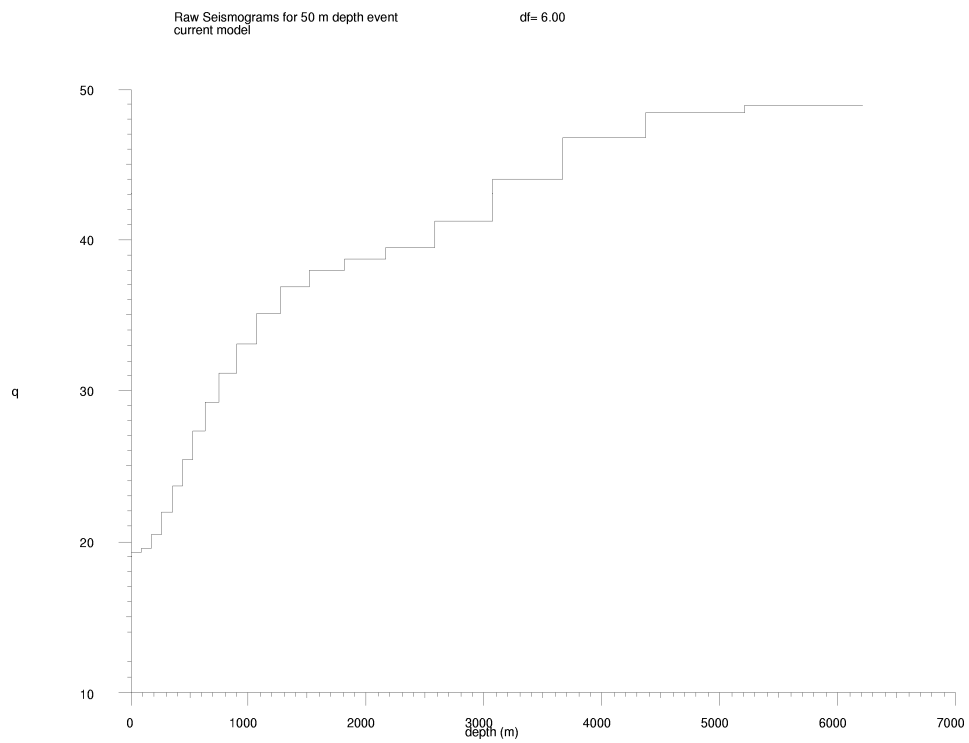


Figure 85: S wave Q model derived from data.

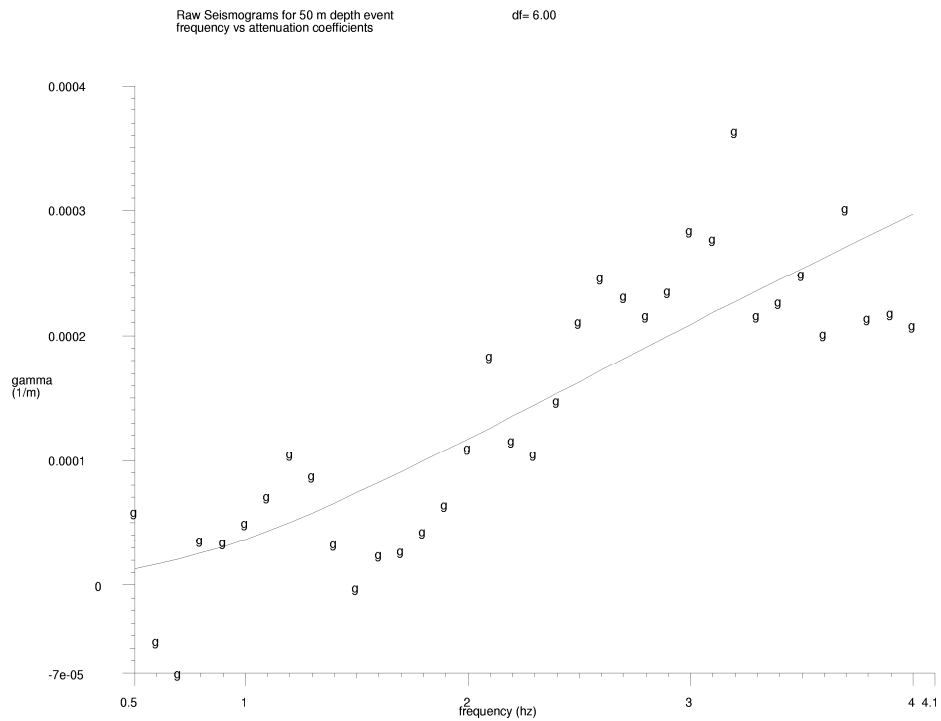


Figure 86: Amplitude data fit for 1.5 degrees of freedom.

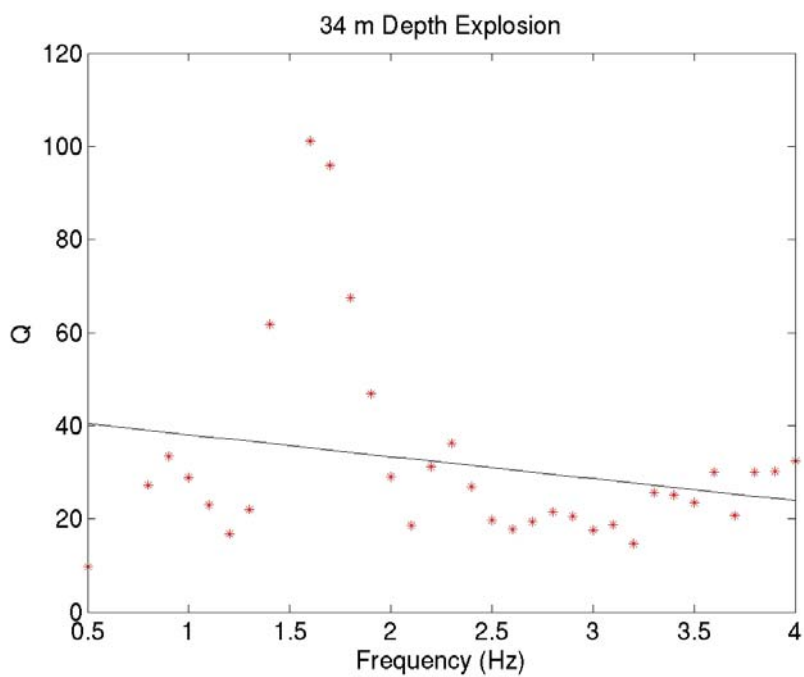


Figure 87: Q vs. frequency from 0.5 to 4 Hz for the 34 m depth Balapan explosion.

Table 10. Model from 34 m depth event Rg inversion.

ΔZ (m)	α (m/s)	β (m/s)	ρ (kg/m ³)	Q
88.25	3797	2131	1785	19.33
88.25	3844	2158	1802	19.56
88.25	4010	2251	1863	20.46
88.25	4233	2376	1944	21.92
88.25	4445	2495	2022	23.65
88.25	4626	2597	2088	25.44
101.8	4792	2690	2148	27.29
121.4	4963	2786	2211	29.23
144.7	5159	2896	2282	31.19
172.6	5395	3028	2368	33.14
205.8	5667	3181	2468	35.07
245.3	5921	3324	2560	36.81
292.5	6081	3413	2619	38.05
348.7	6128	3440	2636	38.74
415.8	6171	3464	2652	39.49
495.7	6380	3581	2728	41.22
591.1	6776	3803	2872	44.01
704.7	7190	4036	3023	46.76
840.2	7453	4183	3119	48.45
1002	7534	4229	3149	48.95

Similar models, with slightly lower Q, are obtained for the 300 m depth explosion. For the 300 m depth event, we obtain a Q of approximately 17, from 0.5 to 4 Hz (Figure 88). It is more difficult to obtain good Rg dispersion and amplitude measurements from the 550 m depth explosion. By eliminating the most complex records, windowing by group velocity to isolate Rg, and using broader Gaussian filters over just the 1 to 3 Hz passband, we obtain a model with poorer data fits and so poorer resolution, but still generally similar to the others. Because of the similarity of the results for the two shallower explosions and the proximity of the two deeper explosions, we assume that to first order, the models derived from the better data of the two shallower events is appropriate for the deepest event as well.

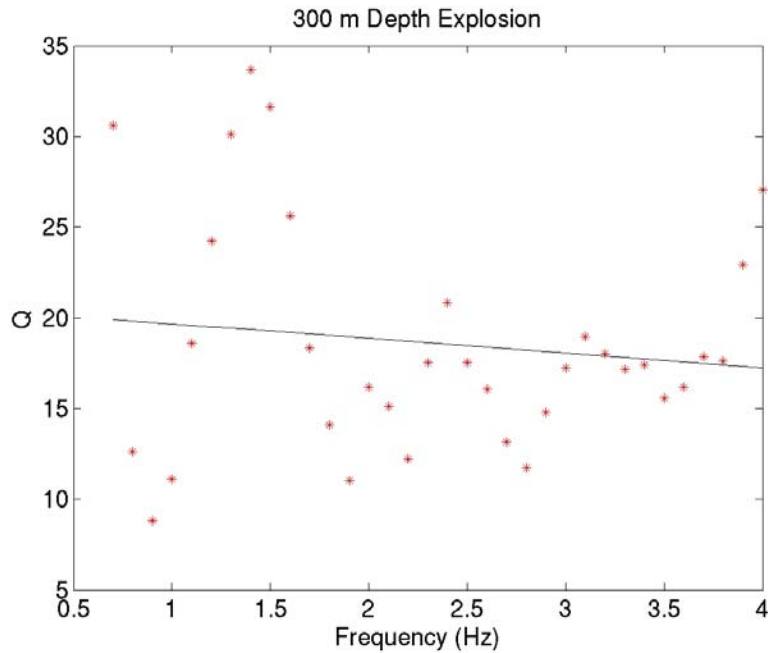


Figure 88: Q vs. frequency from .5 to 4 Hz for the 300 m depth Balapan explosion.

Despite the low Rg Q, we note that below 2 Hz, Rg is still the dominant phase at KUR, 85 km distance (Figure 89). The Rg, arriving at approximately 30 seconds, is so dominant at 0.5 to 1 Hz that it is almost the only phase visible. At 1 to 2 Hz it is still larger than P and as large as the S phase, which arrives at approximately 20 seconds. Note that at 1-2 Hz, the tangential Sg is the largest phase for the 550 m depth event, more prominent relative to other phases than is the case for the two shallower events. We will examine three-component near regional and regional S-wave amplitudes next.

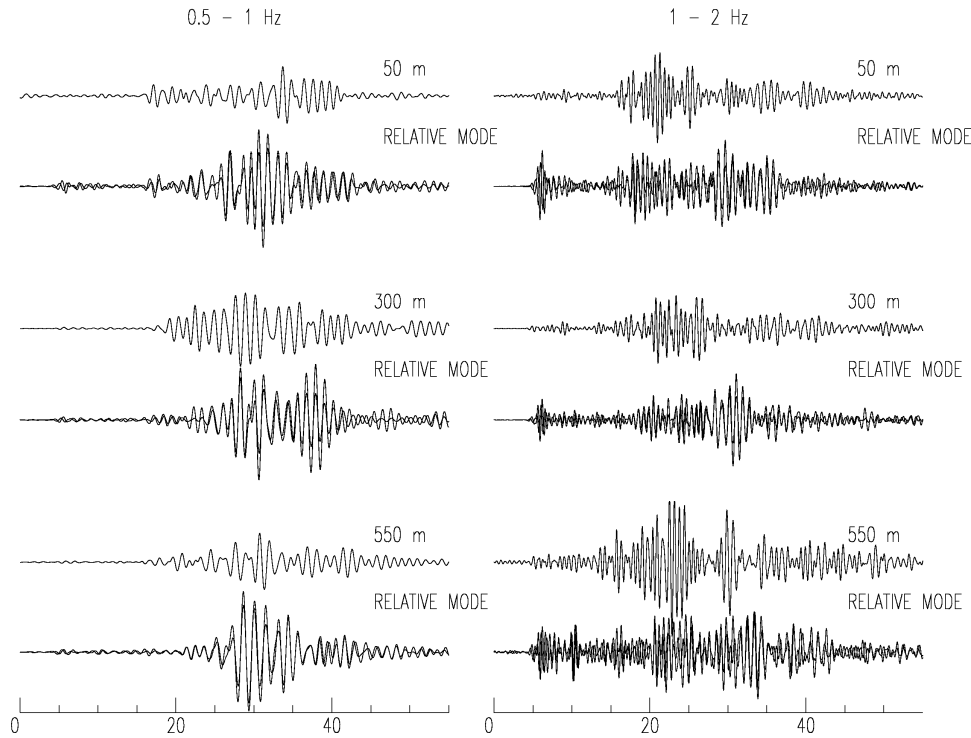


Figure 89: 3-component seismograms for the 50 (upper set), 300 (middle set), and 550 (lower set) meter depth of burial explosions recorded at 85 km distance, at station KUR, filtered from 0.5 to 1 Hz on the left, and 1 to 2 Hz on the right. The upper trace of each set is the tangential component. Below those are overlain the vertical and the Hilbert transformed radial seismograms. All records for each 3-component set are plotted on the same scale.

4.5. Regional Recordings

While $m_b(Lg)$ magnitude differences have been cited as important to understanding Lg generation (Patton et al, 2005), the amplitude variation of all phases due to differences in material strength and overburden pressure complicates their interpretation. The P-to-S amplitude ratio provides a better measure of depth dependence of shear wave generation. The P amplitude provides a means of approximating the effect of material strength and confining pressure on the source volume, which controls the magnitude of seismic energy generated. The P-to-S amplitude ratio then provides a relative measure of shear wave production to event size for each event.

We examine the local records, extending observations to 3-components, and including records from KUR, which were not previously used. Myers et al (1999) specifically showed P-to-S ratios at MAK and VOS and observed increase P-to-S amplitude ratios from 0.7 to 5 Hz with increasing depth of burial, so we look at that passband.

4.5.1. P and S Spectra at KUR

The records at KUR provide an opportunity to compare P and S wave spectra closer to the source, approximately 90 km, yet far enough that the phases are well separated. Choosing the same group velocity windows for each event is complicated by a time error. The P arrival time, location, and origin time for the 50 m event gives a Pg group velocity of just over 7 km/s, while

the same parameters for the other two events yield a more realistic Pg group velocity of almost exactly 6.0 km/s. To ensure that similar phase windows are compared between events, we find the origin time for the 50 m depth event that matches a 6 km/s Pg velocity. We use an Sg window from 3.6 to 3.0 km/s. The Pg window extends from before the Pg arrival to 3.9 km/s, to include as much P coda as possible.

Figure 90 shows the P (left) and S (right) spectra for each event. The S spectra is the average of the horizontal components, and the P is the average of the vertical and radial. The 50 m depth event spectra has larger amplitudes reflecting the much shallower depth and weaker source material. These spectra are not corrected for attenuation, so do not reflect the exact source spectra, but because source-station paths are very similar, they do indicate differences between the source spectra of the shallowest event and the two deeper events. The 300 m depth event has slightly larger amplitudes than the 550 m depth event. This is consistent with previous work, which found increasing corner frequencies and decreasing amplitude with greater depth.

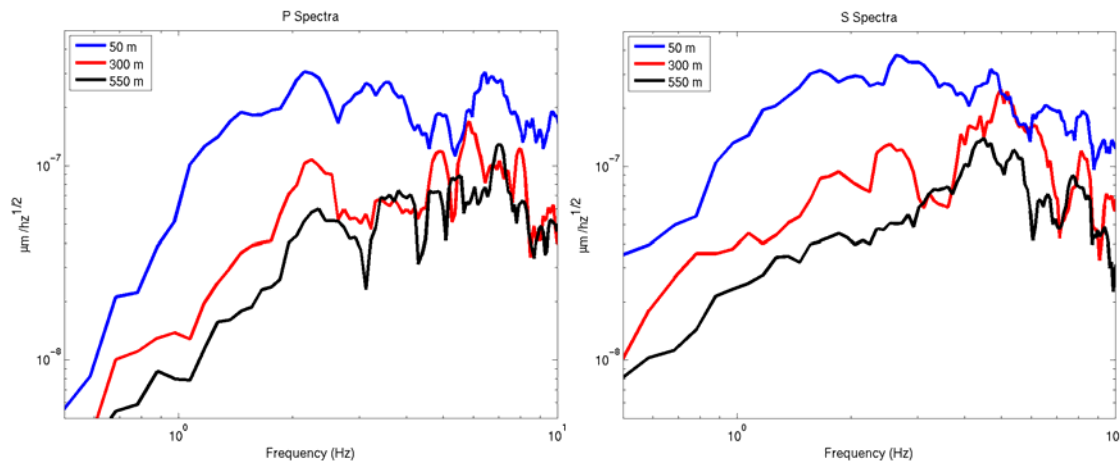


Figure 90: P (left) and S (right) spectra of the three depth of burial events recorded at KUR.

Figure 91 compares the P and S spectra of each event. The two phases have nearly identical spectral ratios for all three events, with the P-to-S ratio actually slightly larger at 1 Hz for the shallowest event. This is inconsistent with previously reported P-to-S ratios from MAK and VOS, and is inconsistent with scattering from Rg controlling the regional P-to-S ratios. The similarity of P and S amplitudes is apparent in the time series as well (Figure 92), which shows the three-component records of each event at KUR. Each set of records is normalized by its vertical P wave amplitude, and all records are plotted on the same scale. The prominent S wave arrives at approximately 25 seconds.

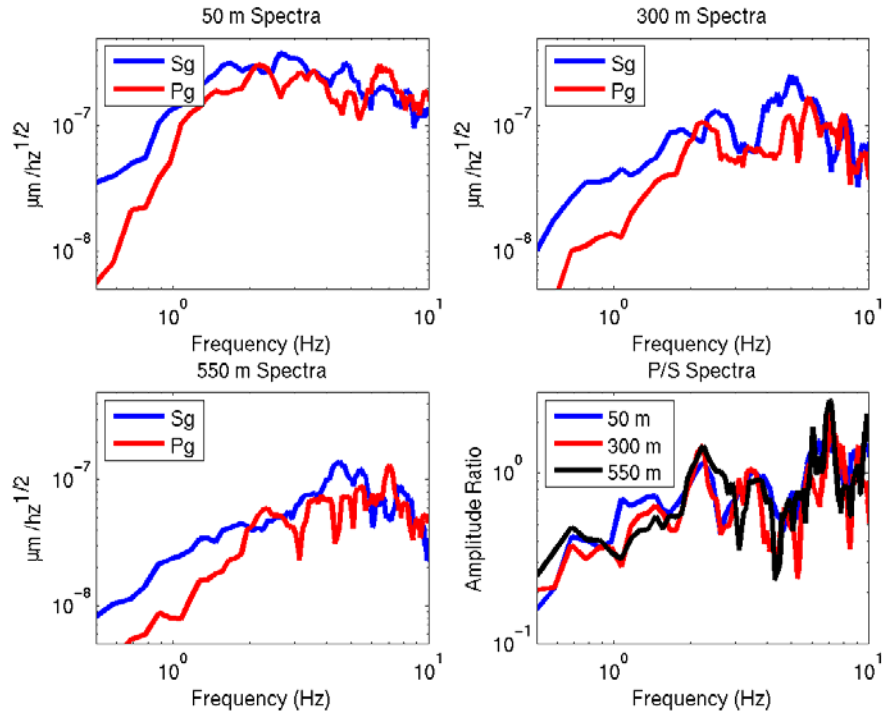


Figure 91: P (blue) and S (red) spectra of the three depth of burial events recorded at KUR, and the P-to-S spectral ratio (lower right).

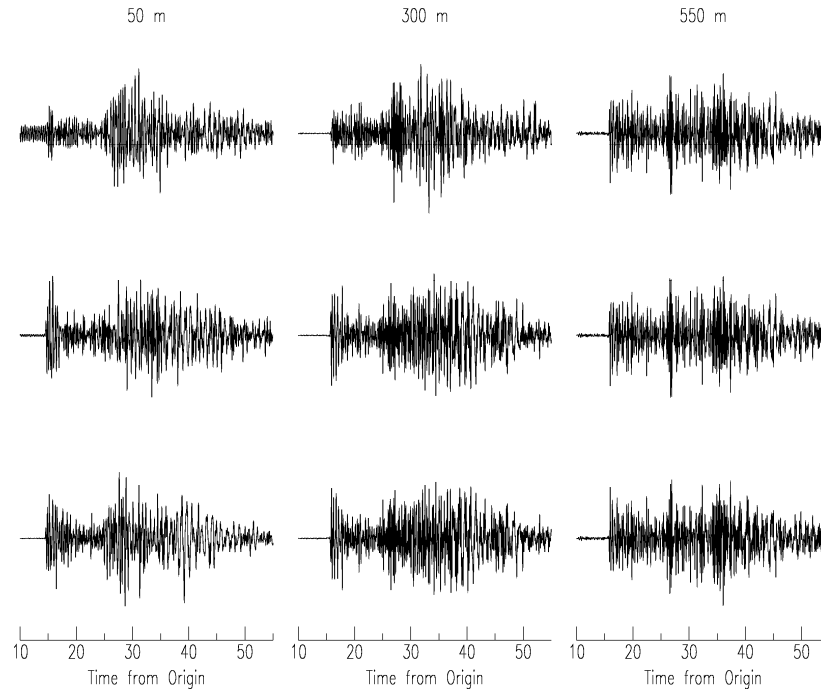


Figure 92: Three component records of the depth of burial explosions recorded at KUR, filtered from 0.7 to 5 Hz. Each set of records is normalized by its vertical P wave amplitude.

4.5.2. P and S Spectra at MAK

Figure 93 and Figure 94 are the same as Figure 90 and Figure 91 above, but for station MAK, at 413 to 423 km distance. For these plots, we show 0.7 to 5 Hz. We use the horizontal components in an Lg window, from 3.6 to 3.0 km/s, for the S spectra, and the radial and vertical P wave from before the first arrival to 4.5 km/s to avoid Sn. Again the shallowest event has the largest amplitudes. The 300 m depth event has poor P-wave signal-to-noise at the lowest frequencies. The spectral ratios (Figure 94, bottom right) show that the 50 and 550 m depth explosions have similar P-to-S ratios from 0.7 to 1 Hz. From 1.5 to 3 Hz, the 550 m depth explosion has larger P-to-S ratios, and the 50 and 300 m depth explosions are smaller. The 50 and 300 m depth events' spectral ratios are similar amplitude in that passband, but have different nulls, which are due to nulls in the P spectra, not peaks in the S. These observations are inconsistent with the P-to-S ratios based on just the vertical component records, and are inconsistent with greater enhancement of low frequency S for the shallowest event due to scattering from its larger Rg phase near the source. To ensure that we are interpreting spectra of each phase, not just noise, and to understand the discrepancy with previous work, we also examine the seismograms in these passbands.

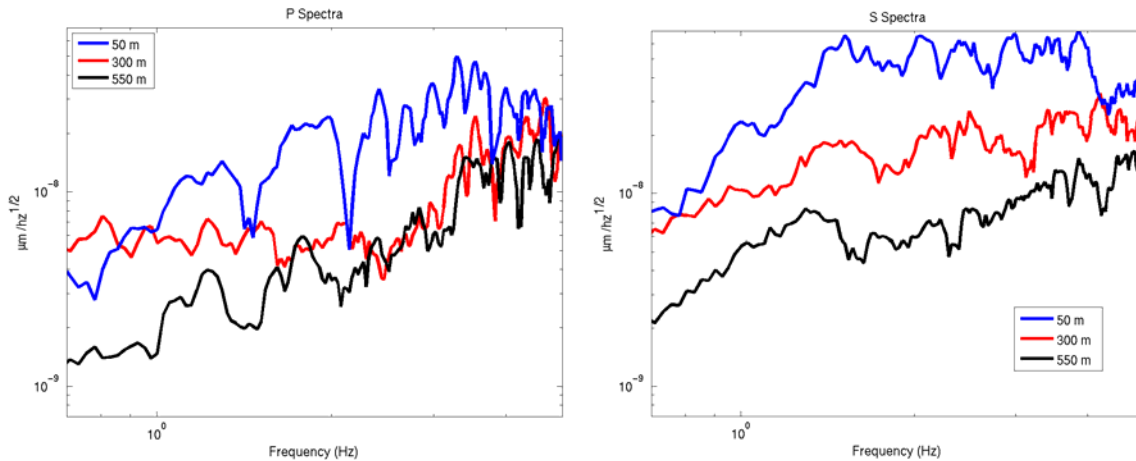


Figure 93: P (left) and S (right) spectra of the three depth of burial events recorded at MAK.

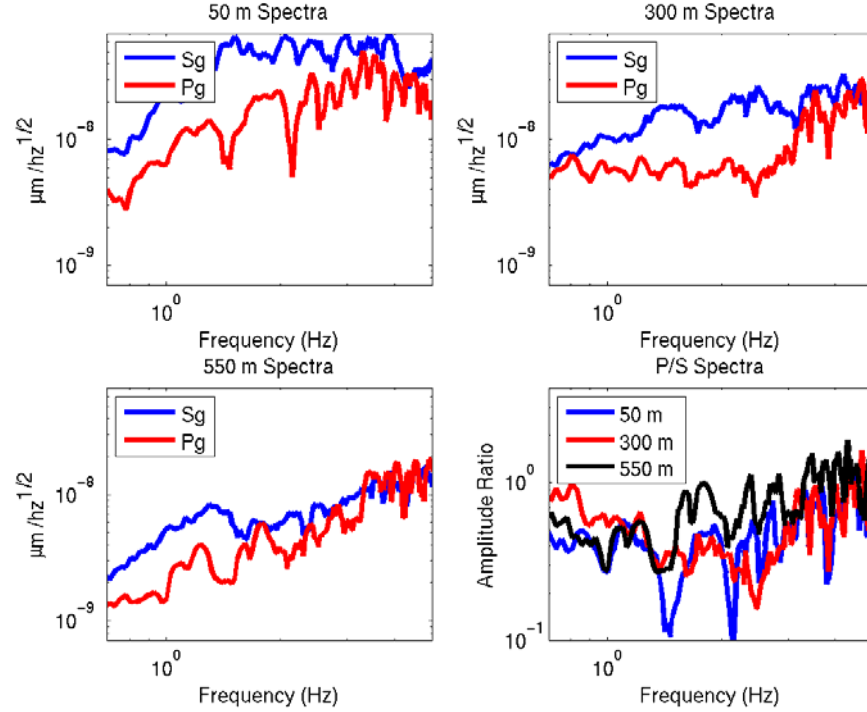


Figure 94: P (blue) and S (red) spectra of the three depth of burial events recorded at MAK, and the P-to-S spectral ratio (lower right).

Figure 95 and Figure 96 show the seismograms in two passbands, 0.7 to 1.2 Hz and 1.5 to 3.0 Hz, respectively. The records are normalized by the vertical P-wave amplitude to account for relative source scaling, and then are all plotted on the same scale. At 1.5 to 3 Hz, normalization by P is equivalent to multiplying the 300 m depth event records by 2.9 and the 550 m depth event records by 4.5. At 0.7 to 1.2 Hz, Lg is just as prominent on the horizontal component records of the deepest event as they are for the shallowest, consistent with the observed spectra. The 300 m depth event records show that the spectral ratios may be biased upward by poor P-wave signal-to-noise. The records confirm the spectral observation that the 300 m explosion produced as large of Lg relative to P as the 50 m depth explosion.

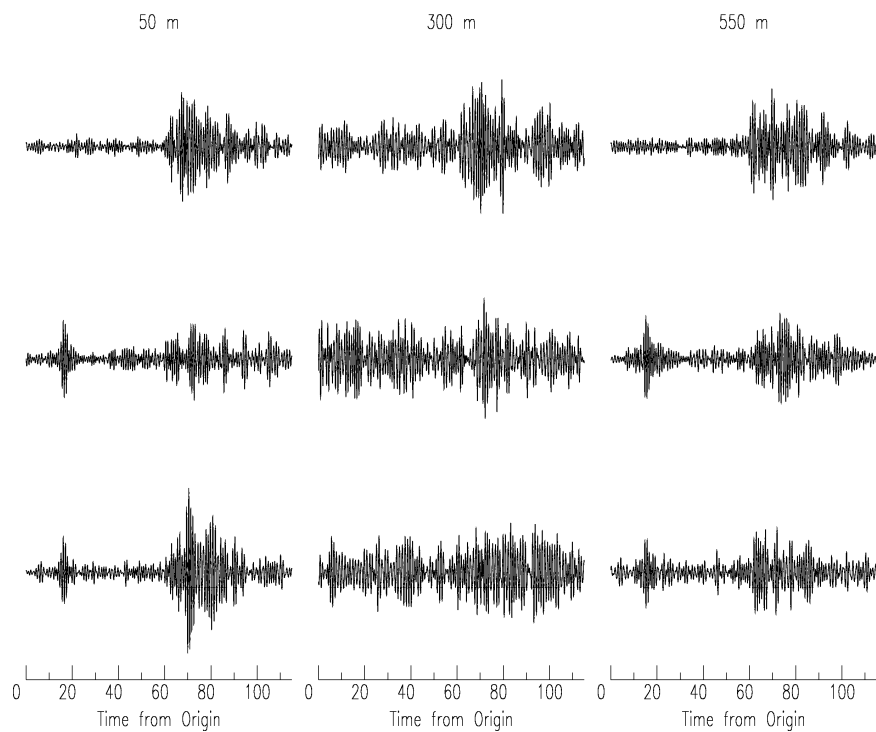


Figure 95: Three-component recordings at MAK for the three depth of burial explosions, at 0.7-1.2 Hz, normalized by the vertical P-wave amplitude. All records are plotted on the same scale.

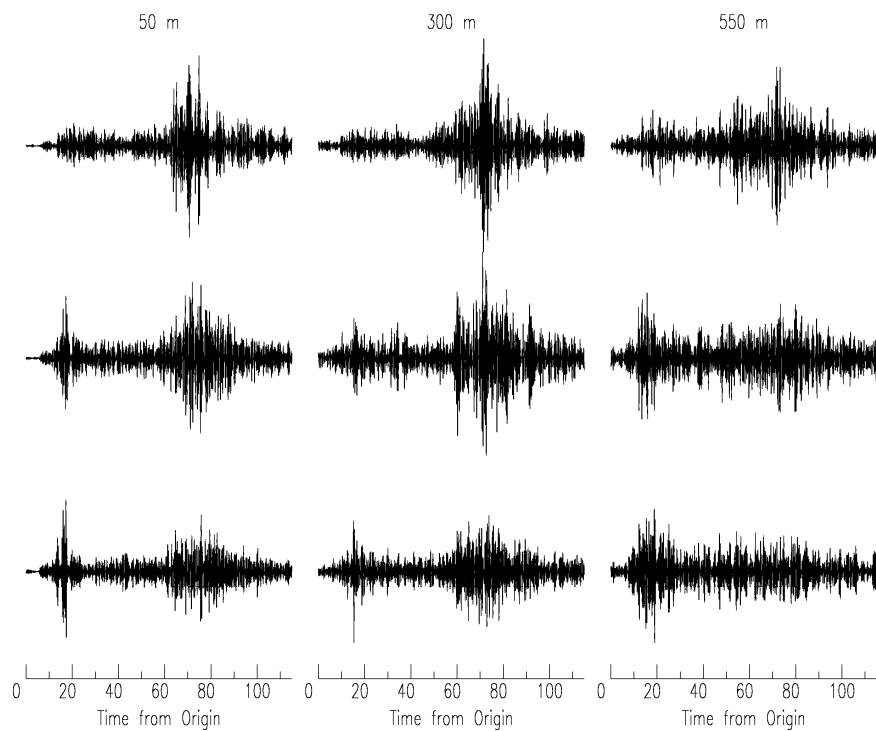


Figure 96: Three-component recordings at MAK for the three depth of burial explosions, at 1.5-3.0 Hz, normalized by the vertical P-wave amplitude. All records are plotted on the same scale.

5. AN UPPER BOUND ON RG TO LG SCATTERING USING MODAL ENERGY CONSERVATION

5.1. Summary

We use conservation of energy to place an upper bound on Lg generated by explosions through Rg scattering. We assume that all of the energy in Rg scatters very rapidly into the higher mode surface waves that make up Lg. We consider Rg generated both directly by the explosion source, and by a collocated, but possibly shallower, CLVD source. We find that Rg scattering may be a viable mechanism for generating Lg at low frequencies (< 1 Hz), but at higher frequencies Lg generated directly by the CLVD or explosion source is comparable to or greater than the upper bound generated by Rg scattering. We also find that either the direct waves or scattering from the spherical explosion Rg will dominate over scattering from the CLVD generated Rg at all frequencies.

5.2. Introduction

Since a point explosion source generates no direct shear waves, all shear waves from a point source are generated by scattering and conversion. However, a real explosion is not a point source, and the region of nonlinear deformation from the explosion can be quite different from spherical due to the effects of the free surface and the variation of overburden pressure with depth (Figure 97). A realistic explosion source therefore does generate shear waves, and the lowest order approximation to this more complex source in an axisymmetric configuration adds a compensated linear vector dipole (CLVD) component to the source.

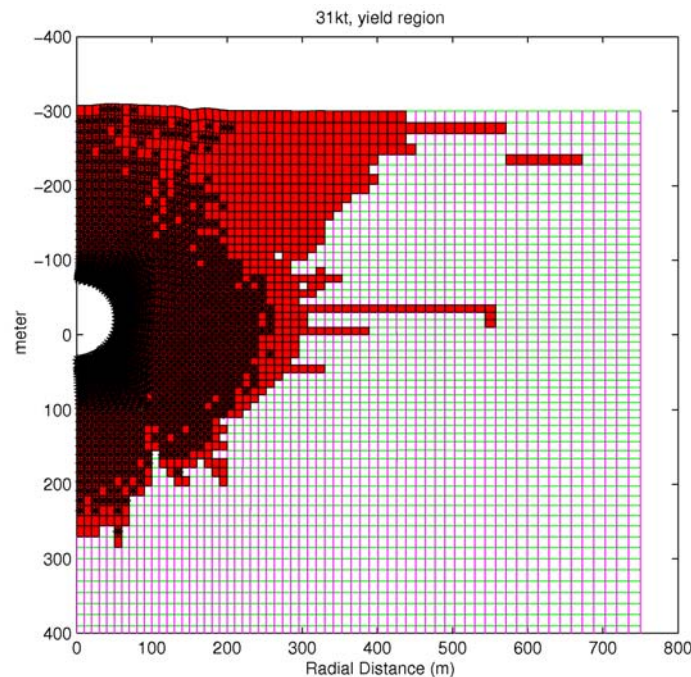


Figure 97. Calculated region of nonlinear deformation for a 31 kiloton explosion at 300 meters depth in a Degelen granite structure (from Stevens et al., 2005).

A number of studies have suggested that Rg to Lg scattering is the dominant mechanism for shear wave generation from explosions (e.g. Patton and Taylor, 1995; Gupta et al, 1997). Rg is generated by both the spherically symmetric and CLVD components of the explosion and so both could provide energy that could be scattered into Lg. It is difficult to quantify Rg to Lg scattering because Rg scatters into other phases (and itself) as well, and so most of the work on Rg to Lg scattering has focused on using spectral characteristics of Rg and Lg to infer a causal mechanism. Since direct S from the CLVD component as well as pS trapped in the crust also contribute to Lg, it has not been possible to uniquely determine the dominant mechanism. In this paper we use conservation of energy to determine an upper bound on the generation of Lg by Rg scattering under the assumption that all Rg is very rapidly scattered to Lg with no energy loss.

5.3. Upper Bound Calculation

We model Rg->Lg scattering under the assumption that Lg is generated by a distribution of surface scatterers and that all energy scattered from Rg is converted to Lg. We make the following assumptions:

- 1) The explosion may be a complex source, but has a known source function and is located at the origin.
- 2) Scattering occurs on the earth's surface and can be modeled as generated by a distribution of vertical point sources.
- 3) No energy is lost in scattering.
- 4) All scattering is from Rg to higher modes. We neglect Rg to Rg scattering, scattering to leaky phases, and scattering to Love waves.
- 5) All energy from Rg is scattered forward.

Under these assumptions, the scattered Rg consists of waves from a cylindrical distribution of point forces at the location of the propagating Rg phase (see Figure 98), and the scattered Rg goes into higher modes. These are optimistic assumptions and should be regarded as providing a high upper bound on Lg generated by Rg scattering. This is likely to be substantially larger than actual Rg to Lg scattering since Rg also scatters to other phases (and itself) and energy will be lost in the process.

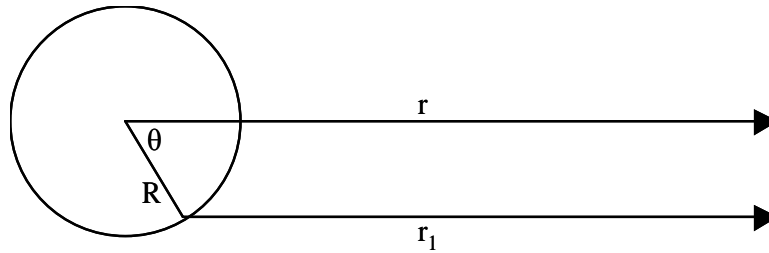


Figure 98. Rg propagates from the origin to radius R where it is scattered to Lg.

5.4. Surface Wave Excitation

The vertical component of a Rayleigh wave from an axisymmetric source located at the radial origin and depth h and measured at distance r and depth z in a plane layered medium has the following form (Takeuchi and Saito, 1972):

$$u_z(\omega, r, z) = \frac{1}{\sqrt{2\pi\omega r}} \sum_{i=1}^n \frac{1}{c_i^{3/2} U_i I_1^i} \exp\left[i(\pi/4 - \omega r/c_i)\right] F_s^i(\omega, h) y_1^i(\omega, z) \quad (1)$$

where I_1^i is the energy integral of the mode defined by $I_1^i = \int_0^\infty \rho \left(|u_z^i|^2 + |u_r^i|^2 \right) dz$, c_i and U_i are the phase and group velocity, respectively, ω is the angular frequency, the source excitation function F_s^i depends on the source type, mode and source depth, and is given for an axisymmetric moment tensor source by:

$$F_s^i(\omega, h) = \left[D \frac{\beta^2}{\alpha^2} \frac{M_{11} + M_{22} + M_{33}}{3} - B \frac{M_{11} + M_{22} - 2M_{33}}{12} \right] \quad (2)$$

$$B = - \left\{ \left(3 - 4 \frac{\beta^2}{\alpha^2} \right) y_3^i(h) + \frac{2}{\rho \alpha^2 k_i} y_2^i(h) \right\}$$

$$D = y_3^i(h) - \frac{1}{2\mu k_i} y_2^i(h)$$

where $y_1^i, y_2^i, y_3^i, y_4^i$ are the vertical displacement, normal stress, horizontal displacement, and shear stress eigenfunctions, respectively, for mode i , k_i is the wave number ω/c_i , and α, β, ρ are the compressional velocity, shear velocity and density at the source, respectively.

F_s^i for a vertical point force of unit impulse is given by

$$F_p^i = c_i y_1^i \quad (3)$$

and y_1^i is normalized to one at the free surface, so $F_p^i = c_i$ for a surface vertical point force. For an explosion with $M_{11} = M_{22} = M_{33} = M_0$,

$$F_x^i = M_0 \frac{\beta^2}{\alpha^2} \left(y_3^i - \frac{y_2^i}{2\mu k_i} \right) \quad (4)$$

and for a CLVD defined as $M_{33} = M_0; M_{11} = M_{22} = -M_0/2$,

$$F_{clvd}^i = \frac{-M_0}{6} \left[\left(3 - 4 \frac{\beta^2}{\alpha^2} \right) y_3^i + \frac{2y_2^i}{\rho \alpha^2 k_i} \right]. \quad (5)$$

For the purposes of this paper, the fundamental mode (mode 0) will be regarded as the Rg phase, and all higher modes as the Lg phase. The vertical displacement from the initial Rg wave u_z^0 has the form

$$u_z^0(\omega, h, z, r) = \frac{1}{\sqrt{r}} A_0^s(\omega, h) G_s(r) \exp(-ik_0 r - \gamma_0 r) y_1^0(k_0, z), \quad (6)$$

and the vertical displacement from the direct Lg wave is:

$$u_z^1(\omega, h, z, r) = \frac{1}{\sqrt{r}} \sum_{i=1}^N A_i^s(\omega, h) \exp(-ik_i r - \gamma_i r) y_1^i(k_i, z) \quad (7)$$

Where the subscript “i” indicates sum over all higher modes, γ_i is the intrinsic attenuation for each mode and G_s represents the attenuation of Rg due to scattering. A_i^s is the amplitude spectrum which depends on characteristics of the source and source region earth structure, and can be identified from equation 1 above as:

$$A_i^s(\omega, h) = \frac{1}{\sqrt{2\pi\omega c_i^{3/2} U_i I_1^i}} \exp(i\pi/4) F_s^i(\omega, h). \quad (8)$$

The radial displacement has a similar form with y_l replaced by the radial eigenfunction y_3 . The energy transfer rate through a cylindrical surface with radius R is given by:

$$\dot{T}^0 = 2\pi R U_0 \int_0^\infty \rho \left(|\dot{u}_z|^2 + |\dot{u}_r|^2 \right) dz \quad (9)$$

Integrating over all time and using Parseval's theorem to express displacement in terms of its Fourier transform, we get:

$$T^0 = 2\pi R U_0 \int_{-\infty}^\infty \omega^2 d\omega \int_0^\infty \rho \left(|u_z|^2 + |u_r|^2 \right) dz \quad (10)$$

The integral over depth can be done by integrating the eigenfunctions to get

$$T^0 = 2\pi U_0 \int_{-\infty}^\infty \omega^2 d\omega G_s^2(R) \exp(-2\gamma_0 R) \left| A_0^s(\omega, h) \right|^2 I_1^0 \quad (11)$$

We now restrict the discussion to single frequencies, although it should be remembered that energy conservation is defined by an integral over all frequencies.

The Rg energy loss rate due to scattering at R is

$$\frac{dT^0}{dR} = 4\pi U_0 \omega^2 \left| A_0^s(\omega, h) \right|^2 I_1^0 G_s \frac{dG_s}{dR} \exp(-2\gamma_0 R) \quad (12)$$

The total energy available for conversion to Lg is minus the integral of this equation. If we assume that G_s has the form $\exp(-\gamma_s R)$:

$$T_0^s = - \int_0^\infty \frac{d}{dR} T_0 dR = 4\pi \gamma_s U_0 \omega^2 \int_0^\infty \exp(-2\gamma_0 R - 2\gamma_s R) dR \left| A_0^s(\omega, h) \right|^2 I_1^0 = \frac{2\pi \omega^2 \gamma_s U_0}{\gamma_0 + \gamma_s} \left| A_0^s(\omega, h) \right|^2 I_1^0 \quad (13)$$

5.5. Conversion to Lg

If part of u_z^0 is converted to a sum of higher modes u_z^c at point R, we have

$$u_z^c = \iint dR d\theta \frac{1}{\sqrt{r_1}} \sum_{i=1}^N S(\omega, R) A_i^p(\omega) \exp(-ik_0 R - ik_i r_1 - \gamma_i r_1) y_1^i(k_i, z), \quad (14)$$

where A_i^p are modal coefficients for a vertical point force at the surface and S is the excitation function corresponding to the energy transfer.

Assuming azimuth independence of scatterers, forward scattering and neglecting small differences in attenuation and geometric spreading between r and r_1 , we get:

$$u_z^c = \frac{1}{\sqrt{r}} \sum_{i=1}^N A_i^p(\omega) \exp(-ik_i r - \gamma_i r) y_1^i(k_i, z) \int_0^\infty dR S(\omega, R) \exp(-ik_0 R + ik_i R), \quad (15)$$

The converted wave has a total energy of

$$T^c = 2\pi \omega^2 \sum_{i=1}^N \left| A_i^p(\omega) \right|^2 \left| U_i I_1^i \exp(-2\gamma_i r) \int_0^\infty dR \exp(-ik_0 R + ik_i R) S(\omega, R) \right|^2 \quad (16)$$

So from equations (13) and (16) and the requirement for conservation of energy:

$$\frac{\gamma_s}{\gamma_0 + \gamma_s} \left| A_0^s(\omega, h) \right|^2 U_0 I_1^0 = \sum_{i=1}^N \left| A_i^p(\omega) \right|^2 \left| U_i I_1^i \int_0^\infty dR \exp(-ik_0 R + ik_i R) S(\omega, R) \right|^2. \quad (17)$$

Equation 17 determines the excitation of the Lg modes under the assumption of exponential decay of scattering with distance.

5.6. Rapid Scattering

Since we expect Lg generation to decrease with distance, we try a solution for S of the form:

$$S(\omega, R) = S_0(\omega) \exp(-\gamma_H R) \quad (18)$$

Then the integral in equation 17 can be evaluated and solved for S_0 :

$$|S_0(\omega)|^2 = \frac{\gamma_s}{\gamma_0 + \gamma_s} |A_0^s(\omega, h)|^2 U_0 I_1^0 \left[\sum_{i=1}^N \left| \frac{1}{\gamma_H + ik_0 - ik_i} \right|^2 |A_i^p(\omega)|^2 U_i I_1^i \right]^{-1} \quad (19)$$

Note that although we have defined S as a general function of frequency and distance in equation 15, the requirement for conservation of energy also makes it dependent on source depth through the source function A_0^s on the right hand side of equation 19. Equation 15 then becomes:

$$u_z^1 = \frac{1}{\sqrt{r}} \sqrt{\frac{\gamma_s U_0 I_1^0}{\gamma_0 + \gamma_s}} |A_0^s(\omega, h)| \left[\sum_{i=1}^N \left| \frac{A_i^p(\omega)}{\gamma_H + ik_0 - ik_i} \right|^2 U_i I_1^i \right]^{-1/2} \sum_{i=1}^N \frac{A_i^p(\omega) \exp(-\gamma_i r - ik_i r) y_1^i(k_i, z)}{\gamma_H + ik_0 - ik_i} \quad (20)$$

In the case of very rapid scattering, $\gamma_s \gg \gamma_0$ and $\gamma_H \gg k_0, k_i$, equation 20 becomes:

$$u_z^c(\omega, h, z, r) = \frac{1}{\sqrt{r}} B(\omega, h) \sum_{i=1}^N A_i^p(\omega) \exp(-ik_i r - \gamma_i r) y_1^i(k_i, z) \quad (21)$$

where $B(\omega, h)$ is given by:

$$B(\omega, h) = \left[\frac{|A_0^s(\omega, h)|^2 U_0 I_1^0}{\sum_{i=1}^N |A_i^p(\omega)|^2 U_i I_1^i} \right]^{1/2} \quad (22)$$

Note comparing equations 21 and 17 that $B(\omega, h)$ is equal to the integral of the scattering function in equation 17. The converted Lg phase is equivalent to the higher modes generated by a vertical point force at the surface modulated by the amplitude function in equation 22. This can be compared with the direct wave (equation 7), which has modal excitation of A_i^s vs. the modal excitation BA_i^p for the (upper bound) scattered Rg wave. Using equation 8 and $F_p^i = c_i$, we can write:

$$B(\omega, h) = \left[\frac{|F_0^s(\omega, h)|^2 / U_0 I_1^0 c_0^3}{\sum_{i=1}^N |F_i^p(\omega)|^2 / U_i I_1^i c_i^3} \right]^{1/2} \quad (23)$$

$$B(\omega, h) A_i^p(\omega) = A_i^s(\omega, h) \frac{|F_0^s(\omega, h)|}{|F_i^s(\omega, h)|} \frac{c_i}{c_0} \left[\frac{1}{U_0 I_1^0 c_0} / \sum_{i=1}^N \frac{1}{U_i I_1^i c_i} \right]^{1/2} \quad (24)$$

The modal coefficients of the (upper bound) scattered wave have the same form as the direct wave multiplied by the factors on the right hand side of equation 24, and the relative amplitudes of the direct vs. scattered wave are controlled by three factors: 1) the mode independent energy transfer function of the fundamental mode to the higher modes (the factor in brackets); 2) the higher mode to fundamental mode phase velocity ratio; and 3) the depth and frequency dependence of the fundamental mode excitation function vs. the higher modes. At zero depth F_i^s is proportional to the modal ellipticity for both explosion and CLVD sources. As we show in the following section, although there is considerable variation in the quantities in equation 24 with mode and frequency, the energy transfer function is ~2-3, the ellipticity ratio is typically ~2 and the phase velocity ratio is ~2-3, so equation 24 is typically about 10 for a surface source, decreasing with depth, and decreasing more rapidly at higher frequencies.

5.7. Examples

We consider two earth structures (Figure 99): a high velocity structure similar to the former Soviet Degelen nuclear test site, and a low velocity structure similar to the Nevada Test Site (NTS). “High velocity” means that the P velocity near the surface is higher than the S velocity in the upper mantle, so pS waves generated by the explosion and converted to S at the surface are not trapped in the crust and leak to the mantle. In a low velocity structure much of the pS phase is trapped in the crust and therefore contributes to the Lg phase. Figure 100 shows the energy

transfer function from equation 23: $\left[\frac{1}{U_0 I_1^0 c_0} / \sum_{i=1}^N \frac{1}{U_i I_1^i c_i} \right]^{1/2}$ for each structure. Although there is a

lot of variation in the amplitude function for each mode, the energy transfer function is relatively smooth and stable, varying from 1 to 5 with an average value of about 2 for both structures.

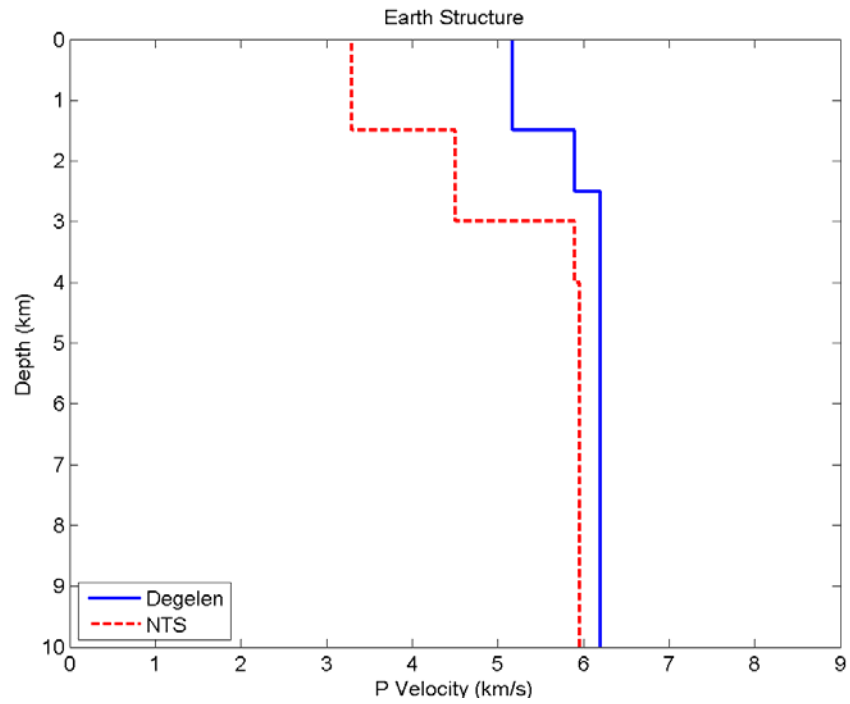


Figure 99. P velocity of upper 10 km used for the Degelen and Nevada test sites. Upper mantle shear velocity is 4.5 km/s.

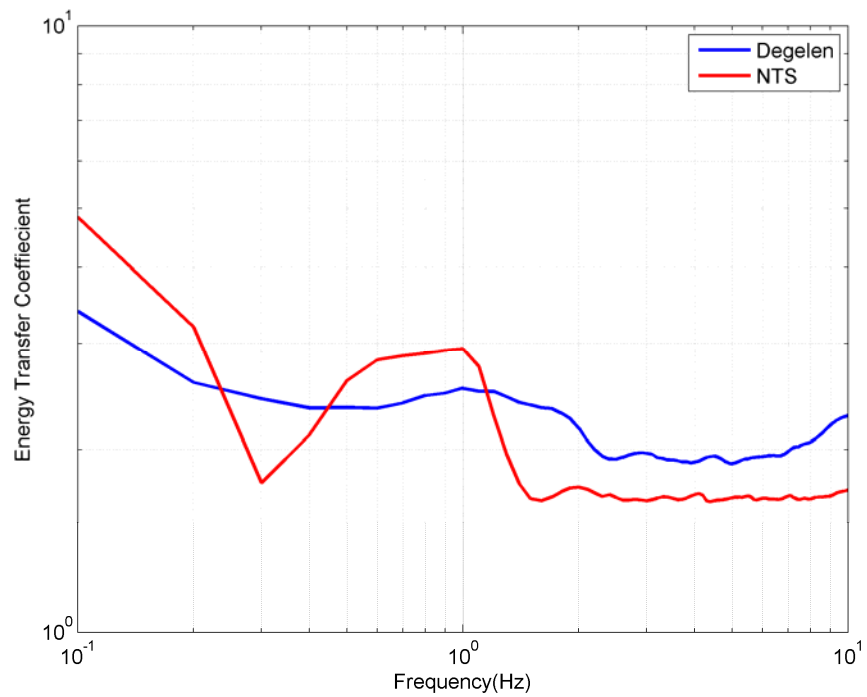


Figure 100. Model energy transfer function for Degelen and NTS structures.

We calculated the direct Lg wave from explosion and CLVD sources (with the same moment) in these two structures at a distance of 500 km, and the upper bound scattered Lg wave from the explosion and CLVD sources. A Mueller-Murphy tuff-rhyolite source typical of NTS has a moment approximately half that of a Mueller-Murphy granite source of the same yield (Mueller and Murphy, 1971), so the moment for the NTS calculation was reduced by a factor of 2 relative to Degelen so that the amplitudes would better correspond to explosion yield. Spectra were calculated using the multi-taper method from the calculated time series in the 3.0-3.6 km/sec time window. The spectra are shown in Figure 101 and Figure 102.

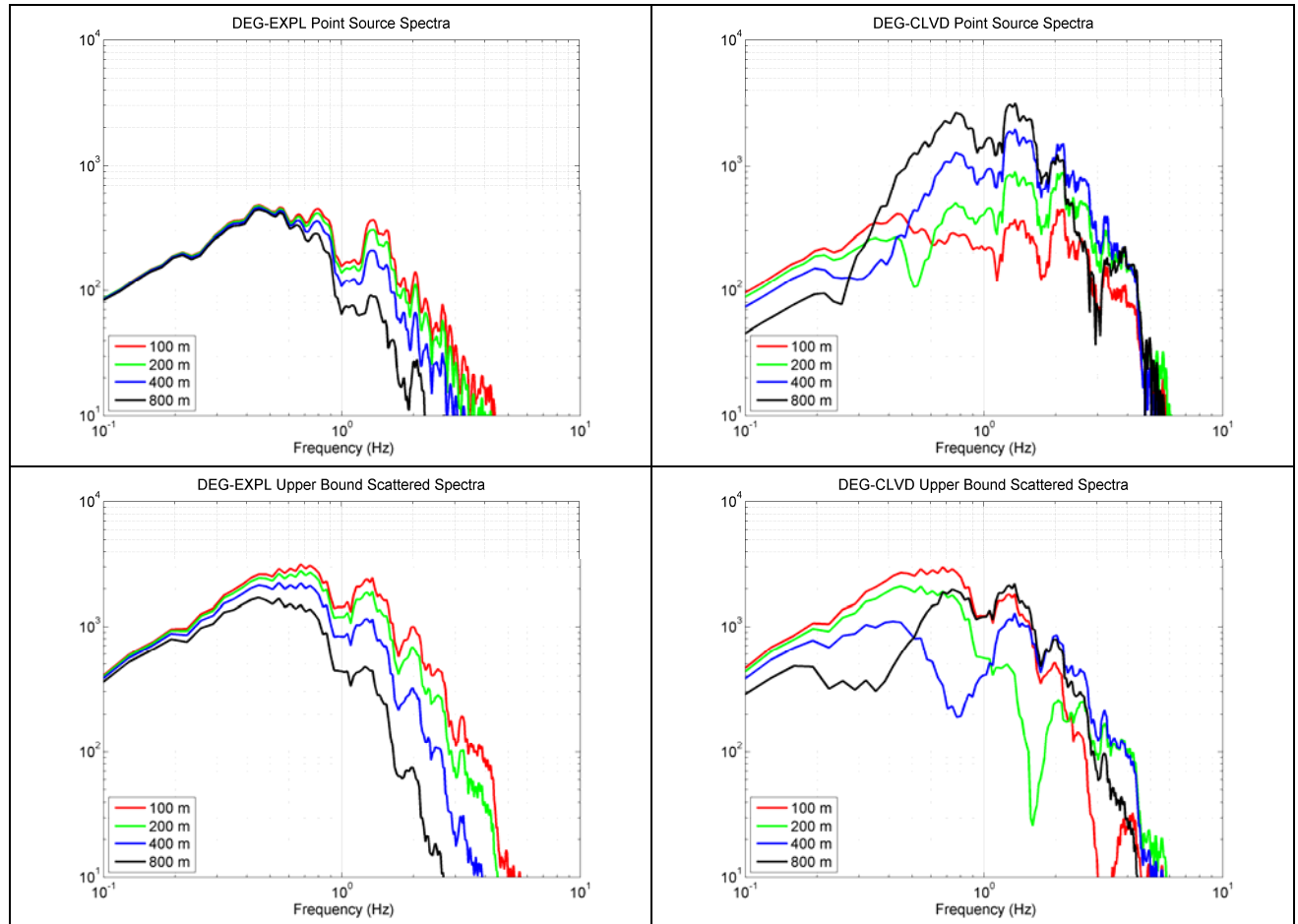


Figure 101. Lg velocity spectra calculated at a distance of 500 km in the Degelen earth structure at source depths of 100, 200, 400 and 800 meters. The four figures are for the direct explosion (upper left), direct CLVD (upper right), upper bound scattered explosion (lower left), and upper bound scattered CVLD (lower right) sources.

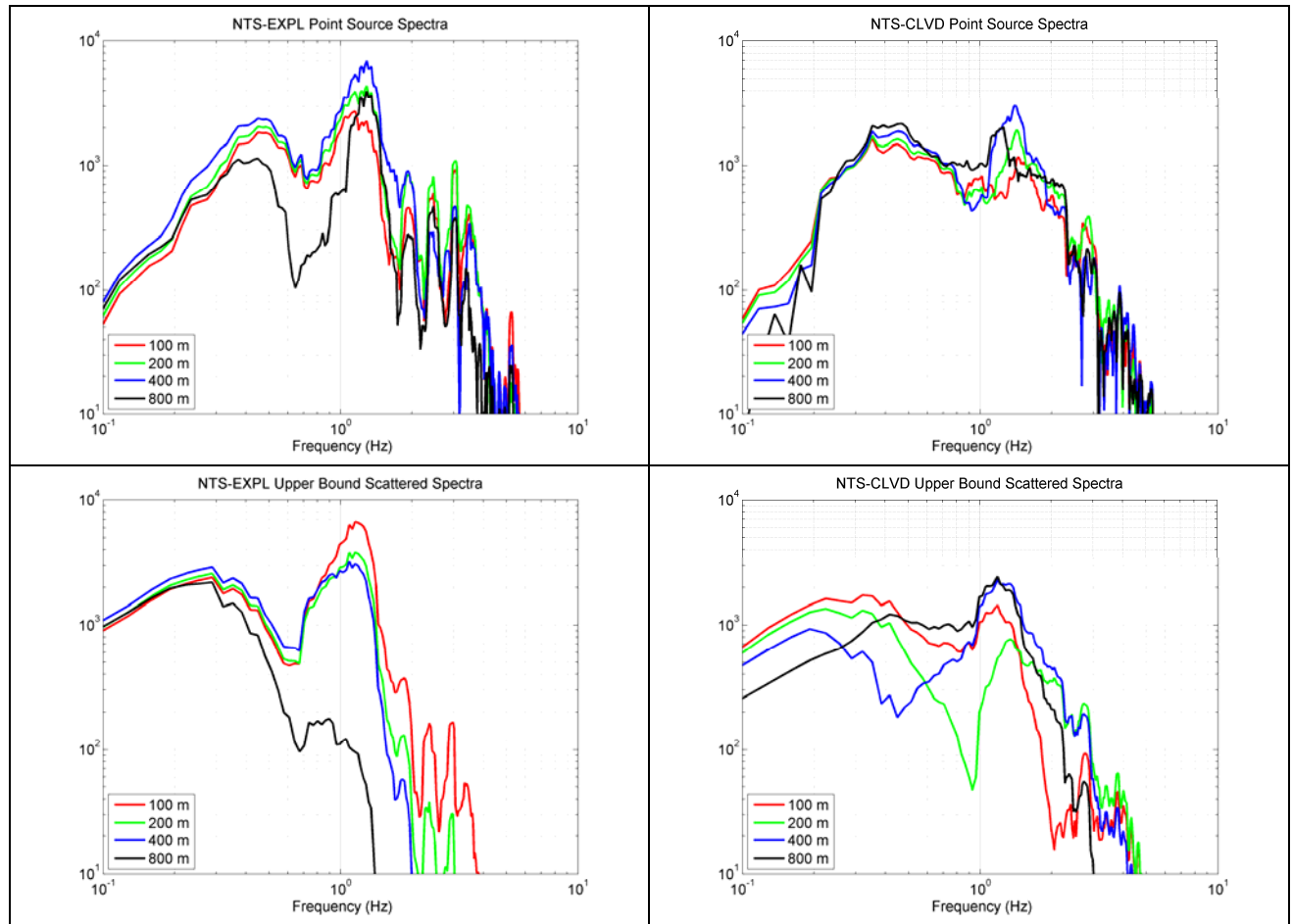


Figure 102. Lg velocity spectra calculated at a distance of 500 km in the NTS earth structure at source depths of 100, 200, 400 and 800 meters. The four figures are for the direct explosion (upper left), direct CLVD (upper right), upper bound scattered explosion (lower left), and upper bound scattered CLVD (lower right) sources.

The results show some strong depth effects. In the Degelen structure, the CLVD spectra become substantially larger with depth at frequencies above 0.5 Hz, while the explosion spectra as well as the scattered explosion spectra decrease significantly with depth over the same frequency band. The direct CLVD therefore becomes a more important component of the source with increasing depth in this structure. The scattered CLVD spectra also decrease with depth, although in a more complicated way due the spectral null which moves to lower frequency with increasing depth.

The results in the NTS structure are more complicated due to more complexity in the spectra caused by the earth structure. The direct explosion spectra are large and insensitive to depth in the upper 500 meters, declining at deeper depths. The direct CLVD spectra are almost independent of depth. The upper bound scattered explosion spectra behave similarly to the direct wave, being insensitive to depth in the upper 500 meters and then decreasing rapidly at deeper depths. As with Degelen, the upper bound scattered CLVD is more complicated due to the varying location of the spectral null with depth.

As discussed earlier, an explosion plus a CLVD is a first order approximation to the real complex explosion source. Analysis of finite difference calculations (Stevens et al., 2005) show that for explosions near normal containment depth, the CLVD component is approximated well by a CLVD with half the explosion moment. The effective depth of the CLVD is not well determined, although the shape of the deformation suggests that it will be somewhat shallower than the explosion depth. Figure 103 shows a comparison of all four spectra: point explosion, upper bound scattered explosion, point CLVD (with half the explosion moment) and upper bound scattered CLVD at depths of 600/400 meters and 300/200 meters for the explosion and CLVD components, respectively, in the NTS and Degelen structures.

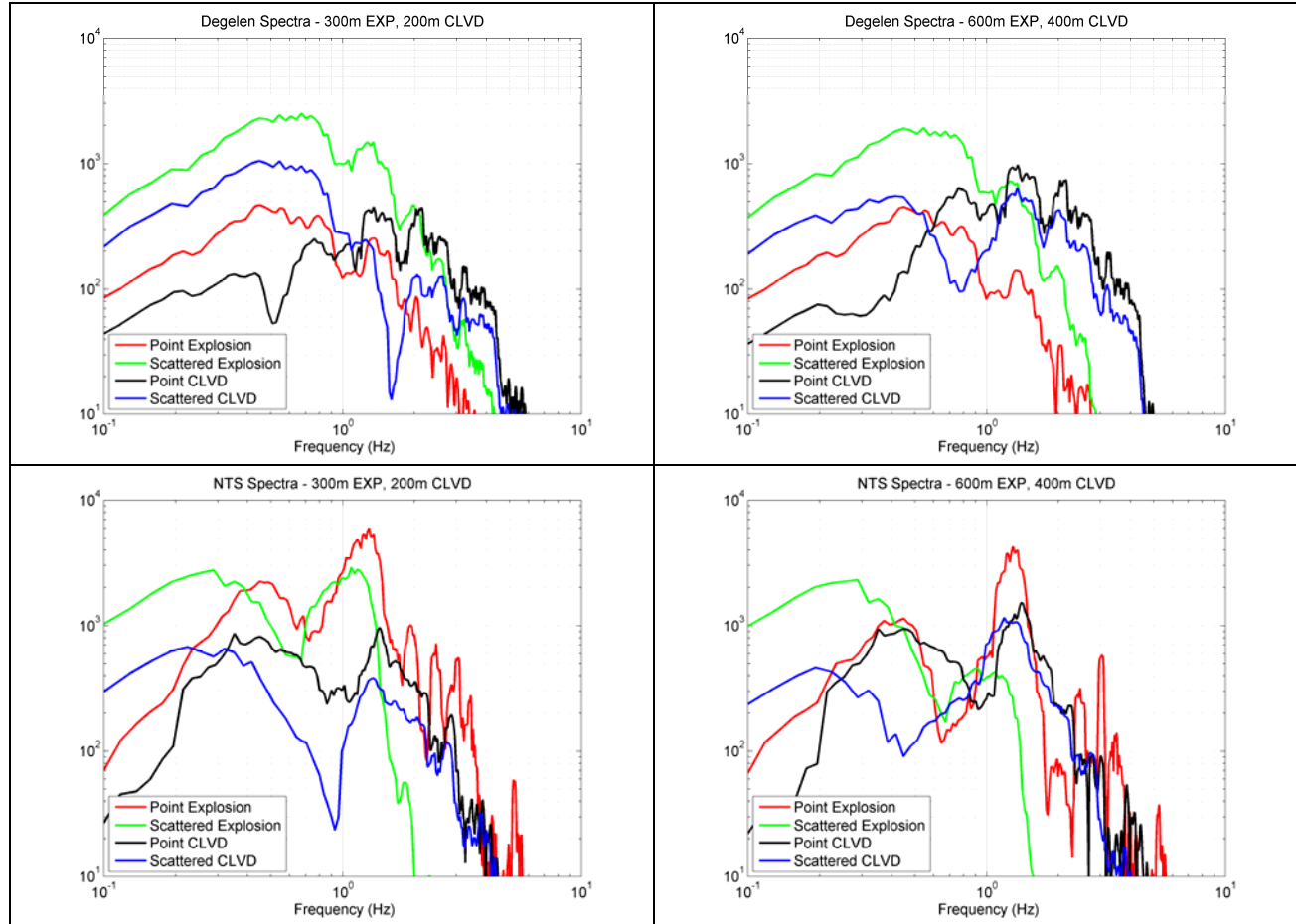


Figure 103. Relative sizes of Lg velocity spectra from a point explosion, a point CLVD with half the explosion moment, and the upper bound scattered Rg to Lg for the same sources in Degelen (top) and NTS (bottom) structures at explosion depths of 300 meters (left) and 600 meters (right), with the CLVD at 2/3 of the explosion depth.

For the Degelen structure, the results show that the direct CLVD will dominate at high frequencies, and that the frequency at which it begins to dominate decreases with increasing depth. At 400 meters depth, it is larger than other sources at frequencies greater than about one Hz, while at 200 meters it is larger than other sources at two Hz. At one Hz, the upper bound scattered explosion spectrum is higher than the direct CLVD spectrum by about a factor of 4, and the upper bound scattered explosion source exceeds other sources at lower frequencies. At frequencies below

~1 Hz, the direct explosion source exceeds the direct CLVD source, and the upper bound scattered explosion source is larger than the upper bound scattered CLVD source at all frequencies less than ~2 Hz.

For the NTS structure the direct explosion source, which in this case corresponds primarily to the pS phase, dominates over all other sources at frequencies above 0.3 Hz, except for a narrow frequency range when the direct CLVD is larger. Above ~2 Hz the direct CLVD is as large as, or a substantial fraction of, the direct explosion source, but does not exceed it.

5.8. Conclusions

Since the upper bound spectra exceed the actual scattered spectra by an unknown amount, we cannot make definite conclusions regarding the contribution of Rg scattering to Lg where the upper bound substantially exceeds the direct wave, which is the case below 1 Hz at Degelen and below 0.3 Hz at NTS for the depth range considered. However, since either the upper bound scattered explosion Rg or one of the direct waves is larger than the upper bound scattered CLVD in all cases, there is no frequency range in either structure where the scattered Rg from the CLVD could dominate the Lg phase. Also, at frequencies higher than ~1 Hz in a high velocity structure such as Degelen, the direct CLVD source will dominate, while at frequencies higher than ~0.3 Hz in a low velocity structure such as NTS, the direct explosion source will dominate. The only region in which Rg to Lg scattering appears to be a viable mechanism to be the dominant source of Lg is at frequencies below ~1 Hz in a high velocity structure and below ~0.3 Hz in a low velocity structure, and in that case the scattered explosion Rg will dominate over the scattered CLVD Rg.

6. THE EFFECT OF PROXIMITY TO A PREVIOUS EXPLOSION ON NEAR FIELD PEAK VELOCITIES

We use near field parametric information obtained under this contract by the Institute for the Dynamics of the Geospheres (IDG) to investigate the effect of proximity to prior explosions. The near field parametric information includes peak velocity, rise time, positive pulse width, and arrival time for 19 STS nuclear explosions from the 1960s and 70s. The near field data from some events in close proximity to earlier events were indistinguishable from the earlier events, however a few events that were detonated close to an earlier event have distinctly different near field data. In Table 11, those events that were both close to an earlier event and which had significantly different near field peak velocity measurements than the earlier event are marked.

Table 11. Near Field Tabular Data collected by IDG.

Date	Yield (kt)	Depth (m)	m_b	Event No.	Near Earlier Event	Lat	Lon
61/10/11	1.16	141	^K 4.78			49.772	77.995
62/02/02	16.9	265	^K 5.63			49.778	78.002
64/03/15	23.6	245	^A 5.56			49.808	78.102
64/05/16	23.7	266	^A 5.55	11		49.775	77.988
64/06/06	1.05	75	^K 4.42			49.809	78.093
64/11/16	23	203	^A 5.64			49.809	78.133
65/02/04	17	262	^A 5.10		X	² 49.773	² 77.991
65/07/29	1.0	126	^I 4.5			² 49.773	² 77.991
65/06/17	12	178	^A 5.24			49.828	78.067
65/09/17	10	148	^A 5.22			49.812	78.147
65/10/08	15	204	^A 5.47	12		49.826	78.111
65/11/21	29	303	^A 5.61			49.819	78.064
65/12/24	6	228	^A 4.94	13	X	49.805	78.107
66/02/13	109-125	343	^A 6.26			49.809	78.121
67/12/08	12.5	166	^A 5.31			49.817	78.164
68/09/29	75	358	^A 5.8			49.812	78.122
73/02/16	25	225	^A 5.48	14	X	49.816	78.116
79/05/31	8.5	183	^A 5.27		X	49.830	78.087
80/06/25	0.3	152	^K 3.70	15		49.826	78.099

m_b from AWE, Khalturin et al (2001) or ISC

Figure 104 shows a map of part of the Degelen test site with 5 events marked (listed by number in Table 11). Peak velocity vs. scaled range measurements (Figure 104, right side) show that events 13 and 14 have significantly lower peak particle velocities than the earlier event that they were very close to, event 11. Event 15 was also close to event 12, but the effect on particle velocity is less clear than for events 13 and 14. The other two events marked in Table 11 were also close to an earlier event and had significantly reduced peak velocities.

Despite the significant effect on peak velocities for some events in the near field, there is no apparent effect on m_b . The events with reduced near field peak velocity fall right into the population of other explosions in a plot of m_b vs. yield (Figure 105) and are quite close to the magnitude/yield curve for this region ($m_b = 0.75 \log Y + 4.45$, where Y is yield in kilotons; Murphy, 1995).

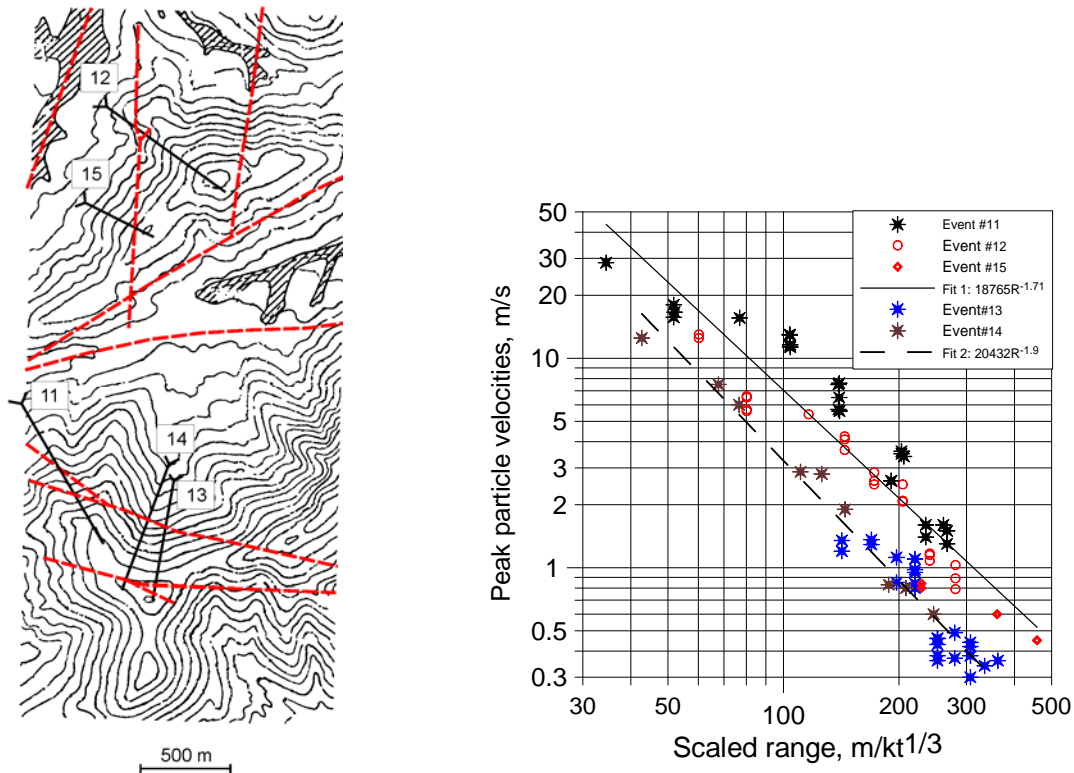


Figure 104. Location of five Degelen explosions (left) and peak particle velocity vs. scaled range (right). Lines on the map show tunnels from the tunnel entrance to the shot location. Number is by the entrance point. Red lines are fault locations. Peak velocities are lower than is typical for some events located near previous events.

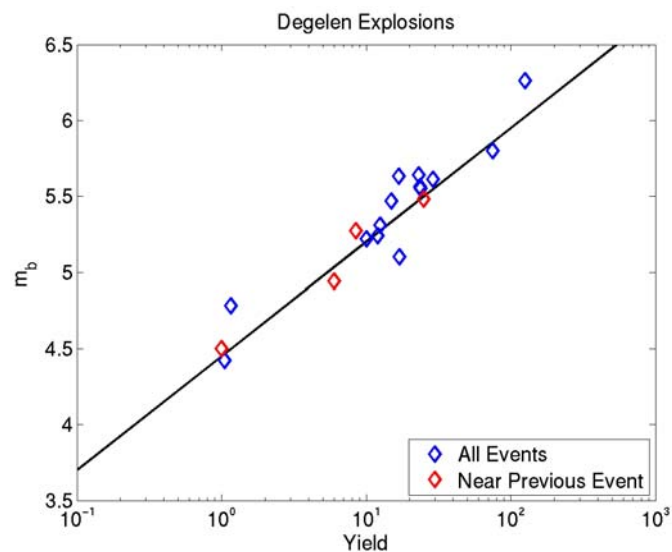


Figure 105. m_b vs. yield for the events in Table 11. Red triangles mark the four events marked in Table 11 as close to another event and having reduced near field peak velocities. The solid line is the nominal m_b /yield curve for this region from Murphy (1995). The effect of previous events on local peak velocities (Figure 104) is not observed in m_b .

REFERENCES

- Baker, G. E., J. L. Stevens, and H. Xu (2004), Lg group velocity: A depth discriminant revisited, *Bull. Seism. Soc. Am.*, 94, 722-739
- Baker, G. E., J. L. Stevens, and H. Xu (2007a), Explosion Shear Wave Generation: Part 1, High Velocity Source Media, Manuscript in prep for submission to *Bull. Seism. Soc. Am.*
- Baker, G. E., J. L. Stevens, and H. Xu (2007b), Explosion Shear Wave Generation: Part 2, Low Velocity Source Media, Manuscript in prep for submission to *Bull. Seism. Soc. Am.*
- Baker, R. G. (1970), Determining magnitude from Lg, *Bull. Seism. Soc. Am.*, 60, 1907-1919
- Baker, R. G. (1970), Preliminary study for determining magnitude from Lg, *Earthquake Notes*, 38, 23-28
- Bannister, S. C., E. S. Husebye, and B. O. Ruud (1990), Teleseismic P coda analyzed by three-component and array techniques: Deterministic location of topographic P-to-Rg scattering near the NORESS array, *Bull. Seism. Soc. Am.*, 80, 1969-1986
- Bard P.-Y and M. Bouchon (1980), The seismic response of sediment filled valleys: Part II. The case of incident P and Sv waves, *Bull. Seism. Soc. Am.*, 70, 1921-1942
- Bard P.-Y. (1982), Diffracted waves and displacement field over two-dimensional elevated topography, *Geophys. J. R. Astr. Soc.*, 71, 731-760
- Boore D., S. C. Harmson, and S. T. Harding (1981), Wave scattering from a step change in surface topography, *Bull. Seism. Soc. Am.*, 71, 117-125
- Bouchon, M. (1973), Effect of topography on surface motion, *Bull. Seism. Soc. Am.*, **63**, 615-632
- Dainty, A. (1990), Studies of coda using array and three-component processing, *Pure Appl. Geophys.*, 132, 221-244
- Day, S. And K. L. Mclaughlin (1991), Seismic source representations for spall *Bull. Seism. Soc. Am.*, **81**, 191 - 201
- Demin, V. (1997) Three experimental test hole closures at the Balapan test field, National Nuclear Center, Republic of Kazakhstan, Final Report, Contract DSWA-0094/1, Item 0009, 108 pp.
- Fisk, M (2006), Source Spectral Modeling of Regional P/S Discriminants at Nuclear Test Sites in China and the Former Soviet Union, *Bull. Seism. Soc. Am.*, **96**, 2348-2367
- Fisk, M (2007), Corner Frequency Scaling of Regional Seismic Phases for Underground Nuclear Explosions at the Nevada Test Site, *Bull. Seism. Soc. Am.*, **97**, 977-988
- Frankel, A. and Clayton, R. W. (1986), Finite difference simulations of seismic scattering: Implications for the propagation of short-period seismic waves in the crust and models of crustal heterogeneity, *J. Geophys. Res.* 91, 6465-6489.
- Gangi A. F. and R. L. Wesson (1978), P-wave to Rayleigh wave conversion coefficients for wedge corners: Model experiments, *J. Comp. Physics*, 29, 370-388
- Goldstein P. (1995), Slopes of P- to S-wave spectral ratios – A broadband regional seismic discriminant and a physical model, *Geophys. Res. Lett.*, 3147-3150

- Gupta, I.N. and R. R. Blandford (1983), A mechanism for generation of short-period transverse motion from explosions, *Bull. Seism. Soc. Am.*, 73, 571-591.
- Gupta, I. N. and R.A. Wagner (1992), Evidence for Rg-to-P scattering in teleseismic P coda of east Kazakh explosions, *Bull. Seism. Soc. Am.*, 82, 2139-2152
- Gupta, I.N., T.R. Zhang, and R. Wagner (1997), Low frequency *Lg* from NTS and Kazakh nuclear explosions – Observations and interpretation, *Bull. Seism. Soc. Am.*, **87**, 1115-1125
- Gupta, I.N., and R.A. Wagner (1998), Study of low and high frequency *Lg* from explosions and its application to seismic monitoring of the CTBT, Multimax Inc Final Report for AFRL-VS-HA-TR-98-0038
- Gupta, I.N., W. Chan, and R. Wagner (2005), Regional Source Discrimination of Small Events Based on the Use of *Lg* Wavetrain, *Bull. Seism. Soc. Am.*, **95**, 341-346
- Gutowski, P., F. Hron, D. E. Wagner, and S. Treitel (1984), *S**, *Bull. Seism. Soc. Am.*, **74**, 61-78
- Hansen, R. A., Ringdal, F. and Richards, P. G. (1990), The stability of RMS *Lg* measurements and their potential for accurate estimation of the yields of Soviet underground nuclear explosions, *Bull. Seis. Soc. Am.*, 80, 2106–2126.
- Hedlin, M. (1991), Analysis of seismic coda to identify regional sources and image strong crustal scatterers, Ph.D. thesis, U.C.S.D.
- Hong, T. and Xie, J. (2005). Phase composition of regional seismic waves from underground nuclear explosions. *Jour. Geophys. Res.* 110(B12): doi: 10.1029/2005JB003753. issn: 0148-0227.
- Hudson, J.A. (1967), Scattered surface waves from a surface obstacle, *Geophys. J. R. Astr. Soc.*, 13, 441-458
- Israelsson, H. (1994), Analysis of historical seismograms - root mean square *Lg* magnitudes, yields and depths of explosions at the Semipalatinsk Test Range, *Geophys. J. Intl.*, 591-609.
- Jih, R.S. (1995), Numerical investigation of relative contributions of Rg scattering and incomplete dissipation to *Lg* excitation, 17th Seismic Research Symposium, 401-410
- Kennett B.L.N. and S. Mykkeltveit (1984), Propagation in laterally varying media - II. *Lg*-waves in north-western Europe, *Geophys. J. R. Astr. Soc.*, 79. 257-267.
- Key, F. A. (1967), Signal generated noise recorded at the Eskdalemuir seismometer array stations, *Bull. Seism. Soc. Am.*, 57, 27-37
- Khalturin, V., T. Rautian, and P. Richards, (2001), A study of small magnitude seismic events during 1961-1989 on and near the Semipalatinsk Test Site, Kazakhstan, *Pure and Appl. Geophy.*, **158**, Issue 1-2, 143-171
- Kim, W. Y., P. Richards, V. Adushkin, and V. Ovtvinnikov (April, 2001), Borovoye digital seismogram archive for underground nuclear tests during 1966-1996, Technical Report
- Levander A. R. (1990), Seismic scattering near the Earth's surface, *Pageoph.*, 132, 21-47
- Levander A. R. and N. R. Hill (1985), P-SV resonances in irregular low-velocity surface layers, *Bull. Seism. Soc. Am.*, 75, 847-864

- Massé, R. (1981), Review of seismic source models for underground nuclear explosions, *Bull. Seism. Soc. Am.*, 71, 1249-1268
- Maupin, V. (1990), Modeling of three-component Lg waves in anisotropic crustal models, *Bull. Seis. Soc. Am.*, 80, 1311-1325.
- Mayeda, K., 1993. mb(LgCoda): A stable single station estimator of magnitude, *Bull. Seis. Soc. Amer.*, 83, 851-861.
- Mayeda, K., and Walter, W., 1996. Moment, energy, stress drop, and source spectra of western United States earthquakes from regional coda envelopes, *J. Geophys. Res.*, **101**, 11195-11208.
- Mayeda, K., M. Pasyanos, J. O'Boyle, S. Myers, W. Walter, and P. Goldstein (2000), Phenomenology research using past Nevada Test Site explosion and earthquake data, 22nd Seismic Research Review on Monitoring of Nuclear Explosions.
- McLaughlin, K. L. and R.-S. Jih (1988). Finite-difference simulations of Rayleigh-wave scattering by shallow heterogeneity, Report AFGL-TR-87-0322, Air Force Geophysics Laboratory, Hanscom Air Force Base, MA, 108 pp.
- McLaughlin, K. L., B. Shkoller, D. E. Wilkins and T. G. Barker (1997), Advances in numerical methods, Maxwell Technologies final report to Air Force Geophysics Laboratory, PL-TR-97-2150, September.
- Myers, S., W. Walter, K. Mayeda, and L. Glenn (1999), Observations in support of Rg scattering as a source of explosion S waves: regional and local recordings of the 1997 Kazakhstan depth of burial experiment, *Bull. Seism. Soc. Am.*, **89**, 544-549.
- Myers, S., J. Wagoner, L. Preston, K. Smith, H. Tkalcic, and S. Larsen (2006), The Effect of Realistic Geologic Heterogeneity on Local and Regional P/S Amplitude Ratios Based on Numerical Simulations, 28th Seism. Res. Rev.
- Mueller, R. A. and J. R. Murphy (1971), Seismic characteristics of underground nuclear detonations, Part 1; seismic spectrum scaling, *Bull. Seis. Soc. Am.*, **61**, 1675-1692
- Murphy, J. R. (1995), "Types of Seismic Events and Their Source Descriptions," in *Monitoring a Comprehensive Test Ban Treaty*, ed. E. Husebye and A. Dainty, P. 225-245, Kluwer Academic Publishers, Boston.
- Murphy, J., B. Barker, and J. Sultanov (2006), A scaling analysis of frequency-dependent energy partition for local and regional seismic phases from explosions, 28th Seism. Res. Rev.
- Nuttli, O. W., *J. Geophys. Res.* (1986a), Yield estimates of Nevada Test Site explosions obtained from seismic Lg waves, 91, 2137-2151. Maupin, V. (1990), Modeling of three-component Lg waves in anisotropic crustal models, *Bull. Seis. Soc. Am.*, 80, 1311-1325
- Nuttli, O. W. (1986b), Lg magnitudes of selected east Kazakhstan underground explosions, *Bull. Seis. Soc. Am.*, 76, 1241 – 1251. Maupin, V. (1990), Modeling of three-component Lg waves in anisotropic crustal models, *Bull. Seis. Soc. Am.*, 80, 1311-1325
- Nuttli, O. W. (1987), Lg magnitudes of Degelen, east Kazakhstan, underground explosions, *Bull. Seis. Soc. Am.*, 77, 679 – 681.

- Nuttli, O. W. (1988), Lg magnitudes and yield estimates for underground Novaya Zemlya nuclear explosions, *Bull. Seis. Soc. Am.*, **78**, 873 – 884.
- Park, J., Lindberg, C.R., and F. Vernon, (1987) Multitaper spectral analysis of high-frequency seismograms, *J. Geophys. Res.*, **92**, 12675-12684.
- Patton, H (1988), Application of Nuttli's method to estimate yield of Nevada Test Site explosions recorded on Lawrence Livermore National Laboratory's digital seismic system, *Bull. Seism. Soc. Am.*, **78**, 1759-1772.
- Patton H. and S. Taylor (1995), Analysis of Lg spectral ratios from NTS explosions: Implications for the source mechanisms of spall and the generation of Lg waves, *Seis. Soc. Am.*, **85**, 220-236
- Patton H. and W. S. Phillips (2005), Regional magnitude research supporting broad-area monitoring of small seismic events, 27th Seismic Research Review
- Patton H. and W. S. Phillips (2006), Regional magnitude research supporting broad-area monitoring of small seismic events, 28th Seismic Research Review
- Patton, H., J. Bonner, and I. Gupta (2005), Rg excitation by underground explosions: insights from source modelling the 1997 Kazakhstan depth-of-burial experiment, *Geophys. Jour. Intl.*, **163**, 1006–1024.
- Phillips, W. S., H. Patton, C. Aprea, H. Hartse, and S. Taylor (2002), Regional magnitude studies in China and surrounding areas, 24th Seismic Research Review - Nuclear Explosion Monitoring, pp. 530-535.
- Press, F. and M. Ewing (1952), Two slow surface waves across North America, *Bull. Seism. Soc. Am.*, **42**, 219-228
- Priestley, K. and H. Patton (1997), Calibration of $m_b(P_n)$, $m_b(L_g)$ scales and transportability of the $M_0:m_b$ discriminant to new tectonic regions, *Bull. Seis. Soc. Am.*, **87**, 1083-1099
- Revenaugh, J. (1995), The contribution of topographic scattering to teleseismic coda in Southern California, *Geophys. Res. Lett.*, **22**, 543-546
- Revenaugh, J. and H. Mendoza (1996), Mapping shallow heterogeneity with teleseismic P to Rg Scattered Waves, *Bull. Seism. Soc. Am.*, **86**, 1194-1199
- Richards, P. G. W. Y. Kim and G. Ekström (1992). The Borovoye Geophysical Observatory, Kazakhstan, *EOS*, **73**, 201-206.
- Richards R., and W. Kim (2005), Equivalent Volume Sources for Explosions at Depth: Theory and Observations, *Bull. Seis. Soc. Am.*, **95**, 401 - 407.
- Ringdal, F., P. Marshall, and R. Alewine (1992), Seismic yield determination of Soviet underground nuclear explosions at the Shagan River test site, *Geophys. J. Intl.*, **109**, 65-77
- Ruud, B., Husebye, E. and Hestholm S. (1993), Rg Observations from Four Continents: Inverse and Forward Modelling Experiments, *Geophys. J. Int.*, **114**, 465-472
- Saikia, C., K. Mayeda, L. Zhu, and R. Herrmann (2005), Developing multiple-frequency discriminants for use with regional coda-amplitude measurements, 27th Seism. Res. Rev.

- Springer, D., G. Pawloski, J. Ricca, R. Rohrer, and D.K. Smith (2002), Seismic Source Summary for All U.S. Below-Surface Nuclear Explosions, *Bull. Seis. Soc. Am.*, **92**, 1806-1840
- Stevens, J. L., G. E. Baker, H. Xu, T. J. Bennett, N. Rimer, and S. Day (2004), The physical basis Lg generation by explosion sources, Final Report to NNSA under contract DE-FC03-02SF22676
- Stevens, J. L., G. E. Baker, H. Xu, T. Bennett, N. Rimer, and S. Day (2004), The physical basis of Lg generation by explosion sources, 26th Seismic Research Review
- Stevens, J. L., G. E. Baker, H. Xu, and T. Bennett (2005), The physical basis of the explosion source and generation of regional seismic phases, 27th Seismic Research Review
- Stevens, J. L., G. E. Baker, and H. Xu (2006), The physical basis of the explosion source and generation of regional seismic phases, 28th Seismic Research Review
- Stevens, J. L., , H. Xu, and G. E. Baker (2007), An Upper Bound on Rg to Lg Scattering Using Modal Energy Conservation, manuscript in prep for submission to *Bull. Seis. Soc. Am.*,
- Takeuchi, H. and M. Saito (1972), Seismic Surface Waves, in *Methods of Computational Physics*, B. A. Bolt (Editor), v. 11, Academic Press, New York, 217-295
- Thomson, D.J., 1982: Spectrum estimation and harmonic analysis, *Proc. IEEE*, 70, 1055-1096.
- Vogfjörd, K. (1997), Effects of explosion depth and earth structure on the excitation of Lg waves: S* revisited, *Bull. Seis. Soc. Am.*, **87**, 1100-1114
- Wuenschel, P.C. (1976), The vertical array in reflection seismology – some experimental studies, *Geophysics*, 41, 219-232
- Xie, X., T. Lay, R. Wu, and Y. He (2006), Near Source Energy Partitioning for Regional Waves in 2D and 3D Models: Contributions of Free Surface Scattering, 28th Seismic Research Review
- Xie, X., Z. Ge, and T. Lay (2005), Investigating Explosion Source Energy Partitioning and Lg-Wave Excitation Using a Finite-Difference plus Slowness Analysis Method *Bull. Seis. Soc. Am.*, **95**, 2412 - 2427.

APPENDIX A: DESCRIPTION OF LOCAL SEMIPALATINSK SEISMOGRAMS

The Institute for Dynamics of the Geosphere (IDG) digitized a large number of local seismic records of 19 nuclear explosions at the Degelen and Balapan test site. For 13 events, no previous local data were available. For 6 events, additional data were added to that delivered under a previous contract. The new data include records from stations not previously available, and records from stations for which data were previously delivered. In the latter case, the new data include longer time series that span the surface waves, which were not included in the earlier dataset. Table 12 (same as in Chapter 2) lists the events and parametric information. The depths and yield are new information delivered with the records. Column 6 lists the number of unique tangential, radial, and vertical records available for each event. There are 309 unique records altogether, 39 tangential, 135 radial, and 134 vertical components. Data represent displacement in mm.

Table 12. Local/near regional data that contain P through Rg arrivals. SD stands for scaled depth, column 6 lists the number of distinct seismograms for each component (there are multiple recordings at many distances – we count these only once). The last column lists location within Semipalatinsk, D for Degelen or B for Balapan.

Date	Time	Yield	Depth	SD	Data t/r/z	Range (km)	m _b	Lat	Lon	Loc
71/12/15	07:52:59	1.3-1.5	146	1.07	3/9/9	7-77	^A 4.68	50.031	77.972	D
85/06/30	02:39:05	100	527	0.93	0/6/5	49-88	^A 5.92	49.857	78.659	B
85/07/20	00:53:16	76	466	0.90	0/8/7	56-86	^A 5.89	49.943	78.783	B
87/05/06 ¹	04:02:08	18	174	0.54	0/9/9	13-83	^I 5.6	49.777	77.984	D
87/07/17 ¹	01:17:09	78	267	0.51	1/7/6	15-84	^I 5.8	49.769	78.035	D
87/10/16 ¹	06:06:07	1.1	82	0.65	0/8/8	19-76	^I 4.6	49.802	78.14	D
87/12/13	03:21:07	130	530	0.86	0/5/5	57-60	^A 6.06	49.957	78.792	B
87/12/20 ¹	02:55:09	3.2	103	0.57	0/8/9	13-83	^S 3.8	49.774	77.975	D
88/04/22 ¹	09:30:09	2	---	---	0/3/3	57-81	^I 4.9	49.824	78.102	D
88/05/04	00:57:06	134	530	0.85	0/6/4	53-84	^A 6.09	49.931	78.741	B
88/06/14	02:27:09	5	271	1.30	0/7/6	67-89	^A 4.8	50.034	78.964	B
88/09/14	04:00:00	140	651	1.03	3/7/7	60-94	^A 6.03	49.879	78.823	B
88/10/18 ¹	03:40:09	2.45	126	0.77	0/8/9	13-83	---	49.802	78.002	D
88/11/12	03:30:06	17	---	---	5/6/7	68-88	^A 5.24	50.048	78.96	B
88/11/23 ¹	03:57:09	19	204	0.63	6/9/9	14-83	^I 5.4	49.765	78.029	D
88/12/17	04:18:09	84	642	1.20	6/6/6	67-98	^A 5.83	49.879	78.924	B
89/01/22	03:57:09	108	580	1.00	6/9/9	58-88	^A 6.10	49.934	78.815	B
89/02/12	04:15:09	74	572	1.12	4/7/9	51-85	^A 5.86	49.911	78.704	B
89/10/04	11:29:57	1.8	94	0.63	5/8/7	16-85	^I 4.6	49.751	78.005	D

¹ Additional data added to that collected under previous contract

^A and ^I indicate m_b from AWE and ISC respectively, ^S indicates Ms from Geoscience Australia's database (http://www.ga.gov.au/oracle/nukexp_form.jsp), which is also the source of event locations

The data are provided in subdirectories of the SEISMOGRAMS directory, named for the event date (e.g. 01-22-89). Each subdirectory has two subdirectories, ASCII and SAC, with data files for each record in the format of the directory name. Filenames are based on the component, the distance to one tenth of a km, and the format. For example, r580.sac is the radial component recorded at 58.0 km. It resides in the SAC subdirectory of SEISMOGRAMS/01-22-89. The

corresponding ascii file is SEISMOGRAMS/01-22-89/ASCII/r580.asc. There are multiple copies of many of the records. Multiples have the suffix '_b' appended to the root of the name. For example, the second copy of the 01-22-89 radial recording at 58.0 km is named r580_b.sac.

APPENDIX B: NEARFIELD PARAMETRIC DATA FROM SEMIPALATINSK EXPLOSIONS

IDG also provided near field tabular data including particle velocity and rise time from 19 Semipalatinsk explosions. The events and their depths and yields are listed in Table 13. The parametric data for each event follow. These are also included in ascii files named parms.txt, in subdirectories named by event date, of the PARAMETRIC directory. These data were used for the analysis reported on in Chapter 6. Subsequent tables also provide the parameters.

Table 13. Local tabular data collected by IDG

Date	Yield (kt)	Depth (m)	m _b
1961/10/11	1.16	141	4.78
1962/02/02	16.9	265	5.63
1964/03/15	23.6	245	5.56
1964/05/16	23.7	266	5.55
1964/06/06	1.05	75	4.42
1964/11/16	23	203	5.64
1965/02/04	17	262	5.1
1965/07/29	1	126	4.5
1965/06/17	12	178	5.24
1965/09/17	10	148	5.22
1965/10/08	15	204	5.47
1965/11/21	29	303	5.61
1965/12/24	6	228	4.94
1966/02/13	125	343	6.26
1967/12/08	12.5	166	5.31
1968/09/29	75	358	5.8
1973/02/16	25	225	5.48
1979/05/31	8.5	183	5.27
1980/06/25	0.3	152	3.7

Date	Yield, kt	Depth, m
11/10/1961	1.16	141

R,m	t ₀ , ms	t _m , ms	t ₊ ,ms	Vm, m/s
-----	---------------------	---------------------	--------------------	---------

Gages which were placed in the main tunnel

6.2	0			
8.7	1			
10.9	1.36			
13.4	2.41			
20	3			
30	4.2			
40	6.2	2.8		18.6

60	10	2.8	6.3	
60	10	2.8	6.3	
60	10	2.8	6.3	
60	8.95			
72	12	1.86		9.85
95	17	1.26		7.23
95	17	2.3		6.4
95	16.6	6.8	7.3	6.5
95	16.6	5	6.3	8
130	23.7	3		5
145	25.1	6	14	3.08
225	39	3.9		2.64
225	39	3.9		2.64
225	42	4.5	18	2.08
244	45	3.5	9	1.87
244		2.5	8.5	2.1
300	56.5			1.85
399	62	5	18	0.9
399	62	5	18	0.67
441	74	4.3	28	0.65
441	74	4.3	28	0.65
555	100	8.6	28	0.49

Gages which were placed in the other tunnels

685	122		28	
827	144		24	
959	168	6.2	27	0.31
1102	198		25	
1130	204	6.8	26.6	0.11
1405	254	9	33	0.158

Date	Yield, kt	Depth, m		
2/2/1962	16.9	265		
R,m	t ₀ , ms	t _m , ms	t ₊ ,ms	Vm, m/s
95	15	3	8	20
95	15	4	12	18
152	26	4	10	16
152	25	3		14

152	25	3		
302	53	6	12	4.8
302	52	5.5	19	6.3
302	52	5.5	19	6.3
360	65	8.5	16	4.8
360	64	7	50	5.7
360	64	7	23	5.7
360	64	7	23	5.7
395	70	3	25	3.4
395	70	9	25	3.75
395	70	1.4	33	3.4
395	70	6	36	3.4
479	85	5.7	19	1.76
479	85	5.7	40	2.85
479	85	5.7	15	2.41
479	86	7	40	2.8
479	86	7	40	2.8
479	86	7	40	2.8
603	110	6	31	1.7
603	110	8	100	1.98
603	109	7	56	1.9
603	109	7	56	1.9
625	112			
625	112	5	46	1.9
625	112	5	40	2.1
625	112	5	40	2.1
625	112	5	40	2.1

Gages which were placed out of main tunnel

961	176	23	56	0.66
961	176	23	56	0.57
961	176	23	56	0.71
1030	201	9.5	44	0.54
1030	201	9.5	44	0.72
1030	201	9.5	44	0.63
1039	203	28	110	0.53
1039	203	13	110	0.53

Date	Yield, kt	Depth, m		
03.15.1964	23.6	245		
points in the main tunnel				
R,m	t0, ms	tn, ms	t+,ms	Vm, m/s
150	25.4	2.9	5.9	17.7
150	26.6	2.6	5.6	
150	26			
250	45	3.4	32.6	10.6
250	45	2.7		
250	44			9.8
300	55	7	34	9.4

300	56	4.4	19.5	6
300	55	2.5		5.5
375	68			3.9
375	68			3.5
375	68.3	4.5		4.5
375	67	3	30	4.3
410	75	5.5	35	3.6
410	74	6.7	38	2.9
410	76	6.6	35	4.5
540	104			1.3
540	104			1.3
540	109	25	85	1.2
540	108	20	95	2.1
540	108	18	77	1.73

points out of the main tunnel

738	134	4.5	45	1.67
1053	192	8	46	0.56
1053	192	8	48	0.67
1639	305	10	60	0.2
2130	392	14	55	0.2
7675	1463	25	76	0.025

Date	Yield, kt	Depth, m		
05.16.1964	23.7	266		
R,m	t0, ms	tm, ms	t+,ms	Vm, m/s
28	3.77			
63.4	10.47			
98.9	15.7	1.6		28.6
148	25.8	1.3	28	18
148	25.3	1.4		15.7
149		1.3	26	16.6
220	38.6			15.6
297	53.4	3		13
297		3.5	33	12.9
298	53			11.6
298	53			11.4
298	54			11.3
398	72.8	2.2		7.5
398	72.5	2.6		5.7
400	72	2		7.6
400	73	2.2		6.5
400		3	20	5.6
549	99	4		2.6
549	97.7	4.5		2.6

581	105	3.8	46	3.5
581	104.5	4.5	46	3.6
593		3.4	28	3.4
676	122.2	7	50	1.6
676	122	7.5	50	1.4
750	140	10	67	1.6
766	142	7	80	1.3
766	142	7	86	1.5

Date	Yield, kt	Depth, m
6/6/1964	1.05	75

R,m	t ₀ , ms	t _m , ms	t ₊ ,ms	Vm, m/s
-----	---------------------	---------------------	--------------------	---------

Gages which were placed in the main tunnel

7.5	0.67			
8.2	0.76			
9	0.87			
16	2.2			
17	2.4			
18	2.56			
28.4	4.6			
29.2	4.9			
30	5			
56	8.5	2.2	8	16
75	16	1.3	22	11
91	16	1.3	16	7
99.5	16.8	1.4		5.9
99.5	16.8	1.4		5.4
147.5	25.8	1.5		2.9
147.5	25	1.3	13	3.65
147.5	25	1.2	9	3.1
198	35.4	2	40	1.25
198	35.4	2	40	1.4

Gages which were placed in the other tunnels

722	130	12	36	0.108
1148	208	15	40	0.055

Date	Yield, kt	Depth, m
11.16.1964	23	203

R,m	t ₀ , ms	t _m , ms	t ₊ ,ms	Vm, m/s
109	18	4.2	12	41.5
279	53	2.8	20	6.8
279	53	2.8	20	6.8
279	53	2.8	20	6.8
380	70	3.5	14	5.46

380	70	3.5	21	6.75
380	70	4		6.46
479	86	5.5	25	3
479	86	5		3

Date	Yield, kt	Depth, m
2/4/1965	17	262

R,m	t ₀ , ms	t _m , ms	t ₊ ,ms	Vm, m/s
27	3.7			
57	9.7			
57	10			
92	16			
147		2.5	50	10
297		3.00	70	4.5
297	54	2.4	59	3.8
297	53.5	2.5		4.2
297	53	2.3		5.3
475	86	5		2.5
475	86	5		2.6
600	108	7	32	2.46
600	109	7	35	2.6
600		8	30	2.39
600	108	9		2.28
750	136	11.5	40	1.68
750	136	11.2	50	1.8
750		15	55	1.82
750	136.5	10		1.4
750	136	11.5		1.56

Date	Yield, kt	Depth, m
06.17.1965	12	178

R,m	t ₀ , ms	t _n , ms	t ₊ ,ms	Vm, m/s
238	44	2.8	44	7.4
238	42.5	2.7	50	6.7
300	54.6	2		5.9
300	55.5	2		5.6
400	73.9	2.8		3.6
400	73	3		2.9
480	88	5.5	78	2.3
480	89	5.8		2.1
480	87	5.5	71	2.1
600	119	23.5	177	0.94

Date	Yield,	Depth,
07.29.1965	kt	m
	1	126

R,m	t0, ms	tm, ms	t+,ms	Vm, m/s
37	6.7	3		15.6
37.4	6.9	3		14.5
38.5	7.1			14.4
38.5	7			13.7
47.5	8.2	3.5		8
47.6	8.4			
48	8.7			9
67	12.3			6.4
67	12.8			6
84	15			
84	14.8	4		4.4
87.8	15.3	7.6	23	3.8
88	15.6			
88	15.4	6.6	27	4.1
88	15.4	6.6	23	4.2
88	15.5			
100	17.8	4.6	25	3.8
112	20.3	4.6	27.5	3.1
112	20.6	4.7	27.4	3.78
116	20.8	5	33	3.2
117	21.6	7.2	36	2.76
117	21	7.7	30	2.9
117	21	7.4	34	3.3
135	25	8.3	39	2.73
135	24	8	37	2.6
162	29.4	6	42.5	1.48
162	29.4	8	43	1.42
164	30	7.6	29	1.36
164	30	8.2	30	1.4
165	30	8.4	47	1.58
165	30	8	45	1.5
165	30	8.1	36	1.46
200	35	8.4		1.06

200	36.4	8.9	46	1.2
247	45	9.8	28	0.9
247	44	10		0.68
248	45	11	25	0.63
249	44	12		0.64
249	43	11	38	0.78
275	48.5	11	35.6	0.59
275	49	11	35	0.58
289	52	11	26	0.53
290	50	11.4	35.6	0.54
290	50.4	12.5	35	0.58
492	93	12	34	0.24
492	90	11.4	31	0.32

Out of the tunnel

650	115	14	35.6	0.19
650	120	12.5	36	0.19
769	147	11.5	37	0.1
769	154	10	38	0.08

Date	Yield, kt	Depth, m		
10/08/1965	15	204		
R,m	t0, ms	tm, ms	t+,ms	Vm, m/s
150	25			13
150	25			12.5
200	32	3		5.7
200	33	2		5.6
200				6.6
200				6.5
290	50	4.5		5.4
360	59	3.7		4.1
360	59	3.7		4.24
360	60	3.7		3.65
430	75	5		2.85
430	74	4		2.6
430	74	4		2.5
510	90	5		2.09
510	90	5		2.5
510	88	5		2.07
600	109	10		1.17
600	108	9		1.15
600	107	8.5		1.08
700	127	11		1.03
700	127	10		0.89
700	130	9		0.79

Date	Yield, kt	Depth, m		
09.17.1965	10	148		
R,m	t0, ms	tm, ms	t+,ms	Vm, m/s
100	13			
150	25			
200	34.5	2	10	9.7
200	36.5			
250	44.6	2	11	8.9
250	45.7	1.5	12	7.5
300	56	1		8
300	55			
350	61.5	1.6		7.9
350	61.8	1.3		7.1
350	61.5	1.6		7.8
400	71.6	1.9		7
400	71.6	1.9		6.15
450	80.7	2.3		3.85
450	80.7	2.3		3.93
450	81.6	2.3		4.3

Date	Yield, kt	Depth, m		
11.21.1965	29	303		
R,m	t0, ms	tn, ms	t+,ms	Vm
150	25.9			19.2
150	25.8			18.6
200	35.6			14.5
200	35.9			15.5
300	52.2			7
300	54.5			7
300	53			6.6
300	54			5.6
307				7
475	90		40	4.8
475	88			3.7
475	88			3.8
475	87			5.2
550	100	7.7		3
550	102	7		2.8
550	99	8		3
550	102	7.5		3
550	104			3
550	103.5			3
550	100			2.6
550	101			2.9
600	111	9	46	2.1
600	110	9.4	60	2.8
600	110	9	65	2.2

600	109	9	62	2.8
600	111	9	64	2.5
600	110			2.2
650	122		51	2.6
650	121	10		2.6
650	122	10		2.7
650	119	10	66	2
695	128	8	71	2.1
695	129	9	63	1.9
695	132	8	75	2
695	128			1.9
740	139	6		1.6
740	140	7		1.5
740	142	7		1.7
740	140			1.3
740	140			1.2

Date	Yield, kt	Depth, m		
12.24.1965	6	228		
R,m	t0, ms	tm, ms	t+,ms	Vm, m/s
258	47	4	20	1.2
258	48			1.35
308	56.5	4	20	1.29
308	58	4.5		1.36
358	67.5	4.8	22	1.12
358	69	5.3		0.85
400	80	8.2	19	1.1
400	77	7.6	18	0.8
400	78	9.7	24	0.98
400	78.5	8.5		0.84
400	78.5	8.5		0.95
458	94		32	0.38
458	91.5	7	26	0.36
458	89	7	40	0.43
458	92			0.46
458	91	8		0.46
508	101	14.8		0.37
508	98	12	40	0.49
558	115	8.5		0.42
558	110	10	50	0.44
558	114	8.5	50	0.38
558	112	9	50	0.3
608	121	16	50	0.34
658	134	16	51	0.36

Date	Yield, kt	Depth, m
------	-----------	----------

02.13.66 109-125 343

R,m	t0, ms	tm, ms	t+,ms	Vm, m/s
-----	--------	--------	-------	---------

Gages which were placed in the main tunnel

247	43.5	7		20
247	42.5	7.6		16
247	43	7		18
297	52	8		15.55
348		10	24	10
348	60	8.6	30	9.23
348	60.6	8.4		8.4
348	60	8.8	30	10.1
397	69	10.5		8.57
397	69	11		10
397	69	10		7.1
398		10	30	7
457	80	10.5		9
457	79.5	10	41	6.9
457.5	80	10	41	7.93
458		10	43	7
497	84	10		8.1
497	86.7	10		8.1

600	104	10.5	37	5.19
600	104	10.5	39	6.2
600	103.5	10.5	35	6.2
600		10	33	6
600	104	10.5		5
600	103.5	8.2		3.6
600	104	9		4.6
700	121	10		3.08
700	121	10		2.9
700	121	10		3.2
700	121	10		3.2
800	138	13		2.6
800	138	13		2.6
800	138	13		2.6
800	138	13		2.6

Gages which were placed in the other tunnel

630	106	14	48	5.07
630	105	14.5	47	5.4
630	105	13.3	51	5.6
778	132	14	30	2.87
778	131			
778	133	14.7	30	2.9
850	147	15.5	83	2.8

878	149	16.2		2.2
878	150	14.7	44	2.37
878	150	15.4	73	2.87
964	165	15.6	90	2.02
964	165	16.3		2.12
964	163	13		1.9
964	165	13.2		2.5
1025	179	14.2	87	2.2
1118	194	15.4	81	1.65
1118	193	13.8	90	1.9
1238	222	16.8		1.36
1400	242	17.3	94	1.4

		Depth, m
Date	Yield, kt	
12/08/1967	12.5	166

R,m	t0, ms	tm, ms	t+,ms	Vm, m/s
164.7				14
163.1				14
298	57.5	6.9		4.25
300	56.7	4.8		5.27
358	69	12.2		4.2
359	69.5	11.5		3.8
359	69.5	12.8		3.76
410	84	10		2.08
410	84	10		2.02
465	91	9.6		1.76
465	90	9.7		1.76
510	104	5.2		1.5
510	104	5.2		1.59

		Depth, m
Date	Yield, kt	
09.29.68	75	358

R,m	t0, ms	tm, ms	t+,ms	Vm, m/s
282	49.3	5.5		12.7
282	49.4	6		13
352	57.8	6	110	8.5
352	58	6		8
352	57.7		110	8.7
532	89.2	8	100	4.2
532	89.2	8	150	4.2
532	89.2	8		4.6
532	89.2	8	109	4.7
622	107			
622	106.5			4.2
622		4.5		4.2
780	139	8.2		1.6

780		7		1.9
927	167	17	104	1.7
927	167	17	109	1.6

Date	Yield, kt	Depth, m			VmR
02.16.1973	25	225			1565
R,m	t0, ms	tm, ms	t+,ms	Vm, m/s	
125	30	3.5	28.5	12.5	1483
198	45	3.5	32.9	7.5	930
224	48	4.7	30.7	6	1030.4
324	67	7.3	30.7	2.87	803.7
368	75	7.3	35.1	2.8	458
423	85	7.9	32.1	1.9	488
550	115	12	33.6	0.83	432
610	125	12.6	38	0.8	
720	151	13.7	40.9	0.6	

Date	Yield, kt	Depth, m			
05.31.1979	8.5	183			
R,m	t0, ms	tn, ms	t+,ms	Vm, m/s	
91	11.2	1.6		12	
110	14.4	1.6		6.3	
143	21.2	1.8		4.5	
195	31.8	2.5		2.8	

Date	Yield, kt	Depth, m			
06.25.1980	0.3 (0.15-?)	152			
R,m	t0, ms	tm, ms	t+,ms	Vm, m/s	
155	32.7	7	28	0.8	
155	34.5	7.5	25	0.84	
244	54	7	40	0.6	
244	54	7	41	0.6	
310	67.5	8.1	46	0.45	
310	68.5	7.2	44	0.45	

